Indian Institute of Technology Guwahati
Department of Physics
Ph.D. Thesis

Generalized Uncertainty Scenario of Quantum Gravity in White Dwarfs and Extended Gravity Scenarios in Quark Stars and Inflationary Cosmology

Arun Mathew

Thesis Supervisor: Dr. Malay Kumar Nandy
December 2020

भारतीय प्रौद्योगिकी संस्थान गुवाहाटी
Indian Institute of Technology Guwahati

Generalized Uncertainty Scenario of Quantum Gravity in White Dwarfs and Extended Gravity Scenarios in Quark Stars and Inflationary Cosmology

A Thesis submitted for the award of the degree of
Doctor of Philosophy in Physics
by

Arun Mathew

Thesis Supervisor: **Dr. Malay Kumar Nandy**

Department of Physics
Indian Institute of Technology Guwahati
Guwahati 781039 India

December 2020

Declaration

The work contained in the thesis entitled "**Generalized Uncertainty Scenario of Quantum Gravity in White Dwarfs and Extended Gravity Scenarios in Quark Stars and Infationary Cosmology**" has been carried out at the Department of Physics, Indian Institute of Technology Guwahati, India, by me with the supervision of Dr. Malay Kumar Nandy. The material of this thesis has not been submitted elsewhere for any other degree. Works presented in the thesis are all my own unless referenced to the contrary in the text.

Sd/-
(Arun Mathew)

23 December 2020


भारतीय प्रौद्योगिकी संस्थान गुवाहाटी
Indian Institute of Technology Guwahati

Disclaimer

The bibliography included in this thesis is by no means complete but contains the ones which are consulted thoroughly by me. I apologize for inadvertently missing out some of the research papers, review articles and other scientific documents pertaining to the focus of this thesis.


भारतीय प्रौद्योगिकी संस्थान गुवाहाटी
Indian Institute of Technology Guwahati

Certificate

Indian Institute of Technology Guwahati
Department of Physics
Guwahati 781039 India

Dr. Malay Kumar Nandy
Associate Professor
Phone: +91-(361)-258-2706, 4706
Mobile: +91-94010-86706
Email: mknandy@iitg.ac.in

This is to certify that the work contained in the thesis entitled "**Generalized Uncertainty Scenario of Quantum Gravity in White Dwarfs and Extended Gravity Scenarios in Quark Stars and Infationary Cosmology**" has been carried out by Mr. Arun Mathew (Roll No. 136121003) with my supervision, and that this work has not been submitted elsewhere for the award of any other degree.

23 December 2020

Sd/-
Dr. Malay Kumar Nandy
(Thesis Supervisor)

To My Wife
Anu Pauly Pudukkaden
and
To My Mother
Mariamma Abraham

Acknowledgements

I would like to extend my heartfelt thanks with a deep sense of gratitude and respect to all who had lent me their help during the course of this programme.

First and foremost, I wish to express my most sincere gratitude to my esteemed supervisor and mentor Prof. Malay Kumar Nandy for his scholarly guidance, comments, suggestions, corrections and wise counsel I received during this research work. I am indebted to him for considering me as a project student and then as a Ph.D student. He graciously gave his valuable time for critical discussion and his insightful feedback pushed me to sharpen my thinking and brought my work to a higher level. Without his guidance and constant encouragement this Ph.D. thesis would not have been achievable. Being one of the best teachers of advanced Physics, I am privileged to gain much knowledge in various fields in physics. He has been a constant source of academic support, and sharpened my individual insight and ideas and trained me to become an independent researcher. I am fortunate to be his student.

I gratefully acknowledge the financial support received from Government of India, Ministry of Human Resource Development for granting a Doctoral Fellowship.

I am indebted to Indian Institute of Technology, Guwahati, and its administrative and technical staff for their official and technical assistants in various matters.

I am extremely grateful to my doctoral committee members, Prof. Amarendra Kumar Sarma (Chairman), Prof. Debaprasad Maity, Prof. Manmohan pandey, Prof. Padma K. Padmanabhan, Prof. Siddhartha Pratim Chakrabarthy for their constructive criticism and appreciation during all my Annual Progress Seminars and Synopsis seminar. I would like to thank Prof. Bibhas Ranjan Majhi for kindly agreeing to head my doctoral committee of the synopsis seminar in the absence of the chairman. I am grateful to all of them for letting my synopsis seminar be an enjoyable moment, and for valuable comments and suggestions. I would also like to thank the present Head of Department of Physics Prof. Subhradip Ghosh and the former Head of the Department Prof. Poulose Poulose for facilitating a comfortable and pleasant environment for this doctoral program.

I am indebted to Mr. Muhammed Shafeeque for his contribution in the study of $f(R,T)$ gravity model in stellar structures that is carried out in Chapter 6 of this thesis. I gratefully acknowledge Dr. Tapas Singha for his support and encouragement during his stay at IIT Guwahatti. I would like to thank Prof. Ravishankar and Prof. Senthilkumaran for their hospitality and for providing various facilities at IIT Delhi during my visit.

I am privileged to have the sincere friendship of Dr. Deep Chandra Joshi, who helped me in my crucial time to whom I am extremely grateful. I would also like to thank the following people for their love, care and support, Mr. Anoop Painkidiyan, Dr. Piyoosh Purushothaman Nair, Dr. Jiss Joseph Nallikkuzhy, Dr. Vasudevan Matampu Suryasarman, Mr. Thomas Thankachan Daniel, Dr. Sonu Johnkutty, Dr. Aneesh Rajendran, Dr. Haris Bavattu Chalil, Dr. Suresh Babu Muraleedharan, Mr. Dileep Purushothaman, Dr. Sajith Soman, Dr. Vivek Lukose, Mr. Hrishikesan Vadakkedath Madhavan, Dr. Vishnu Venugopal Thuruthiyil, Mr. Suvin Padinjare Venthuruthiyil, Mrs. Amartha Suresh, Mr. Jagajeevan Remadevi. They have been unwavering in their personal and professional support during the course of my work.

I wish to express my deepest gratitude to my friends, Abel Mundaparambil Joseph and Paul Soman Kuruvilla for their timely advices and moral supports on my personal matters. I couldn't have survived my hard times without them.

I express my sincere thanks to my high school friends, Dipu Francis, Jobish Kattumattathiil, Dr. Ampady Sreedharan and Tijo Joseph for their unconditional love and support, without whom my life would have been most difficult. I am debted to them for ever. Also I gratefully remember my mathematics teachers Sr. Jain Kuttikal and my uncle Blaithara George Thomas whose pedagogical talent ignited my love for mathematics. I would also extend a special thanks to Mrs. Sudha Suresh for taking extra effort to help me with Malayalam language. I would also like to thank my physics teacher Mrs. Anita.

I am grateful to my parents Mariamma Abraham and Puthenpurayil Varkey Mathew for their unconditional love, trust and endless patience. I thank my mom for her sacrifices, that had laid down the foundations of my academic life, without her effort, I would have perished long back. I thank my father for planting the initial seed of scientific temper in me, which later became my way of life. I am indebted to my cousin Dr. Anup Thomas, and my brother Alwyn Mathew for their love and care.

I would also like to thank my Aunt Joyamma Puthenpurayil Varkey for her timely advices and directions that set my path straight.

Finally, I would like to express my deepest appreciation to my wife, love of my life, Anu Pauly Pudukkaden for her sacrifice and patience during this research period. Despite of all her physical weaknesss (as she was on her family way), she was always there for me giving support and encouragement. Words cannot express how grateful I am to my life partner for all her sacrifices, and patience that she had made during my research period.

23 December 2020 Arun Mathew

Synopsis

The present dissertation deals with a variety of topics in gravitation, such as, stellar structures of white dwarfs and quark stars, as well as reheating following the inflationary phase of the cosmos. Studies in these areas are important in the contemporary times as there have been various unsettled issues in the recent literature in these areas of gravitation.

For example, the well-known Chandrasekhar's limit has been proved to be non-existent in the current literature as the effect of quantum gravity via the generalized uncertainty scenario is taken into account. However, many astrophysical observations are based on the assumption of the existence of Chandrasekhar's limit. In this thesis, by employing general relativity, it is proved that Chandrasekhar's limit robustly exists even when the quantum gravity effects are included.

Furthermore, there have been various astronomical observations on pulsars which are thought to be neutron stars. Recent observations suggest that their masses can be as high as $\sim 2\ \mathrm{M}_\odot$. However, calculations based on general relativity give rise to maximum stable mass configurations substantially lower than $2\ \mathrm{M}_\odot$, the exact value of the maximum mass depends on the equation of state used. In this thesis, an extended gravity model with gravity-matter coupling is employed along with the assumption that the massive pulsars are mostly composed of quark-gluon plasma. With these assumptions, it is proved that such massive stars can reach a maximum stable mass $\sim 2\ \mathrm{M}_\odot$. Thus the extended gravity scenario is able to explain observations at the scales of neutron stars. It would therefore be interesting to study the consequences of the extended gravity scenario at a different scale such as in the inflationary phase of the Universe.

With this motivation, this thesis employs an extended gravity model to study the reheating phase following the inflationary phase in the early Universe. The dynamics of evolutions in different stages in the reheating phase are studied in detail. Since the available literature in the area of reheating is not substantial, this work is expected to find importance in the scientific community.

In the following, we present brief summaries of the Chapters in the thesis together with a few illustrations for convenience in reading.

In Chapter 1, we present introductions to the background concepts that are useful in the subsequent chapters.

Chapter 2 considers the Generalized Uncertainty Principle (GUP) that carries the imprint of quantum gravity and introduces a minimal length scale [100] into the description of space-time. It effectively changes the invariant measure of the phase space [53] through a factor $(1+\beta\mathbf{p}^2)^{-3}$ so that the equation of state for an electron gas undergoes a significant modification from the ideal case. It has been shown [180] that the ideal Chandrasekhar's limit ceases to exist when the modified equation of state due to the generalized uncertainty is taken into account. To assess the situation in a more complete fashion, we analyze in detail the mass-radius relation of Newtonian white dwarfs [132] whose hydrostatic equilibria are governed by the equation of state of the degenerate relativistic electron gas subjected to the generalized uncertainty principle. As the constraint of minimal length imposes a severe restriction on the availability of high momentum states, it is speculated that the central Fermi momentum cannot have values arbitrarily higher than $p_{\max} \sim \beta^{-1/2}$. When this restriction is imposed, it is found that the system approaches limiting mass values higher than the Chandrasekhar mass upon decreasing the parameter β to a value given by a legitimate upper bound. Instead, when the more realistic restriction due to inverse β-decay is considered, it is found that the mass and radius approach the values 1.4518 $\mathrm{M}_\odot$ and 601.18 km [132] near the legitimate upper bound for the parameter β. The result is illustrated in Figure 2.4.

Moreover, the equation of state of the electron degenerate gas in a white dwarf is usually treated by employing the ideal dispersion relation. However, the effect of quantum gravity is expected to be inevitably present and when this effect is considered through a non-commutative formulation, the dispersion relation undergoes a substantial modification [27]. In Chapter 3, we take such a modified dispersion relation and find the corresponding equation of state for the degenerate electron gas in white dwarfs. Hence we solve the equation of hydrostatic equilibrium and find that this leads to the possibility of the existence of excessively high values of masses exceeding the Chandrasekhar limit although the quantum gravity effect is taken to be very small. It is only when we impose the additional effect of neutronization (inverse β-decay) that we obtain white dwarfs with masses close to the Chandrasekhar limit with nonzero radii at the neutronization threshold. We demonstrate these results by giving the numerical estimates for the masses and radii of Helium, Carbon, and Oxygen white dwarfs [133]. Figure 3.3 illustrates the mass-radius relation obtained from this formulation.

As stated earlier, various recent theoretical investigations suggest that gravitational collapse of white dwarfs is withheld for arbitrarily high masses if the equation of state is described by the generalized uncertainty principle (GUP). There have been a few attempts to restore the Chandrasekhar limit but they are found to be inadequate from different perspectives and some of them led to unphysical mass-radius relations [156, 157]. In Chapter 4, we rigorously resolve this problem by analyzing the dynamical instability in general relativity. We confirm the existence of Chandrasekhar's limit as well as stable mass-radius curves that behave consistently with astronomical observations. Moreover, this stability analysis suggests gravitational collapse beyond the Chandrasekhar limit [136] signifying the possibility of compact objects such as neutron stars and black holes. Figure 4.3 illustrates the eigenfrequency curves determining the instability of white dwarfs higher than the Chandrasekhar mass limit.

In addition, Chapter 5 carries out a general relativistic instability analysis of white dwarfs governed by an equation of state coming from a modified dispersion relation. As previously described in Chapter 3, Newtonian gravity predicts the existence of white dwarfs with masses far exceeding the Chandrasekhar limit when the equation of state of the degenerate electron gas incorporates the effect of quantum spacetime fluctuations (via a modified dispersion relation) even when the strength of the quantum gravity fluctuations is taken to be very small. In Chapter 5, we show that this Newtonian "super-stability" does not hold true when the gravity is treated in the general relativistic framework. Employing dynamical instability analysis, we find that the Chandrasekhar limit can be reassured even for a range of high strengths of quantum spacetime fluctuations with the onset density for gravitational collapse practically remaining unaffected [135]. Figure 5.1 illustrates the eigenfrequency curves determining the instability of white dwarfs higher than Chandrasekhar's limit.

We propose a form of gravity-matter interaction in Chapter 6 given by ωRT in the framework of $f(R,T)$ gravity and examine the effect of such interaction in spherically symmetric compact stars. Treating the gravity-matter coupling as a perturbative term on the background of Starobinsky gravity $R+\alpha R^2$, we develop a perturbation theory for equilibrium configurations. For illustration, we take the case of quark stars and explore their various stellar properties. We find that the gravity-matter coupling causes an increase in the stable maximal mass [137] which is relevant for recent observations on binary pulsars [16, 57, 64, 71]. Figure 6.5 illustrates the mass-radius relations for quark stars in this extended gravity model.

Thus the extended gravity scenario is able to explain observations at the scales of compact stars. It would therefore be interesting to study the consequences of the extended gravity scenario at a different scale such as in the inflationary phase of the Universe. Consequently, in Chapter 7, we employ a viable $f(R)$ gravity model capable of giving an inflationary phase in order to study the subsequent reheating phase due to particle creation at the expense of energy in the scalaron field. Since quantum mechanics is expected to play a dominant role in particle creation, we formulate a plausible scenario of reheating obeying Heisenberg's uncertainty principle that imposes constraints on the particles that can be created in the configuration space. We show that, so long as the energy available in the scalaron field is sufficient to populate the entire configuration space, the energy density of the particles grows, attaining a maximum value giving an efficient reheating. Beyond this maximum, the available energy becomes insufficient to populate the entire configuration space leading to a declining energy density [134].

We further find that there is a negligible growth of energy density in the inflationary phase that lasts for $\sim 10^2\, t_{\rm P}$, although particles are constantly created in this phase. The subsequent reheating phase spans for $\sim 10^{11}\, t_{\rm P}$ and it begins with a well-defined preheating stage lasting for $\sim 10^5\, t_{\rm P}$, making a cross-over to a thermilization regime. The temperature at the cross-over is found to be $T_{\rm x} \sim 10^{12}$ GeV corresponding to a temperature of $T_r \sim 10^{13}$ GeV [134] at the end of reheating. Figure 7.8 illustrates the growth in energy density in the reheating phase.

Finally, Chapter 8 presents a brief conclusion of the thesis together with a few open problems. In addition, two Appendices A and B analyze the implication of the extended gravity models in the solar system and on the Jeans instability of the interstellar gas clouds, respectively. It is found that the extended gravity models of Chapters 6 and 7 are consistent with solar system tests and the typical free-fall time scale for star formation, respectively.

List of Publications

1. **Arun Mathew** and Malay K. Nandy, *Existence of Chandrasekhar's limit in generalised uncertainty white dwarfs*, Royal Society Open Science **8**, 210301 (2021)
2. **Arun Mathew** and Malay K. Nandy, *Numerical code and data for the stellar structure and dynamical instability analysis of generalised uncertainty white dwarfs*, Dryad, Dataset (2021) *
3. **Arun Mathew** and Malay K. Nandy, *Primordial reheating in $f(R)$ cosmology by spontaneous decay of scalarons*,arXiv preprint: arXiv:2012.13960 [gr-qc] (December 2020)
4. **Arun Mathew** and Malay K. Nandy, *Prospect of Chandrasekhar's limit against modified dispersion relation*, General Relativity and Gravitation **52**, 38 (2020)
5. **Arun Mathew**, Muhammed Shafeeque, and Malay K. Nandy, *Stellar structure of quark stars in a modified Starobinsky gravity*, The European Physical Journal C **80**, 615 (2020)
6. **Arun Mathew** and Malay K. Nandy, *Effect of minimal length uncertainty on the mass-radius relation of white dwarfs*, Annals of Physics **393**, 184 (2018)
7. **Arun Mathew** and Malay K. Nandy, *Noncommutative dispersion relation and mass-radius relation of white dwarfs*, Research in Astronomy and Astrophysics **18**, 151 (2018)
8. **Arun Mathew** and Malay K. Nandy, *General relativistic calculations for white dwarfs*. Research in Astronomy and Astrophysics, **17**, 61, (2017). *

---

* These publications are not included in the thesis.

Contents

List of Figures

List of Tables

Chapter 1

Introduction

In this Chapter, we introduce the general concepts applicable to a variety of physical systems. This chapter represents a survey across a wide variety of the existing literature useful for the subsequent chapters on specialized topics that represent new research contributions in astrophysics and gravitation in systems such as white dwarfs and quark stars, and the cosmological phenomena of inflation and reheating.

1.1 Generalized uncertainty principle

In recent years we find in the literature a contrasting perspective on the Heisenberg principle of uncertainty. Quantum theories of gravity, namely, string theory [8, 112], black hole physics [123, 124, 189], path-integral quantum gravity [161–164], and lattice quantum gravity [77], predict the existence of a fundamental observable length scale in contrast with the Heisenberg uncertainty principle. Long ago, the existence of a fundamental length was shown by Mead [140] by considering the uncertainty in measuring the position of a particle when it is observed through a Heisenberg microscope by a photon with which the particle is assumed to interact both electromagnetically and gravitationally. More recently, Pedram [171, 172] suggested a possible variant of deformed commutation relation that admits a non-zero minimum uncertainty in position and a maximal observable momentum. Garay [74] has reviewed various routs in quantum gravity theories through which a minimal length uncertainty can be established.

1.1.1 Heisenberg uncertainty relation

The Heisenberg uncertainty principle is based on the interaction between the test particle and photons observed through a classical apparatus. This is evident from the Gedanken-Experiment, where a photon is allowed to scatter off an electron into the Heisenberg's microscope so that the position of the electron could be observed. The precision with which one can measure the position has an uncertainty Δx which is connected to the uncertainty in momentum Δp_x via the Heisenberg uncertainty principle [86, 87, 177]

$$\Delta x\, \Delta p_x \geq \frac{h}{4\pi}. \tag{1.1}$$

The origin of this principle can be understood by the above-mentioned Gedanken-Experiment of observing the electron through the Heisenberg microscope. In the processes of measurement of position, the photon incident on the electron must get scattered (due to electromagnetic interaction) into the microscope with a cone of half-angle θ. The uncertainty in the measurement of position Δx can therefore be estimated as

$$\Delta x = 1.22 \frac{\lambda}{2\mu \sin\theta} \tag{1.2}$$

where λ is the wavelength associated with the photon and μ is the refractive index of the medium (here, $\mu = 1$). The uncertainty in momentum transferred to the electron can be estimated as $\Delta p_x \approx p \sin\theta$, where p is the momentum of the photon given by $p = \frac{h\nu}{c} = \frac{h}{\lambda}$. Thus we have

$$\Delta p_x \approx \frac{h}{\lambda} \sin\theta \tag{1.3}$$

The Heisenberg uncertainty relation (1.1) follows directly from equations (1.2) and (1.3).

1.1.2 Modification in the uncertainty relation due to Newtonian gravity

The next obvious question would be how the Heisenberg uncertainty relation is modified when the gravitational interaction between the electron and the photon is considered in addition to the electromagnetic interaction. A heuristic estimate of the gravitational contribution could be obtained using Newtonian gravity by considering the photon as a point particle with mass $\frac{p}{c}$. If the electron is in a region of characteristic size L, inside of which it interacts with the photon, it experiences a gravitational acceleration estimated as [1]

$$|\vec{g}| \approx \frac{G(p/c)}{L^2}. \tag{1.4}$$

During this interaction, which occurs within the characteristic time scale L/c, the electron acquires a velocity and moves a distance Δx_{grav}, that can be estimated as

$$\Delta x_{\text{grav}} = \frac{1}{2} |\vec{g}| \left(\frac{L}{c}\right)^2 = \frac{G}{c^3} p \approx \frac{\ell_{\text{P}}^2}{\hbar} \Delta p_x \tag{1.5}$$

which is the uncertainty created solely by the gravitational interaction. Thus the total uncertainty in position will be given by

$$\Delta x = \Delta x_{\text{Heisen}} + \Delta x_{\text{Grav}} \approx \frac{\hbar}{\Delta p_x} + \frac{\ell_{\text{P}}^2}{\hbar} \Delta p_x. \tag{1.6}$$

This leads to the modified uncertainty relation

$$\Delta x\, \Delta p_x \approx \hbar + \frac{\ell_{\mathrm{P}}^2}{\hbar}(\Delta p_x)^2. \tag{1.7}$$

As one would expect, the relevance of gravitational interaction in the quantum regime would be appreciable only at high energy scales where such modified uncertainty relation is expected to show its signatures.

The above modification automatically implies the existence of a minimal length $\Delta x_{\mathrm{min}} = 2\ell_{\mathrm{P}}$. The existence of this minimal length is an automatic consequence of quantum gravity that can be connected to a grainy or foamy structure of space-time perceptible at ultra-high energy scales.

The simplest generalized uncertainty relation that incorporates minimal length has the form [100]

$$\Delta x\, \Delta p \geq \frac{\hbar}{2}\left[1 + \beta(\Delta p)^2\right] \tag{1.8}$$

where $\beta \sim \ell_{\mathrm{P}}^2/\hbar^2$. This relation admits a minimal uncertainty in position $\Delta x_{\mathrm{min}} = \hbar\sqrt{\beta}$ in contrast with the standard quantum mechanics where the position uncertainty can be made arbitrarily small by making uncertainty in momentum arbitrarily large. Any pair of observables represented by Hermitian operators A and B satisfies the inequality $\Delta A\, \Delta B \geq |\langle [A, B]\rangle|$. Therefore the commutation relation that leads to the above relation is obtained as $[x_i, p_j] = i\hbar\, \delta_{ij}\left(1 + \beta\mathbf{p^2}\right)$.

1.1.3 Modification in the uncertainty relation due to general relativity

Similar result is obtained in a more rigorous treatment based on general relativity [1], where the motion of the electron is disturbed by the perturbations generated by electromagnetic radiation moving in the Minkowski metric. Consider a plane electromagnetic wave moving in the x-direction generating small perturbations on the metric given by $g_{\mu\nu} = \eta_{\mu\nu} + h_{\mu\nu}$, where $|h_{\mu\nu}| \ll 1$. Imposing Lorentz gauge condition and retaining linear order terms, the Einstein field equations reduce to

$$\Box\left(h_{\mu\nu} - \frac{1}{2}\eta_{\mu\nu}h\right) = -\frac{16\pi G}{c^4}T_{\mu\nu} \tag{1.9}$$

with

$$\Box = \frac{1}{c^2}\frac{\partial^2}{\partial t^2} - \frac{\partial^2}{\partial x^2} - \frac{\partial^2}{\partial y^2} - \frac{\partial^2}{\partial z^2} \quad \text{and} \quad h = \eta^{\mu\nu}h_{\mu\nu}. \tag{1.10}$$

The energy-momentum tensor $T_{\mu\nu}$ of the electromagnetic field is given by

$$T_{\mu\nu} = F_{\mu\alpha}F^{\alpha}_{\nu} + \frac{1}{4}\eta_{\mu\nu}F_{\alpha\beta}F^{\alpha\beta} \tag{1.11}$$

where $F_{\mu\nu}$ is the electromagnetic field tensor. For electromagnetic radiation moving in the x-direction, with the electric field $\mathbf{E}$ in the y-direction and the magnetic field $\mathbf{B}$ in the z-direction, the energy-momentum tensor reduces to

$$T_{\mu\nu} = \frac{\mathbf{E}^2 + \mathbf{B}^2}{2} \begin{pmatrix} 1 & 1 & 0 & 0 \\ 1 & 1 & 0 & 0 \\ 0 & 0 & 0 & 0 \\ 0 & 0 & 0 & 0 \end{pmatrix} = u \begin{pmatrix} 1 & 1 & 0 & 0 \\ 1 & 1 & 0 & 0 \\ 0 & 0 & 0 & 0 \\ 0 & 0 & 0 & 0 \end{pmatrix} \quad \text{where} \quad u = \frac{\mathbf{E}^2 + \mathbf{B}^2}{2} \tag{1.12}$$

with $S_x = cu$ being the only non-vanishing component of the Poynting vector, while the Maxwell stress tensor,

$$\sigma_{ij} = E_i E_j + B_i B_j - \frac{1}{2} \left(\mathbf{E}^2 + \mathbf{B}^2 \right) \delta_{ij} \tag{1.13}$$

has one non-vanishing component, $\sigma_{xx} = -u$. The reduced form of the energy-momentum tensor in this case implies a perturbation in the metric tensor of the form

$$h_{\mu\nu} = \phi(x - ct, y, z) \begin{pmatrix} 1 & 1 & 0 & 0 \\ 1 & 1 & 0 & 0 \\ 0 & 0 & 0 & 0 \\ 0 & 0 & 0 & 0 \end{pmatrix} . \tag{1.14}$$

Substituting equations (1.12) and (1.9) in the field equation, we obtain

$$\Box\phi(x - ct, y, z) = -\frac{32\pi G}{c^4} u(x - ct, y, z). \tag{1.15}$$

If the energy density can be expressed by the product of two functions, $u(x - ct, y, z) = u_{\|}(x - ct)\, u_{\perp}(y, z)$, we expect the metric potential to take a similar form, that is, $\phi(x - ct, y, z) = \phi_{\|}(x - ct)\, \phi_{\perp}(y, z)$, further reducing the field equation to

$$\frac{1}{\phi_{\|}} \left(\frac{1}{c^2} \frac{\partial^2}{\partial t^2} - \frac{\partial^2}{\partial x^2} \right) \phi_{\|}(x - ct) - \frac{1}{\phi_{\perp}} \left(\frac{\partial^2}{\partial y^2} + \frac{\partial^2}{\partial z^2} \right) \phi_{\perp}(y, z) = -\frac{32\pi G}{c^4} \frac{u_{\|}(x - ct)}{\phi_{\|}(x - ct)} \frac{u_{\perp}(y, z)}{\phi_{\perp}(y, z)} \tag{1.16}$$

The above equation is separable in the case $u_{\|}(x - ct) = \phi_{\|}(x - ct)$, whence the field equation becomes

$$\left(\frac{\partial^2}{\partial y^2} + \frac{\partial^2}{\partial z^2} \right) \phi_{\perp}(y, z) = \frac{32\pi G}{c^4} u_{\perp}(y, z) \tag{1.17}$$

with the function $\phi_{\|}(x - ct)$ satisfying the one-dimensional homogeneous wave equation.

To solve equation (1.17), consider a cylindrical envelop of length L and radius R for the radiation field with constant energy density within the envelop given by $u_0 = pc/\pi R^2 L$, where p is the momentum of the radiation field. In cylindrical coordinates (r, φ), and by assuming axial symmetry, equation (1.17) becomes

$$\frac{1}{r}\frac{\partial}{\partial r}\left(r\frac{\partial\phi_\perp(r)}{\partial r}\right)=\frac{32\pi G}{c^4}u_0. \tag{1.18}$$

With proper boundary conditions on the curved surface of the cylinder, the solution of the above differential equation becomes

$$\phi_\perp(r)=\frac{8Gp}{c^3L}\left(\frac{r^2}{R^2}\right). \tag{1.19}$$

Including proper boundary condition on the flat surfaces of the cylinder, the potential is obtained as

$$\phi(x,r)=\frac{8Gp}{c^3L}\left(\frac{r^2}{R^2}\right)\theta(x-ct)\;\theta(ct-x-L), \tag{1.20}$$

where $\theta(\xi)$ is the Heaviside step function.

Thus the distorted metric inside the radiation field is obtained as

$$ds^2=c^2dt^2-\left(dx^2+dr^2+r^2d\varphi^2\right)+\left(\frac{8Gp}{c^3L}\right)\left(\frac{r^2}{R^2}\right)\theta(x-ct)\;\theta(ct-x-L)\,(cdt-dx)^2 \tag{1.21}$$

Since the ratio $r^2/R^2\sim 1$ just inside the cylinder, the deviation of the metric from the flat Minkowski metric is of the order $\sim 8Gp/c^3L$. Moreover, it can be seen that the above metric is a good approximation outside the cylinder so long as we do not go very far from it in order to maintain the approximate cylindrical symmetry involved in the equations. Thus the exterior solution for $r>R$ is obtained from equation (1.20) with the right-hand side set equal to zero, giving $\phi_\perp(r)=\frac{8Gp}{c^3L}+c_1\ln\frac{r}{R}$, where c_1 is an integration constant. Thus the metric remains approximately the same in the vicinity of the cylinder ($r/R\sim 1$) in the exterior region. Therefore an electron in the vicinity of the radiation field would experience a gravitationally induced motion due to which there is an uncertainty in its position. One may estimate this uncertainty by deriving the geodesic equation in the above metric. For the electron moving with non-relativistic velocities, the geodesic equation reduces to

$$\frac{d^2x^i}{dt^2}=-\Gamma^i_{00}c^2, \tag{1.22}$$

where $i=(1,2)$ represent the longitudinal and transverse directions (x,r) respectively.

The corresponding uncertainty in position in both these directions are obtained by integrating the equation of motion in the time interval of passage of the radiation field. It is found that the change in position in both directions are of the same order, given by

$$\Delta x_{\text{grav}}\approx\ell_P^2\frac{p}{\hbar}\quad\text{and}\quad\Delta r_{\text{grav}}\approx\ell_P^2\frac{p}{\hbar}. \tag{1.23}$$

These values agree well with the previous estimate given by equation (1.5). Consequently the same modification occurs in the Heisenberg uncertainty principle as in equation (1.7)

1.1.4 Modification in the uncertainty relation due to quantum gravity

It appears that the existence of a minimal length is a common attribute of any quantum theory of gravity. For instance, the measurement of proper length in the quantum conformal gravity predicts the existence of a minimal length when the Planck scale is approached [151, 161, 162]. Quantum conformal gravity can be thought of as an approximate theory of quantum gravity with a conformal quantum degree of freedom $\phi(\mathbf{x})$, represented by the metric

$$g_{\mu\nu} = [1+\phi(\mathbf{x})]^2 \bar{g}_{\mu\nu}, \tag{1.24}$$

where $\phi(\mathbf{x})$, being a quantum mechanical field, introduces quantum fluctuations in the metric. The path integral

$$K = \int \mathcal{D}g_{\mu\nu}\; e^{iS[g_{\mu\nu}]} \quad \text{with} \quad S[g_{\mu\nu}] = \frac{c^3}{16\pi G}\int R\sqrt{-g}\; d^4x = \frac{1}{12\ell_P^2}\int R\sqrt{-g}\; d^4x \tag{1.25}$$

yields the propagator from state $|1\rangle$ to $|2\rangle$ as

$$K_{1\to 2} = \int \mathcal{D}\phi\; \exp\left\{-\frac{i}{2\ell_P^2}\int \left\{\partial^\mu\phi\,\partial_\mu\phi - \frac{1}{6}\bar{R}(1+\phi)^2\right\}\sqrt{-\bar{g}}\; d^4x\right\}, \tag{1.26}$$

where $\bar{R}$ is the Ricci scalar corresponding to the classical metric. Assuming that the conformal fluctuations are coupled to the Minkowski metric $\bar{g}_{\mu\nu} = \eta_{\mu\nu}$, the propagator reduces to

$$K_{1\to 2} = \int \mathcal{D}\phi\; \exp\left\{-\frac{i}{2\ell_P^2}\int \partial^\mu\phi\,\partial_\mu\phi\; d^4x\right\} \tag{1.27}$$

where

$$S[\phi] = -\frac{i}{2\ell_P^2}\int \partial^\mu\phi\,\partial_\mu\phi\; d^4x \tag{1.28}$$

This leads to the probability of obtaining a given conformal fluctuation $\phi = \phi(\mathbf{x})$ starting initially from $\phi = 0$ as

$$\mathcal{P}[\phi(\mathbf{x})] = N\exp\left\{-\frac{1}{4\pi^2\ell_P^2}\right\}\int d^3x\; d^3y\; \frac{\nabla\phi(\mathbf{x})\cdot\nabla\phi(\mathbf{y})}{|\mathbf{x}-\mathbf{y}|^2} \tag{1.29}$$

We shall see that the measurement of proper length is affected by the conformal fluctuations. Since the spacetime is affected by the conformal fluctuations, we have to measure those fluctuations in order to measure the proper distance. Let the measuring apparatus has spatial resolution of L with a sensitivity profile $f(\mathbf{x})$. The measured average value of the field ϕ over a volume of the order L^3 can be expressed as

$$\Phi(\mathbf{x}) = \int \phi(\mathbf{x}+\mathbf{r})\; f(\mathbf{r})\; d^3\mathbf{r} \tag{1.30}$$

The probability of obtaining a particular value $\Phi = \Phi_0$ is given by

$$\mathcal{P}_0[\Phi_0] = \int \mathcal{D}\phi(\mathbf{x})\ \delta(\Phi - \Phi_0)\mathcal{P}[\phi(\mathbf{x})]. \tag{1.31}$$

Employing Fourier transform of equation (1.29) in (1.31) obtains

$$\mathcal{P}_0[\Phi_0] = \left(\frac{1}{2\pi\Delta^2}\right)^{1/4} e^{-\Phi_0^2/4\Delta^2}, \quad \text{where} \quad \Delta^2 = \ell_P^2 \int \frac{d^3\mathbf{k}}{(2\pi)^2}\frac{|f(\mathbf{k})|^2}{2|\mathbf{k}|} = \frac{\ell_P^2}{4\pi L^2} \tag{1.32}$$

with the resolution length L defined as

$$L^{-2} = \frac{1}{4\pi}\int d^3\mathbf{k}\frac{|f(\mathbf{k})|^2}{|\mathbf{k}|}. \tag{1.33}$$

If the resolution of the apparatus is much larger than the Planck scale ℓ_P, $\Delta \approx 0$, whence the probability sharply peaks at $\Phi_0 = 0$. In this case the quantum fluctuation are unimportant so that length measurement is unaffected by the conformal fluctuations of spacetime. On the other hand, the length measurement is significantly affected when the sensitivity scale L of the apparatus approaches the Planck scale ℓ_P.

The proper length between two points $\mathbf{x}$ and $\mathbf{x} + \mathbf{dx}$ measured at the same time is defined by the vacuum expectation value

$$\langle 0|d\ell^2|0\rangle = \langle 0|g_{ij}|0\rangle dx^i dx^j = (1 + \langle 0|\phi^2(\mathbf{x})|0\rangle)\eta_{ij}dx^i dx^j, \tag{1.34}$$

However since $\langle 0|\phi^2(\mathbf{x})|0\rangle$ diverges, it can be calculated by taking the limit $x^\mu \to y^\mu$,

$$\langle 0|\phi^2(\mathbf{x})|0\rangle = \lim_{x\to y}\langle 0|\phi(\mathbf{x})\phi(\mathbf{y})|0\rangle. \tag{1.35}$$

The vacuum expectation value on the right hand side can be expressed by path integrals as

$$\langle 0|\phi(\mathbf{x})\phi(\mathbf{y})|0\rangle = \frac{\int \mathcal{D}\phi\ \phi(\mathbf{x})\ \phi(\mathbf{y})e^{iS[\phi]}}{\int \mathcal{D}\phi\ e^{iS[\phi]}}. \tag{1.36}$$

Employing the action $S[\phi]$ given by equation (1.28) in equation (1.36), we obtain from equation (1.34)

$$\langle 0|d\ell^2|0\rangle = \lim_{x\to y}\left(1 + \frac{\ell_P^2}{4\pi^2}\frac{1}{|\mathbf{x}-\mathbf{y}|^2}\right)|\mathbf{x}-\mathbf{y}|^2 = \frac{\ell_P^2}{4\pi^2} \tag{1.37}$$

Thus we see that the proper length between two infinitesimally separated events measured at the same time has a minimum value determined by the Planck scale ℓ_P. This suggests the emergence of a grainy or foamy structure of spacetime even in a simple quantum theory such as conformal quantum gravity.

This has given rise to various phenomenological scenarios, one of them being the existence of minimal length in the simultaneous position and momentum measurement of an electron that interacts with the illuminating photons both electromagnetically and gravitationally as discussed earlier.

1.1.5 Minimal length in string theory

The minimal length scenario also follows from the string theory. The Nambu-Goto action for a string [236] is written as

$$S = -\frac{1}{2\pi\alpha'}\int d\tau \int d\sigma \sqrt{(\dot{X}\cdot X')^2 - (\dot{X})^2(X')^2} \tag{1.38}$$

where $X(\tau, \sigma)$ is the string coordinate parametrized by τ and σ on the world sheet swept by the string. The slope parameter α' is related to the string tension T_0 as $\alpha' = \frac{1}{2\pi T_0}$ with the characteristic string length $\ell_s = \sqrt{\alpha'}$.

Extremizing the above action and employing proper parametrization, the following field equation obtains

$$\ddot{X}^\mu - X^{\mu''} = 0, \tag{1.39}$$

which has the same form as the wave equation. The solution of this equation can be represented by

$$X^\mu = \frac{1}{2}\Big\{f^\mu(\tau+\sigma) + f^\mu(\tau-\sigma)\Big\} \tag{1.40}$$

with the Neumann boundary condition $X^{\mu'} = 0$ at the end points $\sigma = 0, \pi$ and $\dot{X}^\mu(0,\tau) = 0$ so that f^μ is a periodic function, giving the solution

$$X^\mu(\tau,\sigma) = x_0^\mu + 2\alpha' p^\mu \tau - i\sqrt{2\alpha'}\sum_{n=1}^{\infty}\left(a_n^{\mu*}e^{in\tau} - a_n^\mu e^{-in\tau}\right)\frac{\cos n\sigma}{\sqrt{n}} \tag{1.41}$$

where p^μ is the total momentum and x_0^μ is an integration constant (or zero mode). Defining $\alpha_0^\mu = \sqrt{2\alpha'}p^\mu$ and $\alpha_n^\mu = a_n^\mu\sqrt{n}$, $(\alpha_n^\mu)^* = \alpha_{-n}^\mu = a_n^{\mu*}\sqrt{n}$, the above solution can be rewritten as

$$X^\mu(\tau,\sigma) = x_0^\mu + \sqrt{2\alpha'}\alpha_0^\mu\tau - i\sqrt{2\alpha'}\sum_{n=1}^{\infty}\frac{1}{n}\left(\alpha_{-n}^\mu e^{in\tau} - \alpha_n^\mu e^{-in\tau}\right)\cos n\sigma. \tag{1.42}$$

In the light-cone gauge with the first two coordinates defined as $X^\pm = (X^0 \pm X^1)/\sqrt{2}$ with the solution $X^+(\tau,\sigma) = 2\alpha' p^+\tau$, the dynamics is determined by the transverse coordinates X^i with $i = 2, 3, ..., D$, so that

$$X^i(\tau,\sigma) = x_0^i + \sqrt{2\alpha'}\alpha_0^i\tau + i\sqrt{2\alpha'}\sum_n \frac{1}{n}\alpha_n^i e^{-in\tau}\cos n\sigma. \tag{1.43}$$

Upon quantization, the amplitudes obey the commutation relations $[\alpha_m^i, \alpha_n^j] = m\eta^{ij}\delta_{m+n,0}$ and $[x_0^i, p^j] = i\eta^{ij}$.

The longitudinal coordinate has the mode expansion

$$X^-(\tau,\sigma) = x_0^- + \sqrt{2\alpha'}\alpha_0^-\tau + i\sqrt{2\alpha'}\sum_{n\neq 0}\frac{1}{n}\alpha_n^- e^{-in\tau}\cos n\sigma. \tag{1.44}$$

Using appropriate constraints, X^- can be written in terms of X^i and p^+, and α_n^- in terms of α_n^i, so that

$$\sqrt{2\alpha'}\alpha_n^- p^+ = L_n^\perp = \frac{1}{2}\sum_m \alpha_{n-m}^i\alpha_m^i, \tag{1.45}$$

where $L_n^\perp$ are the transverse Virasoro operators. Thus the above expression can be written as

$$X^-(\tau,\sigma) = x_0^- + \sqrt{2\alpha'}\alpha_0^-\tau + \frac{i}{p^+}\sum_{n\neq 0}\frac{1}{n}L_n^\perp e^{-in\tau}\cos n\sigma. \tag{1.46}$$

The transverse Virasoro operators obey the commutation relation

$$[L_m^\perp, L_n^\perp] = (m-n)L_{m+n}^\perp + \frac{D-2}{12}m(m^2-1)\delta_{m+n,0}. \tag{1.47}$$

Defining the transverse displacement as $\Delta X^i = X^i - x_0^i$, the dispersion can be calculated as

$$(\Delta X^\perp)^2 = \sum_i \langle \Delta X^i \Delta X^i\rangle \sim \alpha' \sum_{n,m}\frac{1}{n}\frac{1}{m}\langle[\alpha_n^i . \alpha_m^i]\rangle \tag{1.48}$$

Employing the commutator $[\alpha_m^i, \alpha_n^j] = m\eta^{ij}\delta_{m+n,0}$ leads to

$$(\Delta X^\perp)^2 \sim \alpha' \sum_{n=1}^{N}\frac{1}{n} \sim \alpha'\left\{\ln N + \gamma + \mathcal{O}(N^{-1})\right\} \sim \ell_s^2 \ln N, \tag{1.49}$$

where the sum is carried out upto a large integer N and γ is the Euler constant. The sum diverges like $\ln N$ for large N. However, to probe the string we can supply only a finite amount of energy E for a time $\tau \sim 1/E$, so that maximum number of modes excited will be given by $N \sim \ell_s/\tau \sim \ell_s E$. This gives

$$(\Delta X^\perp)^2 \sim \ell_s^2 \, \ln(\ell_s E), \tag{1.50}$$

implying the existence of a minimal length due to the transverse excitations.

On the other hand, the longitudinal displacement $\Delta X^- = X^- - x_0^-$ gives the dispersion

$$(\Delta X^-)^2 = \langle \Delta X^- \Delta X^-\rangle \sim \frac{1}{(p^+)^2}\sum_{n,m}\frac{1}{n}\frac{1}{m}\langle[L_n^\perp, L_m^\perp]\rangle. \tag{1.51}$$

Employing the commutation relation among the transverse Virasoro operators (1.47), the above dispersion can be estimated as

$$(\Delta X^{-})^2 \sim \frac{1}{(p^+)^2}\sum_n n \sim \frac{1}{(p^+)^2}N(N+1) \sim \frac{\ell_s^2}{(p^+)^2}E^2 \tag{1.52}$$

This estimate for the longitudinal minimal length is exponentially larger than the estimate of transverse minimal length.

Thus string theory predicts the existence of a minimal length in a fundamental way.

1.2 Non-commutative Geometry and Modified Dispersion Relation

The Hawking-Wheeler foam [85, 228] of quantum space-time fluctuations can be accounted for by a non-commutative spacetime geometry. Such quantum fluctuations of spacetime would indicate that the space and time coordinates may be treated as operators obeying nontrivial commutation relations.

A long time ago, Snyder [207] showed that non-commutative geometry results from changing the notion of space-time coordinates from continuum variables to Hermitian operators in such a way that the spectra of space-time operators maintain Lorentz invariance. The space-time operators were constructed out of coordinates of a de-Sitter space of constant curvature with an invariant quadratic form and by introducing a natural unit of length a. This construction leads to a discrete spectrum for the space operators with positive or negative integer multiples of the characteristic length, whereas the time operator has a continuous spectrum. Thus a discrete Lorentz invariant space-time emerges out of this construction. This procedure also allowed for the construction of the infinitesimal operators of the Lorentz group, L_i and M_i. The main interesting feature of this construction was that the space-time operators followed the noncommutative algebra,

$$[x^i, x^j] = \frac{ia^2}{\hbar}\epsilon^{ijk}L_k, \tag{1.53}$$

and

$$[t, x^i] = \frac{ia^2}{\hbar c}M^i. \tag{1.54}$$

The general definition of angular momentum operators $L_i = \epsilon_{ijk}\ x^j p^k$ requires that the momentum operators p^i commute with one another and they have continuous spectra. However, the Heisenberg-like commutation relations do not hold any longer; for example,

$$[x^i, p^j] = i\hbar\left\{\delta^{ij} + \left(\frac{a}{\hbar}\right)^2 p^i p^j\right\}. \tag{1.55}$$

Snyder [206] also demonstrated how the notion of quantized spacetime can be employed to modify Maxwell field equations by treating the fields as operators and by replacing the partial derivatives with suitable commutators in a consistent manner.

Doplicher et al. [65, 66] considered the uncertainties in the measurement of spacetime coordinates of an event in the Minkowski space. The energy density required to localize an event and the corresponding energy-momentum tensor can thus be associated with a gravitational potential so that the spacetime quantization can be assumed to follow from classical gravity. The uncertainties involved in the space-time coordinates can then be obtained via promoting them to space-time operators that do not commute with each other. A few simplifying conditions, together with the Lorentz invariant operators, could be employed to rederive the approximate uncertainty relation. The consistency of the uncertainty relation in fact leads to the notion that classical gravity can induce space-time quantization. They also applied this formalism to quantum fields in the non-commutative spacetime. This replaces the local interactions by effective non-local interactions.

Ho and Kao [91] considered a non-commutative space with the time assumed to be commutative. This allowed them to formulate non-commutative quantum mechanics for multi-particle systems. It was found that particles of opposite charges have opposite non-commutativity that made no change in the two-body Hydrogen atom problem. However, for a multi-particle system, the non-commutativity remains in the description, although it is small compared to the size of the system.

Rovelli [186] argued that a material reference system needs to be included in the description in order to have a meaningful interpretation of local observables in general relativity. He further argued [185] that operators in quantum gravity can be defined by the quantum properties of the constituents of the reference frame.

Amelino-Camelia [9, 10], on the basis of limitations due to quantum mechanics and general relativity, proposed that the uncertainty in the measurement of distance between two objects (for example, between a clock and a mirror, the clock emitting a photon towards the mirror and receiving it back registering the time delay) cannot be made arbitrarily small but it will depend on both, the distance between the two objects and the size of the measuring device (the clock), together with the Planck scale ℓ_{P}. He also concluded that this limitation of measurement of distance defined by the material reference system is an evidence for unconventional commutation relations between local observables defined by the material reference frame in quantum gravity. He observed that the κ-deformed Poincaré algebra for the Minkowski space [11]

$$[x^i, x^j] = 0, \tag{1.56}$$

and

$$[x^i, t] = i\lambda x^i, \tag{1.57}$$

where $\lambda \sim t_{\mathrm{P}}$, leads to similar bounds on the measurability of distance between two points using the same clock-mirror arrangement. These non-commutativity relations for the spacetime degrees of freedom suggest that the space and time coordinates cannot be defined simultaneously with arbitrarily high precision, although it is possible to do so with the three commuting space coordinates.

Amelino-Camelia and Majid [15] speculated that very high energy particles could be affected by the Hawking-Wheeler spacetime foam [85, 228] around the Planck scale. They further discussed an effective description of the quantum gravity vacuum based on the non-commutative geometry of the Minkowski spacetime given by (1.56) and (1.57). They considered translation invariant calculus of differentials spanned by dx^i, dt along the lines of Ref. [155]. As a consequence, the partial derivatives of a field $\psi(\mathbf{x},t)$ take the forms

$$\partial_i :\psi(\mathbf{x},t): = :\frac{\partial}{\partial x^i}\psi(\mathbf{x},t):, \quad \partial_0 :\psi(\mathbf{x},t): = :(i\lambda)^{-1}\left(\psi(\mathbf{x},t) - \psi(\mathbf{x},t-i\lambda)\right): \tag{1.58}$$

where the symbol : : represents normal ordering. They further considered a non-Abelian Fourier transform to the non-commutative Minkowski spacetime using quantum group methods [126, 127]. The corresponding momentum space is commutative and non-Abelian. This led to the Fourier transform

$$T(:\psi:)(\mathbf{k},\omega) = \int d^3\mathbf{x}\; dt\; e^{i\mathbf{k}\cdot\mathbf{x}} e^{i\omega t}\psi(e^{\lambda\omega}\mathbf{x},t), \tag{1.59}$$

so that the other Fourier transforms can be written as

$$T(\partial_i\psi) = -T(\psi) i k_i e^{-\lambda\omega}, \quad T(\partial_0\psi) = -T(\psi)\, i\, \frac{1-e^{-\lambda\omega}}{\lambda}. \tag{1.60}$$

For a natural plane wave of the form $\psi_{\mathbf{k},\omega} = e^{i\mathbf{k}\cdot\mathbf{x}}e^{i\omega t}$, an appropriate dispersion relation was obtained by considering the rotation and boost generators of the Lorentz group [128] in the non-Abelian momentum space, which are

$$M_i = -\epsilon_{imn}\, k_m \frac{\partial}{\partial k_n}, \qquad N_i = k_i\frac{\partial}{\partial\omega} - \left(\frac{\lambda}{2}\mathbf{k}^2 + \frac{(1-e^{2\lambda\omega})}{2\lambda}\right)\frac{\partial}{\partial k_i} + \lambda k_i k_j \frac{\partial}{\partial k_j}. \tag{1.61}$$

This led to a deformed dispersion relation of the form

$$\hbar^2\kappa^2(e^{E/\hbar\kappa} + e^{-E/\hbar\kappa} - 2) - p^2c^2e^{-E/\hbar\kappa} = m^2c^4. \tag{1.62}$$

where $E = \hbar\omega$ and $\kappa = \lambda^{-1}$. This deformed dispersion relation (with $m = 0$) implies that the speed of a photon depends on its energy.

Amelino-Camelia et al. [13] further inferred that the vacuum can be pictured as a quantum gravitational medium with quantum fluctuations occurring at scales on the order of the Planck energy.

In this context, it may be noted that there are no fundamental scales of velocity or length in Galilean relativity. On the other hand, a fundamental velocity scale c was introduced by Einstein to construct special relativity that preserves the Lorentz invariance of classical electrodynamics. The granular structure of space-time near the Planck scale demands the inclusion of a fundamental length scale in the physical laws. By noting this, Amelino-Camelia [12] constructed a deformed special relativity where both the speed of light c and the Planck length ℓ_P are constrained to be invariant with respect to all inertial observers. This is consistent with a deformed dispersion relation of the form

$$E^2 - p^2c^2 + F(E, p, m, \ell_P) = m^2c^4. \tag{1.63}$$

In this dispersion relation, the function $F(E, p, m, \ell_P)$ is an undetermined function which is usually chosen phenomenologically.

Magueijo and Smolin [125] constructed a similar modification of special relativity with the condition that the standard theory of relativity is recovered at low energies or large length scales. This required the construction of a modified Lorentz group that acts nonlinearly in the momentum space and it led to the modified invariant $||p||^2 = \frac{\eta^{\mu\nu}p_\mu p_\nu}{(1-\ell_P\, p_0)^2} = m^2$, with m the rest mass of the particle, implying that the ideal dispersion relation $E^2 = \mathbf{p}^2 + m^2$ is deformed in the modified relativity.

It may be worth noting that Pavlopoulos [169] first considered the consequence of the presence of an intrinsic length-scale ℓ to obtain an extended wave equation that implied a wavelength dependent small change in the velocity of light. He also suggested a general dispersion relation of the form $\omega^2 = k^2c^2[1 + f^2(\ell k)]$, connecting frequency ω and wave number k. He speculated that the consequent varying speed of different frequencies could be observed in γ-ray bursts.

Ellis and coworkers [67] proposed that the dispersion of electromagnetic radiation from γ-ray bursts can be explained by a deformed dispersion relation $c^2p^2 = E^2(1 + f(\alpha E))$. This is a consequence of quantum gravity effects, where the energy scale α^{-1} can be of the order of the Planck energy $E_\text{P} \sim 10^{19}$ GeV for the propagation of photons through vacuum. For energies $E \ll \alpha^{-1}$, the dispersion relation can be approximated as $c^2p^2 = E^2[1+\alpha\xi E+O(\alpha^2E^2)]$, which essentially implies that the velocity v $(= \frac{\partial E}{\partial p} = c[1-\alpha\xi E])$ of high energy photons (propagating through vacuum) will be energy dependent. The change in velocity introduces a time delay $\Delta t = \alpha\xi EL/c$ for a photon of energy E travelling a distance L, for a positive sign ambiguity ξ. This time delay is expected to be significant for a γ-ray burst because both E and L are large making the time delay Δt not very small.

The time delay in the signals observed from various data including TeV γ-rays associated with Markarian 421 [30] and various classes of γ-ray bursts [193] further confirm the existence of non-commutative geometry. Another sensational observation was the high level emission observed from Markarian 501, showing a spectrum beyond 10 TeV [178]. It was long thought that γ-rays of energy in the range of TeV and beyond could not travel much farther though the intergalactic space due to strong absorption by the infra-red background [208]. This claim was discarded as the data analyzed from the High Energy

Gamma Ray Astronomy (HEGRA) experiment suggested an energy spectrum much beyond 10 TeV [2]. It was suggested by Kifune [106] and later by Protheroe [178] that the modified dispersion relation obtained as a consequence of non-commutativity of space-time actually reduces the absorption in the intergalactic space, making it more transparent to high energy photons.

1.3 Einstein Field Equations

The Einstein field equations can be obtained from the extremum of the Einstein-Hilbert action. The gravitational part of the action is expressed as

$$S_{\text{grav}} = \frac{c^3}{16\pi G} \int d^4x \sqrt{-g}\, R, \tag{1.64}$$

where R is the Ricci scalar and g the determinant of the metric tensor $g_{\mu\nu}$. The variation of this action is

$$\delta S_{\text{grav}} = \frac{c^3}{16\pi G} \int d^4x \Big\{ R\, \delta(\sqrt{-g}) + \sqrt{-g}\, \delta R \Big\}, \tag{1.65}$$

with the variation of $\sqrt{-g}$ as

$$\delta(\sqrt{-g}) = -\frac{1}{2}\sqrt{-g}\, g_{\mu\nu}\, \delta g^{\mu\nu}, \tag{1.66}$$

and the variation in R is given by

$$\delta R = \delta(R_{\mu\nu}\, g^{\mu\nu}) = g^{\mu\nu}\, \delta R_{\mu\nu} + R_{\mu\nu}\, \delta g^{\mu\nu}, \tag{1.67}$$

where $R_{\mu\nu}$ is the Ricci tensor, which is related to the Riemann curvature tensor as $R_{\mu\nu} = R^{\alpha}_{\mu\alpha\nu}$. The Riemann tensor is defined as

$$R^{\beta}_{\mu\alpha\nu} = \partial_\alpha \Gamma^{\beta}_{\nu\mu} - \partial_\nu \Gamma^{\beta}_{\alpha\mu} + \Gamma^{\beta}_{\alpha\lambda}\Gamma^{\lambda}_{\nu\mu} - \Gamma^{\beta}_{\nu\lambda}\Gamma^{\lambda}_{\alpha\mu}, \tag{1.68}$$

and its variation is given by

$$\delta R^{\beta}_{\mu\alpha\nu} = \partial_\alpha\, \delta\Gamma^{\beta}_{\nu\mu} - \partial_\nu\, \delta\Gamma^{\beta}_{\alpha\mu} + \delta\Gamma^{\beta}_{\alpha\lambda}\, \Gamma^{\lambda}_{\nu\mu} + \Gamma^{\beta}_{\alpha\lambda}\, \delta\Gamma^{\lambda}_{\nu\mu} - \delta\Gamma^{\beta}_{\nu\lambda}\, \Gamma^{\lambda}_{\alpha\mu} - \Gamma^{\beta}_{\nu\lambda}\, \delta\Gamma^{\lambda}_{\alpha\mu}. \tag{1.69}$$

Since $\delta\Gamma^{\beta}_{\mu\nu}$ is a tensor, its covariant derivative is

$$\nabla_\lambda(\delta\Gamma^{\alpha}_{\mu\nu}) = \partial_\lambda \delta\Gamma^{\alpha}_{\mu\nu} + \Gamma^{\alpha}_{\sigma\lambda}\, \delta\Gamma^{\sigma}_{\mu\nu} - \Gamma^{\sigma}_{\mu\lambda}\, \delta\Gamma^{\alpha}_{\sigma\nu} - \Gamma^{\sigma}_{\nu\lambda}\, \delta\Gamma^{\alpha}_{\mu\sigma}. \tag{1.70}$$

Using this expression, we can rewrite the variation of the Riemann tensor (1.69) as

$$\delta R^{\beta}_{\mu\alpha\nu} = \nabla_\alpha\, (\delta\Gamma^{\beta}_{\nu\mu}) - \nabla_\nu\, (\delta\Gamma^{\beta}_{\alpha\mu}), \tag{1.71}$$

so that the variation of the Ricci tensor is

$$\delta R_{\mu\nu} = \nabla_\lambda\,(\delta\Gamma^\lambda_{\nu\mu}) - \nabla_\nu\,(\delta\Gamma^\lambda_{\lambda\mu}), \tag{1.72}$$

and the variation of the Ricci scalar (1.67) is obtained as

$$\delta R = g^{\mu\nu}\left(\nabla_\lambda\,\delta\Gamma^\lambda_{\nu\mu} - \nabla_\nu\,\delta\Gamma^\lambda_{\lambda\mu}\right) + R_{\mu\nu}\,\delta g^{\mu\nu}. \tag{1.73}$$

Substituting the above expressions and rearranging, the variation of the gravitational action (1.65) takes the form

$$\delta S_{\text{grav}} = \frac{c^3}{16\pi G}\left\{\int d^4x\sqrt{-g}\left(R_{\mu\nu} - \frac{1}{2}Rg_{\mu\nu}\right)\delta g^{\mu\nu} + \int d^4x\sqrt{-g}\,\nabla_\lambda\left(g^{\mu\nu}\delta\Gamma^\lambda_{\mu\nu} - g^{\mu\lambda}\delta\Gamma^\nu_{\mu\nu}\right)\right\}. \tag{1.74}$$

Since the second integral contains a divergence, it can be reduced to a surface integral, and therefore it vanishes at the surface. Thus the variation of the gravitational action reduces to

$$\delta S_{\text{grav}} = \frac{c^3}{16\pi G}\int d^4x\sqrt{-g}\left(R_{\mu\nu} - \frac{1}{2}Rg_{\mu\nu}\right)\delta g^{\mu\nu}. \tag{1.75}$$

The total action of the gravitational field created by matter is written as $S = S_{\text{grav}} + S_m$, where the matter part of the action can be expressed as

$$S_m = \int d^4x\sqrt{-g}\,\mathcal{L}_m. \tag{1.76}$$

The variation of the integrand in equation (1.76) is given by

$$\delta(\sqrt{-g}\,\mathcal{L}_m) = -\frac{1}{2c}\sqrt{-g}\,T_{\mu\nu}\,\delta g^{\mu\nu} \tag{1.77}$$

where the energy momentum tensor $T_{\mu\nu}$ is defined as

$$\frac{1}{2}\sqrt{-g}\,T_{\mu\nu} = \frac{\partial}{\partial g^{\mu\nu}}(\sqrt{-g}\mathcal{L}_m) - \frac{\partial}{\partial x^\lambda}\frac{\sqrt{-g}\mathcal{L}_m}{\partial\frac{\partial g^{\mu\nu}}{\partial x^\lambda}}. \tag{1.78}$$

The variation δS_m of the matter part of the action (1.76) is thus

$$\delta S_m = -\frac{1}{2c}\int d^4x\sqrt{-g}\,T_{\mu\nu}\,\delta g^{\mu\nu}. \tag{1.79}$$

Thus the variation of the total action is

$$\delta S = \delta S_{\text{grav}} + \delta S_m = \frac{c^3}{16\pi G}\int d^4x\,\sqrt{-g}\left(R_{\mu\nu} - \frac{1}{2}g_{\mu\nu}R - \kappa T_{\mu\nu}\right)\delta g^{\mu\nu} \tag{1.80}$$

where $\kappa = \frac{8\pi G}{c^4}$.

From the extremum principle $\delta S = 0$, and noting the arbitrariness of the variation

$\delta g^{\mu\nu}$, we obtain the equation of motion

$$R_{\mu\nu} - \frac{1}{2} g_{\mu\nu} R = \kappa T_{\mu\nu}, \tag{1.81}$$

the celebrated Einstein field equations. The corresponding trace equation is

$$R = -\kappa T \tag{1.82}$$

where T is the trace of the energy-momentum tensor, given by $T = g^{\mu\nu} T_{\mu\nu}$

1.4 Static solution of Einstein Field equations for spherical distribution of matter

For spherical distribution of matter, the static solution of the Einstein field equations can be obtained by assuming the line element of the form [217]

$$ds^2 = e^{\nu} dt^2 - e^{\lambda} dr^2 - r^2 d\theta^2 - r^2 \sin^2\theta d\phi^2 \tag{1.83}$$

with the metric potentials ν and λ functions of radial coordinate r only. For our purpose, the matter content is taken to be that of a perfect fluid, given by the energy-momentum tensor

$$T^{\mu\nu} = (\varepsilon + P) u^{\mu} u^{\nu} - P g^{\mu\nu}. \tag{1.84}$$

The components are given in terms of proper energy density ε, proper pressure P and four velocity $u^{\mu} = \frac{dx^{\mu}}{ds}$. Thus the non-vanishing components of the field equations (1.81) are

$$e^{-\lambda}\left(\frac{\lambda'}{r} - \frac{1}{r^2}\right) + \frac{1}{r^2} = \frac{8\pi G}{c^4}\varepsilon, \tag{1.85}$$

$$e^{-\lambda}\left(\frac{\nu''}{2} - \frac{\nu'\lambda'}{4} + \frac{\nu'^2}{4}\right) - \frac{\nu'\lambda'}{2r} = \frac{8\pi G}{c^4}P, \tag{1.86}$$

$$e^{-\lambda}\left(\frac{\nu'}{r} + \frac{1}{r^2}\right) - \frac{1}{r^2} = \frac{8\pi G}{c^4}P. \tag{1.87}$$

Two of the above three equations are of interest as the third equation gives no additional information. However, the vanishing covariant divergence of the energy-momentum tensor, $\nabla_{\mu} T^{\mu\nu} = 0$, provides an additional dynamical equation. For a perfect fluid, this reduces to

$$\frac{dP}{dr} = -\frac{1}{2}(\varepsilon + P)\frac{d\nu}{dr} \tag{1.88}$$

Thus we have three differential equations for four unknowns. A solution is realized when a fourth independent equation is given. For a realistic situation, this additional information is obtained in the form of an equation of state describing the relation between the pressure

P and energy density ε of the fluid in consideration [159, 217].

The boundary of the matter distribution is set at $r = R$ for which $P = 0$, such that for $r < R$, the proper pressure $P > 0$. Thus the interior gravitational field depends on the equation of state of the fluid. On the other hand, an analytical expression of the exterior solution is immediately obtained by setting $P = \varepsilon = 0$ in the field equations, leading to

$$e^{-\lambda(r)} = 1 - \frac{2GM}{c^2 r} \quad \text{and} \quad e^{\nu(r)} = 1 - \frac{2GM}{c^2 r}, \tag{1.89}$$

where M is the mass of the fluid sphere. Using the equation of state $P = P(\varepsilon)$ and the boundary conditions, we integrate the field equations in the interior of the matter distribution to obtain

$$e^{\nu(r)} = \left[1 - \frac{2GM}{c^2 r}\right] \exp\left[-\int_0^{P(r)} \frac{2dP}{P+\varepsilon}\right] \quad \text{and} \quad e^{-\lambda(r)} = 1 - \frac{2Gm(r)}{c^2 r}, \tag{1.90}$$

where $m(r)$ can be identified as the mass enclosed within a sphere of radius r. Using this definition of $m(r)$, the field equations and covariant divergence of the energy-momentum tensor are cast into the celebrated Tolman-Oppenheimer-Volkoff (TOV) equations [159, 217], namely,

$$\frac{dP}{dr} = -\frac{G}{c^2}\frac{(\varepsilon + P)}{r(r - 2Gm/c^2)}\left[\frac{4\pi P r^3}{c^2} + m\right] \quad \text{and} \quad \frac{dm}{dr} = \frac{4\pi}{c^2}\varepsilon r^2. \tag{1.91}$$

In the Newtonian limit, the TOV equations reduce to

$$\frac{dP}{dr} = -\frac{Gm\rho}{r^2} \quad \text{and} \quad \frac{dm}{dr} = 4\pi\rho r^2, \tag{1.92}$$

where ρ is the rest mass density of the matter. These differential equations are integrated simultaneously with initial conditions $P = P_c$ and $m = 0$ from $r = 0$ until the boundary of the matter distribution is reached at $r = R$, where $P(R) = 0$.

1.5 Dynamical instability in general relativity

For the matter interior to the star, the equilibrium values of the pressure $P(r)$ and energy density $\varepsilon(r)$ are determined by the Tolman-Oppenheimer-Volkoff (TOV) equations (1.91) and the interior Schwarzschild metric potentials satisfying the Einstein field equations (1.85) [159, 217]. However it is important to know whether such equilibrium configurations are dynamically stable so that small perturbations about these solutions do not bring about a collapse of the star.

Dynamical stability analysis consists of the investigation of the time evolution of homologous (with respect to the radial coordinate) infinitesimal perturbation about the equilibrium configuration [50–52]. In the framework of general relativity, this corresponds to a time-dependent interior solution of the form

$$ds^2 = e^{\nu+\delta\nu}c^2dt^2 - e^{\lambda+\delta\lambda}dr^2 - r^2(d\theta^2 + \sin^2\theta\, d\phi^2), \tag{1.93}$$

where $\nu(r)$ and $\lambda(r)$ are the equilibrium metric potentials and the perturbations $\delta\nu(r,t)$ and $\delta\lambda(r,t)$ are due to small radial Lagrangian displacements $\zeta(r,t)$. This induces perturbations $\delta P(r,t)$ and $\delta\varepsilon(r,t)$ to the equilibrium pressure $P(r)$ and energy density $\varepsilon(r)$. The smallness of the perturbation allows one to consider sinusoidal displacements $\zeta(r,t) = r^{-2}e^{\nu/2}\psi(r)e^{i\omega t}$. The corresponding equation for the radial oscillation can be obtained in the Sturm-Liouville form [23]

$$\frac{d}{dr}\left(U\frac{d\psi}{dr}\right) + \left(V + \frac{\omega^2}{c^2}W\right)\psi = 0, \tag{1.94}$$

satisfying the boundary conditions $\psi = 0$ at $r = 0$ and the Lagrangian change in pressure $\delta P = -e^{\nu/2}\frac{\gamma P}{r^2}\frac{d\psi}{dr} = 0$ at $r = R$. In the above equation,

$$U(r) = e^{(\lambda+3\nu)/2}\frac{\gamma P}{r^2}, \tag{1.95}$$

$$V(r) = -4\frac{e^{(\lambda+3\nu)/2}}{r^3}\frac{dP}{dr} - \frac{8\pi G}{c^4}\frac{e^{3(\lambda+\nu)/2}}{r^2}P(P+\varepsilon) + \frac{e^{(\lambda+3\nu)/2}}{r^2}\frac{1}{P+\varepsilon}\left(\frac{dP}{dr}\right)^2 \tag{1.96}$$

$$W(r) = \frac{e^{(3\lambda+\nu)/2}}{r^2}(P+\varepsilon), \tag{1.97}$$

with the adiabatic index γ, given by

$$\gamma = \frac{\varepsilon + P}{P}\left(\frac{dP}{d\varepsilon}\right)_s. \tag{1.98}$$

Integrating Eq. (1.94) upon left-multiplying by ψ, one obtains the integral

$$J[\psi] = \int_0^R \left\{U\psi'^2 - V\psi^2 - \frac{\omega^2}{c^2}W\psi^2\right\}dr \tag{1.99}$$

where $\psi' = d\psi/dr$, and the boundary conditions eliminate the surface term. It can be shown that Eq. (1.94) is reproduced from the variational principle $\delta J[\psi] = 0$. Thus the lowest characteristic eigenfrequency of the normal mode is obtained from

$$\frac{\omega_0^2}{c^2} = \min_{\psi(r)}\frac{\int_0^R\{U\psi'^2 - V\psi^2\}\,dr}{\int_0^R W\psi^2 dr}. \tag{1.100}$$

The star remains in stable equilibrium so long as this equation yields positive values of ω_0^2. On the other hand, a negative ω_0^2 signifies unstable equilibrium. A power series solution of Eq. (1.94) about $r = 0$ gives $\psi(r) \propto r^3$ in the leading order for which $\zeta(r)$ and $\zeta'(r)$ are finite. A good approximation for the trial function of the fundamental mode can be taken as the simple form $\psi(r) = c_0 r^3$ [50, 51, 229]. With this choice, the onset of instability, hence the critical density ε_c^* for gravitational collapse, can be identified with a zero eigenfrequency solution of Eq. (1.99).

1.6 Extended Theories of Gravity

In formulating the general theory of relativity, Einstein postulated that the field equations may have only second derivatives of the metric tensor, leading to the field equations, $G_{\mu\nu} = \kappa T_{\mu\nu}$. This equation can be derived from the Einstein-Hilbert action $S = \frac{c^3}{16\pi G}\int d^4x\sqrt{-g}R + S_m$ that contains the Ricci scalar R at linear order. However, inclusion of quantum vacuum polarization can change the linear form. In principle, since the action is a scalar, the Lagrangian can contain any scalar constructed from the Riemann curvature tensor — the Ricci scalar happens to be only one such scalar.

Such non-linear extension of the form of the Lagrangian was postulated by Penchlaner and Sexl [170] drawing analogy with quantum electrodynamics. When quantum vacuum polarizations are included, the classical electrodynamic Lagrangian $\mathcal{L}_{\text{class}} = \frac{1}{2}(\mathbf{E}^2 - \mathbf{H}^2)$ acquires vacuum polarization corrections leading to the effective Lagrangian $\mathcal{L}_{\text{eff}} = \frac{1}{2}(\mathbf{E}^2 - \mathbf{H}^2) + \frac{2\alpha^2}{45m^4}[(\mathbf{E}^2 - \mathbf{H}^2)^2 + 7(\mathbf{E}\cdot\mathbf{H})^2] + \ldots$, which involves the two invariants $\mathbf{E}^2 - \mathbf{H}^2$ and $\mathbf{E}\cdot\mathbf{H}$ of the electromagnetic field. Proposing analogous arguments, they postulated that quantum vacuum fluctuations could generate the higher order geometric invariants R^2, $R_{\mu\nu}R^{\mu\nu}$ and $R^{\mu\nu\alpha\beta}R_{\mu\nu\alpha\beta}$ in the effective Lagrangian. One of them could be excluded since the Gauss-Bonnet term $R^2 - 4R_{\mu\nu}R^{\mu\nu} + R^{\mu\nu\alpha\beta}R_{\mu\nu\alpha\beta}$ determines a topological invariant, the Euler characteristic of the 4-dimensional manifold. For simplicity, one more term was neglected leading to the model $R + \alpha R^2$ for the effective gravitational Lagrangian. On the other hand, Buchdahl [37] considered a general function $f(R)$ for the effective Lagrangian, with the requirement that the conservation law $\nabla_\mu T^{\mu\nu} = 0$ is preserved.

On a more fundamental level, it was shown by Shore [202] that quantum fluctuations of scalar fields in a de-Sitter spacetime can give rise to an effective potential in the Lagrangian from the vacuum expectation value $\langle T_{\mu\nu}^{\text{QM}}\rangle$ in the Einstein field equation. Moreover, Birrell and Davies [31] calculated the one-loop corrections to $\langle T_{\mu\nu}^{\text{QM}}\rangle$ due to vacuum fluctuations of scalar fields living in a Robertson-Walker spacetime. This approach of obtaining the functional form of $f(R)$ is more fundamental in nature since we expect that the vacuum fluctuation of the standard model particles must be present.

The basic idea can be illustrated by taking a Lagrangian of a scalar field,

$$\mathcal{L} = \frac{1}{2}\partial_\mu\phi\,\partial^\mu\phi - \frac{1}{2}m^2\phi^2, \tag{1.101}$$

minimally coupled to gravity. In order to deal with such a theory, one has to consider the vacuum expectation value of $\langle 0|\phi^2(x)|0\rangle$, which is a divergent quantity. To treat this divergence one considers the two-point propagator

$$G(x,x') = \langle 0|\phi(x)\phi(x')|0\rangle, \tag{1.102}$$

which will be evaluated in the limit $x' \to x$. Calculation shows that the ultraviolet divergence appears in a Laurent series as

$$G(x,x') = \frac{A}{\varepsilon} + B\ln\varepsilon + C \tag{1.103}$$

where A, B, C are well-behaved functions of x and x' and $\varepsilon = |x - x'|$.

The vacuum expectation value of the energy-momentum tensor is given by

$$\langle 0|T_{\mu\nu}|0\rangle = \frac{1}{2}\left[\partial_\mu\partial'_\nu - \frac{1}{2}g_{\mu\nu}\partial_\lambda\partial'^\lambda\right]G(x,x') \tag{1.104}$$

The above form depends on the direction of the vector $x - x'$. Averaging over the directions gives

$$\langle 0|T_{\mu\nu}|0\rangle = C_1\frac{g_{\mu\nu}}{\varepsilon^2} + C_2\frac{G_{\mu\nu}}{\varepsilon} + (C_3P_{\mu\nu} + C_4Q_{\mu\nu})\ln\varepsilon \tag{1.105}$$

where $C_{i=1,2,3,4}$ are constants and $G_{\mu\nu}$ is the Einstein tensor. The covariantly conserved tensors $P_{\mu\nu}$ and $Q_{\mu\nu}$ can be obtained by the following variations

$$P_{\mu\nu} = \frac{1}{\sqrt{-g}}\frac{\delta}{\delta g^{\mu\nu}}\left(\sqrt{-g}R^2\right) \tag{1.106}$$

and

$$Q_{\mu\nu} = \frac{1}{\sqrt{-g}}\frac{\delta}{\delta g^{\mu\nu}}\left(\sqrt{-g}R_{\rho\sigma}R^{\rho\sigma}\right). \tag{1.107}$$

Since these terms are produced as one-loop corrections, we must start with the action

$$S_{\text{Grav}} = \frac{1}{16\pi G_0}\int(R - 2\Lambda_0 + \alpha_0R^2 + \beta_0R_{\rho\sigma}R^{\rho\sigma})\sqrt{-g}\,d^4x, \tag{1.108}$$

so that the bare field equation has the form

$$G_{\mu\nu} + \Lambda_0g_{\mu\nu} + \alpha_0P_{\mu\nu} + \beta_0Q_{\mu\nu} = 8\pi G_0\ \langle 0|T^{\text{QM}}_{\mu\nu}|0\rangle \tag{1.109}$$

where $T^{\text{QM}}_{\mu\nu}$ is the energy-momentum tensor of the scalar field.

Inserting the one-loop contributions of the vacuum expectation value $\langle 0|T^{\text{QM}}_{\mu\nu}|0\rangle$, and defining renormalized quantities as

$$\frac{1}{8\pi G} = \left(\frac{1}{8\pi G_0} - \frac{C_2}{\varepsilon}\right), \qquad \frac{\Lambda}{8\pi G} = \frac{\Lambda_0}{8\pi G_0} - \frac{C_1}{\varepsilon^2},$$
$$\frac{\alpha}{8\pi G} = \frac{\alpha_0}{8\pi G_0} - C_3 \ln\varepsilon, \qquad \frac{\beta}{8\pi G} = \frac{\beta_0}{8\pi G_0} - C_4 \ln\varepsilon, \tag{1.110}$$

one obtains the renormalized field equation

$$G_{\mu\nu} + \Lambda g_{\mu\nu} + \alpha P_{\mu\nu} + \beta Q_{\mu\nu} = 0 \tag{1.111}$$

where G, Λ, α and β are physically measurable parameters.

A further extension of such a modified gravity model was suggested by Harko [81] by considering a function $f(R,T)$ as the Lagrangian in the gravitational action. Since the Lagrangian itself involves the trace T of the energy-momentum tensor, the conservation law $\nabla_\nu T^{\mu\nu} = 0$ is now violated. Moreover the particle trajectories will no longer follow the geodesics. It was suggested that such an extension may arise due to quantum mechanical corrections and exotic matters, although the origin of such an extension is not very clear at the outset. It may however be visualized as a gravity-matter interaction if a coupling between the scalars R and T is present in the functional form $f(R,T)$.

1.6.1 $f(R)$ gravity

New challenges raised by recent cosmological observations lead to the consideration of modified Einstein-Hilbert action to include higher order curvature invariants in the gravitational Lagrangian. In this context, we present here the simplest form of this modification known as $f(R)$ gravity [62, 83], with an action given by

$$S_{\text{grav}} = \frac{c^3}{16\pi G}\int f(R)\sqrt{-g}\; d^4x \tag{1.112}$$

where $f(R)$ is an arbitrary analytical function of the Ricci scalar R that possesses a Taylor series expansion. Thus $f(R)$ gravity is equivalent to a Brans-Dicke theory with $\omega = 0$ in the Einstein frame.

For any gravitational system, the full action is therefore given by

$$S = \int d^4x\sqrt{-g}\left\{\frac{1}{2\kappa}f(R) + \mathcal{L}_m\right\}, \tag{1.113}$$

where $\mathcal{L}_m$ is the matter Lagrangian density.

The variation of the action S_{grav} is obtained as

$$\delta S_{\text{grav}} = \frac{1}{2}\int d^4x\,\delta(\sqrt{-g})f(R) + \frac{1}{2}\int d^4x\,\sqrt{-g}\delta f(R) \tag{1.114}$$

with variation of $\sqrt{-g}$ given as

$$\delta\sqrt{-g} = -\frac{1}{2\sqrt{-g}}\delta g. \tag{1.115}$$

Since $\ln(\det A) = \mathrm{tr}(\ln A)$, where A is a matrix, an infinitesimal change is $\frac{\delta \det A}{\det A} = \mathrm{Tr}(A^{-1}\delta A)$. Thus we obtain $\delta g = g g^{\mu\nu}\delta g_{\mu\nu}$. Using $g^{\mu\nu}\delta g_{\mu\nu} = -g_{\mu\nu}\delta g^{\mu\nu}$ we immediately obtain

$$\delta\sqrt{-g} = -\frac{1}{2}\sqrt{-g}\, g_{\mu\nu}\, \delta g^{\mu\nu}. \tag{1.116}$$

The variation in $f(R)$ is not straight forward as in the case of the original Einstein-Hilbert action, where $f(R) = R$. Here, the variation leads to

$$\delta f(R) = f_R \delta(R_{\mu\nu} g^{\mu\nu}) = f_R g^{\mu\nu}\delta R_{\mu\nu} + f_R R_{\mu\nu}\delta g^{\mu\nu}, \tag{1.117}$$

with $f_R = \partial f/\partial R$. The variation of Ricci tensor is straight forward from its definition, that is, $\delta R_{\mu\nu} = \nabla_\lambda(\delta\Gamma^\lambda_{\nu\mu}) - \nabla_\nu(\delta\Gamma^\lambda_{\lambda\mu})$. This reduces the above equation to

$$\delta f(R) = f_R g^{\mu\nu}\left(\nabla_\lambda \delta\Gamma^\lambda_{\nu\mu} - \nabla_\nu \delta\Gamma^\lambda_{\lambda\mu}\right) + f_R R_{\mu\nu}\delta g^{\mu\nu}. \tag{1.118}$$

Variation of the Christoffel symbols is $g^{\mu\nu}(\nabla_\lambda\delta\Gamma^\lambda_{\nu\mu} - \nabla_\nu\delta\Gamma^\lambda_{\lambda\mu}) = -\nabla_\mu\nabla_\nu\delta g^{\mu\nu} + g_{\mu\nu}\Box\delta g^{\mu\nu}$. Using this, the variation in $f(R)$ reduces to

$$\delta f(R) = f_R\left(R_{\mu\nu}\delta g^{\mu\nu} + g_{\mu\nu}\Box\delta g^{\mu\nu} - \nabla_\mu\nabla_\nu\delta g^{\mu\nu}\right) \tag{1.119}$$

The variation of the gravitational action thus becomes

$$\delta S_{\text{grav}} = \frac{1}{2}\int d^4x\sqrt{-g}\left\{\left(f_R R_{\mu\nu} - \frac{1}{2}f(R)g_{\mu\nu}\right)\delta g^{\mu\nu} + f_R\left(g_{\mu\nu}\Box\delta g^{\mu\nu} - \nabla_\mu\nabla_\nu\delta g^{\mu\nu}\right)\right\}, \tag{1.120}$$

which, on integration by parts, leads to

$$\delta S_{\text{grav}} = \frac{1}{2}\int d^4x\sqrt{-g}\left\{f_R R_{\mu\nu} - \frac{1}{2}g_{\mu\nu}f(R) + \left(g_{\mu\nu}\Box - \nabla_\mu\nabla_\nu\right)f_R\right\}\delta g^{\mu\nu} \tag{1.121}$$

Together with the variation of the matter Lagrangian $\mathcal{L}_m$ with respect to the metric tensor $g_{\mu\nu}$, we obtain the field equation

$$f_R R_{\mu\nu} - \frac{1}{2}g_{\mu\nu}f(R) + \left(g_{\mu\nu}\Box - \nabla_\mu\nabla_\nu\right)f_R = \kappa T_{\mu\nu}. \tag{1.122}$$

The above field equation corresponds to a fourth-order partial differential partial equation in $g_{\mu\nu}$, whereas the Einstein-Hilbert action leads only to a second-order partial differential equation. For $f_R = 1$, the above field equation reduces to the Einstein field equation.

The trace of above equation is

$$f_R R - 2f(R) + 3\Box f_R = \kappa T, \tag{1.123}$$

which is different from the original trace equation $R = -\kappa T$. This means, for the case $T = 0$, the modified trace equation (1.123) does not necessarily imply $R = 0$. In other words, $T = 0$ does not necessarily lead to a vacuum solution as in the original theory of general relativity. For the case $R = \text{const}$ and $T = 0$, the trace equation (1.123) reduces to

$$f_R R - 2f(R) = 0 \tag{1.124}$$

The form of the function $f(R)$ will tell us the type of the maximally symmetric solutions as follows. If $f(R)$ is chosen such that $R = 0$ is a root of equation (1.124) and we introduce this solution in equation (1.122), then we obtain $R_{\mu\nu} = 0$, and the maximally symmetric spacetime will be Minkowskian. When the form of $f(R)$ leads to the root $R = \pm R_0$ from equation (1.124), it follows that $R_{\mu\nu} = \frac{1}{4} g_{\mu\nu} R_0$, in which case the maximally symmetric solutions will be de-Sitter ($+R_0$) or anti-de-Sitter ($-R_0$) spacetime, analogous to general relativity with a cosmological constant Λ.

1.6.1.1 Conformal Transformation

We have defined the action (1.112) for $f(R)$ gravity in the Jordan frame. It may be worthwhile to note that any general form of $f(R)$ gravity can be transformed into the Einstein frame by means of a conformal transformation

$$\tilde{g}_{\mu\nu} = \Omega^2 \, g_{\mu\nu} \,, \tag{1.125}$$

where Ω^2 is the conformal factor connecting the metric $g_{\mu\nu}$ in the Jordan frame with the metric $\tilde{g}_{\mu\nu}$ in the Einstein frame. Consequently, the scalar curvatures in the two frames are related by

$$R = \Omega^2 \left\{ \tilde{R} + 6\tilde{\Box}\phi - 6\tilde{g}^{\mu\nu}\partial_\mu\phi\partial_\nu\phi \right\} \tag{1.126}$$

where $\phi = \ln \Omega$ and symbols with a tilde represent quantities in the Einstein frame.

The action (1.112) can be rewritten in the form

$$S_{\text{grav}} = \int d^4x \sqrt{-g} \left(\frac{1}{2\kappa^2} f_R R - V \right) \tag{1.127}$$

where $V(R) = \frac{1}{2\kappa^2}(f_R R - f)$.

Using Eq. (1.126) and the relation $\sqrt{-g} = \Omega^{-4}\sqrt{-\tilde{g}}$, the action (1.127) becomes

$$S_{\text{grav}} = \int d^4x \sqrt{-\tilde{g}} \left[\frac{1}{2\kappa^2} f_R \Omega^{-2} (\tilde{R} + 6\tilde{\Box}\phi - 6\tilde{g}^{\mu\nu}\partial_\mu\phi\partial_\nu\phi) - \Omega^{-4} V \right] \tag{1.128}$$

The matter action $S_m = \int d^4x \, \mathcal{L}_m(g_{\mu\nu}, \Psi_m)$ therefore transforms as

$$S_m = \int \mathrm{d}^4x \mathcal{L}_m(\Omega^{-2} \, \tilde{g}_{\mu\nu}, \Psi_m) \,. \tag{1.129}$$

For the choice $\Omega^2 = f_R$, and since the integral $\int d^4x \sqrt{-\tilde{g}} \, \tilde{\Box}\phi$ vanishes on account of the Gauss theorem, one obtains the total action in the Einstein frame as

$$S_{\mathrm{E}} = \int d^4x\, \sqrt{-\tilde{g}} \left[\frac{1}{2\kappa^2}\tilde{R} - \frac{1}{2}\tilde{g}^{\mu\nu}\partial_\mu\Phi\partial_\nu\Phi - U(\Phi) \right] + \int \mathrm{d}^4x\, \mathcal{L}_m(f_R^{-1}(\Phi)\tilde{g}_{\mu\nu}, \Psi_m)\,, \quad (1.130)$$

where $\Phi = \sqrt{6}\phi/\kappa$ and the new potential U is defined as

$$U(\Phi) = \frac{V}{f_R^2} = \frac{f_R R - f}{2\kappa^2 f_R^2}\,. \quad (1.131)$$

The choice $\Omega^2 = f_R$ is consistent with the condition $f_R > 0$ [62].

The matter in the Einstein frame is directly coupled to the scalar field Φ. Variation of the action (1.130) with respect to the scalar field Φ gives

$$\tilde{\Box}\Phi - U_{,\Phi} + \frac{1}{\sqrt{-\tilde{g}}}\frac{\partial \mathcal{L}_m}{\partial \Phi} = 0, \quad (1.132)$$

and the functional derivative of the matter Lagrangian with respect to Φ is

$$\frac{\partial \mathcal{L}_m}{\partial \Phi} = \frac{\delta \mathcal{L}_m}{\delta g^{\mu\nu}}\frac{\partial g^{\mu\nu}}{\partial \Phi} = \frac{1}{f_R(\Phi)}\frac{\delta \mathcal{L}_m}{\delta \tilde{g}^{\mu\nu}}\frac{\partial (f_R(\Phi)\tilde{g}^{\mu\nu})}{\partial \Phi} = -\sqrt{-\tilde{g}}\,\frac{f_{,\Phi}}{2f_R}\,\tilde{T}^{(m)}_{\mu\nu}\tilde{g}^{\mu\nu}\,. \quad (1.133)$$

Thus the equation of motion of the scalar field Φ becomes

$$\tilde{\Box}\Phi - U_{,\Phi} - \frac{f_{R,\Phi}}{2f_R}\tilde{T} = 0\,. \quad (1.134)$$

The strength of the coupling between the scalar field Φ and matter can be quantified by

$$q = -\frac{f_{R,\Phi}}{2\kappa f_R} = -\frac{1}{\sqrt{6}} \quad (1.135)$$

which is a constant in $f(R)$ gravity. This makes the field equation in the Einstein frame as

$$\tilde{\Box}\Phi - U_{,\Phi} + \kappa q \tilde{T} = 0, \quad (1.136)$$

showing that the field Φ is directly coupled to matter.

For a massless scalar field Φ such that $U(\Phi) = 0$, there exist a long range additional force with a large coupling q. This is not be consistent with experimental tests in the solar system. However, this situation need not occur in $f(R)$ gravity when $U(\Phi) \neq 0$. Thus it is possible to formulate $f(R)$ gravity consistent with solar system tests [35, 103, 104].

1.6.2 $f(R,T)$ gravity

In this section ,we briefly present the preliminary details of $f(R,T)$ gravity needed for our later developments. The action of the most general $f(R,T)$ gravity is given by [84]

$$S = \frac{c^3}{16\pi G}\int d^4x\sqrt{-g}\, f(R,T) + \int d^4x\sqrt{-g}\, L_m, \tag{1.137}$$

where L_m is the Lagrangian density of matter. The stress-energy tensor $T_{\mu\nu}$ is obtained from the matter Lagrangian L_m as

$$T_{\mu\nu} = g_{\mu\nu}L_m - 2\frac{\partial L_m}{\partial g^{\mu\nu}}. \tag{1.138}$$

Field equations following from Eq. (1.137) are

$$f_R R_{\mu\nu} - \frac{1}{2}f g_{\mu\nu} + (g_{\mu\nu}\nabla^\alpha\nabla_\alpha - \nabla_\mu\nabla_\nu)f_R = \kappa T_{\mu\nu} - f_T T_{\mu\nu} - f_T\Theta_{\mu\nu} \tag{1.139}$$

where $\Theta_{\mu\nu} = g^{\alpha\beta}\frac{\delta T_{\alpha\beta}}{\delta g^{\mu\nu}}$, $f_R = \frac{\partial f}{\partial R}$, $f_T = \frac{\partial f}{\partial T}$.

The covariant divergence of the above field equation with the identity [110]

$$\nabla^\mu\left[f_R R_{\mu\nu} - \frac{1}{2}f g_{\mu\nu} + (g_{\mu\nu}\nabla^\alpha\nabla_\alpha - \nabla_\mu\nabla_\nu)f_R\right] = 0 \tag{1.140}$$

leads to

$$\nabla^\mu T_{\mu\nu} = \frac{f_T}{\kappa - f_T}\left[(T_{\mu\nu} + \Theta_{\mu\nu})\nabla^\mu \ln f_T + \nabla^\mu\Theta_{\mu\nu}\right] \tag{1.141}$$

This shows that the stress-energy tensor of the matter distribution is no longer conserved covariantly, $\nabla_\mu T^{\mu\nu} \neq 0$. Consequently, the particles of matter do not follow geodesic paths. This can be illustrated for the simple case of a prefect fluid with $\Theta_{\mu\nu} = -2T_{\mu\nu} + Pg_{\mu\nu}$, giving

$$\nabla^\mu T_{\mu\nu} = \frac{1}{\kappa - f_T}\left[T_{\mu\nu}\nabla^\mu f_T + g_{\mu\nu}\nabla^\mu(f_T\, P)\right] \tag{1.142}$$

By introducing the projection operator $J_{\mu\nu} = g_{\mu\nu} - u_\mu u_\nu$, one directly obtains the geodesic equation as

$$\frac{d^2x^\mu}{ds^2} + \Gamma^\mu_{\nu\lambda}u^\nu u^\lambda = \kappa\frac{\nabla_\nu P}{(\varepsilon + P)(\kappa + f_T)}J^{\mu\nu}. \tag{1.143}$$

The gradient on the right-hand side can be expressed as the covariant derivative of a scalar, $\nabla_\nu \ln\sqrt{Q}$. Thus we have

$$\frac{d^2x^\mu}{ds^2} + \Gamma^\mu_{\nu\lambda}u^\nu u^\lambda = J^{\mu\nu}\nabla_\nu \ln\sqrt{Q}. \tag{1.144}$$

Since $J_{\nu\mu}u^\mu = 0$, the force on the right-hand side is orthogonal to the four velocity u^μ. Moreover, for a pressure-less fluid, we obtain the original geodesic equation.

Constraints coming from solar system tests give an upper bound on the extra-acceleration a_E generated by the extended $f(R,T)$ theories of gravity. The change in the precession angle $\Delta\phi$ of the perihelion of Mercury is given by

$$\Delta\phi = \frac{6\pi G M_\odot}{a\left(1-e^2\right)} + \frac{2\pi a^2\sqrt{1-e^2}}{G M_\odot} a_E \,, \tag{1.145}$$

where a is the semi-major axis and e is the eccentricity of the orbit. The first term is the contribution from general relativity and the second term originates from $f(R,T)$ gravity.

For Mercury, $a = 57.91 \times 10^6$ km, and $e = 0.205615$. The standard general relativistic value for the precession angle is $(\Delta\phi)_{\mathrm{GR}} = 42.962$ arcsec per century, while the observed value is $(\Delta\phi)_{\mathrm{obs}} = 43.11 \pm 0.21$ arcsec per century [195]. Therefore the difference

$$(\Delta\phi)_{\mathrm{E}} = (\Delta\phi)_{\mathrm{obs}} - (\Delta\phi)_{\mathrm{GR}} = \frac{2\pi a^2\sqrt{1-e^2}}{G M_\odot} a_E \sim 0.358 \;\; \text{arcsec per century}, \tag{1.146}$$

which may be identified with effects due to an extended gravity such as the $f(R,T)$ scenario. Hence the observational constraints requires that the value of the extra acceleration a_E must satisfy the condition $a_E \lesssim 10^{-9}$ cm/s^2.

1.7 Friedmann Equations

Our Universe contains many galaxies that form clusters and superclusters. While a spiral galaxy such as the Milky Way is of the size $\sim$ 30 kpc, typical sizes of clusters and superclusters are $\sim$ 5 Mpc and $\sim$ 50 Mpc, respectively. There are large empty spaces or voids $\sim 100 - 200$ Mpc in the distribution of superclusters [152]. At length scales much larger than this, the distribution of matter can be considered to be uniform. Observations suggest that the Universe is spatially homogeneous and isotropic in the distribution of matter. Moreover, the cosmic microwave background radiation, originating around $\sim 10^5$ years after the Big Bang, also is observed to be spatially homogeneous and isotropic.

These facts suggest that a model for the Universe ought to be homogeneous and isotropic in space implying that the space part of the metric should be the same at all points and in all directions. Friedmann was the first to consider an isotropic cosmological model in 1922.

In discussing the geometry of the homogeneous isotropic space, we shall follow Landau and Lifshitz [113]. A General line element for spatial separation is given by

$$dl^2 = \gamma_{ij} dx^i dx^j \,, \tag{1.147}$$

where γ_{ij} is the three-dimensional metric tensor. Analogous to the Riemann tensor, curvature of space is completely determined by the three-curvature tensor K^i_{jkl}. For an isotropic manifold, the curvature tensor can be expressed in terms of the metric γ_{ij} as

$$K^i_{jkl} = \lambda \left(\delta^i_k \gamma_{lj} - \delta^i_l \gamma_{kj} \right) \tag{1.148}$$

where λ is a constant. Consequently, the Ricci tensor and scalar curvature are

$$K_{ij} = 2\lambda \gamma_{ij} \tag{1.149}$$

and

$$K = 6\lambda, \tag{1.150}$$

respectively. Thus the characteristics of an isotropic space are determined by a single parameter λ. There are in general three different possibilities, (1) space of constant positive curvature (2) space of constant negative curvature and (3) space of null curvature ($\lambda = 0$).

We shall now consider the geometry of an isotropic three sphere as the geometry on a hypersurface in a fictitious four dimensional space. The equation of a hypersphere of radius a in the four dimensional Euclidean space is

$$x_1^2 + x_2^2 + x_3^2 + x_4^2 = a^2 \tag{1.151}$$

and the line element has the form

$$dl^2 = dx_1^2 + dx_2^2 + dx_3^2 + dx_4^2 \tag{1.152}$$

Eliminating the fictitious coordinate x_4, we get

$$dl^2 = dx_1^2 + dx_2^2 + dx_3^2 + \frac{(x_1 dx_1 + x_2 dx_2 + x_3 dx_3)^2}{a^2 - x_1^2 - x_2^2 - x_3^2} \tag{1.153}$$

In spherical coordinates, the line element takes the form

$$dl^2 = \frac{dr^2}{1 - \frac{r^2}{a^2}} + r^2 (d\theta^2 + \sin^2\theta \, d\phi^2), \qquad \lambda = \frac{1}{a^2}, \tag{1.154}$$

$$dl^2 = dr^2 + r^2 (d\theta^2 + \sin^2\theta \, d\phi^2), \qquad \lambda = 0, \tag{1.155}$$

$$dl^2 = \frac{dr^2}{1 + \frac{r^2}{a^2}} + r^2 (d\theta^2 + \sin^2\theta \, d\phi^2), \qquad \lambda = -\frac{1}{a^2}, \tag{1.156}$$

where the last line element corresponds to a space of constant negative curvature, obtained from the geometry of a pseudosphere of imaginary radius (that is, by replacing a by ia). On the other hand, the line element for $\lambda = 0$ corresponds to a flat geometry.

Using the coordinate transformation $r = a\xi$ and introducing a parameter k for the sign of the space curvature, one can write a general form of the above line elements as

$$dl^2 = a^2 \left\{ \frac{d\xi^2}{1 - k\xi^2} + \xi^2 (d\theta^2 + \sin^2\theta \, d\phi^2) \right\}, \tag{1.157}$$

where the curvature parameter $k = +1, 0, -1$ for positive, null and negative curvature, respectively.

The isotropy in space suggests that g_{0i} components of the metric must vanish due to equivalence of different directions. Thus the spacetime line element must have the form

$$ds^2 = g_{00} \, c^2 \, dt^2 - dl^2 \tag{1.158}$$

where g_{00} is a function of time t only, which can be set equal to unity by a proper redefinition of the time coordinate. Thus the four dimensional line element becomes

$$ds^2 = c^2 dt^2 - a^2(t) \left\{ \frac{d\xi^2}{1 - k\xi^2} + \xi^2 (d\theta^2 + \sin^2\theta \, d\phi^2) \right\}, \tag{1.159}$$

where $a(t)$ is represented as a function of time in order to describe the dynamics of the Universe.

The non-vanishing components of the metric tensor are

$$g_{00} = 1, \qquad g_{11} = -\frac{a^2(t)}{1 - k\xi^2}, \qquad g_{22} = -a^2(t) \, \xi^2, \qquad g_{33} = -a^2(t) \, \xi^2 \sin^2\theta. \tag{1.160}$$

Employing these line elements in the Einstein field equations (1.81) with energy-momentum tensor (1.84), the following dynamical equations are obtained,

$$\left(\frac{\dot{a}}{a} \right)^2 = \frac{8\pi G}{3c^2} \varepsilon - \frac{kc^2}{a^2}, \tag{1.161}$$

$$\frac{\ddot{a}}{a} = -\frac{4\pi G}{3c^2} (\varepsilon + 3P), \tag{1.162}$$

which are known as the Friedmann first and second equations, respectively. Moreover, conservation of energy-momentum tensor, $\nabla_\mu T^{\mu\nu} = 0$, gives the equation of continuity

$$\dot{\varepsilon} + 3 \left(\frac{\dot{a}}{a} \right) (\varepsilon + P) = 0. \tag{1.163}$$

1.8 Inflationary Cosmology and Reheating

Inflation was proposed to address the fundamental issues associated with the Standard Model Big Bang of Cosmology, which based on the Friedmann-Lemaitre-Robertson-Walker (FLRW) model. These issues are known as the flatness problem, the horizon problem, the magnetic monopole problem, and the origin of large-scale structures in the universe. The cosmic microwave background (CMB) radiation, that carries the imprint of the early universe since the period of recombination, is found to be homogeneous and isotropic having a temperature 2.725 K [131] with a nearly perfect black-body spectrum and the anisotropies are almost negligible. This uniformity is found to exist over causally disconnected regions of the sky. Such large-scale correlation is impossible to obtain from the causal processes in the FLRW metric after the Big Bang.

The particle horizon is defined as

$$\eta = \int_{t_1}^{t_2} \frac{dt}{a(t)} = \int_{a_1}^{a_2} \frac{da}{a^2 H(a)}, \tag{1.164}$$

(with $c = 1$) since light travels a comoving distance of $dr = dt/a(t)$ in a time interval dt. For the equation of state given by $p = \omega\rho$, the Hubble rate goes like $H \propto a^{-3(1+\omega)/2}$, so that

$$\eta = \int_{a_1}^{a_2} \frac{da}{a^{(1+3\omega)/2}} = a^{\frac{1+3\omega}{2}}\Big|_{a_1}^{a_2} \tag{1.165}$$

Thus the particle horizon since the Big Bang to the period of recombination is roughly ~ 284 Mpc and the particle horizon from the recombination to the present epoch is 14.4 Gpc. We can therefore expect a correlation over an angular spread $\sim 284/14400 = 1.1^\circ$. On the contrary, the CMB exhibit a nearly perfect correlation over the entire sky. This contradiction between the standard model and observation is known the *Horizon Problem.*

Observations suggest that the density parameter $\Omega = \rho/\rho_c$ is very close to unity $\Omega \approx 1$. Since the curvature parameter $k = 0$ is at the boundary between the open and closed universe models, this implies that nearly flat universe. However from Friedmann equation, one obtains $|\Omega - 1| = \frac{k}{a^2 H^2} \propto k a^{\frac{1+3\omega}{2}}$, which represents a universe that was extremely flat in the early epoch. For a non-zero curvature parameter k, the consistency with observation would require an extra-ordinary fine tuning of the initial conditions. This is gives rise to the *Flatness Problem.*

Super-symmetric grand-unified theories (GUT) suggest that the three coupling constants of electromagnetic, weak, and strong interactions approach the same value at the grand-unification energy scale of $\sim 10^{16}$ GeV. This corresponds to the unification $U(1) \times SU(2) \times SU(3) \to G$. Thus a spontaneous symmetry breaking can occur as the universe cools to a critical temperature of $T_c \sim 10^{16}$ GeV. This phase transition is capable of producing topological defects such as magnetic monopoles. This can be illustrated by a simple $SO(3)$ gauge theory which is spontaneously broken to $U(1)$ by the Higgs mechanism [111]. In this process, two of the gauge bosons acquire mass and there may arise a solution of hedgehog configuration, for the Higgs field $\Phi^a \to \sigma\hat{\mathbf{r}}$ and the gauge boson $A^a_\mu \to \epsilon_{\mu ab}\hat{\mathbf{r}}_b/er$ as $r \to \infty$, where σ is the minima of the Higgs field.

The magnetic field

$$B^a_i = \frac{1}{2}\epsilon_{ijk}F^a_{jk} = \frac{\hat{\mathbf{r}}_i\hat{\mathbf{r}}^a}{er^2} \tag{1.166}$$

resembles the configuration of a magnetic monopole. Thus a magnetic monopole is generated with a mass $\frac{4\pi\sigma}{e} = \frac{M_{\rm V}}{\alpha}$. Since the mass of the vector boson $M_{\rm V} = e\sigma \sim 10^{16}$ GeV, the magnetic monopole is extremely heavy with mass 10^{18} GeV which is also the characteristic critical temperature T_c of this phase transition.

The number density of such monopoles created in this phase transition can be estimated as

$$n_M \sim H^3 \sim \left(\frac{\rho}{m_P^2}\right)^{3/2} \sim \left(\frac{\pi^2 g^*}{30}\right)^{3/2} \frac{T_c^6}{m_{\rm P}^3}, \tag{1.167}$$

assuming the formation of one single monopole per Hubble volume. Dividing it by entropy density $s \sim g^* T^3$, we get

$$\frac{n_M}{s} \sim \left(\frac{T_c}{m_{\rm P}}\right)^3. \tag{1.168}$$

Thus the number of monopoles per baryon number is

$$\frac{n_M}{n_B} = \frac{n_M}{s}\frac{s}{n_B} \sim 10^{-3} \times 10^{10} \sim 10^7, \tag{1.169}$$

which is obviously an unphysical number. Needless to say, we do not find any magnetic monopoles around us in contradiction to the above estimate from the Standard Model of Cosmology. Several magnetic monopole searches, for example in iron and other ferromagnetic ores, have consistently given negative results. This is the *Magnetic Monopole Problem*

The Standard Big Bang model predicts that the universe remains homogenous and isotropic in its evolution. Since it does not have any mechanism to introduce inhomogeneity, it cannot predict the formation of inhomogeneous structures such as galaxies and clusters that we observe today. On the other hand, high resolution observations show that there are very small inhomogeneities ($\sim 10^{-5}$) in the CMB radiation which are basically the seeds to the formation of large-scale structures. These observed inhomogeneities cannot follow from the Big Bang model, giving rise to yet another problem with the Standard Model of Cosmology.

As shown by Guth [79], the above problems are solved by an inflationary model where the universe undergoes an exponentially fast expansion in the beginning. It is then immediately obvious that the magnetic monopoles formed via the GUT phase transition would be diluted away exponentially quickly, so that we practically find no magnetic monopoles in the present epoch, solving the Monopole problem. Since the scale factor goes like $a \sim e^{Ht}$ in the inflationary phase, $|\Omega - 1|$ approaches zero very quickly giving negligible contribution from the curvature k dependent term in the evolution, thus solving the Flatness Problem. Moreover, quantum fluctuations in the inflationary phase act as seeds to anisotropy that form inhomogeneous structures like galaxies and clusters in the later stages of the evolution. In addition, an inflationary theory should also include a mechanism for particle production and its thermalisation in order to give rise to the observed correlation in the CMB radiation, hence solving the Horizon Problem.

1.8.1 Inflationary Phase

In the (new) inflationary model, the main contribution to the energy-momentum tensor comes from a scalar field ϕ (dubbed *inflaton*) with the Lagrangian density

$$\mathcal{L}(\phi) = \frac{1}{2}\partial_\mu\phi\partial^\mu\phi - V(\phi), \tag{1.170}$$

where $V(\phi)$ is the potential of the scalar field. Ignoring the spatial dependence, the energy density and the pressure is obtained as $\rho = \frac{\dot{\phi}^2}{2} + V(\phi)$ and $p = \frac{\dot{\phi}^2}{2} - V(\phi)$, respectively. Consequently, the evolution of the Friedmann-Lemaitre-Robertson-Walker metric [73, 182, 222] is obtained from Einstein field equation as

$$H^2 = \frac{8\pi}{3m_{\rm P}^2}\rho = \frac{8\pi}{3m_{\rm P}^2}\left\{\frac{\dot{\phi}^2}{2} + V(\phi)\right\}, \tag{1.171}$$

and

$$\frac{\ddot{a}}{a} = -\frac{4\pi}{3m_{\rm P}^2}(\rho + 3p) = -\frac{8\pi}{3m_{\rm P}^2}\left\{\dot{\phi}^2 - V(\phi)\right\}, \tag{1.172}$$

where H is the Hubble parameter defined as $H = \frac{\dot{a}}{a}$. The evolution of the scalar field, on the other hand, is given by the Klein-Gordon equation,

$$\ddot{\phi} + 3H\dot{\phi} + V_{,\phi} = 0. \tag{1.173}$$

Inflation requires $\ddot{a} > 0$ so that the universe undergoes an accelerated expansion. This condition in turn requires $\rho + 3p < 0$ or $\dot{\phi}^2 < V(\phi)$ as seen from equation (1.172). For sufficient inflation, the appropriate condition is $\dot{\phi}^2 \ll V(\phi)$ that allow one to defines the well-known slow-roll parameters measuring the number of e-foldings during the inflationary phase. The first slow-roll parameter ϵ is obtained from

$$\epsilon = -\frac{\dot{H}}{H^2}, \tag{1.174}$$

that measures the change in Hubble rate per e-folding. For a large inflation, the parameter $\epsilon \ll 1$, whereas for a sufficiently long inflation, one requires ϵ to remain small for a long time, measured by a second parameter η, given by

$$\eta = \frac{\dot{\epsilon}}{\epsilon H}. \tag{1.175}$$

For a prolonged inflation, one requires $\eta \ll 1$.

Using Friedmann equations (1.171) and (1.172), the slow-roll parameters can be expressed in terms of the inflaton potential as

$$\epsilon = \frac{m_{\mathrm{P}}^2}{16\pi}\left(\frac{V_{,\phi}}{V}\right)^2 \quad \text{and} \quad \eta = \frac{m_{\mathrm{P}}^2}{8\pi}\frac{V_{,\phi\phi}}{V}. \tag{1.176}$$

For illustration, we shall consider the chaotic inflationary model with the potential $V(\phi) = \frac{1}{2}m^2\phi^2$. In this case, the slow-roll conditions give $\epsilon = \eta = m_{\mathrm{P}}^2/(4\pi\phi^2) \ll 1$, implying a large initial value $\phi \gg m_{\mathrm{P}}$. However, towards the end of inflation these parameters approach unity, where $\phi \sim m_{\mathrm{P}}/\sqrt{4\pi}$.

As the inflaton rolls down, it reaches the minimum of the potential $V(\phi)$ where the scalar field undergoes a damped oscillation, given by

$$\ddot{\phi} + 3H\dot{\phi} + m^2\phi = 0. \tag{1.177}$$

The oscillation is damped due to the expansion of the universe represented by the term $3H\dot{\phi}$. Together with equation (1.171), the above equation yields

$$\phi(t) = \frac{m_{\mathrm{P}}}{\sqrt{3\pi}mt}\sin mt. \tag{1.178}$$

After the first oscillation, $mt = 2\pi$, so that the amplitude of the oscillation drops significantly, $\phi \sim 0.05 m_{\mathrm{P}}$. Substituting equation (1.178) in equation (1.171), we can estimate the Hubble rate during this phase,

$$H \approx \frac{2}{3t}, \tag{1.179}$$

so that

$$a(t) \approx a_0 t^{2/3}, \tag{1.180}$$

and the energy density of the inflaton field is given by

$$\rho \approx \frac{m_{\mathrm{P}}^2}{6\pi}\left(\frac{a}{a_0}\right)^{-3}. \tag{1.181}$$

Thus the energy density of the inflation field decreases similar way as a dust-filled universe.

1.8.2 Reheating Phase — Perturbative Treatment

If we allow the inflaton to interact with the standard model fields, the inflaton can decay to produce particles of those fields. This process will make the amplitude of the inflaton oscillation decay faster than that determined by the Hubble expansion. This phase after inflation is called the *Reheating Phase* where ultra relativistic particles are created.

Following Kofman et al. [109], we demonstrate the reheating phase in the following. Assuming that the inflaton field ϕ interacts with only a boson field χ, the Lagrangian density can be written as

$$\mathcal{L} = \frac{1}{2}\partial_\mu\phi\partial^\mu\phi - \frac{1}{2}m^2\phi^2 + \frac{1}{2}\partial_\mu\chi\partial^\mu\chi - \frac{1}{2}m_\chi^2\chi^2 - \frac{1}{2}g^2\phi^2\chi^2, \tag{1.182}$$

where m_χ is the mass of a χ-particle and g is the coupling constant. Now the Klein-Gordon equation for the inflaton takes the form

$$\ddot{\phi} + 3H(t)\dot{\phi} + [m^2 + \Pi(\omega)]\phi = 0, \tag{1.183}$$

where $\Pi(\omega)$ is the self-energy due to vacuum polarization giving correction to m^2 for the case $\omega = m \ll 2m_\chi$. For the opposite case, $m \gg 2m_\chi$, the correction acquires an imaginary part, $\mathrm{Im}\,\Pi(\omega) = m\Gamma$, where Γ is the decay rate of the inflaton. The latter case is relevant to reheating, for which the solution of equation (1.183) takes the form

$$\phi(t) = \phi_0 e^{-\frac{1}{2}(3H+\Gamma)t} e^{imt}, \tag{1.184}$$

assuming a constant expansion rate H. Thus the decay of the inflaton amplitude is now enhanced by a factor of $e^{-\frac{\Gamma t}{2}}$ due to particle production.

Including spontaneous symmetry breaking by $\phi \to \phi - \sigma$, the true minima of the potential occurs at $\phi = \sigma$. This leads to an additional interaction term, namely, $g^2\phi\chi^2$, giving rise to the decay channel $\phi \to \chi\chi$. The corresponding decay rate is given by

$$\Gamma(\phi \to \chi\chi) = \frac{g^4\sigma^2}{8\pi m}. \tag{1.185}$$

We have seen above that the damping of the inflaton is determined by the Hubble rate H and the decay rate Γ. The corresponding solution can be obtained by adding a damping term $\Gamma\dot{\phi}$ in the dynamics of the inflaton field [4], so that

$$\ddot{\phi} + 3H(t)\dot{\phi} + \Gamma\dot{\phi} + m^2\phi = 0. \tag{1.186}$$

Now Substituting $\phi(t) = \Phi(t)\, e^{imt}$ in the above equation, we obtain

$$\ddot{\Phi} + [3H(t) + \Gamma]\dot{\Phi} = 0. \tag{1.187}$$

and

$$2\dot{\Phi} + [3H(t) + \Gamma]\Phi = 0. \tag{1.188}$$

Rewriting the latter equation, the amplitude Φ satisfies the differential equation

$$\frac{1}{a^3}\frac{d}{dt}(a^3\Phi^2) = -\Gamma\Phi^2. \tag{1.189}$$

Since the energy density of the inflaton field is related to its amplitude as $\rho = \frac{1}{2}m^2\Phi^2$, we obtain

$$\frac{1}{a^3}\frac{d}{dt}(a^3\rho) = -\Gamma\rho, \tag{1.190}$$

implying that the comoving energy density of the inflaton field decreases exponentially due to particle production.

The decay of the inflaton field gives rise to production of χ-particles with the source $\Gamma\rho$. Since this energy density ρ is related to the number density n_ϕ as $\rho = mn_\phi$, the time evolution for the number density n_χ is given by

$$\frac{1}{a^3}\frac{d}{dt}(a^3 n_\chi) = +2\Gamma n_\phi, \tag{1.191}$$

where the factor 2 accounts for the creation of two χ-particles out of a single ϕ-particle in the decay channel $\phi \to \chi\chi$. In terms of densities this equation becomes

$$\frac{1}{a^3}\frac{d}{dt}(a^3\rho_\chi) = +\left(\frac{2m_\chi}{m}\right)\Gamma\rho. \tag{1.192}$$

Since $m \gg m_\chi$, the energy density ρ_χ increases at a much slower pace than the rate of decrease of ρ given by equation (1.191)

Reheating occurs so long as $H > \Gamma$ and it stops when the condition $H \sim \Gamma$ is reached. The created particles cannot thermalize when $H < \Gamma$. This condition gives an estimate for the reheating energy density ρ_r as

$$\rho_r \simeq \frac{3\Gamma^2 m_{\rm P}^2}{8\pi}, \tag{1.193}$$

which corresponds to a reheating temperature

$$T_r \simeq \left(\frac{45}{4\pi^3 g^*}\right)^{1/4}\sqrt{\Gamma m_{\rm P}}, \tag{1.194}$$

where g^* is the number of degrees of freedom. For the standard model particles $g^* \sim 100$ [95].

1.8.3 Reheating via Parametric Resonance

In the previous subsection, we described the perturbative theory of reheating induced by a constant inflaton field σ. However, reheating can happen via parametric resonance induced by the oscillating inflaton field.

To demonstrate this, we consider the Lagrangian

$$\mathcal{L} = \frac{1}{2}\partial_\mu\phi\partial^\mu\phi - \frac{1}{2}m^2(\phi-\sigma)^2 + \frac{1}{2}\partial_\mu\chi\partial^\mu\chi - \frac{1}{2}m_{\chi,0}^2\chi^2 - \frac{1}{2}g^2\phi^2\chi^2. \tag{1.195}$$

The classical χ field, when quantized, can be represented in the Heisenberg picture by the field operator

$$\hat{\chi}(\mathbf{x},t) = \frac{1}{(2\pi)^{3/2}} \int d^3x \left\{ \hat{a}_k \chi_k(t) e^{-i\mathbf{k}\cdot\mathbf{x}} + \hat{a}_k^\dagger \chi_k^*(t) e^{i\mathbf{k}\cdot\mathbf{x}} \right\}, \tag{1.196}$$

where a_k and $a_k^\dagger$ are the annihilation and creation operator for a χ-particle of momentum $\mathbf{k}$ and χ_k is the corresponding mode function. In the FLRW metric with zero spatial curvature, the time evolution of the mode function $\chi_k(t)$ is given by the differential equation

$$\ddot{\chi}_k + 3H\dot{\chi}_k + \left(\frac{\mathbf{k}^2}{a^2} + m_{\chi,0}^2 + g^2\phi^2 \right) \chi_k = 0, \tag{1.197}$$

where $\mathbf{k}/a$ is the physical momentum. The differential equation represents a damped oscillator with a time varying frequency that depends on the inflation field $\phi(t)$ and the scale factor $a(t)$. Making the transformation $(\phi - \sigma) \to \phi$ in equation (1.195), we obtain the Lagrangian

$$\mathcal{L} = \frac{1}{2}\partial_\mu\phi\partial^\mu\phi - \frac{1}{2}m^2\phi^2 + \frac{1}{2}\partial_\mu\chi\partial^\mu\chi - \frac{1}{2}m_\chi^2\chi^2 - \frac{1}{2}g^2\phi^2\chi^2 - g^2\sigma\phi\chi^2 \tag{1.198}$$

where $m_\chi^2 = m_{\chi,0}^2 + g^2\sigma^2$, with the interaction Lagrangian

$$\mathcal{L}_{\text{int}} = -g^2\sigma\phi\chi^2 - \frac{1}{2}g^2\phi^2\chi^2. \tag{1.199}$$

These interactions represent two decay channels, $\phi \to \chi\chi$ and $\phi\phi \to \chi\chi$. The transformed Lagrangian given by (1.198) gives the time evolution of the mode function as

$$\ddot{\chi}_k + 3H\dot{\chi}_k + \left(\frac{\mathbf{k}^2}{a^2} + m_{\chi,0}^2 + g^2\sigma^2 + 2g^2\sigma\phi + g^2\phi^2 \right) \chi_k = 0. \tag{1.200}$$

In the following discussion, we shall consider $m_{\chi,0} \ll g^2\sigma^2$ so that it can be neglected. Moreover, we shall consider the spacetime to be Minkowskian so that we can set $a = 1$ which amounts to neglecting the effect of the expansion of the universe.

1.8.3.1 Narrow Resonance

We shall first consider the case $\phi \ll \sigma$ so that the amplitude of the inflaton field is very small compared to its vacuum expectation value σ. Consequently, the time evolution of the mode function can be written as

$$\ddot{\chi}_k + \left(k^2 + g^2\sigma^2 + 2g^2\sigma\Phi\sin mt \right) \chi_k = 0, \tag{1.201}$$

where $k = |\mathbf{k}|$ and the time varying frequency of the oscillator is

$$\omega_k^2(t) = k^2 + g^2\sigma^2 + 2g^2\sigma\Phi\sin mt. \tag{1.202}$$

It may be recalled that the term $2g^2\sigma\phi$ comes from the interaction term $-g^2\sigma\phi\chi^2$ in the Lagrangian given by (1.198). Consequently, the decay channel $\phi \to \chi\chi$ is dominant in this case.

Making a change of variable $mt = 2\tau - \pi/2$, the well known Mathieu Equation is obtained,

$$\chi_k'' + (A_k - 2q\cos 2\tau)\chi_k = 0, \tag{1.203}$$

with $A_k = 4(k^2 + g^2\sigma^2)m^{-2}$ and $q = 4m^{-2}g^2\sigma\Phi$.

The Mathieu equation admits solutions of exponential instability $\chi_k \propto e^{\mu_k^{(n)}\tau}$ within a continuous range of momenta $\Delta k^{(n)}$, where n labels the band. This instability corresponds to particle production with the occupation number growing exponentially, $n_k \propto |\chi_k|^2 \propto e^{2\mu_k^{(n)}\tau}$.

For the case $g\Phi \ll g\sigma \ll m$, we have $q \ll 1$. In this case, resonance occurs in a narrow band $\Delta k^{(n)} \sim mq^n$ near $A_k^{(n)} = n^2 + \mathcal{O}(q)$, where $n = 1, 2, 3, \ldots$ (as observed in stability-instability chart). Thus the band-width is negligible for $n = 2, 3, \ldots$. Consequently we shall consider only the first band, $n = 1$, with the approximation $A_k^{(1)} \sim 1 \pm q$. The corresponding instability parameter is given by

$$\mu_k^{(1)} = \sqrt{\left(\frac{q}{2}\right)^2 - \left(\frac{2k}{m} - 1\right)^2}, \tag{1.204}$$

which is real for $k = \frac{m}{2}(1 \pm \frac{1}{2}q)$. This represents a region of resonance in the band $\Delta k = \frac{1}{2}mq$. This band is *narrow* as $q \ll 1$. Within the same band, the maximum instability occurs at $k = \frac{m}{2}$, corresponding to a growth $n_k \propto e^{qmt/2}$.

1.8.3.2 Broad Resonance

In the simple chaotic inflation, we have seen that the initial amplitude $\Phi \gtrsim m_{\mathrm{P}}$, so that sufficient inflation can be achieved. This means that the amplitude satisfies the condition $\phi \gg \sigma$ together with $g\phi \gg m$. Thus in this case, the terms $g^2\sigma^2$ and $2g^2\sigma\phi$ can be neglected in comparison to $g^2\phi^2$ in equation (1.200). Consequently, in the Minkoviskian approximation, equation (1.200) reduces to

$$\ddot{\chi}_k + \left(k^2 + g^2\Phi^2\sin^2 mt\right)\chi_k = 0. \tag{1.205}$$

It may be recalled that the term $g^2\phi^2$ comes from the interaction term $-\frac{1}{2}g^2\phi^2\chi^2$ in the Lagrangian given by (1.198). Consequently, the decay channel $\phi\phi \to \chi\chi$ is dominant in the present case.

As compared to the previous case of narrow resonance, now we find a parametric oscillator with a different time dependency in frequency given by

$$\omega_k^2(t) = k^2 + g^2\Phi^2\sin^2 mt. \tag{1.206}$$

Since the effective mass $m_\chi(t) = g\phi(t) \gg m$, a large number of oscillations occur in each mode χ_k within one period of oscillation of the inflaton field.

Using the change of variable $\tau = mt$ and rearranging, equation (1.205) reduces to the Mathieu equation,

$$\chi_k'' + \{A_k - 2q\cos 2\tau\}\,\chi_k = 0, \tag{1.207}$$

with $A_k = k^2/m^2 + 2q$ and $q = g^2\Phi^2/4m^2$. Since $g\Phi \gg m$, we have $q \gg 1$ in this case, in contrast with the case of narrow resonance where $q \ll 1$.

The Mathieu equation given by (1.207) admits solution of exponential instability of the form $\chi_k \propto e^{\mu_k \tau}$. The corresponding stability-instability chart [108] gives significant values of the instability parameter, namely, $2\pi\mu_k \sim \mathcal{O}(1)$. The resonant modes k lie above the line $\frac{k^2}{m^2} = A_k - 2q$ within every instability band. Along the line $A_k = 2q$, that is for the vanishing mode, $\mu_k \sim \frac{\ln 3}{2\pi}$ in the instability band.

The frequency of the χ-field given by (1.206) changes slowly near the peak $\phi = \pm\Phi$ occurring at $mt = (2l+1)\frac{\pi}{2}$, with l an integer. Near the peak, χ_k oscillates with a frequency $\omega_k \approx \sqrt{k^2 + g^2\Phi^2}$, whereas the inflaton field oscillates with a frequency m. Since $g\Phi \gg m$, the inflaton field varies very slowly compared to the time period of χ_k near the peak. This slow variation allows one to invoke the adiabatic hypothesis, leading to an adiabatic invariant $I = E/\omega$, where E is the energy of the system and ω is its frequency [115]. The energy is given by the first integral of the equation of motion (1.205), so that

$$E_k = \frac{1}{2}\dot{\chi_k}^2 + \frac{1}{2}\omega_k^2\chi_k^2, \tag{1.208}$$

and the adiabatic invariant is thus obtained as

$$n_k = \frac{E_k}{\omega_k} = \frac{1}{2\omega_k}\dot{\chi_k}^2 + \frac{1}{2}\omega_k\chi_k^2. \tag{1.209}$$

Thus n_k is expected to be almost constant around the peaks of the inflaton fields.

On the other hand, the inflaton field changes rapidly around $\phi = 0$, when $mt = l\pi$, with l an integer. This leads to the possibility of particle production in a narrow window when the condition $|\dot{\omega}| > \omega^2$ is satisfied. Using equation (1.206), this condition translates to

$$mg^2\Phi\phi \gtrsim (k^2 + g^2\phi^2)^{3/2}, \tag{1.210}$$

where we have used $\dot{\phi} = m\Phi\cos mt \sim m\Phi$, around $\phi \sim 0$. Rearranging, we have

$$k^2 \lesssim (mg^2\Phi\phi)^{2/3} - g^2\phi^2. \tag{1.211}$$

The right-hand side of the above expression has the time dependence $\phi = \Phi\sin mt$. Consequently, the above condition can be met only up to a certain value of ϕ, say ϕ_*. This means that the above condition holds in the window $-\phi_* < \phi < \phi_*$. The band in which the resonance occurs can be defined as $0 \lesssim k \lesssim k_*$, where

$$k_*^2 = (mg^2\Phi\phi_*)^{2/3} - g^2\phi_*^2 \tag{1.212}$$

The estimate for ϕ_* and k_* can be obtained from the condition (1.211) by noting that the right-hand side has three zeros, at $\phi = 0, \pm\sqrt{\frac{m\Phi}{g}}$. The maxima k_* occurs at

$$\phi_* = \frac{1}{3^{3/4}}\sqrt{\frac{m\Phi}{g}} = \frac{1}{3^{3/4}\sqrt{2}}\Phi q^{-1/4}, \tag{1.213}$$

with the value

$$k_* = \frac{\sqrt{2}}{3^{3/4}}\sqrt{gm\Phi} = \left(\frac{2}{3}\right)^{3/4} mq^{1/4}. \tag{1.214}$$

In the interval between the maxima, that is in the range $-\phi_* \leq \phi \leq \phi_*$, the momenta of the created particles lies in the range $0 \leq k \leq k_*$. As seen from equation (1.214), this range is *broad* as $q \gg 1$. A typical value of momentum can be taken as $k_*/2$. We can say that the momenta of the created particles occur in the range $m \ll k_* \ll g\Phi$ in the broad resonance regime.

The inflaton field spends a time Δt_* in the range $-\phi_* \leq \phi \leq \phi_*$ giving the estimate $2\phi_* \approx \dot{\phi}\Delta t_*$, or

$$\Delta t_* \approx \frac{2\phi_*}{m\Phi} = \frac{2}{3^{3/4}}\frac{1}{\sqrt{gm\Phi}} = \left(\frac{2}{3}\right)^{3/2} k_*^{-1} \sim 0.54\ k_*^{-1}. \tag{1.215}$$

As ϕ is small during this time interval, we have $\omega \approx k_*$, so that $\omega\Delta t_* \sim 1$. This means that particle production happens within one time-period of oscillation of the χ-field. This relation is consistent with the uncertainty relation $\Delta E\ \Delta t \geq \frac{1}{2}\hbar$.

Chapter 2

Newtonian white dwarfs with generalized uncertainty EoS

.

As we have seen in Chapter 1, Generalized Uncertainty Principle carrying the imprint of quantum gravity, introduces a minimal length scale. Thus it is important to look for physical systems where its effect can be demonstrated. Since GUP effectively changes the invariant measure of the phase space through a factor $(1+\beta\mathbf{p}^2)^{-3}$ *the equation of state for an electron degenerate gas undergoes a significant modification from the ideal case. It has been shown in the literature [180] that the ideal Chandrasekhar limit ceases to exist when the modified equation of state due to the generalized uncertainty is taken into account. To assess the situation in a more complete fashion, we analyze in detail the mass-radius relation of Newtonian white dwarfs whose hydrostatic equilibria are governed by the equation of state of the degenerate relativistic electron gas subjected to the generalized uncertainty principle. As the constraint of minimal length imposes a severe restriction on the availability of high momentum states, it is speculated that the central Fermi momentum cannot have values arbitrarily higher than* $p_{\max} \sim \beta^{-1/2}$*. When this restriction is imposed, it is found that the system approaches limiting mass values higher than the Chandrasekhar mass upon decreasing the parameter* β *to a value given by a legitimate upper bound. Instead, when the more realistic restriction due to inverse* β*-decay is considered, it is found that the mass and radius approach the values* 1.4518 $M_\odot$ *and* 601.18 *km near the legitimate upper bound for the parameter* β*.*

Assuming that the Generalized Uncertainty Principle (described in Section 1.1) considers the effects of quantum gravity correctly, we expect an observable deviation from the contemporary physics at ultra-fine length scales or ultra-high densities. Thus the best

---

The content of this chapter is published: A. Mathew, M. K. Nandy, Ann. Phys. (N. Y.) **393**, 184 (2018) systems to search for such an anomaly are the ultra-dense compact stars that have offered themselves as model systems to investigate upon the fundamental principles of physics.

To study the properties of such systems, it is necessary to formulate the problem based on generalized commutation relations admitting a minimum observable length without any bound on the momentum. This was extensively studied by Maggiore [123], Kempf et al. [100] and Hossenfelder [92]. Moreover, utilising the generalized commutation relations

$$[\hat{x}_i, \hat{p}_j] = i\hbar\delta_{ij}(1 + \beta\hat{\mathbf{p}}^2), \qquad [\hat{p}_i, \hat{p}_j] = 0, \tag{2.1}$$

$$[\hat{x}_i, \hat{x}_j] = 2i\hbar\beta(\hat{p}_i\hat{x}_j - \hat{p}_j\hat{x}_i), \tag{2.2}$$

Chang et al. [53] considered a classical analogue (Liouville theorem) of the time evolution and demanded invariance of the phase volume under infinitesimal time-translation. The invariant measure of the phase volume thus turned out to be $(1 + \beta\mathbf{p}^2)^{-3}\ d^3x\ d^3p$.

The magnitude of the quantum gravity parameter β in the generalized uncertainty principle is presently unknown and there exist estimates for upper (and lower) bounds. Brau [33] calculated a correction to the Hydrogen atom energy levels due to GUP and compared the corresponding change in the 1S-2S transition with the experimental uncertainty in the frequency of the transition, yielding an uncertainty of $\Delta x_0 \leq 0.01$ fm. Subsequently, Brau and Buisseret [34] compared the first-order perturbation due to GUP in the energy spectrum of a neutron in a gravitational quantum well with the error bars in the energy spectrum obtained in the GRANIT experiment [153] and obtained the upper bound for $\hbar^2\beta$ as 2×10^{-5} fm^2. These estimates correspond to an upper bound for

$$\beta_0 = \beta M_P^2 c^2 \tag{2.3}$$

to be 7.6564×10^{34}, where M_P is the Planck mass.

Das and Vagenas [58] obtained a few upper bounds on the GUP parameter β_0 by considering simple quantum mechanical systems. They showed that the accuracy of precision measurements of the Lamb shift in hydrogen atom predicted the upper bound $\beta_0 < 10^{36}$, which is compatible with the bound $\beta_0 \leq 10^{34}$ set by the electroweak length scale. On the other hand, the accuracy in the measurements of Landau levels using a scanning tunneling microscope (STM) suggested a higher value for the upper bound, namely, $\beta_0 < 10^{50}$. However, it may be noted that the accuracy in an STM is about 1 part in 10^3, and therefore this higher value of the bound is not as reliable as in the case of Lamb shift measurements where the accuracy is about 1 part in 10^{12}. In fact, they showed that if the GUP induced excess current in the tunnelling of electrons in an STM cannot be measured in a time-scale of one year, the upper bound shifts to $\beta_0 < 10^{21}$, whereas if this time-scale is chosen to be 1 second, the upper bound is $\beta_0 < 10^{29}$. There is also an estimate, namely $\beta_0 = 82\pi/5$, from a calculation based on black hole thermodynamics [192].

On the basis of Hagedron temperature for relativistic strings, Wang et al. [224] suggested a lower bound for β_0, namely, $\beta_0 > 10^4$. In addition, they considered the case of ultra-relativistic ($E = pc$) Fermi gas at $T = 0$ and, approximating the density to be constant, obtained corrections in the leading order of the parameter β. They found that the GUP correction resists gravitational collapse as it tends to raise the mass of white dwarfs by a small amount, namely, $\Delta M \sim 10^{-10} M_\odot$ for $\beta_0 = 10^{36}$. They further showed that the radius tends to diverge for low and high values of β_0 whereas a minimum radius $\beta_0 \ell_P$ occurs in between implying the absence of a singularity (zero radius), which is of course a consequence of the minimum length uncertainty.

Ali [6], on the other hand, used a different uncertainty relation that corresponds to a commutative space and obtained an invariant measure of the phase volume, namely $(1-\alpha p)^{-4} d^3x\, d^3p$, along the lines of Chang et al. [53]. In a successive work, Ali and Tawfik [7] considered the case of white dwarfs assuming uniform density with ultra-relativistic Fermi gas. In a similar manner to Wang et al. [224], they calculated the mass of the white dwarf and found the GUP correction to be higher, namely $\Delta M \sim 10^{-5} M_\odot$ for $\alpha M_P c = 10^{17}$, whereas the radius decreases with increasing Fermi energy.

There is an alternative approach through which a high energy scale (or a small length scale) can enter into the description. This constitutes the postulate of a non-commutative space-time breaking Lorentz invariance and leading to a deformed dispersion relation (between energy and momentum) involving the high energy scale. Following this approach, Camacho [41] obtained the mass-radius relation of white dwarfs assuming their densities to be uniform. For a negative definite deformation parameter occurring in the dispersion relation, he predicted the existence of white dwarfs with very large radii and masses close to the Chandrasekhar mass. Gregg and Major [78] considered the realistic case of white dwarfs of non-uniform density and reported results that were quite distinct from the previous predictions. They arrived at new limiting masses about 10% higher (lower) than the Chandrasekhar mass limit for positive (negative) deformation parameter occurring in the dispersion relation. Amelino-Camelia et al. [14] analyzed the problem of employing both the deformed dispersion relation and deformed momentum space measure to obtain the mass-radius relation. This method introduced a shift in the deformation parameter that did not bring in any qualitative change in the mass-radius relationship.

Rashidi [180], on the other hand, considered the case of Helium white dwarfs assuming an ultra-relativistic ($E = pc$) Fermi gas and, using the generalized uncertainty invariant measure $(1+\beta p^2)^{-3} d^3x\, d^3p$, obtained the equation of state in the ideal degenerate case. He further considered the hydrostatic equilibrium with a non-uniform density and analyzed a generalized version of the Lane-Emden equation as an initial value problem. In the limit of infinite central Fermi momentum, the differential equation reduces to the Lane-Emden equation of index zero, immediately leading to the mass and radius behaving as $M \sim p_{\mathrm{Fc}}^{3/2}$ and $R \sim p_{\mathrm{Fc}}^{1/2}$. It follows that both mass and radius of white dwarfs increase unboundedly with an indefinite increase in central Fermi momentum $p_{\mathrm{F}c}$ so that the ideal Chandrasekhar limit ceases to exit.

In this Chapter, we shall examine in detail the effect of generalized uncertainty on Helium white dwarfs with invariant measure $(1+\beta p^2)^{-3}d^3x\ d^3p$. We shall take the full equation of state for a completely degenerate electron gas with the relativistic dispersion relation ($E^2 = p^2c^2 + m_e^2c^4$) and study the implication of the quantum gravity parameter β (or $\beta_0 = \beta M_P^2c^2$) on the mass-radius relation. We first perform a heuristic analysis by taking the density to be uniform and consider the effect of increasing the Fermi momentum p_{F} unboundedly. We find that the mass and radius behave as $M \sim p_{\mathrm{F}}^{3/2}$ and $R \sim p_{\mathrm{F}}^{1/2}$. To analyze the problem in somewhat more detail, we approximately solve the equation of hydrostatic equilibrium relaxing the previous assumption of uniform density. We find that, in the asymptotic limit of high central Fermi momentum, the white dwarf has a core of approximately uniform density and an envelope where the density falls off. It is interesting to note that the mass and radius of the core behave as $\sim p_{\mathrm{F}c}^{3/2}$ and $\sim p_{\mathrm{F}c}^{1/2}$. Thus, in both of these analyses, the mass and radius approach the same asymptotic behavior as obtained by Rashidi [180].

In the next program of our calculations, we take the realistic case of varying density and use the exact equations of hydrostatic equilibrium. We first solve these equations numerically and determine the mass-radius relation for different values of the GUP parameter β_0 to assess the situation of the mass-radius relationship. It is found that, with increase in the central Fermi momentum, the radius approaches a minimum value while the mass increases slowly. However, beyond this minimum radius value, the mass and radius start to increase unboundedly. This latter regime is identified with the previous asymptotic analysis for infinitely large Fermi momentum.

We next note that the GUP factor $(1+\beta\mathbf{p}^2)^{-3}$ puts a severe restriction on the availability of ultra-high momentum states as this factor reduces to a small value for $\sqrt{\beta}p = 1$. We thus consider four different cases with the maximum value $(\sqrt{\beta}p)_{\max}$ =1.0, 1.25, 1.5, and 3.0. In each of these cases we calculate the mass and radius for different choices of β_0. Within these restrictions we find that both mass and radius are finite if the upper bound of β_0 is taken to be 10^{36}. However, if $(\sqrt{\beta}p)_{\max}$ is increased unboundedly, the mass and radius values also increase unboundedly.

In a white dwarf, a realistic upper bound for the central Fermi energy is the threshold energy for inverse β-decay. We therefore next take the central Fermi momentum to be the neutronization threshold given by $E_{\mathrm{N}}^2 = p_N^2c^2 + m_e^2c^4$. Consequently we take different cases corresponding to β_0 ranging from 10^{44} to 10^{36}. We find that both mass and radius approach approximately constant values, namely, 1.4518 $M_{\odot}$ and 601.18 km, as the GUP parameter β_0 is decreased to 10^{36}. However, if β_0 is increased unboundedly, both the mass and radius values also increase unboundedly.

The rest of the Chapter is organized as follows. In Section 2.1, we find the expression for density and pressure in terms of the Fermi momentum for an electron gas with the GUP invariant measure, where we also analyze the asymptotic behavior of these quantities and discuss the restriction on momentum states by the GUP. In Section 2.2, we consider the equation of hydrostatic equilibrium for a white dwarf with Newtonian gravity and work out a few approximate solutions for the mass and radius, where we also report an exact solution by a numerical scheme. In Section 2.3, we numerically solve the equation of hydrostatic equilibrium with restrictions due to GUP and neutronization. Finally, discussion and conclusion are given in Section 2.4.

2.1 Fermi gas GUP equation of state

In this section, we derive the expression for the number density n of electrons and its pressure P in a degenerate electron gas using the grand canonical partition function. The effect of GUP commutation relation is taken into account by considering the modified invariant measure. The asymptotic behavior for n and P are analyzed in Section 2.2. The GUP modification of density of states puts a severe restriction on the high momentum states which is discussed in the Section 2.3, where we also lay out the assumption on the maximum momentum.

2.1.1 Grand canonical ensemble

The Grand partition function [114] for a Fermi gas at temperature T can be written as

$$\mathcal{Z} = \prod_{\mathbf{p}} \left\{ \sum_{n_{\mathbf{p}}} \exp\left(-\frac{(E_{\mathbf{p}} - \mu) n_{\mathbf{p}}}{k_B T} \right) \right\}^g \tag{2.4}$$

where $E_{\mathbf{p}} = \sqrt{\mathbf{p}^2 c^2 + m_e^2 c^4}$, $n_{\mathbf{p}}$ is the number of fermions in the momentum state $|\mathbf{p}\rangle$ with degeneracy g, μ is the chemical potential, and k_B is the Boltzmann constant. Since $n_{\mathbf{p}} = 0, 1$ and $g = 2$ for electrons, the grand potential $\Omega = -k_B T \ln \mathcal{Z}$ turns out to be

$$\Omega = -2 k_B T \sum_{\mathbf{p}} \ln \left\{ 1 + \exp\left(-\frac{(E_{\mathbf{p}} - \mu)}{k_B T} \right) \right\}. \tag{2.5}$$

so that the number of electrons is given by

$$N = -\frac{\partial \Omega}{\partial \mu} = 2 \sum_{\mathbf{p}} \left\{ \exp\left(\frac{E_{\mathbf{p}} - \mu}{k_B T} \right) + 1 \right\}^{-1}. \tag{2.6}$$

Since the GUP formalism demands that the number of states available be transformed according to

$$\sum_{\mathbf{p}} \equiv \int \frac{V d^3 p}{h^3} \frac{1}{(1 + \beta \mathbf{p}^2)^3} \tag{2.7}$$

where h is the Planck's constant, we therefore obtain the number density $n = N/V$ as

$$n = \frac{2}{h^3} \int_0^\infty \frac{4\pi p^2 dp}{(1 + \beta p^2)^3} \left\{ \exp\left(\frac{E_{\mathbf{p}} - \mu}{k_B T} \right) + 1 \right\}^{-1}. \tag{2.8}$$

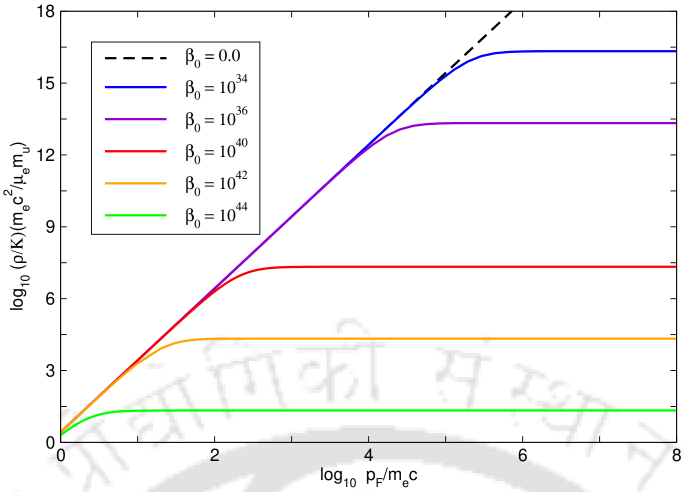

Figure 2.1: Dimensionless density $(\rho/K)(m_e c^2/\mu_e m_u)$ versus dimensionless Fermi momentum $p_{\rm F}/m_e c$ for various values of β_0.

Since $\Omega = -PV$, we readily obtain the pressure as

$$P = \frac{2k_B T}{h^3} \int_0^\infty \frac{4\pi p^2 dp}{(1+\beta p^2)^3} \ln\left\{1 + \exp\left(-\frac{E_{\mathbf{p}} - \mu}{k_B T}\right)\right\} \tag{2.9}$$

As we can treat the electron gas in white dwarfs to be completely degenerate, we take the limit $T \to 0$ in the above integrands and obtain

$$n = \frac{8\pi}{h^3} \int_0^{p_{\rm F}} \frac{p^2 dp}{(1+\beta p^2)^3} \tag{2.10}$$

and

$$P = \frac{8\pi}{h^3} \int_0^{p_{\rm F}} \frac{p^2 dp}{(1+\beta p^2)^3} \left(E_{\rm F} - E_{\mathbf{p}}\right), \tag{2.11}$$

where $E_{\rm F} = \sqrt{p_{\rm F}^2 c^2 + m^2 c^4}$ is the Fermi energy (or the chemical potential μ at $T = 0$), and $p_{\rm F}$ is the Fermi momentum.

Integrating the above two equations, Eqs (2.10) and (2.11), we obtain

$$n(p_{\rm F}) = \frac{\pi}{(h\sqrt{\beta})^3} \left\{\tan^{-1}(\sqrt{\beta} p_{\rm F}) - \frac{\sqrt{\beta} p_{\rm F}(1 - \beta p_{\rm F}^2)}{(1 + \beta p_{\rm F}^2)^2}\right\} \tag{2.12}$$

and

$$\begin{aligned} P(p_{\rm F}) = \frac{\pi}{(h\sqrt{\beta})^3} \sqrt{p_{\rm F}^2 c^2 + m_e^2 c^4} \qquad & \left\{\tan^{-1}(\sqrt{\beta} p_{\rm F}) - \frac{\sqrt{\beta} p_{\rm F}}{(1 - \beta m_e^2 c^2)(1 + \beta p_{\rm F}^2)}\right\} \\ & + \frac{\tanh^{-1}\left(\frac{p_{\rm F}\sqrt{1-\beta m_e^2 c^2}}{\sqrt{p_{\rm F}^2 + m_e^2 c^2}}\right)}{(1 - \beta m_e^2 c^2)^{\frac{3}{2}}}. \end{aligned} \tag{2.13}$$

Using the dimensionless quantities $\xi = p_{\rm F}/m_e c$ and $\alpha = m_e c\sqrt{\beta}$, we can express the above equations as

$$n(\xi) = \frac{K}{m_e c^2} \tilde{n}(\xi) \tag{2.14}$$

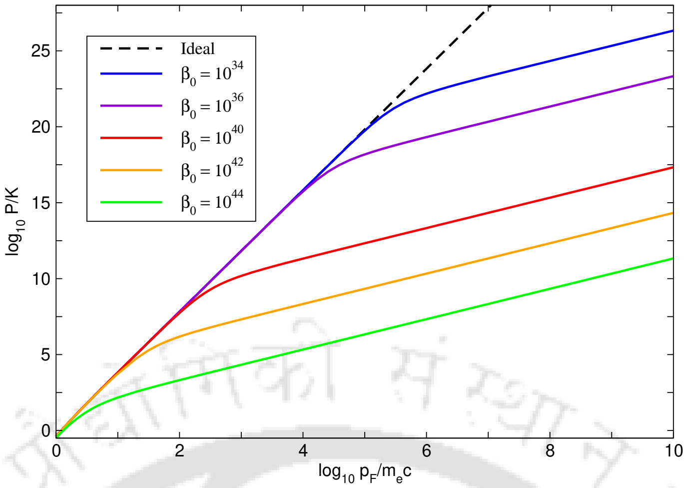

Figure 2.2: Dimensionless pressure P/K versus dimensionless Fermi momentum $p_{\rm F}/m_ec$ for various values of β_0.

and

$$P(\xi) = K\tilde{P}(\xi) \tag{2.15}$$

with $K = \pi m_e^4 c^5/h^3 = 1.8007 \times 10^{22}$ N/m^2 having the dimension of pressure and

$$\tilde{n}(\xi) = \frac{1}{\alpha^3}\left\{\tan^{-1}(\alpha\xi) - \frac{\alpha\xi(1-\alpha^2\xi^2)}{(1+\alpha^2\xi^2)^2}\right\}, \tag{2.16}$$

$$\tilde{P}(\xi) = \frac{\sqrt{1+\xi^2}}{\alpha^3}\left\{\tan^{-1}(\alpha\xi) - \frac{\alpha\xi}{(1-\alpha^2)(1+\alpha^2\xi^2)}\right\} + \frac{\tanh^{-1}\left(\frac{\xi\sqrt{1-\alpha^2}}{\sqrt{1+\xi^2}}\right)}{(1-\alpha^2)^{\frac{3}{2}}}. \tag{2.17}$$

Knowing the electron number density n, the mass density ρ can be written as $\rho = \mu_e m_u n$. Consequently

$$\rho(\xi) = K\left(\frac{\mu_e m_u}{m_e c^2}\right)\tilde{n}(\xi) \tag{2.18}$$

with $\mu_e = A/Z$ representing the number of nucleons per electron and $m_u = 1.6605 \times 10^{-27}$ kg is the atomic mass unit.

The quantum gravity parameter $\sqrt{\beta} = \sqrt{\beta_0}/M_P c$ is determined by the dimensionless parameter β_0 and the Planck mass $M_P = \sqrt{\hbar c/G} = 2.1765 \times 10^{-8}$ kg. We shall choose different values of β_0 to tune the parameter β. Table 2.1 shows different values of α corresponding to β_0. Figure 2.1 shows how the density ρ changes with respect to $\xi = p_{\rm F}/m_e c$ for different values of the parameter β_0. It is noticed that the density saturates to different constant values for large values of ξ corresponding to different choices for β_0. As β_0 is decreased, the density resembles more closely to the $\beta_0 = 0$ case and the (higher) saturation value of ρ shifts to higher values of ξ. Figure 2.2 displays the variation of pressure P with respect to $\xi = p_{\rm F}/m_e c$ for different value of β_0. It is seen that, for higher values of ξ, pressure varies proportionally to ξ. The $\beta_0 = 0$ line corresponds to $P \sim \xi^4$

Table 2.1: Different values of β_0 and the corresponding α values with asymptotic values of $\tilde{n}(\xi)$ and $\tilde{P}(\xi)$ for large values of ξ.

β_0	$\alpha/4.1854$	$\tilde{n}(\infty)/2.1425$	$\tilde{P}(\xi)=\tilde{n}(\infty)\xi+B(\alpha)$
10^{44}	10^{-1}	10^{01}	$2.1425\times10^{01}\ \xi-7.0071\times10^{01}$
10^{42}	10^{-2}	10^{04}	$2.1425\times10^{04}\ \xi-6.5232\times10^{05}$
10^{40}	10^{-3}	10^{07}	$2.1425\times10^{07}\ \xi-6.5176\times10^{09}$
10^{38}	10^{-4}	10^{10}	$2.1425\times10^{10}\ \xi-6.5176\times10^{13}$
10^{36}	10^{-5}	10^{13}	$2.1425\times10^{13}\ \xi-6.5176\times10^{17}$

which is true for higher values of ξ. We see that, as β_0 is decreased, the linear regime shifts to higher and higher values of ξ.

2.1.2 Asymptotic behavior

The above expression for number density approaches a constant value $n(\infty)=\pi^2m_e^3c^3/2h^3\alpha^3$ as the function $\tilde{n}(\xi)$ approaches a constant

$$\tilde{n}(\infty)=\frac{\pi}{2\alpha^3} \tag{2.19}$$

in the limit $\xi\to\infty$. This situation is unlike the HUP electron number density $n_{\text{HUP}}(\xi)=8\pi m_e^3c^3\xi^3/3h^3$ that approaches infinity in the same limit. The saturation values $\rho(\infty)$ can be clearly seen in Figure 2.1 for different value of β_0.

Minimum distance between the particles is expected to be $d_{\text{min}}=(16\pi)^{1/3}\Delta x_0$ where Δx_0 is the minimum uncertainty in position imposed by the GUP. This minimum distance will be approached in an electron gas of extremely high density which will be the case when the Fermi momentum is extremely high . This is consistent with the fact that the GUP number density given by Eq. (2.14) approaches a constant value $n(\infty)$ in the limit $\xi\to\infty$.

The original degenerate case is expected to be reproduced in the limit $\alpha\to0$, corresponding to low values of β_9. The leading order term in the expansion of the function $\tilde{n}(\xi)$ for finite values of ξ gives $\tilde{n}(\xi)\to3\xi^3/8$ yielding $n(\xi)\to n_{\text{HUP}}(\xi)=8\pi m_e^3c^3\xi^3/3h^3$ which is the original degenerate case. Since $n(\xi)$ approaches the same limit in the limit $\xi\to0$, the number density $n(\xi)$ approaches $n_{\text{HUP}}(\xi)$ for low values of ξ. This behavior can be seen in the plot for $\rho(\xi)$ in Figure 2.1 for various values of β_0 in the region of low ξ.

In a similar manner, the original degenerate pressure is recovered in the limit $\alpha\to0$, yielding $P(\xi)\to P_{\text{HUP}}(\xi)$, namely

$$P_{\text{HUP}}(\xi)=\frac{K}{3}\left\{\xi\sqrt{1+\xi^2}(2\xi^2-3)+3\sinh^{-1}\xi\right\} \tag{2.20}$$

For moderately large values of ξ, the HUP pressure behaves as $P_{\text{HUP}}(\xi)\sim2K\xi^4/3$. However, for large values of ξ, the GUP pressure given by Eq.(2.15) goes asymptotically as

$$P(\xi)\to K\left\{\tilde{n}(\infty)\xi+B(\alpha)\right\} \tag{2.21}$$

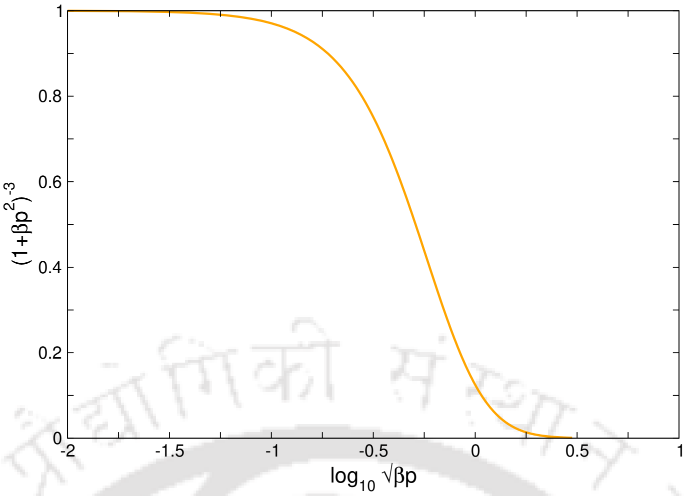

Figure 2.3: Variation of the GUP deformation factor $f = (1+\beta p^2)^{-3}$ with respect to the dimensionless quantity $\sqrt{\beta}p$ showing suppression of the high momentum states. The abscissa is plotted in logarithmic scale in order to accommodate a wide range of $\sqrt{\beta}p$.

where

$$B(\alpha) = \frac{\tanh^{-1}(\sqrt{1-\alpha^2})}{(1-\alpha^2)^{3/2}} - \frac{1}{\alpha^4}\frac{(2-\alpha^2)}{(1-\alpha^2)}. \tag{2.22}$$

This linear behavior of the GUP pressure (with respect to ξ) can clearly be seen in Figure 2.2 where the curve departs from the ξ^4 regime to an ξ regime changing its slope from 4 to 1. Thus, unlike the HUP pressure, the GUP pressure increases more slowly for large values of ξ. It may also be noted that, in a linear plot for Eq. (2.21), the slope and intercept both will depend on the value of α.

2.1.3 GUP restriction on momentum

The center of a white dwarf is expected to have a high value of Fermi momentum. However, the GUP deformation factor $f(p) = (1+\beta p^2)^{-3}$ imposes a severe restriction on the allowed values of momenta. Figure 2.3 shows the variation of $f(p)$ with respect to the dimensionless quantity $\sqrt{\beta}p$. It is seen that this factor suppresses the high momentum states as the curve decreases strongly for high values of momenta. For example, for $\sqrt{\beta}p = 1$, this factor reduces to $f = 0.125$; for $\sqrt{\beta}p = 1.25$, which corresponds to $\log_{10}\sqrt{\beta}p = 0.097$, $f = 0.059$; for $\sqrt{\beta}p = 1.50$, or $\log_{10}\sqrt{\beta}p = 0.176$, f reduces to 0.029, and for $\sqrt{\beta}p = 3.00$, or $\log_{10}\sqrt{\beta}p = 0.477$, f reduces to 0.001. Consequently there is less or even negligible contribution from momentum states belonging to momentum values higher than these values. In fact, this behavior suggests that the integral in momentum space has an effective cutoff $p_{\max} \sim \beta^{-1/2}$ and thus there is negligible contribution from momenta higher than $p_{\max}$. It is thus important to take values of Fermi momentum p_F equal to or lower than $p_{\max}$. We shall therefore choose the maximum Fermi momentum p_F (at the center of white dwarf) corresponding to these four maximum values of $(\sqrt{\beta}p)_{\max}$. These four choices for

Table 2.2: Four choices of the maximum value of $\sqrt{\beta}p$ as suggested by Figure 2.3 beyond which the momentum states have small contributions. Different choices of β_0 correspond to different values of $\xi_{\max}$. The corresponding values of the dimensionless number density $\tilde{n}(\xi_{\max})$ and pressure $\tilde{P}(\xi_{\max})$ are also shown.

$\sqrt{\beta}p_{\max}$	β_0	$\xi_{\max}$	$\tilde{n}(\xi_{\max})$	$\tilde{P}(\xi_{\max})$
1.00	10^{44}	2.389×10^{0}	1.071×10^{01}	7.951×10^{00}
	10^{40}	2.389×10^{2}	1.071×10^{07}	9.300×10^{08}
	10^{34}	2.389×10^{5}	1.071×10^{16}	2.146×10^{20}
1.25	10^{44}	2.986×10^{0}	1.368×10^{01}	1.482×10^{01}
	10^{40}	2.986×10^{2}	1.368×10^{07}	1.663×10^{09}
	10^{34}	2.389×10^{5}	1.363×10^{16}	1.663×10^{21}
1.50	10^{44}	3.584×10^{0}	1.583×10^{01}	2.329×10^{01}
	10^{40}	3.584×10^{2}	1.583×10^{07}	2.548×10^{09}
	10^{34}	3.584×10^{5}	1.583×10^{16}	2.548×10^{21}
3.00	10^{44}	7.168×10^{0}	2.031×10^{01}	8.935×10^{01}
	10^{40}	7.168×10^{2}	2.031×10^{07}	9.278×10^{09}
	10^{34}	7.168×10^{5}	2.031×10^{16}	9.278×10^{21}

the maximum values are shown in Table 2.2 that also shows the maximum values $\xi_{\max}$, $\tilde{n}(\xi_{\max})$ and $\tilde{P}(\xi_{\max})$ corresponding to different choices of β_0.

2.2 White Dwarfs with GUP

In this section we obtain the mass-radius relation of Helium white dwarfs in the Newtonian gravity employing the modified equation of state following from the generalized uncertainty principle as obtained in the previous section. The condition of hydrostatic equilibrium for a spherical distribution of matter is given by

Substituting Eqs. (2.18) and (2.15) in Eq. (1.92) yields

$$\frac{1}{4\pi GK}\left(\frac{m_e c^2}{\mu_e m_u}\right)^2\left[\frac{1}{r^2}\frac{d}{dr}\left(\frac{r^2\tilde{P}'(\xi)}{\tilde{n}(\xi)}\frac{d\xi}{dr}\right)+\tilde{n}(\xi)\right]=0 \tag{2.23}$$

where $\tilde{P}'(\xi) = d\tilde{P}/d\xi$. Using the dimensionless variable $x = r/R_0$, where $R_0 = \frac{1}{\sqrt{4\pi GK}}\left(\frac{m_e c^2}{\mu_e m_u}\right)$, the above equation reduces to

$$\frac{1}{x^2}\frac{d}{dx}\left(\frac{x^2\tilde{P}'(\xi)}{\tilde{n}(\xi)}\frac{d\xi}{dx}\right)+\tilde{n}(\xi)=0. \tag{2.24}$$

From Eqs. (2.17) and (2.16), we find $\tilde{P}'(\xi) = \frac{\xi}{\sqrt{1+\xi^2}}\tilde{n}(\xi)$, so that the above equation reduces to

$$\frac{1}{x^2}\frac{d}{dx}\left(x^2\frac{d\sqrt{1+\xi^2}}{dx}\right)+\tilde{n}(\xi)=0. \tag{2.25}$$

Before considering the complete solution, we shall first analyze the problem heuristically and then consider the asymptotic behavior of the above equation in the extreme limits $\xi \to 0$ and $\xi \to \infty$.

2.2.1 Heuristic treatment

We first analyze the problem heuristically by assuming the density to be uniform (that is, a uniform value of Fermi momentum) and obtain an approximate mass-radius relation as follows. Using $n = \frac{K}{m_e c^2}\tilde{n}(\xi)$ and $n = \frac{3}{4\pi}\frac{m_e c^2}{\mu_e m_u}\frac{M}{R^3}$, and expanding $\tilde{n}(\xi)$ as $\tilde{n}(\xi) = \frac{\pi}{2\alpha^3} + \frac{8}{3\alpha^6}\frac{1}{\xi^3} - \ldots$ for large values of ξ, we obtain

$$\xi^3 = \frac{16}{3\pi\alpha^3}\left(1 - \frac{m_e c^2}{\mu_e m_u}\frac{3}{4\pi K}\frac{M}{R^3}\right)^{-1} = \left(\frac{16}{3\pi\alpha^3}\right)\left(1 - \frac{6\alpha^3}{\pi}\frac{\tilde{M}}{\tilde{R}^3}\right)^{-1} \tag{2.26}$$

where $\bar{M} = M/M_0$ and $\bar{R} = R/R_0$ with $M_0 = \frac{1}{\sqrt{4\pi K}}\left(\frac{1}{G}\right)^{3/2}\left(\frac{m_e c^2}{\mu_e m_u}\right)^2$.

The pressure can be estimated from equating the work done in compressing the star from infinite dilution to a radius R in the absence of gravity and by equating it with the gravitational self-energy, yielding [94]

$$P = \frac{\gamma}{4\pi}\frac{GM^2}{R^4} = K\gamma\frac{\bar{M}^2}{\bar{R}^4} \tag{2.27}$$

where γ is a constant of $\mathcal{O}(1)$. Expanding $\tilde{P}(\xi)$ in the limit of large ξ, we have

$$\tilde{P} = \frac{\pi}{2\alpha^3}\xi + B(\alpha) + \frac{\pi}{4\alpha^3}\frac{1}{\xi} + \ldots \tag{2.28}$$

Eliminating ξ from Eqs. (2.26) and (2.28), and using (2.27), we obtain

$$\gamma\frac{\bar{M}^2}{\bar{R}^4} = C(\alpha)\left(1 - \frac{6\alpha^3}{\pi}\frac{\bar{M}}{\bar{R}^3}\right)^{-1/3} + B(\alpha) + A(\alpha)\left(1 - \frac{6\alpha^3}{\pi}\frac{\bar{M}}{\bar{R}^3}\right)^{1/3} \tag{2.29}$$

where $A(\alpha) = \frac{\pi}{4\alpha^2}\left(\frac{3\pi}{16}\right)^{1/3}$ and $C(\alpha) = \frac{\pi}{2\alpha^4}\left(\frac{16}{3\pi}\right)^{1/3}$. A solution to the above equation can be obtained in parametric form by defining $\left(1 - \frac{6\alpha^3}{\pi}\frac{\bar{M}}{\bar{R}^3}\right)^{1/3} = z$ and $\frac{\bar{M}^2}{\bar{R}^4} = \frac{y}{z}$ so that it can be written in the form

$$\gamma y = A(\alpha)z^2 + B(\alpha)z + C(\alpha) \tag{2.30}$$

The z^2 term is negligible compared to the other terms for $z < 1$. For example, for $\alpha = 0.4185$, $A(\alpha) = 3.7590$, $B(\alpha) = -70.0968$ and $C(\alpha) = 61.0878$. Thus y is related to z almost linearly with a negative slope.

Since $\tilde{n}(\xi) < \frac{\pi}{2\alpha^3}$, it follows that $\frac{6\alpha^3}{\pi}\frac{\bar{M}}{\bar{R}^3} < 1$, so that $z > 0$. Moreover the above definition of y suggests that $y > 0$. For the case $\alpha = 0.4185$, this condition is fulfilled for $0 < z < 0.9165$.

Thus the solutions for $\bar{M}$ and $\bar{R}$ are obtained in terms of z as

$$\bar{M} = \left(\frac{6\sqrt{\gamma}\alpha^3}{\pi}\right)^2\left\{\frac{y(z)}{z(1-z^3)^{4/3}}\right\}^{3/2} \tag{2.31}$$

and

$$\bar{R} = \left(\frac{6\sqrt{\gamma}\alpha^3}{\pi}\right)\left\{\frac{y(z)}{z(1-z^3)^2}\right\}^{1/2} \tag{2.32}$$

These expressions hold good for large ξ or small z. As $z \to 0$, we find $\bar{M} \sim z^{-3/2}$ and $\bar{R} \sim z^{-1/2}$. Since $z \sim \xi^{-1}$, it follows that $\bar{M} \sim \xi^{3/2}$ and $\bar{R} \sim \xi^{1/2}$. Thus this simple treatment suggests that both mass and radius increase unboundedly with indefinite increase in the Fermi momentum.

2.2.2 Asymptotic solutions

In the limit $\xi \to 0$, that is for low values of ξ, we see that $\tilde{n}(\xi) \sim 3\xi^3/8$. We thus obtain

$$\frac{1}{x^2}\frac{d}{dx}\left(x^2\frac{d\sqrt{1+\xi^2}}{dx}\right)+\frac{3}{8}\xi^3=0. \tag{2.33}$$

Letting $\sqrt{1+\xi^2}=c_0\phi(x)$ and using the new dimensionless radius defined by $\eta=(\sqrt{3}c_0/2\sqrt{2})x$, the above equation becomes

$$\frac{1}{\eta^2}\frac{d}{d\eta}\left(\eta^2\frac{d\phi}{d\eta}\right)+\left(\phi^2-\frac{1}{c_0^2}\right)^{3/2}=0 \tag{2.34}$$

where c_0 is related to the central value ξ_c by $c_0=\sqrt{1+\xi_c^2}$, when $\phi(0)=1$. Chandrasekhar [49] obtained the above equation for the case of ideal degenerate white dwarfs. For small values of ξ_c we thus expect the mass-radius relation obtained with GUP equation of state to be the same as that obtained by Chandrasekhar. Since the above equation does not involve the parameter α, this indicates that the effect of quantum gravity is imperceptible at low densities.

On the other hand, for the asymptotic limit $\xi \to \infty$, the leading order term in $\tilde{n}(\xi)$ becomes a constant. Thus Eq.(2.25) behaves like

$$\frac{1}{x^2}\frac{d}{dx}\left(x^2\frac{d\xi}{dx}\right)+\frac{\pi}{2\alpha^3}=0. \tag{2.35}$$

Putting $\xi/\xi_c=\phi(\zeta)$ in the above equation and redefining the dimensionless radius $\zeta=\pi x/2\alpha^3$, we get the zeroth order Lane-Emden equation whose solution is well known, namely, $\phi(\zeta)=c_1-\frac{c_2}{\zeta}-\frac{\zeta^2}{6}$, giving

$$\frac{\xi(\zeta)}{\xi_c}=c_1-\frac{c_2}{\zeta}-\frac{\zeta^2}{6}. \tag{2.36}$$

The undetermined constants can be fixed using the boundary condition $\xi(0)=\xi_c$. Accordingly we get $c_1=1$ and $c_2=0$, so that

$$\xi(x)=\xi_c\left\{1-\frac{\pi}{12\xi_c\alpha^3}x^2\right\}. \tag{2.37}$$

Similarly, the asymptotic behavior of the mass can be obtained from the integral expression obtained from the mass equation in (1.92), namely,

$$M=4\pi\int_0^R\rho(r)r^2dr=4\pi K\left(\frac{\mu_e m_u}{m_e c^2}\right)\int_0^R\tilde{n}(\xi)r^2dr, \tag{2.38}$$

so that

$$\bar{M} = \int_0^{\tilde{R}} \tilde{n}(\xi) x^2 dx. \tag{2.39}$$

Since in the limit $\xi \to \infty$, $\tilde{n}(\xi)$ approaches the constant value $\pi/2\alpha^3$, and since it is nearly true in the central region, we can define a core of approximately constant density. This is because of the fact that $\tilde{n}(\xi)$ already becomes 99.9% of $\pi/2\alpha^3$ when $\alpha\xi \approx 10.88$. Above this value, $\tilde{n}(\xi) \approx \pi/2\alpha^3$. Thus we can calculate the mass of the core $\bar{M}_{\rm core}$ from the asymptotic limit $\tilde{n}(\xi)$ tending to $\pi/2\alpha^3$. This approximation will be no longer valid in the outer region. Assuming that the core extends up to a radius $\bar{R}_{\rm core}$, we get $\bar{M}_{\rm core} = \tilde{n}(\infty)\bar{R}^3_{\rm core}/3$.

An estimate for the pressure inside the core can be obtained as

$$P = \frac{\gamma}{4\pi} \frac{GM^2_{\rm core}}{R^4_{\rm core}} \tag{2.40}$$

where γ is a constant of order unity. Thus using Eq. (2.21) we obtain

$$K\left\{\tilde{n}(\infty)\xi_c + B(\alpha)\right\} = \frac{\gamma}{4\pi} \frac{GM^2_{\rm core}}{R^4_{\rm core}} \tag{2.41}$$

Converting mass and radius into dimensionless quantities, we obtain

$$\frac{\bar{M}_{\rm core}}{\bar{R}^2_{\rm core}} = \frac{1}{\sqrt{\gamma}} \left\{\frac{\pi}{2\alpha^3}\xi_c + B(\alpha)\right\}^{1/2} \tag{2.42}$$

From Eq. (2.37), we can identify the radius of the core as $\xi(\bar{R}_{\rm core}) = \xi_s$, so that

$$\bar{R}_{\rm core} = \left(\frac{12\alpha^3}{\pi}\xi_c\right)^{1/2} \left(1 - \frac{\xi_s}{\xi_c}\right)^{1/2} \tag{2.43}$$

where ξ_s is the value of ξ such that $\tilde{n}(\infty)$ drops to 99.9% of the central value $\tilde{n}(\infty)$. It is noticed from the $N(\xi)$ curve (Figure 2.1) that the density reaches approximately constant values [99.9% of $\tilde{n}(\infty)$] for values of ξ such that $\alpha\xi \geq 10.88$, so that we can take $\xi_s = 10.88/\alpha$.

The above two relations lead to the mass of the core as

$$\bar{M}_{\rm core} = \left(\frac{12\alpha^3}{\pi}\xi_c\right) \frac{1}{\sqrt{\gamma}} \left\{\frac{\pi}{2\alpha^3}\xi_c + B(\alpha)\right\}^{1/2} \left(1 - \frac{\xi_s}{\xi_c}\right) \tag{2.44}$$

Thus for $\xi_c \gg \xi_s$, $\bar{M}_{\rm core} \sim \xi_c^{3/2}$ and $\bar{R}_{\rm core} \sim \xi_c^{1/2}$. This implies that the mass and radius of white dwarfs increase unboundedly with unbounded increase in the central Fermi momentum. These results, including the scaling exponents with respect to the central Fermi momentum, are consistent with the results of Rashidi [180]. They are also consistent with our previous heuristic analysis. In other words, the core dictates the mass-radius relation for excessively large central values of Fermi momentum $\xi = p_{\rm F}/m_e c$.

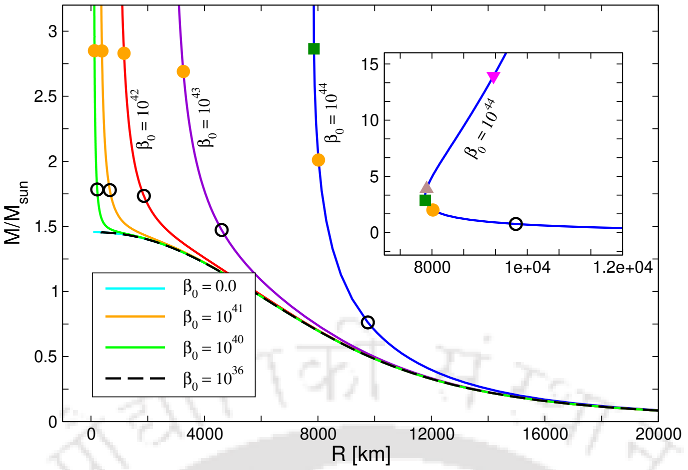

Figure 2.4: Mass-radius curves for Helium white dwarfs with the GUP equation of state for different values of β_0. The inset displays the mass-radius curve for $\beta_0 = 10^{44}$ up to very large values of the Fermi momentum ξ_c. The marked points on the mass-radius curves correspond to $\alpha\xi_c = 0.50$ (open circles), 1.0 (solid circles), 1.25 (solid squares), 1.5 (solid triangle), 3.0 (solid inverted triangle). If the corresponding values are chosen as $\xi_{\max}$ $(= j\frac{M_P}{m_e}\frac{1}{\sqrt{\beta_0}}$, where $j = 0.5, 1.0, 1.25, 1.5$, and $3.0)$, the curves would terminate at the marked points after beginning from the right hand part of the plots.

2.2.3 Exact solution

Now we shall consider the full equation of state (instead of asymptotics) in the Newtonian gravity. Thus, after substituting Eqs. (2.18) and (2.15) and using the definitions $m = M_0 u$ and $r = R_0 x$ in Eq. (1.92)

$$\frac{d\xi}{dx} = -\frac{\tilde{n}(\xi)}{\tilde{P}'(\xi)}\frac{u(x)}{x^2} \tag{2.45}$$

and

$$\frac{du}{dx} = \tilde{n}(\xi)x^2 \tag{2.46}$$

Since $\tilde{P}'(\xi) = \frac{\xi}{\sqrt{1+\xi^2}}\tilde{n}(\xi)$, Eq. (2.45) reduces to

$$\frac{d\xi}{dx} = -\frac{\sqrt{1+\xi^2}}{\xi}\frac{u(x)}{x^2} \tag{2.47}$$

Using Eq. (2.16) in Eq. (2.46), we obtain

$$\frac{du}{dx} = \frac{1}{\alpha^3}\left\{\tan^{-1}(\alpha\xi) - \frac{\alpha\xi(1-\alpha^2\xi^2)}{(1+\alpha^2\xi^2)^2}\right\}x^2 \tag{2.48}$$

We integrate the above two equations, namely, Eqs. (2.47) and (2.48), simultaneously with the boundary condition $\xi(0) = \xi_c$ and $u(0) = 0$ until the surface defined by $\xi(\bar{R}) = 0$ is reached. The result of the numerical integration for different values of ξ_c and β_0 are shown in Figure 2.4. For comparison, Chandrasekhar's ideal degenerate case is also shown in the same figure.

We see that, for large values of β_0, the mass-radius relation departs more strongly from the ideal case than for smaller values. This is not a surprise since we expect the effect of

GUP to be stronger for large values of β_0. Further, we note that the Chandrasekhar limit does not exist for any non-zero value of β_0 because the effect of quantum gravity takes over at large values of Fermi momentum ξ. Since the value of β_0 has a lower bound of 10^4, α can be as low as 4.1854×10^{-21}, so that the effect of GUP can be almost imperceptible. However to assess the GUP effect, we took an exaggerated value of β_0, namely, 10^{44}. This situation is shown in the inset of Figure 2.4.

Thus, for the case of $\beta_0 = 10^{44}$ (or equivalently $\alpha = 0.4185$), it is observed from the right-hand part of Figure 2.4 that the mass-radius curve coincides with Chandrasekhar curve for low vales of ξ_c. As ξ_c is increased, the mass increases slowly and the radius decreases, reaching a minimum value ~ 7853 km, as can be seen in the inset of Figure 2.4. On further increasing ξ_c, the mass and radius both increase boundlessly which is consistent with the asymptotic analysis presented in Section 3.2, where we found that there exists a core of uniform density whose mass and radius are determined by the central value ξ_c.This is unlike the ideal case where the radius decreases to zero and the mass increases and approaches the Chandrasekhar limit for increasing ξ_c. Thus it suggests that quantum gravity effect plays a significant role in determining the mass-radius relation.

It may also be worth noting that a star of exceedingly high mass can have the same radius as a lower mass star as seen from the inset of Figure 2.4. The modified GUP equation of state can make the higher mass star stable against gravitational collapse as a result of developing a core of almost constant density because the availability of the high momentum states are restricted with the increase in the Fermi momentum. This situation is unlike in the theories of spontaneous scalarization [54, 90], constructed by means of including a scalar field ϕ in the Einstein-Hilbert action. Spontaneous scalarization is realized when the minimum of the effective potential shifts from zero to a non-zero value of ϕ at a critical value of the matter density. The theory may be constructed in such a way that the effective strength of the gravitational field at high densities is reduced [146] allowing for a more dense matter that can exist without undergoing gravitational collapse. Thus in the GUP case the stability of massive stars is governed by the modified structure of the phase space, the gravity remaining unaffected, whereas in the spontaneous scalarization case, the effective gravity is weakened and the structure of the phase space remains unmodified.

2.3 Mass and radius with restrictions

The above study suggests an unrestricted increase in the mass and radius with unrestricted increase in the central value of the Fermi momentum $\xi_c = p_{\mathrm{F}c}/m_e c$. However, the above analysis was performed without any restrictions that may otherwise alter the situation. In this section, we consider this and perform detailed analyses of the equations of hydrostatic equilibrium, namely Eqs. (2.47) and (2.48), by numerical means.

2.3.1 GUP Restriction

As we discussed in Section 2.3, the GUP factor $f = (1+\beta p^2)^{-3}$ imposes a severe restriction on the availability of momentum states as it effectively puts an ultraviolet cutoff around $p_{\max} \sim \beta^{-1/2}$ (or equivalently $\xi_{max} \sim \alpha^{-1}$). Thus it may not be appropriate to consider the central values for the Fermi momentum much higher than $p_{\max}$. Consequently, as discussed earlier in Section 2.3, we shall take four different cases corresponding to $(\sqrt{\beta}p)_{\max} = (\alpha\xi)_{\max} = 1.00, 1.25, 1.50,$ and 3.00. For these cases, f reduces to $0.125, 0.059, 0.029$ and 0.001, respectively, signifying the fact that momentum states corresponding to the higher values of $\alpha\xi$ are scarcely available . We shall thus consider the central values of Fermi momentum such that $p_{\mathrm{Fc}} \leq p_{\max}$ (or equivalently $\xi_c \leq \xi_{\max}$) for different choices of β_0 (or α). Moreover, as indicated in Section 1, there have been suggestions for lower and upper bounds for the parameter β_0, the extreme limits being $\beta_0 > 10^4$ and $\beta_0 < 10^{50}$. These bounds are equivalent to $\alpha > 4.1854 \times 10^{-21}$ and $\alpha < 4.1854 \times 10^2$. Since the upper bound 10^{50} is less reliable compared to the other upper bounds such as 10^{36} or 10^{34}, we shall therefore consider cases when β_0 value is decreased through 10^{36} (which we shall consider to be a legitimate upper bound) for which α becomes very small. It will be noticed that α becomes so small that we would even describe it as the limit $\alpha \to 0$.

It may however be noted that the equation of state connecting $\rho(\xi)$ and $P(\xi)$ via Eqs. (2.18) and (2.15) reduces to the ideal equation of state for the limiting case $\alpha\xi \ll 1$. The ideal case ($\alpha = 0$) is recovered in this way for which we would expect the Chandrasekhar limit. This is indeed the case when we solve equations following from the approximation $\alpha\xi \ll 1$ in Eqs. (2.47) and (2.48), that results in

$$\frac{d\xi}{dx} = -\frac{\sqrt{1+\xi^2}}{\xi}\frac{u(x)}{x^2} \tag{2.49}$$

and

$$\frac{du}{dx} = \frac{8}{3}\xi^3 x^2 \tag{2.50}$$

which are exactly the same as those in the ideal case ($\alpha = 0$). Solving these two equations numerically for increasingly higher values of the central Fermi momentum ξ_c we obtain the Chandrasekhar limiting mass as 1.4562 $M_\odot$ and zero radius. (The slight departure from the well-known value of 1.44 $M_\odot$ is due to a slightly different numerical accuracy in the present computation.)

On the other hand, the ideal ($\alpha = 0$) case is different from the case of a low value of α, however small. This is because the GUP equation of state reduces to the ideal case only when both limits $\alpha \ll 1$ and $\xi \ll 1$ are taken simultaneously so that the condition $\alpha\xi \ll 1$ is met to obtain Eq.(2.50) from (2.48). However, in a massive white dwarf, high values of ξ are expected in the central region so that the condition $\alpha\xi \ll 1$ may not be met even when $\alpha \ll 1$. In fact, for $\xi \gg 1$, it is possible to have values of $\alpha\xi \sim 1$ or higher even when $\alpha \ll 1$. We thus expect quite different solutions from the ideal case from Eqs. (2.47) and (2.48) for low values of α and hence the limit $\alpha \to 0$ does not coincide with the solution of Eqs. (2.49) and (2.50). This can be seen by employing the transformations $\tilde{\xi} = \alpha\xi$ and $\tilde{x} = x/\alpha$ in Eqs. (2.47) and (2.48), giving

$$\frac{d\tilde{\xi}}{d\tilde{x}} = -\frac{\sqrt{\alpha^2 + \tilde{\xi}^2}}{\tilde{\xi}} \frac{u(\tilde{x})}{\tilde{x}^2} \tag{2.51}$$

and

$$\frac{du}{d\tilde{x}} = \left\{ \tan^{-1}\tilde{\xi} - \frac{\tilde{\xi}(1-\tilde{\xi}^2)}{(1+\tilde{\xi}^2)^2} \right\} \tilde{x}^2. \tag{2.52}$$

Thus taking the limit $\alpha \to 0$ in Eqs. (2.51) and (2.52) yield equations quite different from Eqs. (2.49) and (2.50). Consequently, these differential equations do not reduce to the ideal differential equations even for very small values of α, that is $\alpha \to 0$. Eq. (2.52) will truly reduce to the ideal form $\frac{du}{d\tilde{x}} = \frac{8}{3}\tilde{\xi}^3\tilde{x}^2$ only when $\tilde{\xi} \ll 1$, which is not generally valid and we would expect $\tilde{\xi} \sim 1$ or higher in the central region of massive white dwarfs.

We solve the above two differential equations, namely, Eqs. (2.51) and (2.52), for the central values of $\tilde{\xi}_c$ running from 3.0 to 0.1, for different decreasing values of α. Mass versus the scaled radius R/α are shown in Figure 5(a) for a few representative values of α, namely, $0.4, 0.1, 0.05$ and 0.01. As we can see, the curves do not collapse, which is a consequence of the presence of α in Eq. (2.51). The tendency of the curves to collapse in the limit $\alpha \to 0$ can also be seen in Figure 5(a). However, we see that the curves are well-separated in Figure 5(b) where the mass is plotted with respect to the actual radius R. In all cases, including the $\alpha = 0.001$ case, we see that the mass of the white dwarf can be as high as $\sim 14\ M_{\odot}$.

Table 2.3 shows the masses and radii for different central values, namely, $\tilde{\xi}_c = \alpha\xi_c = 1.0, 1.25, 1.5$ and 3.0. For each case, the parameter α is decreased down to 10^{-6} (which corresponds to $\beta_0 = 5.7085 \times 10^{32}$). It is apparent that, as $\alpha \to 0$, the radius approaches zero, while the mass approaches a value that depends weakly on the choice of α but strongly on the value of $\tilde{\xi}_c = \sqrt{\beta} p_{\mathrm{Fc}}$. This indicates that the maximum value of the allowed momentum plays a dominant role in determining the mass of the white dwarf. Moreover the limiting mass values so obtained do not seem to yield the Chandrasekhar limit even in the limit $\alpha \to 0$.

The above behavior is connected with the fact that Eq. (2.52), obtained from the GUP equation of state, does not reduce to the standard non-GUP equation $\frac{du}{d\tilde{x}} = \frac{8}{3}\xi^3\tilde{x}^2$ for $\tilde{\xi} \sim 1$ or higher even in the limit $\alpha \to 0$, so that we do not expect the Chandrasekhar limit. In fact, for very high values of $\tilde{\xi}$, we have already seen that Eqs. (2.51) and (2.52) yield the Lane-Emden equation of index zero whose solution, given by Eqs.(2.43) and (2.44), indicate the behaviors $M \sim \tilde{\xi}_c^{3/2}$ and $R \sim \alpha\tilde{\xi}_c^{1/2}$. Although these are asymptotic solutions, we expect the same trend to be followed by the solution of Eqs. (2.51) and (2.52). We thus expect that the radius would approach zero while the mass would approach a constant value in the limit $\alpha \to 0$. We indeed see these behaviors to emerge for a few given choices of $\tilde{\xi}_c$, namely, $\tilde{\xi}_c = 1.0, 1.25, 1.5$ and 3.0, when we plot the mass and radius as functions of

Table 2.3: Four choices of $\tilde{\xi}_c$ and the corresponding values of mass and radius as β_0 decrease from 7.94292×10^{43} to 5.70857×10^{32}.

β_0	α	$\tilde{\xi}_c = 1.0$		$\tilde{\xi}_c = 1.25$		$\tilde{\xi}_c = 1.5$		$\tilde{\xi}_c = 3.0$	
		R (km)	M ($M_\odot$)	R (km)	M ($M_\odot$)	R (km)	M ($M_\odot$)	R (km)	M ($M_\odot$)
7.94292×10^{43}	0.373015	7380.5923	2.1168	7193.0451	2.9803	7186.8669	4.0253	8364.3115	14.1001
6.30929×10^{42}	0.105130	2673.1655	2.7424	2472.1223	3.5955	2377.6702	4.6455	2517.7272	14.8649
3.16223×10^{41}	0.023536	675.0628	2.8436	604.2194	3.6820	569.0310	4.7251	576.9071	14.9451
9.99812×10^{39}	0.004185	124.3514	2.8498	110.1106	3.6871	103.0309	4.7297	103.1906	14.9494
3.97865×10^{37}	0.000264	7.9054	2.8500	6.9834	3.6872	6.5253	4.7298	6.5187	14.9495
1.64978×10^{35}	0.000017	0.4990	2.8500	0.4407	3.6872	0.4118	4.7298	0.4113	14.9495
5.70857×10^{32}	0.000001	0.0396	2.8500	0.0350	3.6872	0.0327	4.7298	0.0327	14.9495

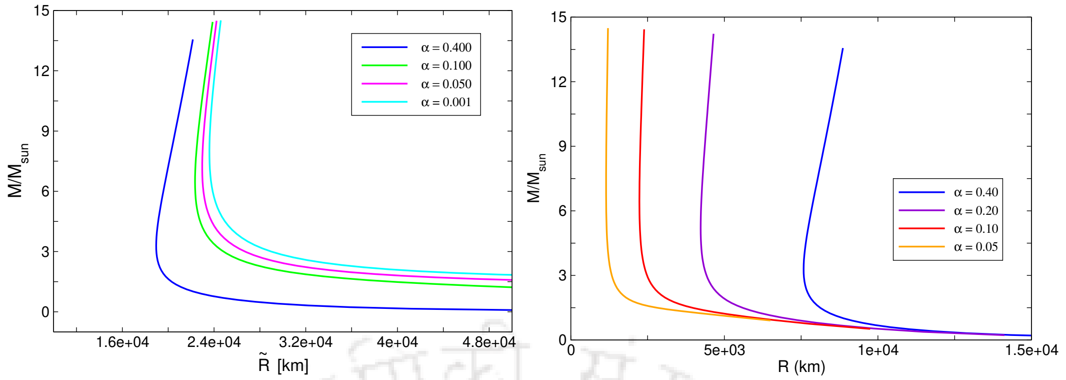

(a) **(b)**

Figure 2.5: (a) Mass versus $\tilde{R}$ for different values of α showing the tendency of curve-collapse for low values of α. The curves are obtained for the central values of $\tilde{\xi}_c$ running from 3.0 to 0.10. (b) Mass versus Radius R for different values of α.

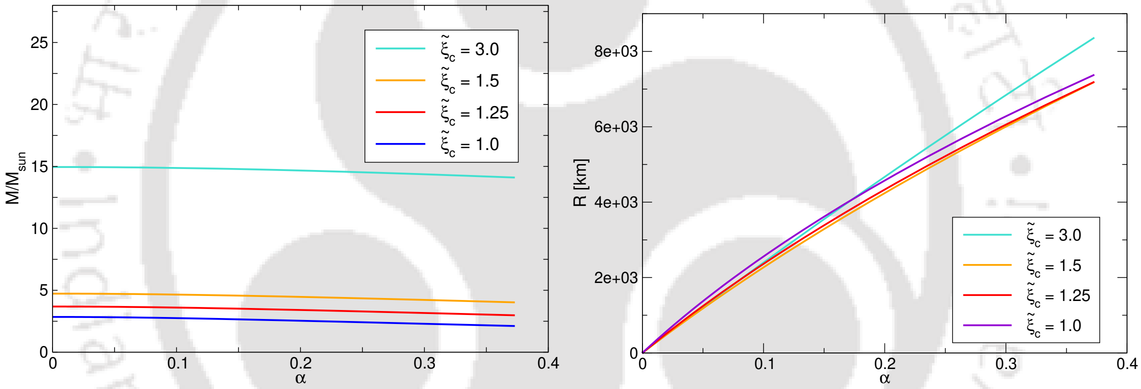

(a) **(b)**

Figure 2.6: (a) Mass vs α and (b) Radius vs α for four different choices: $\tilde{\xi}_c$ = 1.0, 1.25, 1.5, and 3.0.

α obtained from the numerical solutions of Eqs. (2.51) and (2.52) as displayed in Figures 6(a) and 6(b). It is interesting to note from Figure 6(a) that the mass values depend only on the given value of $\tilde{\xi}_c$ with a very weak dependence on α whereas Figure 6(b) demonstrates that the radius decreases to zero as the α value approaches zero.

In Figure 2.7, we display the mass-radius relation holding $\tilde{\xi}_c$ $(= \alpha\xi_c)$ at four constant values. Each curve corresponds to solutions of Eqs. (2.51) and (2.52) with the parameter α decreasing continuously from right to left (down to 10^{-6}). The constancy of the mass value with respect to the radius for a given value of $\tilde{\xi}_c$ immediately follows from Figures 6(a) and 6(b) because the mass being approximately constant with respect to α and the radius being approximately proportional to α would imply that the mass would be approximately constant with respect to the radius.

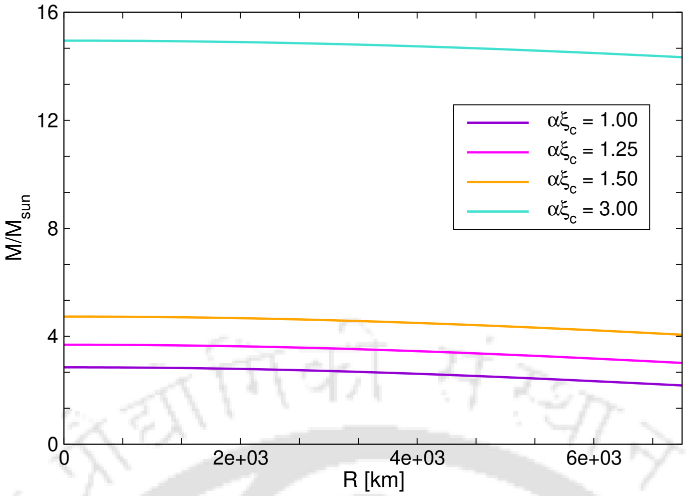

Figure 2.7: Mass-radius curves for four choices of $\tilde{\xi}_c$ (or $\alpha\xi_c$). The value of α decreases from right to left. A few representative numerical values are displayed in Table 2.3.

2.3.2 Restriction due to Neutronization

Inverse β-decay (${}^A_ZX + e \longrightarrow {}_{Z-1}^{\;\;A}Y + \nu_e$), or neutronization, sets in at a sufficiently high density when the condition on the Fermi energy $E_F \geqslant \varepsilon_Z$ is satisfied, where ε_Z is the difference in binding energies of the parent and daughter nuclei. The threshold density ρ_N for the ideal degenerate case was calculated by Salpeter [187] by setting $E_F = \varepsilon_Z$. Following Salpeter, we obtain the neutronization threshold Fermi momentum p_N as

$$\xi_N = \frac{p_N}{m_e c} = \sqrt{\frac{\varepsilon_Z^2 + 2m_e c^2 \varepsilon_Z}{m_e^2 c^4}}. \tag{2.53}$$

The inverse β-decay energy ε_Z for Helium can be found from Table II of Rotondo et al. [184]. The β-decay energies ε_Z for various isotopes of different elements were obtained from least square fits to the experimental data by Wapstra and Bos [225]. For ${}^4_2\mathrm{He}, \varepsilon_Z = 20.596$ MeV and the corresponding $\xi_N = 41.2932$.

Since in the GUP framework, the equations for hydrostatic equilibrium are expressed by Eqs. (2.51) and (2.52) in term of $\tilde{\xi} = \alpha\xi$, the neutronization threshold value $\tilde{\xi}_N = \alpha\xi_N$ takes different values for different choices of α, or equivalently β_0. Consequently we solve the full equations Eqs. (2.51) and (2.52) numerically for different values of α taking the central value as $\tilde{\xi}_N$. Table 2.4 gives the values of $\tilde{\xi}_N$ corresponding to different deceasing values of α. The corresponding mass and radius of the white dwarfs are shown in the last two columns. One may notice that both mass and radius approach finite limiting values. For excessively large values of β_0, such as 10^{44} (and higher), both mass and radius increase to very high values. However, as the β_0 value is decreased to 10^{40}, the mass and radius are 1.4898 M$_\odot$ and 601.34 km.

Although a high value of the upper bound such as 10^{50} has been suggested on the basis of inaccuracy in STM measurements of Landau levels, this upper bound is not reliable because STM measurements are accurate only up to 1 part in 10^3. On the other hand, the accuracy of Lamb shift in the hydrogen atom is at the level of 1 part in 10^{12}, and therefore the corresponding upper bound of 10^{36} is more reliable. We see from Table 2.4 that the mass and radius values are 1.4518 $\mathrm{M}_\odot$ and 601.18 km for the legitimate choice of $\beta_0 = 10^{36}$.

We also see from Table 2.4 that as β_0 value is decreased to 10^{34}, α reduces to a very small number $\sim 10^{-6}$ and $\tilde{\xi}_N$ reduces to $\sim 10^{-4}$, so that $\alpha \ll \tilde{\xi}_N$. On further decreasing β_0 to 10^{32}, we get $\alpha \sim 10^{-7}$ and $\tilde{\xi}_N \sim 10^{-5}$, and it becomes very difficult to solve Eqs. (2.51) and (2.52) numerically. Thus for $\beta_0 \leq 10^{32}$, we solve Eqs. (2.51) and (2.52) approximately by assuming $\alpha \ll \tilde{\xi}_N$, obtaining

$$\frac{d\tilde{\xi}}{d\tilde{x}} = -\frac{u(\tilde{x})}{\tilde{x}^2} \tag{2.54}$$

and

$$\frac{du}{d\tilde{x}} = \frac{8}{3}\tilde{\xi}^3\tilde{x}^2, \tag{2.55}$$

since $\tilde{\xi}_N$ becomes very small as indicated above. It may however be noted that these approximate equations are based on the assumption that $\alpha \ll \tilde{\xi}$ and $\tilde{\xi} \ll 1$ throughout the star. Although the approximation $\alpha \ll \tilde{\xi}$ is valid near the center, it will not be valid near the surface. We may however analyze these equation to get an approximate picture of the situation. Combining Eqs. (2.54) and (2.55), and defining a new dimensionless radius $\eta = \sqrt{\frac{8}{3}}\tilde{\xi}_c\tilde{x}$, and defining $\theta = \tilde{\xi}/\tilde{\xi}_c$, we obtain

$$\frac{1}{\eta^2}\frac{d}{d\eta}\left(\eta^2\frac{d\theta}{d\eta}\right) + \theta^3 = 0 \tag{2.56}$$

with boundary conditions $\theta(0) = 1$ and $\theta(\eta_R) = 0$, where η_R corresponds to the radius of the white dwarf. Eq. (3.34) is the Lane-Emden equation of index 3, whose numerical solutions are already known. From Eq. (2.55) we obtain the mass of the white dwarf in terms of the new coordinate as

$$\tilde{M}_N = -\sqrt{\frac{3}{8}}\eta_R^2\left(\frac{d\theta}{d\eta}\right)_{\eta=\eta_R} \tag{2.57}$$

Numerical solution for the Lane-Emden equation of index 3 can be found in Weinberg [226]. For $n = 3$, $-\eta_R^2\left(\frac{d\theta}{d\eta}\right)_{\eta=\eta_R} = 2.01824$, thus giving

$$M_N = M_0\tilde{M}_N = 1.4563\ \mathrm{M}_\odot. \tag{2.58}$$

We also obtain the radius of the white dwarf as

$$\tilde{R}_N = \sqrt{\frac{3}{8}}\frac{\alpha}{\tilde{\xi}_N}\eta_R = \sqrt{\frac{3}{8}}\frac{1}{\xi_N}\eta_R \tag{2.59}$$

where, for $n = 3$, $\eta_R = 6.89685$, thus

$$R_N = R_0\tilde{R}_N = 648.81\ \text{km}. \tag{2.60}$$

We note that the factors of α in the expression for radius given by Eq.(2.59) get canceled making it independent of α. This appears to be the feature when the α value is low. These approximate mass and radius values are close to the exact values shown in the last few rows of Table 2.4.

It may be important to analyze the nature of approximation just stated in the above paragraph. Since we have chosen a finite value of the central Fermi momentum $\xi_c = \xi_N = 41.2932$, this implies $\tilde{\xi}_c \sim 10^{-5}$ for a low value of α such as $\alpha = 10^{-6}$. Thus the approximation $\alpha^2 \ll \tilde{\xi}^2$ or $\sqrt{\alpha^2 + \tilde{\xi}^2} \approx \tilde{\xi}$, and hence Eq. (2.54), will be valid near the center of the star. However, as ξ approaches very small values near the surface, the approximation $\alpha^2 \ll \tilde{\xi}^2$ does not hold and Eq. (2.54) cannot be taken as an approximation for Eq. (2.51). This is not the case with Eq. (2.55) which is a good approximation of equation Eq. (2.52) because $\tilde{\xi} \ll 1$ throughout the star for these choices of ξ_c and α. In fact Eq. (2.54) amounts to the approximation $\sqrt{1+\xi^2} \approx \xi$ making the electron gas ultra-relativistic throughout the star. This is the main reason that the Lane-Emden equation of index 3 is obtained approximately throughout the star that yields the mass and radius as $1.4563 M_\odot$ and 648.81 km when the central Fermi momentum is taken as the neutronization threshold value ξ_N.

As we have already remarked, the Chandrasekhar limit is truly obtainable with vanishing radius for infinite central Fermi momentum with the standard (non-GUP) equation of state. In the standard (non-GUP) case the index of the Lane-Emden equation varies from 3 to 3/2 from the center to the surface. As stated earlier, when the non-GUP equations of hydrostatic equilibrium, namely, Eqs. (2.49) and (2.50), are solved numerically for increasingly higher values of the central Fermi momentum (beyond the neutronization threshold), we obtain the Chandrasekhar limiting mass as 1.4562 $M_\odot$ and zero radius. The slight departure from the well-known value of 1.44 $M_\odot$ is due to a slightly different numerical accuracy in the present computation.

On the other hand, in the present analysis with neutronization threshold, a mass slightly different from the Chandrasekhar mass 1.4562 $M_\odot$ and a non-zero radius are obtained for $\alpha \ll 1$. When we solve the full GUP equations of hydrostatic equilibrium, namely, Eqs (2.51) and (2.52), with the central Fermi momentum as $\xi_N = 41.2932$ and $\alpha = 10^{-6}$, we obtain $M_N = 1.4518$ $M_\odot$ and $R_N = 601.18$ km. These values, and the results of numerical integration for lower values of α, are shown in the last three rows of Table 4. The mass value is slightly lower than the Chandrasekhar limit 1.4562 $M_\odot$ and the radius does not change as the α value decreases below 10^{-6}.

We further obtained the mass and radius values of white dwarfs at the neutronization threshold by numerically solving the full equations, Eqs (2.51) and (2.52), for decreasing values of α and displayed them as functions of α in Figures 8(a) and 8(b). We observe that the mass and radius values become independent of the α value and approach constant values for very low values of α. This is confirmed by numerical computation below $\alpha =$

Table 2.4: Mass and radius for different values of β_0 when the central Fermi momentum is taken to be the neutronization threshold $\xi_N = 41.2932$. The third entry, $\beta_0 = 7.9 \times 10^{41}$, corresponding to $\tilde{\xi}_N \approx 1.5$, has been included to make a comparison with the GUP restriction $\tilde{\xi}_{\mathrm{max}} = 1.5$.

β_0	α	$\tilde{\xi}_N$	R_{N} (km)	M_{N} ($\mathrm{M}_\odot$)
10^{44}	0.4185393	17.28244	21374.79	294.7161
10^{42}	0.0418539	1.72824	972.63	5.8438
7.9×10^{41}	0.0373024	1.54030	885.73	4.9054
10^{41}	0.0132354	0.54652	614.74	1.8457
10^{40}	0.0041854	0.17282	601.34	1.4898
10^{38}	0.0004185	0.01728	601.18	1.4521
1.3×10^{36}	0.0000474	0.00194	601.18	1.4518
10^{34}	4.2×10^{-6}	0.00017	601.18	1.4518
5.7×10^{32}	1.0×10^{-6}	6.1×10^{-5}	601.18	1.4518
5.7×10^{28}	1.0×10^{-8}	4.1×10^{-7}	601.18	1.4518

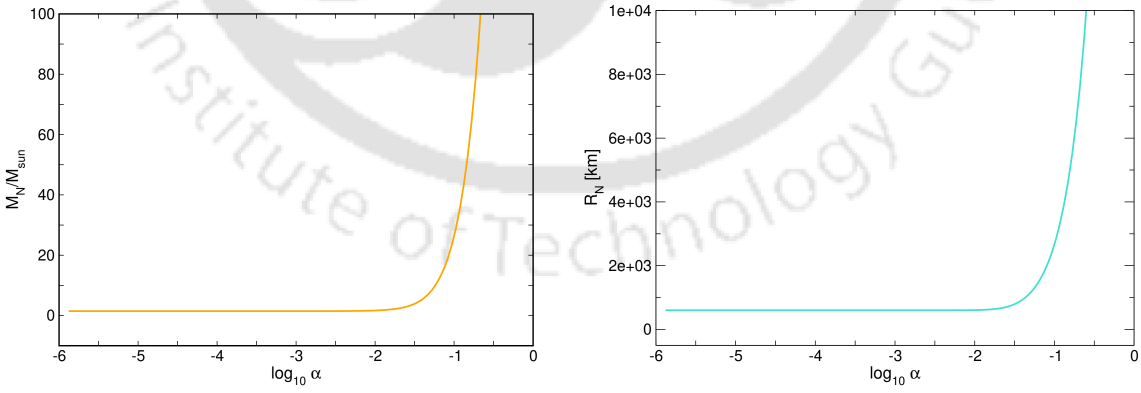

(a) **(b)**

Figure 2.8: Variation of (a) mass and (b) radius of white dwarfs when the central Fermi momentum is taken to be the neutronization threshold $\xi_N = 41.2932$ as the α value decreases down to 10^{-6}.

10^{-6} that yields the same values $M_N = 1.4518$ $\mathrm{M}_\odot$ and $R_N = 601.18$ as displayed in Table 2.4. This feature was also observed in the approximate solutions given by Eqs. (2.57) and (2.59).

We analyze the above limiting values by reconsidering Eq. (2.52) with the central Fermi momentum as $\xi_N = 41.2932$ and $\alpha = 10^{-6}$. The central value $\tilde{\xi}_c \sim 10^{-5}$ implies $\tilde{\xi} \ll 1$ throughout the star and Eq. (2.52) reduces to Eq. (2.55) in this approximation. However, since ξ becomes very small near the surface, the approximation $\alpha^2 \ll \tilde{\xi}^2$ is not valid throughout the star. Consequently we have to consider Eq. (2.51) coupled with Eq. (2.55). Transforming back to the variables $\xi = \tilde{\xi}/\alpha$ and $x = \alpha\tilde{x}$, we see that α scales out of both equations giving the ideal equations, namely, Eqs. (2.49) and (2.50). We note that this reduction is possible only for finite values of the central Fermi momentum (such as $\xi_c = \xi_N$) coupled with extremely low values of α. With these conditions, since α disappears from the description, we expect the mass and radius values to be independent of α. We observe exactly the same feature as described in the previous paragraph based on solutions of the full GUP Eqs. (2.51) and (2.52) where we saw that the mass and radius approach constant (α independent) values, namely, 1.4518 $\mathrm{M}_\odot$ and 601.18 km. These results are also confirmed by independent numerical solution of Eqs. (2.49) and (2.50) that yield exactly the same mass and radius values for the choice $\xi_c = \xi_N$. The Chandrasekhar limiting value with zero radius does not follow since the central Fermi momentum is not taken to be infinitely large.

2.4 Discussion and Conclusion

In this Chapter, we considered the effect of generalized uncertainty principle on the mass-radius relationship of Helium white dwarfs. The generalized uncertainty is believed to have its origin in quantum gravity and such uncertainty relations have been framed in string theory. The generalized uncertainty relation we have considered modifies the measure of the phase space integral by introducing a factor of $(1 + \beta\mathbf{p}^2)^{-3}$. As a consequence, the expressions for the density and pressure of the degenerate electron gas assume forms different from the ideal case and they now depend on the parameter β. We saw that the density now approaches a constant value whereas the pressure increases linearly in the region of ultra-high Fermi momentum. This is quite unlike the ideal case ($\beta = 0$) where both these quantities increase boundlessly with respect to the Fermi momentum. In consequence, the equation of state connecting the density and pressure has a completely different behavior from the ideal case. Since the stability of a star is determined by the equation of state of the matter it contains, we expect a different mass-radius relation for white dwarfs from the ideal case.

Assuming the density to be uniform, we first carried out a heuristic analysis and derived an approximate mass-radius relation in a parametric form. This yielded the behavior

$M \sim \xi^{3/2}$ and $R \sim \xi^{1/2}$ for ultra-high values of the Fermi momentum. Thus this simple analysis suggested that the mass and radius increase boundlessly in the limit of high Fermi momentum.

To obtain a better picture, we carried out an asymptotic analysis of the hydrostatic equilibrium (incorporating density variation) in the limit of high Fermi momentum. This analysis suggested that a white dwarf with ultra-high central Fermi momentum ξ_c will have a core of constant density determined by the Fermi momentum ξ_s above which the density remains constant. Both the mass and radius of the core are determined by the onset value ξ_s and the central value ξ_c. However, for arbitrarily high values of the central Fermi momentum $\xi_c \gg \xi_s$, the core mass and radius acquire negligible contribution from ξ_s, yielding $M_{\rm core} \sim \xi_c^{3/2}$ and $R_{\rm core} \sim \xi_c^{1/2}$. The same behavior was obtained by Rashidi [180] in the limit $\xi_c \to \infty$. These analyses suggest that the mass and radius increase boundlessly with unbounded increase in the central Fermi momentum.

To get a full picture of the mass-radius relationship, we obtained an exact solution of the hydrostatic equation of equilibrium by a numerical scheme. It was observed that, for $\beta_0 = 10^{36}$ (corresponding to $\alpha = 4.1854 \times 10^{-5}$), the mass-radius relation follows closely the original relation (without GUP) down to ~ 100 km. The same situation occurs for any value of $\beta_0 < 10^{36}$. For $\beta_0 = 10^{40}$ (corresponding to $\alpha = 4.1854 \times 10^{-3}$), the mass-radius curve diverges for low values of radii. Thus for the case $\beta_0 = 10^{36}$ also we expect the same kind of divergence to occur towards a much lower value of radius. The mass-radius relation can be analyzed in a better way by looking at the behavior for large values for β_0. Thus, for the case $\beta_0 = 10^{44}$ (correspondingly to $\alpha = 0.4185$), it is observed from the right hand part of Figure 2.4 that the mass-radius curve coincides with the Chandrasekhar curve for low values of ξ_c. As ξ_c is increased, the mass increases slowly and the radius decreases, reaching a minimum value ~ 7853 km as can be seen in the inset of Figure 2.4 (moving from right to left). On further increasing ξ_c, both the mass and radius increase boundlessly, which is consistent with our previous asymptotic analysis where we found that there exists a core of uniform density whose mass and radius are determined by the central value of ξ_c. Thus, this ultra-high region of Fermi momenta corresponds to a the behavior $M \sim \xi_c^{3/2}$ and $R \sim \xi_c^{1/2}$, which was also obtained by [180].

We also noted that the GUP factor $(1 + \beta \mathbf{p}^2)^{-3}$ imposes a severe restriction on the allowed values of momentum as this factor effectively puts an ultraviolet cutoff $p_{\rm max} \sim \beta^{-1/2}$ in the momentum integral. Thus, it appears that the center of a white dwarf cannot have an arbitrarily high value of Fermi momentum. To address this problem, we took four representative values, $(\sqrt{\beta} p_{\rm F})_{\rm max} = 1.00, 1.25, 1.50,$ and 3.00. Noting that the GUP parameter β_0 (or equivalently α) can be as low as 10^4 (or equivalently α as low as 4.1854×10^{-21}), we obtained the limiting mass in each case by decreasing the value of β_0 down to 10^{32} (or equivalently $\alpha \sim 10^{-6}$). We note that, for a particular choice of $(\sqrt{\beta} p_{\rm F})_{\rm max}$ the mass appears to converge to a limiting value whereas the radius approaches zero, which can be seen already at $\beta_0 \sim 10^{32}$ when the β_0 value is gradually decreased from $\beta_0 \sim 10^{43}$. As demonstrated in Table 2.3, such GUP restrictions lead to different values of limiting mass that are higher than the Chandrasekhar limit. On the other hand, if the GUP restriction is relaxed, and the central value of $\sqrt{\beta} p_{\mathrm{F}}$ is allowed to take arbitrarily high values, the mass increases boundlessly as demonstrated in Figure 5(a).

Since Inverse β-decay puts a *realistic* restriction on the extremal values of the mass and radius of a white dwarf, we next considered the maximum value of the central Fermi momentum to be determined by the neutronization threshold. However, since the value of the parameter β_0 is presently unknown, we considered different values of β_0 ranging from 10^{44} to 10^{34}. We solved the equations of hydrostatic equilibrium numerically with these β_0 values. For the case $\beta_0 = 10^{44}$, the mass and radius turn out to have large values, ~ 295 $\mathrm{M}_\odot$ and ~ 21375 km. On the other hand, for $\beta_0 = 10^{42}$, the mass is ~ 6 $\mathrm{M}_\odot$ and radius is ~ 970 km, whereas for $\beta_0 = 10^{40}$, we obtained ~ 1.5 $\mathrm{M}_\odot$ and ~ 601 km, respectively. Although an upper bound of 10^{50} for β_0 was suggested on the basis of STM measurements of Landau levels, this upper bound is not reliable because STM measurements have a low accuracy of 1 part in 10^3. On the other hand, measurements on Lamb shift in a Hydrogen atom with a much higher accuracy of 1 part in 10^{12} yielded an upper bound of 10^{36}. Consequently we take this more reliable upper bound for granted. We thus considered the value $\beta_0 = 10^{36}$ and performed the numerical calculations with the neutronization threshold ξ_N as the central Fermi momentum. We found that the mass and radius now turn out to be 1.4518 $\mathrm{M}_\odot$ and 601.18 km, respectively. We also considered the value 10^{34} and lower and the numerical solutions yielded the same values of mass and radius. Since in stable Helium white dwarfs, the central Fermi energy is expected to be lower than the neutronization threshold value of 20.596 MeV, they are expected to have masses lower than 1.4518 $\mathrm{M}_\odot$ and radii larger than 601.18 km. This can be confirmed by solving Eqs. (2.47) and (2.48) with central Fermi energy less than 20.596 MeV and $\beta_0 \leq 10^{36}$. Moreover, for stable white dwarfs with core composition other than Helium the neutronization threshold value is much lower than 20.596 MeV. For example, for ${}^{12}_{6}\mathrm{C}$, ${}^{16}_{8}\mathrm{O}$, and ${}^{20}_{10}\mathrm{Ne}$, the neutronization threshold values are 13.370 MeV, 10.419 MeV, and 7.026 MeV, [184, 225] respectively. Consequently white dwarfs with these compositions are expected to have central Fermi energies lower than these values. Since most white dwarfs occurring in Nature have their cores composed of these elements, they are expected to have masses much lower than 1.4518 $\mathrm{M}_\odot$ and radii much larger than 601.18 km. These conclusions are consistent with the observations of non-magnetic white dwarfs that are usually found to be in the mass range from 0.17 $\mathrm{M}_\odot$ [107] to 1.33 $\mathrm{M}_\odot$ [101, 129, 219, 220] with radii ranging from 0.0153 $R_\odot$ (10644 km) to 0.0071 $R_\odot$ (4939 km) [32, 199–201].

We conclude by noting that the above discussions based on inverse β-decay threshold suggest that the range of mass and radius values of white dwarfs observed in Nature are dictated by the neutronization threshold even in the presence of the effects of quantum gravity.

Chapter 3

Newtonian white dwarfs with noncommutative EoS

In this Chapter, we consider an alternative scenario of quantum gravity, namely, the modified dispersion relation as described in Section 1.2 of Chapter 1. The equation of state of the electron degenerate gas in a white dwarf is usually treated by employing the ideal dispersion relation. However, the effect of quantum gravity is expected to be inevitably present and when this effect is considered through a non-commutative formulation, the dispersion relation undergoes a substantial modification. In this Chapter, we take a modified dispersion relation and find the corresponding equation of state for the degenerate electron gas in white dwarfs. Hence we solve the equation of hydrostatic equilibrium and find that this leads to the possibility of the existence of excessively high values of masses exceeding the Chandrasekhar limit although the quantum gravity effect is taken to be very small. It is only when we impose the additional effect of neutronization that we obtain white dwarfs with masses close to the Chandrasekhar limit with nonzero radii at the neutronization threshold. We demonstrate these results by giving the numerical estimates for the masses and radii of Helium, Carbon, and Oxygen white dwarfs.

We discussed in Chapter 2 that the generalized uncertainty scenario of quantum gravity leads to excessively massive stable white dwarfs. However, when the condition of neutronization was imposed together with a legitimate upper bound for β, a mass value close to the Chandrasekhar mass was obtained.

Since there are various alternative descriptions of quantum gravity, it becomes a natural question whether the above feature is preserved in an alternative formulation. It is thus important to analyze the problem in an alternative perspective of quantum gravity. Our

---

The content of this chapter is published: A. Mathew, M. K. Nandy, Res. Astron. Astrophys. **18**, 151 (2018) discussion on quantum spacetime fluctuations in Section 1.2 suggests that the dispersion relation is substantially modified from the ideal case due to the effect of quantum gravity through non-commutative relations (1.56) and (1.57). A general phenomenological form of the modified dispersion relation was motivated in equation (1.63).

With a modified dispersion relation of the form $E^2 - p^2c^2f(E) = 0$, Alexander and Magueijo [5] addressed the horizon and flatness problems in a Friedmann cosmology with three different choices: $f(E) = (1+\lambda E)^2$, $f(E) = 4\lambda^2E^2/(1-e^{-2\lambda E})^2$ and $f(E) = (1+\lambda E)^{2\gamma}$. Bertolami and Zarro [27], considering the form $f(E) = (1+\lambda E)^2$, employed the deformed dispersion relation, $E^2 = p^2c^2(1+\lambda E)^2 + m^2c^4$, for massive particles. Taking the approximate form $E = \lambda p^2c^2 + \sqrt{p^2c^2 + m^2c^4}$ for low values of λ, they employed it to study the stellar structure of astrophysical objects such as main sequence stars, white dwarfs and neutron stars. In particular, they found that the $\mathcal{O}(\lambda)$ correction to the electron degenerate pressure enhances the stability of white dwarfs.

Since the modified dispersion relation $E^2 = p^2c^2(1+\lambda E)^2 + m^2c^4$ is different from the ideal dispersion relation, $E^2 = p^2c^2 + m^2c^4$, we expect a modification in the equation of state of the electron degenerate gas in a white dwarf. This is expected to alter the stability of the star. Consequently in this Chapter, we take this modified dispersion relation to find the equation of state of the degenerate electron gas in a white dwarf and hence we solve the equation of hydrostatic equilibrium employing Newtonian gravity. We find that white dwarfs of excessively high values of masses beyond the Chandrasekhar mass are supported although the quantum gravity parameter λ is taken to be very small. It is only when we impose neutronization into the problem, we get the mass values close to the Chandrasekhar limit. It is thus evident that whichever way we take the effect of quantum gravity, we reach the same conclusion: unbounded mass limits for white dwarfs although the effect of quantum gravity is taken to be very small. Since the effect of quantum gravity is inevitably present, it suggests that neutronization may be is responsible for the limiting mass being nearly the Chandrasekhar mass.

We note that the effect of noncommutative dispersion relation was considered earlier for white dwarfs by [41] and [78]. The latter study reported slight increase or decrease in the limiting mass depending on the sign of the parameter λ, whereas the alternative approach via the generalized uncertainty relation formalism predicted an unbounded increase in mass and radius ([180]). On the other hand, in this work we analyze the effect of the modified dispersion relation in detail revealing features such as the possibility of excessively high values of masses of white dwarfs and the effect of neutronization that limits the mass of the white dwarf as indicated in the previous paragraph.

In the present scenario, we further note that the behavior of the density ρ with respect to the Fermi momentum p_{F} remains the same as in the ideal case ($\rho \sim p_{\mathrm{F}}^3$) and the non-commutative dispersion relation has no effect on it. This feature is quite unlike the behavior found with the generalized uncertainty relation where the density approaches a constant value as $p_{\rm F} \to \infty$. Despite this disparity in the two approaches, we still find in the present case of non-commutative dispersion relation that white dwarfs can acquire arbitrarily high values of masses and radii similar to that in the case of generalized uncertainty relation. However, when we consider the role of neutronization together with a feasible value for the parameter λ, we find that the maximum possible masses for different white dwarfs (for example Helium, Carbon and Oxygen) are close to the Chandrasekhar limits.

The outline of the chapter is as follows. In Section 3.1, we derive the equation of state for a degenerate electron gas where we also analyze the related asymptotic behaviors. In Section 3.2, we consider the equations of hydrostatic equilibrium and discuss its asymptotic and exact solutions. In Section 3.3, we consider the limitation due to neutronization. Finally, we present a discussion and conclude the chapter in Section 3.4.

3.1 Non-commutative Equation of State

In this section, we obtain the number density n and pressure P of a degenerate electron gas employing the modified dispersion relation. The asymptotic behavior of pressure P in the limits of low and high Fermi momenta are also analyzed.

3.1.1 Modified Thermodynamic Behavior

We employ the grand canonical ensemble ([114]) for the electron gas, for which the grand potential can be expressed as

$$\Omega = -PV = -\frac{k_B T V}{\hbar^3 \pi^2} \int_0^\infty dp\, p^2 \ln\left[1 + \exp\left\{-\frac{(E_{\mathbf{p}} - \mu)}{k_B T}\right\}\right]. \tag{3.1}$$

The pressure P can be immediately obtained from the above integral. In addition, the identity $N = -\partial\Omega/\partial\mu$ gives the number density as

$$n = \frac{N}{V} = \frac{1}{\hbar^3 \pi^2} \int_0^\infty dp\, p^2 \left[\exp\left\{\frac{E_{\mathbf{p}} - \mu}{k_B T}\right] + 1\right\}^{-1}. \tag{3.2}$$

Since the electron gas in white dwarfs is completely degenerate to a very good approximation, we take the limit $T \to 0$ in the above expressions and obtain

$$n = \frac{1}{\hbar^3 \pi^2} \int_0^{p_{\rm F}} dp\, p^2 \quad \text{and} \quad P = \frac{1}{\hbar^3 \pi^2} \int_0^{p_{\rm F}} dp\, p^2 \left(E_{\rm F} - E_{\mathbf{p}}\right), \tag{3.3}$$

where $p_{\rm F}$ is the Fermi momentum and $E_{\rm F}$ is the Fermi energy.

Since the number density n given by Eq. (3.3) remains unaffected by the modified dispersion relation, non-commutativity has no effect on it and we obtain the same expression as in the ideal case. We rewrite it in terms of the dimensionless variable $\xi = p_{\rm F}/m_e c$ to obtain $n(\xi) = m_e^3 c^3 \xi^3/(3\hbar^3\pi^2)$ and hence the mass density

$$\rho(\xi) = \mu_e m_u n(\xi) = K \left(\frac{\mu_e m_u}{m_e c^2}\right) \frac{\xi^3}{3}, \tag{3.4}$$

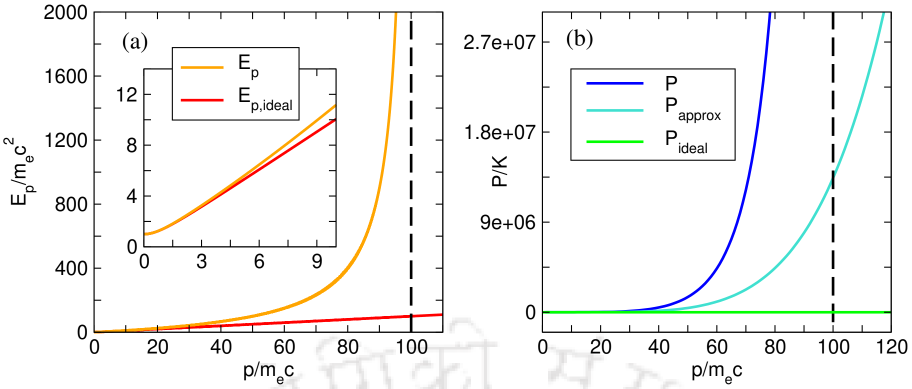

Figure 3.1: (a) Non-commutative dispersion relation E_p/m_ec^2 (orange curve) as a function of $\tilde{p} = p/m_ec$ for the case $\alpha = 0.01$ so that $\tilde{p}_{\max} = 1/\lambda m_ec^2 = 1/\alpha = 100$. Ideal dispersion $E_{p,\mathrm{ideal}}/m_ec^2$ (red curve) is also shown. The inset compares the two curves for low values of momentum. (b) Comparison of the noncommutative pressure P (blue curve) with approximate P_{approx} (cyan curve), and ideal P_{ideal} (green curve) expressions given by Eqs. (3.8), (3.14) and (3.13), respectively, for $p_{\mathrm{Fmax}}/m_ec = 1/\alpha = 100$.

with $\mu_e = A/Z$ the number of nucleons per electron, $K = m_e^4c^5/\hbar^3\pi^2$, and $m_u = 1.6605 \times 10^{-24}$ g is the atomic mass unit.

It has been shown that the noncommutative formulation of quantum gravity leads to a dispersion relation more complicated than the ideal one [12, 15]. [27] employed a simplified form of the dispersion relation

$$E_{\mathbf{p}}^2 = \mathbf{p}^2c^2(1 + \lambda E_{\mathbf{p}})^2 + m^2c^4 \tag{3.5}$$

where the parameter λ quantifies the effect of quantum gravity.

Unlike the number density, the pressure P is modified due to the modification in the dispersion relation. This dispersion relation can be rearranged to obtain

$$E_{\mathbf{p}} = \frac{\lambda p^2c^2 + \sqrt{p^2c^2 + m^2c^4(1 - \lambda^2p^2c^2)}}{1 - \lambda^2p^2c^2} \tag{3.6}$$

This dispersion relation imposes a momentum cutoff at $p_{\max} = (\lambda c)^{-1}$ beyond which $E_{\mathbf{p}}$ becomes unphysical (cf. Figure 3.1a). We may rewrite it in terms of $\tilde{\mathbf{p}} = \mathbf{p}(m_ec)^{-1}$ as

$$f(\tilde{p}) = \frac{E_{\mathbf{p}}}{m_ec^2} = \frac{\alpha\tilde{p}^2 + \sqrt{(1 - \alpha^2)\tilde{p}^2 + 1}}{1 - \alpha^2\tilde{p}^2}. \tag{3.7}$$

where $\alpha = \lambda m_ec^2$. The behavior of $f(\tilde{p})$ is shown in Figure 3.1a. For comparison, the ideal dispersion relation $E_{\mathbf{p},\mathrm{ideal}} = \sqrt{p^2c^2 + m_e^2c^4}$ is also plotted in the same figure. We note that if we make the approximation $E_{\mathbf{p}} \approx \sqrt{p^2c^2 + m^2c^4} + \lambda p^2c^2$ by neglecting the $O(\lambda^2)$ terms, the intrinsic momentum cut-off will be lost. We therefore avoid making this approximation to treat the high momentum region carefully. It may also be noted that this modified dispersion relation dictates the existence of a maximum density $\rho_{\max} = K\mu_em_u/(3m_ec^2\alpha^3)$ corresponding to the maximum cutoff in momentum $p_{\max}$. For example, for $\alpha = 10^{-3}$, $\rho_{\max} = 1.9478 \times 10^{15}$ g cm^{-3}, and for $\alpha = 10^{-4}$, $\rho_{\max} = 1.9478 \times 10^{18}$ g cm^{-3}.

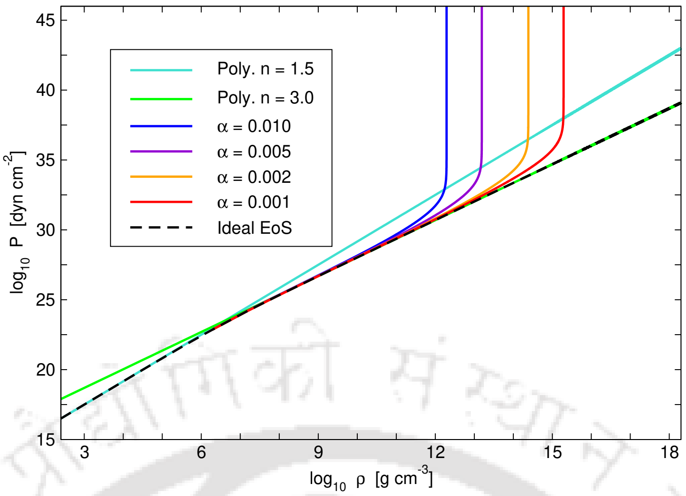

Figure 3.2: Comparison of the noncommutative equation of state (for different values of α) given by Eqs. (3.4) and (3.8) with the ideal equation of state given by Eqs. (3.4) and (3.13). Also shown are the polytropic equations of state $P = K_n\rho^{1+1/n}$ with $n = 3/2$ and 3.

We obtain the pressure P from Eq. (3.3) employing the complete noncommutative dispersion relation, given by Eq. (3.6), as

$$P(\xi) = K\left\{f(\xi)\int_0^\xi \tilde{p}^2 d\tilde{p} - \int_0^\xi f(\tilde{p})\tilde{p}^2 d\tilde{p}\right\} = K\left\{f(\xi)\frac{\xi^3}{3} - g(\xi)\right\} = Kh(\xi) \tag{3.8}$$

with

$$g(\xi) = \frac{1}{\alpha^4}\left\{2\tanh^{-1}\alpha\xi + \tanh^{-1}\frac{\xi(1-\alpha^2)}{\alpha+\sqrt{1+(1-\alpha^2)\xi^2}} - \frac{(2-\alpha^2)}{2\sqrt{1-\alpha^2}}\sinh^{-1}\xi\sqrt{1-\alpha^2}\right\}$$
$$-\frac{\xi}{3\alpha^3}\left\{3+\alpha^2\xi^2+\frac{3\alpha}{2}\sqrt{1+(1-\alpha^2)\xi^2}\right\} \tag{3.9}$$

The behavior of $P(\xi)$ is shown in Figure 3.1b. We see that momenta higher than $\xi_{\rm max}$, determined by the cutoff $p_{\rm max}$ of the noncommutative dispersion relation (3.6), are forbidden and the curve does not go beyond this limit. In Figure 3.2, we compare the noncommutative equation of state given by Eqs. (3.4) and (3.8) with the ideal equation of state and the polytropic equations of state $P = K_n\rho^{1+1/n}$ with $n = 3$ and $3/2$, where $K_3 = \frac{1}{4}\left(\frac{3}{K}\right)^{1/3}\left(\frac{m_e c^2}{\mu_e m_u}\right)^{4/3}$ and $K_{3/2} = \frac{1}{5}\left(\frac{3}{K}\right)^{2/3}\left(\frac{m_e c^2}{\mu_e m_u}\right)^{5/3}$. The noncommutative equation of state clearly indicates that the density cannot exceed the maximum values $\rho_{\rm max}$ for different values of α. This implies that the effect of quantum gravity forbids the star to have an infinite density (at the center).

Consistency of the equation of state connected by the above noncommutative expressions for $P(\xi)$ and $n(\xi)$ follows immediately as they satisfy the well-known thermodynamic relation $dP/d\mu = n$, where μ is the chemical potential. The left-hand side of this relation, in terms of the dimensionless parameter ξ, becomes

$$\frac{dP}{d\mu} = \frac{K}{m_e c^2} \frac{dh}{d\xi} \frac{1}{df/d\xi}, \tag{3.10}$$

where we have used $\mu = m_e c^2 f(\xi)$, which is the modified expression for the Fermi energy. The differentials in the above equation can be obtained from Eqs. (3.7), (3.9) and (3.8) as

$$\frac{df}{d\xi} = \xi \left\{ \frac{(1+\alpha^2\xi^2) + (1-\alpha^2\xi^2)\alpha^2 + 2\alpha\sqrt{1+(1-\alpha^2)\xi^2}}{(1-\alpha^2\xi^2)^2\sqrt{1+(1-\alpha^2)\xi^2}} \right\} \tag{3.11}$$

and

$$\frac{dh}{d\xi} = \frac{\xi^3}{3} \frac{df}{d\xi}. \tag{3.12}$$

Using Eq. (3.12) in (3.10), it immediately follows that $dP/d\mu = (K/3m_e c^2)\xi^3 = n$, ensuring consistency with the thermodynamic relation.

We thus see that, in noncommutative geometry, the equation of state undergoes a drastic modification due an intrinsic momentum cutoff inherent in the modified dispersion relation. This situation is quite unlike the scenario following from the generalized uncertainty principle where the equation of state undergoes a drastic modification due to a change in the measure of the phase space despite the dispersion relation remains ideal. A detailed analysis of this latter scenario is given in Ref. [132].

3.1.2 Ideal and Asymptotic Behaviors

It is easy to show that, in the limit $\alpha \to 0$, the parametric forms of the pressure corresponding to the ideal degenerate case can be recovered. The leading order terms in the expansion of Eq. (3.8) are obtained as

$$P_{\text{ideal}}(\xi) = \frac{K}{24} \left\{ \sqrt{1+\xi^2}(2\xi^3 - 3\xi) + 3\sinh^{-1}\xi \right\}. \tag{3.13}$$

Figure 3.1b compares the noncommutative pressure $P(\xi)$ given by Eq. (3.8) with the ideal pressure $P_{\text{ideal}}(\xi)$ given by Eq. (3.13). It may be noted that there is a large deviation between the two expressions for higher values of Fermi momentum. In the noncommutative case, the pressure increases faster and approaches infinity as the Fermi momentum approaches p_{max}. This behavior is quite different from the ideal case where the energy density approaches infinity at a slower rate beyond p_{max}.

A first correction to the ideal case can be obtained by a Taylor expansion about $\lambda = 0$ and by retaining the $O(\lambda)$ term. In this approximation, $E_{\mathbf{p},\text{approx}} = \lambda p^2 c^2 + \sqrt{p^2c^2 + m^2c^4}$. The corresponding pressure turns out to be

$$P_{\text{approx}}(\xi) = K \left\{ \frac{1}{24}\sqrt{1+\xi^2}(2\xi^3 - 3\xi) + \frac{1}{8}\sinh^{-1}\xi + 2\alpha\frac{\xi^5}{15} \right\} = P_{\text{ideal}} + \frac{2}{15}K\alpha\xi^5, \tag{3.14}$$

This approximate expression is also compared with the other cases in Figures 3.1b. We see that the noncommutative momentum cutoff p_{max} (or $\xi_{\text{max}} = \alpha^{-1}$) of the complete dispersion relation is not respected by the approximate expression $P_{\text{approx}}(\xi)$ and it deviates strongly from the noncommutative expression $P(\xi)$. This indicates that the approximate form $P_{\rm approx}(\xi)$ is not a good approximation for high values of Fermi momentum near $\xi_{\rm max}$. This is due to the fact that the approximate dispersion relation given by $E_{\mathbf{p},\rm approx}$ does not impose any restriction on the momentum values. On the other hand, the complete noncommutative dispersion relation $E_{\mathbf{p}}$ constrains momentum values by imposing a momentum cutoff $p_{\rm max}$. The importance of our present analysis lies in the fact that we use the complete noncommutative dispersion relation without making any approximations so that its basic feature of a maximum attainable momentum $p_{\rm max}$ is retained.

We next analyze the asymptotic behavior of the noncommutative pressure $P(\xi)$ given by Eq. (3.8) in the low and high momentum limits, $\xi \to 0$ and $\xi \to \xi_{\rm max}$. For low values of ξ, it is obtained as

$$P_{\rm low}(\xi) = K(1+2\alpha)\frac{\xi^5}{15}. \tag{3.15}$$

It is important to note that, even in this limit, the effect of noncommutativity persists due to the presence of the term proportional to α at the order ξ^5. We shall see this feature to be present when we analyze the mass-radius relation for low values of central Fermi momentum ξ_c. Moreover, Eqs. (3.4) and (3.15) imply $P_{\rm low} \sim \rho^{5/3}$ which can be seen in Figure 3.2 where the noncommutative and the ideal equations of state coincide in the low momentum region.

In the high momentum region $\xi \sim \xi_{\rm max}$, we expand the noncommutative expression for pressure P assuming the momentum to be close to $p_{\rm max}$ (or $\xi_{\rm max}$), to obtain

$$P_{\rm high}(\xi) = \frac{K}{\alpha^4}\left\{\frac{1}{1-\alpha\xi} - \ln\left(\frac{2\alpha^2}{1-\alpha\xi}\right) - C(\alpha)\right\} \tag{3.16}$$

where

$$C(\alpha) = \tanh^{-1}\left(\frac{1-\alpha^2}{1+\alpha^2}\right) - \sinh^{-1}\frac{1}{\alpha} - \frac{11}{6} \tag{3.17}$$

Thus, when the central Fermi momentum ξ_c is close to $\xi_{\rm max} = \alpha^{-1}$, the central pressure approaches infinity. This boundless increase in the pressure for very high values of ξ should be able to counteract gravitational pull in very massive white dwarfs. This feature will show up more explicitly later when we analyze the mass-radius relation for high values of the central Fermi momentum. Moreover, this feature can be seen in Figure 3.2 where the pressure approaches infinity and the density approaches constant values $\rho_{\rm max} = K\mu_e m_u/(3m_e c^2\alpha^3)$ as implied by Eq. (3.4). Unlike the ideal case, where $P_{\rm high} \sim \rho^{4/3}$, the behaviour is remarkably different in the high momentum region of the noncommutative equation of state.

3.2 Noncommutative white dwarfs

In this section, we obtain the mass-radius relation of Helium white dwarfs with the equation of state obtained in Section 3.1.1 from the noncommutative dispersion relation. In the framework of Newtonian gravity, the condition of hydrostatic equilibrium for a spherical distribution of matter is given by Eqs. (1.92). Substituting Eqs. (3.4) and (3.8) and using the dimensionless variable $x = r/R_0$ in Eq. (1.92) yield

$$\frac{1}{x^2}\frac{d}{dx}\left(x^2 f'(\xi)\frac{d\xi}{dx}\right) + \frac{\xi^3}{3} = 0 \tag{3.18}$$

where $R_0 = (4\pi GK)^{-1/2}\left(m_e c^2/\mu_e m_u\right) = 2242.77$ km.

3.2.1 Asymptotic Solutions

In the limit $\xi \to 0$, that is, for low values of ξ, it can be shown that $f'(\xi) = (1+2\alpha)\xi$. Thus Eq. (3.18) can be rewritten as

$$\frac{(1+2\alpha)}{2}\frac{1}{x^2}\frac{d}{dx}\left(x^2\frac{d\xi^2}{dx}\right) + \frac{\xi^3}{3} = 0 \tag{3.19}$$

Now, taking $\xi^2(x)/\xi_c^2$ as $\theta(x)$, with ξ_c the central dimensionless Fermi momentum, and defining a new dimensionless coordinate $\eta = \sqrt{2/3}\sqrt{\xi_c/(1+2\alpha)}\ x$, we reduce the above equation to

$$\frac{1}{\eta^2}\frac{d}{d\eta}\left(\eta^2\frac{d\theta}{d\eta}\right) + \theta^{3/2} = 0 \tag{3.20}$$

which is the Lane-Emden equation of index 3/2. The numerical solution for this differential equation is given in [226]. For the boundary conditions $\theta(0) = 1$ and $\theta'(0) = 0$, one can immediately obtain the radius of the white dwarf as

$$R = \sqrt{\frac{3}{2\xi_c}}\ (1+2\alpha)^{1/2} R_0 \eta_R \tag{3.21}$$

where $\eta_R = 3.65375$ is the first zero of the Lane-Emden function $\theta(\eta)$ of index 3/2.

Similarly the asymptotic behavior of the mass of the white dwarf can be obtained from the integral expression of mass from equation (1.92), namely,

$$M = 4\pi\int_0^R \rho(r) r^2 dr = 4\pi K\left(\frac{\mu_e m_u}{m_e c^2}\right)\int_0^R \frac{\xi^3}{3} r^2 dr. \tag{3.22}$$

Using $\tilde{M} = M/M_0$ and $\tilde{R} = R/R_0$ with $M_0 = (4\pi K)^{-1/2} G^{-3/2}\left(m_e c^2/\mu_e m_u\right)^2 = 0.41659\ \mathrm{M}_\odot$ in the above equation, we get $\tilde{M} = \frac{1}{3}\int_0^{\tilde{R}} \xi^3 x^2 dx$. We rewrite this equation in the new dimensionless variable η, yielding

$$\tilde{M} = \sqrt{\frac{3\xi_c^3}{8}}\ (1+2\alpha)^{3/2}\int_0^{\eta_R} \theta^{3/2}\eta^2 d\eta, \tag{3.23}$$

thus obtaining the mass of the white dwarf as

$$M = -\sqrt{\frac{3\xi_c^3}{8}}(1+2\alpha)^{3/2} M_0 \eta_R^2 \left(\frac{d\theta}{d\eta}\right)_{\eta=\eta_R} \tag{3.24}$$

The value of $\left(-\eta^2 d\theta/d\eta\right)_{\eta=\eta_R}$ is 2.71406 ([226]). Thus the above asymptotic analysis predicts that $R \sim (1+2\alpha)\xi_c^{-1/2}$ and $M \sim (1+3\alpha)\xi_c^{3/2}$ indicating the persistence of the effect of noncommutativity through the presence of the parameter α even for very low values of the central Fermi momentum. The presence of α (or $\lambda m_e c^2$) in these expressions suggests increase on the order of α in mass and radius of white dwarfs. We also note that for $\alpha = 0$, the above mass-radius relation approaches the Chandrasekhar relation for low values of central Fermi momentum.

On the other hand, in the limit $\xi \to \xi_{\max} = \alpha^{-1}$, $f'(\xi) = (1/\alpha^2)\,(\xi - 1/\alpha)^{-2}$, so that Eq. (3.18) reduces to

$$\frac{1}{x^2}\frac{d}{dx}\left(\frac{x^2}{(\xi-\frac{1}{\alpha})^2}\frac{d\xi}{dx}\right)+\frac{1}{3\alpha}=0 \tag{3.25}$$

Letting $\phi = \alpha/(1-\alpha\xi)$ yields

$$\frac{1}{x^2}\frac{d}{dx}\left(x^2\frac{d\phi}{dx}\right)+\frac{1}{3\alpha}=0 \tag{3.26}$$

Defining $(\phi(x)-\alpha)/(\phi_c-\alpha) = \theta(x)$, where $\phi_c = \alpha/(1-\alpha\xi_c)$ and redefining the dimensionless radius as $x = \sqrt{3\alpha(\phi_c-\alpha)}\zeta$, the above equation takes the form

$$\frac{1}{\zeta^2}\frac{d}{d\zeta}\left(\zeta^2\frac{d\theta}{d\zeta}\right)+1=0, \tag{3.27}$$

which is the Lane-Emden equation of index zero whose numerical solution is already known. Thus the radius of the white dwarf is given by

$$R = \alpha\sqrt{\frac{3\alpha\xi_c}{1-\alpha\xi_c}}R_0\zeta_R \tag{3.28}$$

where $\zeta_R = \sqrt{6}$ is the zero for the Lane-Emden function $\theta(\zeta)$ of index zero.

The mass of the white dwarf can be obtained from Eq. (3.22) by taking the appropriate limit $\xi \to \xi_{\max}$ and using the above dimensionless coordinate ζ, we get

$$\tilde{M} = \frac{1}{9}\left(\frac{3\alpha\xi_c}{1-\alpha\xi_c}\right)^{3/2}\zeta_R^3. \tag{3.29}$$

Consequently the mass of the white dwarf is obtained as

$$M = \frac{M_0}{9}\left(\frac{3\alpha\xi_c}{1-\alpha\xi_c}\right)^{3/2}\zeta_R^3. \tag{3.30}$$

Since Eqs. (3.28) and (3.30) were obtained with the assumption of the central Fermi momentum ξ_c approaching the maximum value α^{-1}, they are valid near $\xi_{\max}$ $(=\alpha^{-1})$. In this limit the quantity $(1-\alpha\xi_c)$ approaches zero so that the mass and radius diverge as $M \to (1-\alpha\xi_c)^{-3/2}$ and $R \sim (1-\alpha\xi_c)^{-1/2}$ as ξ_c tends to $\xi_{\max}$. In fact, the largeness of the mass and radius will depend on how close is ξ_c with respect to α^{-1}. Thus, both mass and radius increase unboundedly as the central Fermi momentum ξ_c approaches the maximum cutoff value $\xi_{\max} = \alpha^{-1}$.

From Eqs. (3.28) and (3.30) we obtain MR^{-3} = Const. Since those expressions are valid for excessively high values of the Fermi momentum, this implies $M \sim R^3$. Since

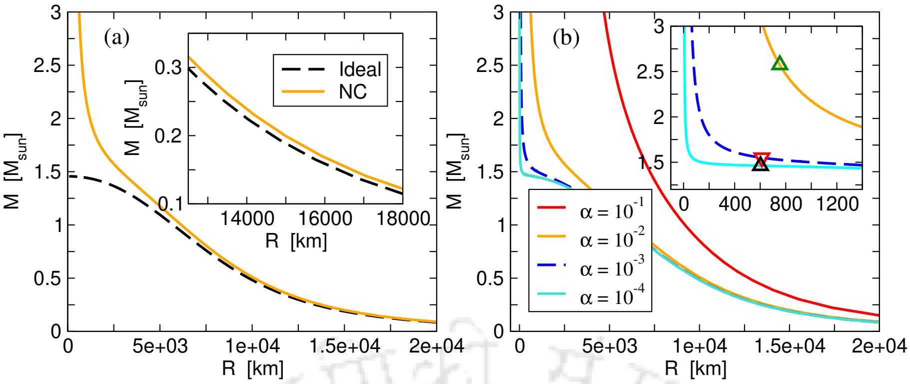

Figure 3.3: Mass-radius relations for Helium white dwarfs. (a) Solid curve (noncommutative equation of state with $\alpha = 10^{-2}$) and dot-dashed curve (ideal equation of state). The inset shows slight departure of the noncommutative curve from the ideal curve for low ξ_c. (b) Plots with noncommutaive equation of state for different values of α. The inset shows the behavior near the "turning points" where the symbols represent the neutronization threshold points: $M = 2.5734\ \mathrm{M}_\odot$, $R = 753.24$ km (up-triangle) for $\alpha = 10^{-2}$, $M = 1.5495\ \mathrm{M}_\odot$, $R = 613.28$ km (down-triangle) for $\alpha = 10^{-3}$, and $M = 1.4614\ \mathrm{M}_\odot$, $R = 602.35$ km (up-triangle) for $\alpha = 10^{-4}$. In the inset of (b), the x-axis denotes the radius R (in km) and the y-axis denotes the mass M (in $\mathrm{M}_\odot$).

a solid sphere of uniform density has its mass proportional to its volume ($\sim R^3$), this suggests an approximately constant density in most part of the star. In an alternative description ([132]) based on the generalized uncertainty principle of quantum gravity, the same features were observed although with a completely different equation of state.

3.2.2 Exact Solutions

We employ the noncommutative equation of state obtained in Section 3.1.1. Substituting Eq. (3.12), and using the definitions $m = M_0 u$ and $r = R_0 x$ in Eqs. (1.92), we obtain

$$\frac{d\xi}{dx} = -\frac{1}{f'(\xi)}\frac{u(x)}{x^2} \tag{3.31}$$

and

$$\frac{du}{dx} = \frac{1}{3}\xi^3 x^2. \tag{3.32}$$

The above two first-order differential equations are integrated simultaneously employing the fourth order Runge-Kutta method with the boundary conditions $\xi(0) = \xi_c$ and $u(0) = 0$ until the surface defined by $\xi(\tilde{R}) = 0$ is reached. The results of numerical integration are shown in Figures 3.3a and 3.3b.

In Figure 3.3a, we notice that for large central Fermi momenta ξ_c, the mass-radius relation of the noncommutative case departs considerably from the ideal (commutative) case. On the other hand, the two mass-radius curves come very close to each other (without coinciding) for lower values of the central Fermi momentum, as shown in the inset of Figure 3.3a. Our numerical data indicate an increase of about 3.2% in the mass for a white dwarf of 0.17 $\mathrm{M}_\odot$ for $\alpha = 10^{-2}$, whereas this increase is about 0.03% for $\alpha = 10^{-4}$.

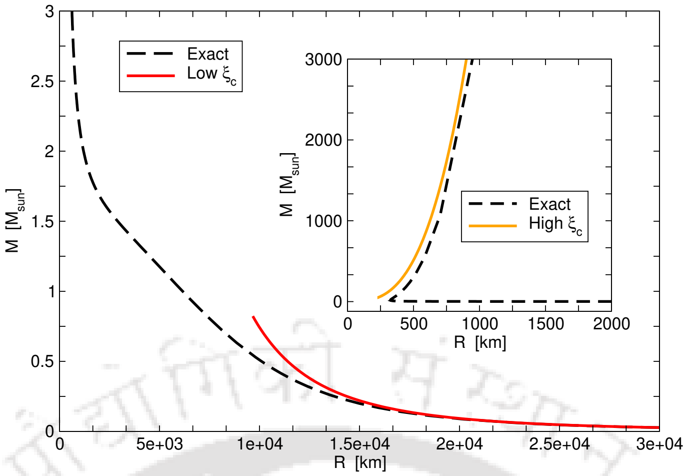

Figure 3.4: Mass-radius curves for Helium white dwarfs with the noncommutative equation of state for $\alpha = 0.01$. The dashed curve represents the exact solution. The solid curve (Low ξ_c) represents the approximate solutions (3.24) and (3.21). The inset shows slight departure of the asymptotic (High ξ_c) solutions (3.30) and (3.28) from the exact solution.

It is important to note that, for small values of the central Fermi momentum, the mass-radius relation due to the noncommutative dispersion relation does not coincide with the ideal degenerate case, which is shown in the inset of Figure 3.3a. This behavior can be seen from the asymptotically obtained mass and radius expressions given by Eqs. (3.24) and (3.21). The persistence of the deformation parameter α even in the low momentum regime exhibits this disparity on the right-hand part of the mass-radius curve. This result leads to the implication that the value of the deformation parameter λ due to the effect of quantum gravity may possibly be observed via high precision measurements on naturally existing white dwarfs.

In Figure 3.3b, we display the mass-radius relations with the noncommutative equation of state given by Eqs. (3.4) and (3.8) for different values of α, namely, $\alpha = 0.0001$, 0.001, 0.01, and 0.1. We see that, for large values of α, the mass-radius relation departs from those of smaller values. This is expected since the effect of quantum gravity is expected to be stronger for large values of α. Besides this, we also note that the Chandrasekhar limit is never attained for a nonzero value of α and large values of central Fermi momentum. One can truly obtain Chandrasekhar's limiting mass by completely neglecting the effect of quantum gravity by setting $\alpha = 0$ as shown in Figure 3.3a. Thus the noncommutative situation is quite unlike the standard theory of white dwarfs where one can reach the Chandrasekhar mass in the limit $\xi_c \to \infty$.

Although the deformation parameter α is expected to be small, we presume that the effect of Planck scale physics (quantum fluctuation of space-time) provides an effective large-distance description which would alter the dynamics of large-scale systems existing on such backgrounds. Moreover, it is difficult to tackle numerical values with high precision for very small values of α. Consequently, to assess the effect, we take $\alpha = 0.01$, the result

Table 3.1: Masses and radii of Helium white dwarfs with noncommutative equation of state for $\alpha = 0.01$. The columns marked "Asymptotic" correspond to the approximate Eqs. (3.24), (3.21), (3.30), and (3.28). The columns marked "Exact" represent the exact solutions of Eqs. (3.31) and (3.32).

Low	Asymptotic		Exact		High	Asymptotic		Exact	
ξ_c	R [km]	M [M$_\odot$]	R [km]	M [M$_\odot$]	ξ_c	R [km]	M [M$_\odot$]	R [km]	M [M$_\odot$]
0.09	33786.90	0.0193	33777.13	0.0192	95.0	414.76	292.7555	473.68	242.6950
0.10	32053.07	0.0225	32041.25	0.0225	96.0	466.15	415.6153	518.51	350.0674
0.11	30561.40	0.0260	30547.46	0.0259	97.0	541.06	649.9058	586.17	558.8757
0.12	29260.31	0.0296	29244.17	0.0295	98.0	666.07	1212.4638	702.76	1072.0714
0.13	28112.40	0.0334	28093.96	0.03321	99.0	946.79	3481.9895	972.68	3205.1357

of which is shown in Figure 3.4. For low values of ξ_c, it is observed from the right-hand part of Figure 3.4 that the mass-radius curve approaches the asymptotic behavior $M/M_\odot = 4.6475(1+2\alpha)^3(R_0/R)^3$ as obtained from Eqs. (3.24) and (3.21), which is also shown on the right hand part of the figure. As ξ_c is increased, the mass increases slowly and the radius decreases, reaching a minimum value ≈ 326 km, as can be seen in the inset of Figure 3.4. On further increasing ξ_c, the mass and radius both increase boundlessly and behave similar to the asymptotic expression $M/M_\odot = 0.04628\ (R/\alpha R_0)^3$ obtained from Eqs. (3.30) and (3.28), as shown in the inset of Figure 3.4. However for large ξ_c, the asymptotic expression does not coincide exactly with the exact solution because the exact solution has a core of approximately uniform density and the density falls off outside this core whereas the asymptotic was based on the approximate Lane-Emden equation of order zero implying a constant density throughout the star. These features are displayed in Table 3.1 where it is shown that the asymptotic values are in better agreement with the exact ones for low values of ξ_c than for high values of ξ_c.

Although these conclusions are based on not very small value of α ($= 0.01$), we expect the same qualitative behavior for lower values of α. This is in fact clear from the mass-radius curves shown in Figure 3.3b where the mass is seen to diverge for very large values of ξ_c even for the case $\alpha = 10^{-4}$. To get an approximate idea, we calculate mass and radius values from the asymptotic relations given by Eqs. (3.30) and (3.28) with central Fermi momentum close to $\xi_{\max}$. If we take $\xi_c = (1-\delta)\xi_{\max} = (1-\delta)/\alpha$, then the asymptotic values of mass and radius turn out to be $M = \{18(1-\delta)/\delta\}^{3/2}M_0/9$ and $R = \alpha\{18(1-\delta)/\delta\}^{1/2}R_0$. Table 3.2 demonstrates that the mass and radius values can be excessively large when the central Fermi momentum ξ_c approaches $\xi_{\max}$ sufficiently closely, when α is made very small.

Thus for very low values of α we do not expect the Chandrasekhar limit even when the central Fermi momentum is taken to be very large. This behavior is in contrast with the ideal (commutative) case where the radius decreases to zero and the mass increases and approaches the Chandrasekhar limit as $\xi_c \to \infty$. Thus it suggests that quantum gravity plays a significant role in determining the mass-radius relation.

Table 3.2: Asymptotic values of masses and radii of Helium white dwarfs with noncommutative equation of state following from Eqs. (3.30) and (3.28) when ξ_c is close to $\xi_{\max}$ such that $\xi_c = (1-\delta)\xi_{\max}$, with δ small.

$\alpha = 1.0 \times 10^{-05}$			$\alpha = 3.0 \times 10^{-10}$			$\alpha = 5.0 \times 10^{-22}$		
δ	R [km]	M [M$_\odot$]	δ	R [km]	M [M$_\odot$]	δ	R [km]	M [M$_\odot$]
10^{-6}	9.4×10^{01}	3.1×10^{10}	10^{-12}	2.9×10^{00}	3.1×10^{19}	10^{-30}	4.7×10^{-3}	3.1×10^{46}
10^{-12}	9.4×10^{04}	3.1×10^{19}	10^{-18}	2.9×10^{04}	3.1×10^{28}	10^{-40}	4.7×10^{02}	3.1×10^{61}
10^{-18}	9.4×10^{07}	3.1×10^{28}	10^{-26}	2.9×10^{07}	3.1×10^{40}	10^{-50}	4.7×10^{07}	3.1×10^{76}

3.3 Limitation due to Neutronization

The preceding analysis suggests that the inclusion of quantum gravity (via a noncommutative geometry) in the dispersion relation and hence into the equation of state affects the existence of the Chandrasekhar limit significantly. It predicts white dwarfs with mass exceedingly larger than the Chandrasekhar mass with large radii. This obviously is in disagreement with observed non-magnetic white dwarfs that are found only in the mass range 0.17 M$_\odot$–1.33 M$_\odot$ ([107, 129, 199–201, 219, 220]). In this section, we propose a realistic model of white dwarfs by including neutronization which can actually resolve these difficulties.

It is well-known that neutronization, or inverse β-decay (${}^A_Z X + e \longrightarrow {}^{A}_{Z-1} Y + \nu_e$), takes place at a sufficiently high density. Since the density determines the Fermi energy E_F, condition of inverse β-decay is satisfied when $E_F \geqslant \varepsilon_Z$, where ε_Z is the difference in binding energies of the parent and daughter nuclei. Following [187], we calculate the threshold density ρ_β by setting $E_F = \varepsilon_Z$ (excluding the electron rest mass) and obtain ξ_β $(= p_\beta/m_e c)$ as

$$\xi_\beta = \frac{\varepsilon_Z}{m_e c^2}\left\{1+2\frac{m_e c^2}{\varepsilon_Z}\right\}^{1/2}\left\{1+\alpha\left(1+\frac{\varepsilon_Z}{m_e c^2}\right)\right\}^{-1} \tag{3.33}$$

using the noncommutative dispersion relation given by Eq. (3.6). For Helium, $\varepsilon_Z = 20.596$ MeV, as obtained from Table II of [184].

In the noncommutative framework, the equations for hydrostatic equilibrium are expressed by Eqs. (3.31) and (3.32). Since Eq. (3.31) contains the parameter α through its dependence on the noncommutative dispersion function $f(\xi)$, their solution yields different values for different choices of α, or equivalently λ. Consequently, we solve Eqs. (3.31) and (3.32) numerically for different values of α taking the central value as the neutronization threshold ξ_β. It may be noted that ξ_β also depends on the choice of the α value through Eq. (3.33). The inset of Figure 3.3b shows the neutronization points for $\alpha = 10^{-2}$, 10^{-3}, and 10^{-4} (triangle, square, and circle, respectively).

Table 3.3 gives the values of ξ_β corresponding to different deceasing values of α, or λ. It is clear that it is not possible to have an exceedingly large central value ξ_c corresponding to these values of α due to the neutronization threshold. The mass and radius of white dwarfs obtained via exact solution of Eqs. (3.31) and (3.32) are shown in the last two columns of Table 3.3. We note that both mass and radius take finite values. For large values of α, such as 10^{-2} (and higher), the mass increase to values higher than the Chandrasekhar mass. However, as the α value is decreased to 10^{-3}, the mass is 1.5495 $\mathrm{M}_\odot$, and the radius 613.2817 km. On gradually decreasing α, we see that the mass appears to approach the limits 1.4518 $\mathrm{M}_\odot$ and the radius 601.1821 km, which are obtained for the case $\alpha = 10^{-7}$. This is not a very low value for α, because if we speculate that $\lambda \sim 1/M_P c^2$, where $M_P = \sqrt{\hbar c/G}$ is the Planck mass, $\alpha = \lambda m_e c^2 \sim m_e/M_P \sim 10^{-23}$. We see that the $\alpha = 10^{-7}$ values are close to the ideal ($\alpha = 0$) values of 1.4518 $\mathrm{M}_\odot$ and the radius 601.18 km for $\xi_\beta = 41.2932$. However when we disregard the neutronization threshold for the ideal case and seek solutions for very large value of ξ_c (beyond ξ_β) we obtain the Chandrasekhar limiting mass as 1.4562 $\mathrm{M}_\odot$ with zero radius. The slight difference from the quoted value of 1.44 $\mathrm{M}_\odot$ is because of a slightly different numerical accuracy in our computation.

An estimate of the quantum gravitational parameter $E_{\mathrm{QG}} \sim \lambda^{-1}$ (defined in Section 3.4) was obtained from the observed time-delay in the arrival of TeV-scale photons from γ-ray flares in a distant galaxy, the AGN Markarian 421. This suggested a lower bound of $E_{\mathrm{QG}} \sim 10^{16}$ GeV (or $\lambda \sim 10^{-20}$ MeV^{-1}) ([30]). On the other hand, a value of $E_{\mathrm{QG}} \sim 10^{18}$ GeV (or $\lambda \sim 10^{-21}$ MeV^{-1}), was suggested from the compatibility between data obtained from AGN Markarian 501 and PKS 2155-304 ([68]). This latter value of λ gives $\alpha \sim 5 \times 10^{-22}$, suggesting the limit $\alpha \ll 10^{-7}$.

We see from Table 3.3 that $\alpha \ll \xi_\beta$ for low values of α and we thus make use of this limit to solve Eqs. (3.31) and (3.32) approximately. Eq. (3.11) gives $f'(\xi) \approx 1$ for extremely low values of α, so that Eq. (3.18) approximates to

$$\frac{1}{\eta^2}\frac{d}{d\eta}\left(\eta^2\frac{d\theta}{d\eta}\right) + \theta^3 = 0, \tag{3.34}$$

where $\theta = \xi/\xi_c$ and $\eta = \xi_c\ x/\sqrt{3}$ is a dimensionless radius. This equation is solved with boundary conditions $\theta(0) = 1$ and $\theta(\eta_R) = 0$, where η_R corresponds to the radius of the white dwarf. Eq. (3.34) is the Lane-Emden equation of index 3, whose numerical solution is given in [226].

From Eq. (3.22) we obtain the dimensionless mass and radius and using Eq. (3.33) in the limit $\alpha \ll 10^{-7}$, we obtain the dimensionless radius of the white dwarf as

$$\tilde{M}_\beta = \sqrt{3}\left(-\eta^2\frac{d\theta}{d\eta}\right)_{\eta=\eta_R} \quad \text{and} \quad \tilde{R}_\beta = \frac{m_e c^2}{\varepsilon_Z}\sqrt{\frac{3}{1+\frac{m_e c^2}{\varepsilon_Z}}}\,\eta_R \tag{3.35}$$

giving the mass as $M_\beta = M_0\tilde{M}_\beta = 1.4563$ $\mathrm{M}_\odot$ and the radius as $R_\beta = R_0\tilde{R}_\beta = 648.809$ km, using $\eta_R = 6.89685$ and $-\eta^2\left(d\theta/d\eta\right)_{\eta=\eta_R} = 2.01824$ for $n = 3$. These mass and radius values, being approximate, do not coincide with the numerical solutions given in the last few rows of Table 3.3. We also note that for values of ξ_c lower than the ξ_β, lower values of masses with higher values of radii are possible solutions (for any value of α) as shown in the right-hand part of Figure 3.3b.

Table 3.3: Masses and radii of Helium white dwarfs with the noncommutative equation of state for different values of α when the central Fermi momentum is taken to be the neutronization threshold ξ_β, Eq. (3.33), the corresponding neutronization density ρ_β is given by Eq. (3.4). The displayed results represent exact solutions of the equation of hydrostatic equilibrium, Eqs. (3.31) and (3.32).

α	λ [MeV^{-1}]	ξ_β	ρ_β [g/cm^3]	R_β [km]	M_β [M$_\odot$]
2.0×10^{-2}	3.91×10^{-2}	22.613	2.252×10^{10}	948.55	3.9954
1.0×10^{-2}	1.96×10^{-2}	29.223	4.861×10^{10}	753.24	2.5736
1.0×10^{-3}	1.96×10^{-3}	39.655	1.214×10^{11}	613.28	1.5495
1.0×10^{-4}	1.96×10^{-4}	41.123	1.355×10^{11}	602.35	1.4614
1.0×10^{-5}	1.96×10^{-5}	41.276	1.370×10^{11}	601.30	1.4527
1.0×10^{-7}	1.96×10^{-7}	41.293	1.371×10^{11}	601.18	1.4518

Table 3.4: Masses and radii of Carbon and Oxygen white dwarfs with the noncommutative equation of state for different values of α when the central Fermi momentum is taken to be the neutronization threshold ξ_β, Eq. (3.33), the corresponding neutronization density ρ_β is given by Eq. (3.4). The displayed values of masses and radii represent exact solutions of the equation of hydrostatic equilibrium, Eqs. (3.31) and (3.32).

	${}^{12}_{6}\mathbf{C}$, $\varepsilon_Z = 13.370$ MeV				${}^{16}_{8}\mathbf{O}$, $\varepsilon_Z = 10.419$ MeV			
α	ξ_β	ρ_β (g/cm^3)	R_β (km)	M_β (M$_\odot$)	ξ_β	ρ_β (g/cm^3)	R_β (km)	M_β (M$_\odot$)
2.0×10^{-2}	17.590	1.060×10^{10}	1206.20	2.9795	14.964	6.527×10^{09}	1406.70	2.5994
1.0×10^{-2}	21.347	1.895×10^{10}	1028.13	2.1463	17.601	1.062×10^{10}	1236.10	1.9783
1.0×10^{-3}	26.428	3.595×10^{10}	895.22	1.5100	20.919	1.783×10^{10}	1105.41	1.4903
1.0×10^{-4}	27.072	3.865×10^{10}	883.98	1.4525	21.320	1.888×10^{10}	1093.92	1.4453
1.0×10^{-5}	27.139	3.893×10^{10}	882.89	1.4468	21.361	1.898×10^{10}	1092.79	1.4409
1.0×10^{-7}	27.146	3.896×10^{10}	882.77	1.4462	21.366	1.899×10^{10}	1092.67	1.4404

As noted earlier in Table 3.2, the noncommutative equation of state allows for extremely high values of mass and radius if the effect of neutronization is neglected so that the central Fermi momentum could approach $\xi_{\text{max}} = 1/\alpha$. However, due to the constraint of neutronization, the ξ_c value cannot approach a value higher than ξ_β. Together with the neutronization constraint on ξ_c, when we take $\alpha \ll 10^{-7}$ as suggested by observations from γ-ray bursts, the mass and radius values approach finite values as we see in Tables 3.3 and 3.4.

3.4 Discussion and Conclusion

The effect of quantum gravity, although very small, is inevitably present everywhere. We thus expect that it will modify the stability of astrophysical objects such as white dwarfs. In particular, it is already well-known that the noncommutative formulation of quantum gravity modifies the dispersion relation of any particle. To study the effect of such modification on the stability of white dwarfs, we employed a modified dispersion relation of the form $E_{\mathbf{p}}^2 = \mathbf{p}^2c^2(1+\lambda E_{\mathbf{p}})^2 + m^2c^4$ and observed that the equation of state of a degenerate electron gas undergoes a substantial modification as a result of the emergence of a cutoff momentum $p_{\rm max} = 1/\lambda c$ inherent in the dispersion relation. As a consequence, the possible values of masses and radii of white dwarfs change from the ideal case.

We have analyzed the situation in two different ways in the framework of Newtonian gravity. First, we employed the equation of hydrostatic equilibrium to obtain an approximation in the limit of low central Fermi momentum resulting in the Lane-Emden equation of index 3/2. On analyzing the solutions we found that both the mass and radius are affected by the parameter λ indicating the persistence of the effect of noncommutative equation of state even for low mass white dwarfs. Next, we analyzed the problem when the central Fermi momentum $p_{\rm Fc}$ approaches $p_{\rm max} = 1/\lambda c$. On working out the asymptotics, the Lane-Emden equation of index zero is obtained that clearly indicated that both mass and radius would approach infinity when the central Fermi momentum approaches $p_{\rm max} = 1/\lambda c$.

Finally, we solved the equations of hydrostatic equilibrium exactly by numerical means with the noncommutative equation of state without making any approximations to the modified dispersion relation. We found that the modified mass-radius curve did not coincide with the ideal degenerate curve even in the low central Fermi momentum region. This can be associated with the previous asymptotic solution in the low momentum limit where the masses and radii were found to have small departures in terms of the noncommutative parameter λ. On the other hand, we observed a strong departure from the ideal mass-radius curve for high values of the central Fermi momentum even for a low value such as $\alpha = \lambda m_e c^2 = 10^{-4}$. This trend is expected to be qualitatively the same for values of α lower that 10^{-4}. Since it is difficult to handle very low values of α numerically, we assessed the situation for a few higher values of α such as 10^{-1}, 10^{-2}, 10^{-3}, and 10^{-4}. For all these cases, we found masses excessively larger than the Chandrasekhar bound. The approach to high mass values is delayed (with respect to increase in central Fermi momentum) when the α value is decreased. It was clear that even for lower values of α, the mass would approach very large values higher than the Chandrasekhar limit with large values of radii. This was confirmed from our asymptotic analysis for any low magnitude of α when ξ_c approaches $\xi_{\rm max}$.

The above situation is remarkably different from observations on non-magnetic white dwarfs because they are found in the mass range from 0.17 $M_\odot$ ([107]) to 1.33 $M_\odot$ ([101, 129, 219, 220]) with radii ranging from 0.0153 $R_\odot$ (10644 km) to 0.0071 $R_\odot$ (4939 km) ([199–201]). This disagreement can be reconciled by noting that the central Fermi momentum of white dwarfs cannot take arbitrarily high values as it is limited by the neutronization threshold. In addition, the quantum gravity parameter λ is also not large. Consequently we solved the equations of hydrostatic equilibrium with a few values of α

ranging from 10^{-2} to 10^{-7} with the central Fermi momentum taken as the neutronization threshold. Although the case $\alpha = 10^{-2}$ yielded a mass as large as 2.5736 $M_{\odot}$ for Helium, as the α value is decreased to 10^{-5}, we found the mass as 1.4527 $M_{\odot}$ with a radius 601.29 km. On further deceasing the α value these values did not change appreciably.

The parameter λ may be inversely proportional to the quantum gravity parameter E_{QG} that occurs in the dispersion relation $c^2p^2 = E^2[1 + \sigma E/E_{QG} + \ldots]$ for propagation of photons through vacuum. In particular, [68] predicted the time delay in receiving γ-ray photons from distant active galaxies that suggested the value $E_{QG} \sim 10^{18}$ GeV. This value of E_{QG} translates to $\alpha \sim 5 \times 10^{-22}$ if we assume $\lambda \sim E_{QG}^{-1}$. We thus expect that the α value to be lower than 10^{-5}. In our numerical calculation, when we decreased the α value from 10^{-4} to 10^{-7}, we saw that the mass and radius approach the limiting values of 1.45 $M_{\odot}$ and 601 km (for Helium) at the neutronization threshold. For values of the central Fermi momentum lower than the neutronization threshold, we obtained lower values of masses with larger values of radii.

It may however be noted that the above observations are for photons from γ-ray bursts propagating through vacuum. Equivalent data for massive particles, such as electrons, do not exist in the literature and it is difficult to guess the value of α for electrons. Consequently, we have shown the neutronization threshold values for the masses and radii of some white dwarfs ($^{4}_{2}\mathbf{He}$, $^{12}_{6}\mathbf{C}$, and $^{16}_{8}\mathbf{O}$) for values of α ranging from 2.0×10^{-2} to 1.0×10^{-7} in Tables 3.3 and 3.4. We note that the neutronization threshold value for a pure $^{16}_{8}\mathbf{O}$ white dwarf should be the same as that of a carbon-oxygen white dwarf because the core of the latter is expected to be purely $^{16}_{8}\mathbf{O}$ and neutronization is expected to begin at the center ([42]). The top row of Table 3.4 for $\alpha = 2.0 \times 10^{-2}$ indicates that a carbon-oxygen white dwarf would have a critical mass of 2.5994 $M_{\odot}$. There have been a few observations of over-luminous type Ia SNe (SN 2003fg, SN 2006gz, SN 2007if, SN 2009dc) ([89, 93, 188, 203, 230]) that produced a high amount of $^{56}\mathbf{Ni}$ ranging from 1.2 $M_{\odot}$ to 1.7 $M_{\odot}$ suggesting their progenitors to be super-Chandrasekhar white dwarfs ranging from 2.2 $M_{\odot}$ to 2.8 $M_{\odot}$.

However, [89] argued that the type Ia SN 2006gz was a double degenerate (DD) merger of two sub-Chandrasekhar white dwarfs as supported by the unusually low and slowly declining Silicon velocity which is also predicted by DD models. [203] speculated that SN 2009dc was very likely due to the merger of two white dwarfs as supported by simulations. [55] considered a single-degenerate white dwarf supported by differential rotation accreting at a low rate from a normal companion. With an initial 1.2 $M_{\odot}$, they found the possibility of having a super-Chandrasekhar SNe Ia event. However, white dwarfs with mass exceeding 1.7 $M_{\odot}$ was predicted to be not likely. [59] indicated that the presence of a strong magnetic field ($\sim 10^{15}$ Gauss) in a white dwarf can support a mass of 2.3–2.6 $M_{\odot}$ due to the role of Landau levels. On the other hand, pointing to various disagreements among the existing SNe Ia models, [218] argued that SNe Ia events generally happen due to the merger of two carbon-oxygen white dwarfs.

Thus it appears that the super-Chandrasekhar scenario is not possible in the case of a normal white dwarf (without rotation or magnetic field). We are thus led to infer that it is neutronization that would constrain white dwarfs within the Chandrasekhar limit. This implies that α should be very small ($\sim 10^{-7}$ or lower) so that a mass close to the Chandrasekhar limit is obtained as a consequence of the neutronization threshold. If this was not the case, that is, in the absence of neutronization, the modified dispersion relation would support excessively high mass values (beyond the Chandrasekhar mass) even for very low values of α such as 10^{-7} or lower. It is only when we impose the condition of neutronization (on the top of the effect of quantum gravity) that we get mass limits close to the Chandrasekhar mass.

We further note that since the effect of quantum gravity must be inevitably present, we should consider it in the analysis. There are two simple ways to take the effect of quantum gravity into account. One way is to take this effect through noncommutativity that modifies the dispersion relation as presented in this Chaper. Another way is to take this effect through a generalized uncertainty relation as discussed earlier in [132]. Based on these two differing approaches, we may state that whichever way we attempt to include the effect of quantum gravity in the description, we find that white dwarfs with excessively high masses (beyond the Chandrasekhar mass) would be supported although the quantum gravity parameter is taken to be extremely small. In both approaches, we find that it is only when we impose the condition of neutronization that we obtain mass limits close to the Chandrasekhar mass. Thus, in realistic situations, such mass limits exist because of the neutronization threshold that destabilizes the white dwarf due to the onset of inverse β-decay.

Since the above discussion applies to white dwarfs when the equilibrium is governed by Newtonian gravity, the situation is expected to alter when general relativity is employed for the hydrostatic equilibrium. It is already known that the gravitational instability sets in before the neutronization instability for ${}^{4}_{2}\mathbf{He}$ and ${}^{12}_{6}\mathbf{C}$ white dwarfs, whereas, for ${}^{16}_{8}\mathbf{O}$ white dwarfs, it is the instability due to neutronization that sets in before the gravitational instability ([196]). However, in the present case of noncommutative equation of state, the neutronization threshold depends on the noncommutative parameter α according to Eq. (3.33). Consequently, it would be interesting to analyze the problem in the general relativistic framework to see to what extent the above situation changes in determining the competition between the two kinds of instabilities. We leave this motivation as an interesting research problem for the future.

Chapter 4

Relativistic white dwarfs with generalized uncertainty EoS

.

As described in Chapter 2, various recent theoretical investigations suggest that gravitational collapse of white dwarfs is withheld for arbitrarily high masses beyond Chandrasekhar's limit if the equation of state incorporates the effect of quantum gravity via the generalized uncertainty principle (GUP). There have been a few attempts to restore the Chandrasekhar limit but they are found to be inadequate. In this Chapter, we rigorously resolve this problem by analyzing the dynamical instability in general relativity. We confirm the existence of Chandrasekhar's limit as well as stable mass-radius curves that behave consistently with astronomical observations. Moreover, this stability analysis suggests gravitational collapse beyond the Chandrasekhar limit signifying the possibility of compact objects denser than white dwarfs.

The existence of Chandrasekhar's limit has played various decisive roles in astronomical observations for many decades. It is well-known that the existence of Chandrasekhar's limit results in Type Ia supernovae (SN Ia) from the explosion of carbon-oxygen (degenerate core) white dwarfs due to accretion from a companion star. Such supernovae have well-defined light-curves with nearly the same peak brightness and their maximum brightnesses have a definite correlation with their light curve decline rates. This property makes them standard candles in astronomy, facilitating measurements on high-redshift Type Ia supernovae, and revealing the accelerated expansion of the Universe [176, 181]. Importantly, this ground-breaking finding is based on the existence of Chandrasekhar's limit.

However, it has recently been argued that the generalized uncertainty principle (GUP) removes the Chandrasekhar limit [149, 156, 157, 180]. This is due to the fact that the

---

The content of this chapter is published: A. Mathew, M. K. Nandy, R. Soc. open sci. **8**, 210301 (2021) inclusion of GUP via the equation of state gives white dwarfs of excessively high masses, irrespective of the smallness of the parameter β. In other words, the mass is no longer bound from above, so that

$$M_{\rm GUP} = 12\sqrt{2}\left(\frac{\hbar c}{G}\right)^{3/2}\frac{1}{(\mu_e m_u)^2}\,(\beta p_{\rm Fc}^2)^{3/4}, \tag{4.1}$$

in the high momentum limit. This implies that the GUP-enhanced equation of state prevents gravitational collapse and halts the formation of compact astrophysical objects denser than white dwarfs. This prediction contradicts astronomical observations that confirm the existence of pulsars [57, 88, 142] and black holes [40, 122, 223]. Moreover, it has been observed that the masses of white dwarfs fall well within the Chandrasekhar limit [107, 199, 201],

$$M_{\rm Ch} = 2.0182\frac{\sqrt{3\pi}}{2}\left(\frac{\hbar c}{G}\right)^{3/2}\frac{1}{(\mu_e m_u)^2} \approx \frac{5.76}{\mu_e^2}M_\odot, \tag{4.2}$$

apart from the super-Chandrasekhar white dwarfs, that may well be double-degenerate mergers [89, 203, 218].

A solution to the problem was proposed in Chapter 2 by imposing a cutoff in the Fermi momentum at the neutronization threshold [132]. Since the process of neutronization is not built into the dynamical equations, and it is imposed *by hand*, this solution is not a dynamical consequence of the theory. A more satisfying solution ought to be based on a theory where a collapse happens as a dynamical consequence of the underlying equations of the theory.

It is important to note that there exists sign ambiguity in the quantum gravity parameter β and it appears to be related with the nature of physical system under consideration. In particular, the sign of β plays a very important role in determining the stellar structure of white dwarfs. The excessive mass of white dwarfs results when the GUP parameter β is considered to be positive. The minimum uncertainty in length in one of the the GUP scenarios is given by $\Delta x_{\rm min} = \hbar\sqrt{\beta}\sqrt{1+\beta\langle\mathbf{p}\rangle^2}$ [100]. Although this implies that β is a positive quantity due to $\Delta x_{\rm min}$ being real valued, there have been various other scenarios [98, 190, 191] which suggest that β may as well be a negative quantity.

For example, a comparison between GUP corrected black hole temperature with that following from a deformed Schwarzschild metric suggested a negative value of the GUP parameter β [190, 191]. The same suggestion was made [98] by a comparison between the non-commutative space-time correction to the black hole temperature with the GUP corrected black hole temperature.

However, the sign ambiguity of the GUP parameter β is still an unresolved problem. For example, on the basis of horizon quantum mechanics [48], it was suggested that β should be negative. On the other hand a corpuscular scenario of gravity, where a black hole is pictured as a Bose-Einstein condensate of gravitons, led to a positive value of β [39]. It may also be noted that a lattice model with Planckian lattice constant resulted in a negative sign for the GUP parameter β [97]. On the other hand, a string theoretic consideration with a length scale ℓ_* leads to an uncertainty in position of the order of $\ell_*^2 \Delta p/\hbar$ [8, 112], implying β is positive, which consistent with the thought experiment described earlier. In addition, measurement of the radius of an extremal black hole by dropping a photon into it and by observing the remitted photon gives a similar (positive) estimate for the uncertainty [74, 123, 124].

Importantly, it has been shown that a negative GUP parameter β gives rise to an unphysical mass-radius relation for white dwarfs [156]. Consequently, we include the effect of quantum gravity on white dwarfs via the GUP with a positive sign for β. However, this poses the well-known problem that the Chandrasekhar limit ceases to exist. It was in fact suggested in Ref. [156] that a consistent solution of the problem could be obtained within the framework of general relativity. Since white dwarfs respect the Chandrasekhar limit, it is extremely important to solve this problem posed by GUP. A satisfactory model of white dwarfs ought to be based on a rigorous treatment of the gravitational field so that the gravitational collapse for a sufficiently massive white dwarf is well-represented.

In this Chapter, we present a complete and rigorous approach to resolve this problem. We take the framework of general relativity (GR) and calculate the stellar structure of white dwarfs for positive GUP parameter β. We carry out a dynamical stability analysis of the equilibrium configurations so that the maximal stable configuration is identified. In this framework we rigorously confirm the existence of Chandrasekhar limit within the electroweak upper bound [58] of the GUP parameter β. More precisely, we find that the Chandrasekhar limit robustly exists even when the value of β is made four orders higher than the electroweak bound.

The remainder of the Chapter is organized as follows. In Section 4.1 we present the fermionic equation of state following from GUP. In Section 4.2 we give details of the mass-radius relation in the framework of general relativity. Section 4.3 presents the dynamical stability analysis confirming the Chandrasekhar limit. A discussion and conclusion is presented in Section 4.4.

4.1 Generalised uncertainty principle and fermionic equation of state

The inclusion of quantum gravitational fluctuations via the generalized uncertainty principle in the equation of state of a degenerate electron gas was studied earlier in different contexts [132, 148, 154, 224, 234]. In this section, we present the number density n, pressure P and energy density ε of the electron degenerate gas. With the modified phase volume, we employ the standard method of statistical mechanics to the relativistic electron gas assuming $T = 0$, yielding

$$n = \frac{8\pi}{h^3} \int_0^{p_F} \frac{p^2 dp}{(1+\beta p^2)^3}, \tag{4.3}$$

and

$$P = \frac{8\pi}{h^3} \int_0^{p_F} \frac{p^2 dp}{(1+\beta p^2)^3} (E_F - E_{\mathbf{p}}), \tag{4.4}$$

leading to

$$n(\xi) = \frac{K}{m_e c^2} \tilde{n}(\xi), \quad \text{and} \quad P(\xi) = K\tilde{P}(\xi), \tag{4.5}$$

where

$$\tilde{n}(\xi) = \frac{1}{\alpha^3} \left[\tan^{-1}(\alpha\xi) - \frac{\alpha\xi(1-\alpha^2\xi^2)}{(1+\alpha^2\xi^2)^2} \right] \tag{4.6}$$

and

$$\tilde{P}(\xi) = \frac{\sqrt{1+\xi^2}}{\alpha^3} \left\{ \tan^{-1}(\alpha\xi) - \frac{\alpha\xi}{(1-\alpha^2)(1+\alpha^2\xi^2)} \right\} + \frac{1}{(1-\alpha^2)^{3/2}} \tanh^{-1} \frac{\xi\sqrt{1-\alpha^2}}{\sqrt{1+\xi^2}} \tag{4.7}$$

with $\xi = p_F/m_e c$, p_F being the Fermi momentum, $\alpha^2 = \beta m_e^2 c^2 = \beta_0 m_e^2/M_P^2$ ($M_P = \sqrt{\hbar c/G} = 2.1765 \times 10^{-5}$ g) and $K = \pi m_e^4 c^5/h^3$.

The internal kinetic energy $\varepsilon_{\text{int}}(\xi)$ of the electron gas for $T = 0$ is given by

$$\varepsilon_{\text{int}}(\xi) = \frac{8\pi}{h^3} \int_0^{p_F} \frac{p^2 dp}{(1+\beta p^2)^3} \left\{ \sqrt{p^2c^2 + m_e^2 c^4} - m_e c^2 \right\}. \tag{4.8}$$

In the dimensionless quantities, the above equation becomes

$$\varepsilon_{\text{int}}(\xi) = \frac{8\pi m_e^4 c^5}{h^3} \int_0^{\xi} \frac{\xi'^2 d\xi'}{(1+\alpha^2\xi'^2)^3} \left\{ \sqrt{\xi'^2+1} - 1 \right\}, \tag{4.9}$$

leading to

$$\varepsilon_{\text{int}}(\xi) = \left\{ \frac{\xi\sqrt{1+\xi^2}[1+(2-\alpha^2)\xi^2]}{(1-\alpha^2)(1+\alpha^2\xi^2)^2} - \frac{1}{(1-\alpha^2)^{3/2}} \tanh^{-1} \frac{\xi\sqrt{1-\alpha^2}}{\sqrt{1+\xi^2}} \right\} - \tilde{n}. \tag{4.10}$$

The rest mass density $\rho_0(\xi) = m_u \mu_e n(\xi)$ is related to the energy density as $\varepsilon(\xi) = \rho_0(\xi)c^2 + \varepsilon_{\text{int}}(\xi)$, where $m_u = 1.6605 \times 10^{-24}$ g is the atomic mass unit and $\mu_e = A/Z$, with A the mass number and Z the atomic number. Thus the energy density

$$\varepsilon(\xi) = \frac{K}{q} \tilde{\varepsilon}(\xi), \tag{4.11}$$

where $q = m_e/\mu_e m_u$ and the dimensionless energy density $\tilde{\varepsilon}(\xi)$ is given by

$$\tilde{\varepsilon}(\xi) = (1-q)\tilde{n} + q\left\{\frac{\xi\sqrt{1+\xi^2}[1+(2-\alpha^2)\xi^2]}{(1-\alpha^2)(1+\alpha^2\xi^2)^2} - \frac{1}{(1-\alpha^2)^{3/2}}\tanh^{-1}\frac{\xi\sqrt{1-\alpha^2}}{\sqrt{1+\xi^2}}\right\}, \quad (4.12)$$

In the high Fermi momentum limit, that is $\xi \to \infty$,

$$\tilde{n}(\xi) \longrightarrow \frac{\pi}{2\alpha^3} = k_1, \quad (4.13)$$

$$\tilde{P}(\xi) \longrightarrow k_1\xi - k_2 \quad (4.14)$$

and

$$\tilde{\varepsilon} \longrightarrow k_1(1-q) + qk_2 = 3\kappa \quad (4.15)$$

with

$$k_2 = \frac{1}{\alpha^4}\frac{(2-\alpha^2)}{(1-\alpha^2)} - \frac{\tanh^{-1}\sqrt{1-\alpha^2}}{(1-\alpha^2)^{3/2}}. \quad (4.16)$$

where k_1, k_2 and κ are constants. These high momentum limits are drastically different from the ideal case due to the role of the generalized uncertainty principle.

Moreover, the relativistic adiabatic index γ for the degenerate electron gas is obtained as

$$\gamma = \frac{\varepsilon + P}{P}\left(\frac{dP}{d\varepsilon}\right)_s = \frac{1}{8}\left(\frac{\tilde{n}^2}{\tilde{P}}\right)\frac{(1+\alpha^2\xi^2)^3}{\xi\sqrt{1+\xi^2}}, \quad (4.17)$$

so that $\gamma \to \frac{\pi}{16}\alpha^3$ in the limit $\xi \to \infty$, unlike the ideal case ($\gamma_{\text{ideal}} = \frac{4}{3}$).

4.2 Mass-radius relation

We study mass-radius relation of the equilibrium configurations in the framework of general relativity in this section. For the matter interior to the star, the equilibrium values of the pressure $P(r)$ and energy density $\varepsilon(r)$ are therefore determined by the Tolman-Oppenheimer-Volkoff (TOV) equations [159, 217], gives by equations (1.91)

It may be observed that the equation of state is in a parametric form where the Fermi momentum p_F of the electron degenerate gas occurs in the expressions for pressure and energy density given by equations (4.5), (4.7), (4.11) and (4.12). We express the TOV equations (1.91) in terms of the dimensionless quantities $\xi = p_F/m_e c$, $v = m/m_0$ and $\eta = r/r_0$, where $m_0 = (qc^2)^2/G^{3/2}\sqrt{4\pi K}$ and $r_0 = (qc^2)/\sqrt{4\pi GK}$. Thus we obtain

$$\frac{d\xi}{d\eta} = -\frac{1}{\eta}\frac{\sqrt{1+\xi^2}}{\xi}\left(1 - q + q\sqrt{1+\xi^2}\right)\frac{v + q\tilde{P}\eta^3}{\eta - 2qv} \quad (4.18)$$

and

$$\frac{dv}{d\eta} = \tilde{\varepsilon}\eta^2. \quad (4.19)$$

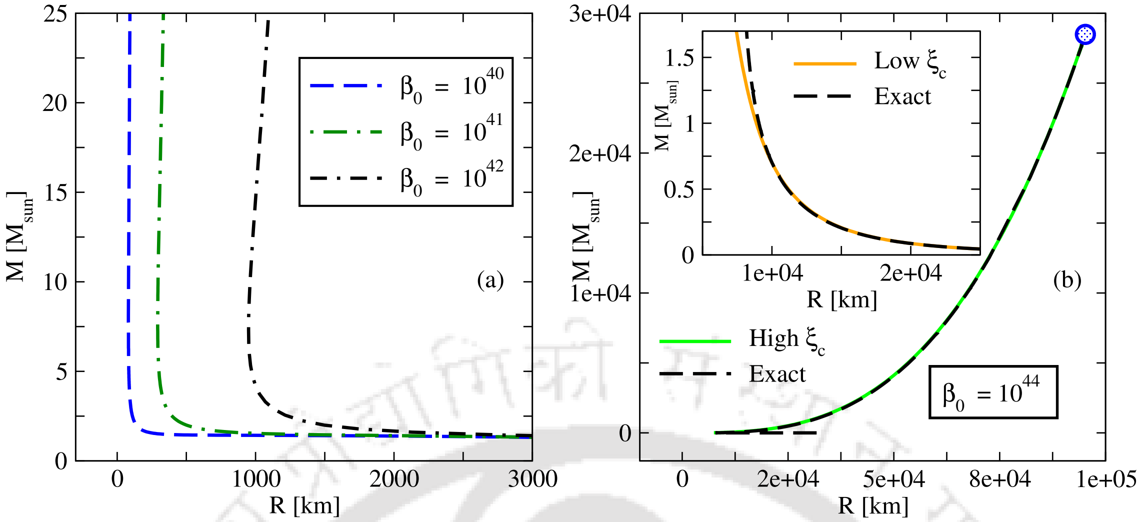

Figure 4.1: (a) Exact mass-radius relations for white dwarfs with GUP equation of state for $\beta_0 = 10^{42}$, 10^{41} and 10^{40}. (b) Exact mass-radius relations (dashed curves) for $\beta_0 = 10^{44}$ in comparison with the corresponding analytically obtained asymptotic solution (smooth curve) given by Eqs. (4.24) and (4.27) in the high ξ_c limit. The open circle represents the maximum values of mass $M_{\max}$ and radius $R_{\max}$. The lower left region of the exact mass-radius curve is blown up (dashed curve) in the inset where it is compared with the analytically obtained asymptotic solution in the low ξ_c limit (smooth curve).

4.2.1 Asymptotic solutions

For a preliminary idea about the mass-radius relation, we study the asymptotic solutions of the TOV equations in the low and high Fermi momentum limits.

4.2.1.1 Low momentum limit, $\xi \to 0$

For low values of ξ, it can be shown that equations (4.18) and (4.19) reduce to

$$\xi \frac{d\xi}{d\eta} = -\frac{v}{\eta^2} \tag{4.20}$$

and

$$\frac{dv}{d\eta} = \frac{8}{3}\xi^3\eta^2. \tag{4.21}$$

which can be combined to form a second order differential equation, given by

$$\frac{3}{16}\frac{1}{\eta^2}\frac{d}{d\eta}\left(\eta^2\frac{d\xi^2}{d\eta}\right) + \xi^3 = 0. \tag{4.22}$$

Defining $\xi^2(\eta)/\xi_c^2$ as $\theta(\zeta)$, with ξ_c the central dimensionless Fermi momentum, and ζ is a new dimensionless coordinate $\zeta = \sqrt{16\xi_c/3}\;\eta$, we reduce the above equation to

$$\frac{1}{\zeta^2}\frac{d}{d\zeta}\left(\zeta^2\frac{d\theta}{d\zeta}\right) + \theta^{3/2} = 0, \tag{4.23}$$

which is the Lane-Emden equation of index 3/2. Numerical solution for this differential equation is given in Weinberg [226]. For the boundary conditions $\theta(0) = 1$ and $\theta'(0) = 0$, one can immediately obtain the radius of the white dwarf as

$$R = \sqrt{\frac{3}{16\xi_c}}\, r_0 \zeta_R \tag{4.24}$$

where $\zeta_R = 3.65375$ is the first zero of the Lane-Emden function $\theta(\zeta)$ of index 3/2.

Similarly the asymptotic behavior of the mass of the white dwarf can be obtained from the integral expression dm/dr in Eq. (1.91), namely,

$$M = \frac{4\pi}{c^2} \int_0^R \varepsilon(r) r^2 dr = \frac{4\pi}{c^2} \frac{A}{q} \frac{8}{3} \int_0^R \xi^3 r^2 dr. \tag{4.25}$$

We rewrite this equation in the new dimensionless variable ζ, yielding

$$M = \sqrt{\frac{3\xi_c^3}{64}}\, m_0 \int_0^{\zeta_R} \theta^{3/2} \zeta^2 d\zeta, \tag{4.26}$$

thus obtaining the mass of the white dwarf as

$$M = -\sqrt{\frac{3\xi_c^3}{64}}\, m_0 \zeta_R^2 \left(\frac{d\theta}{d\zeta}\right)_{\zeta=\zeta_R} \tag{4.27}$$

The value of $\left(-\zeta^2 d\theta/d\zeta\right)_{\zeta=\zeta_R}$ is 2.71406 [226].

Thus the above asymptotic analysis predicts that $R \sim \xi_c^{-1/2}$ and $M \sim \xi_c^{3/2}$, giving the mass-radius relation $R \sim M^{-1/3}$, implying that the radius decreases as the mass increases.

It is important to note that, these expressions of mass and radius are independent of the GUP parameter α (or, equivalently β). Thus for low mass white dwarfs the GUP has insignificant effect on the mass-radius relation and we expect that the mass-radius curve would coincide with that of Chandrasekhar's for low values of central Fermi momentum ξ_c (or, equivalently low central density ρ_c).

4.2.1.2 High momentum limit, $\xi \to \infty$

For high values of ξ, the TOV equations reduce to

$$\frac{d\xi}{d\eta} = -\frac{k_1}{3} \frac{\eta}{1 - 2q\kappa\eta^2} \left(1 - q + q\xi\right) \left(1 - q + 3q\xi - 2q\frac{k_2}{k_1}\right) \tag{4.28}$$

and

$$v = \kappa\eta^3. \tag{4.29}$$

Since typically $\alpha \sim 0.1$, the ratio $k_2/k_1 \sim (4/\pi\alpha)$, hence the last term in the second bracket can be ignored if $\alpha\xi \gg 8/3\pi$. Since we are looking for the solutions of $\xi \to \infty$, we shall ignore this term, obtaining

$$\frac{d\xi}{d\eta} = -\frac{k_1}{3}\frac{\eta}{1-2q\kappa\eta^2}\left(1+q\xi\right)\left(1+3q\xi\right), \tag{4.30}$$

where we have used the fact that $q \sim 10^{-4}$. The solution of the above equation is given by

$$\frac{1+3q\xi}{1+q\xi} = \left(1-2q\kappa\eta^2\right)^{-k_1/6\kappa} + \text{const.} \tag{4.31}$$

Using the boundary conditions we can immediately obtain the integration constant and hence the radius of the star as

$$\eta_R = \frac{1}{\sqrt{2q\kappa}}\left\{1-\left(\frac{1+q\xi_c}{1+3q\xi_c}\right)^{6\kappa/k_1}\right\}^{1/2}. \tag{4.32}$$

Since $6\kappa/k_1 \approx 2$, we have

$$\eta_R = \frac{1}{\sqrt{2q\kappa}}\left\{1-\left(\frac{1+q\xi_c}{1+3q\xi_c}\right)^{2}\right\}^{1/2} \tag{4.33}$$

Thus from Eq. (4.29) the mass become

$$v_R = \left(\frac{1}{2q}\right)^{3/2}\frac{1}{\sqrt{\kappa}}\left\{1-\left(\frac{1+q\xi_c}{1+3q\xi_c}\right)^{2}\right\}^{3/2} \tag{4.34}$$

As the the central Fermi momentum approaches larger and larger values, we see that the radius and mass approach maximum values, given by

$$R_{\max} = \frac{2}{3}\frac{r_0}{\sqrt{q\kappa}}, \quad \text{and} \quad M_{\max} = \frac{8}{27}\frac{m_0}{\sqrt{\kappa}q^{3/2}} \tag{4.35}$$

4.2.2 Exact solutions

In this section we obtain exact solutions of the TOV equations (4.18) and (4.19) employing the GUP equation of state expressed by equations (4.7) and (4.12) in parametric form. The numerical integrations are carried out with the boundary conditions $\xi(0) = \xi_c$, $v(0) = 0$ and $\xi(\eta_R) = 0$, where η_R denotes the dimensionless radius of the star. The resulting mass-radius relations for different strengths of the dimensionless GUP parameter β_0 are shown in Figures 4.1 and 4.2.

It is apparent from Figures 4.1 and 4.2 that, for large values of β_0, the mass-radius relations given by the GUP equation of state deviate significantly from the ideal case, whereas for smaller values of β_0, such deviations are smaller.

In Figures 4.1(a) and 4.1(b), we display the mass-radius curves for higher magnitudes of the GUP parameter such as $\beta_0 = 10^{44}$, 10^{42}, 10^{41} and 10^{40}. We see that the mass-

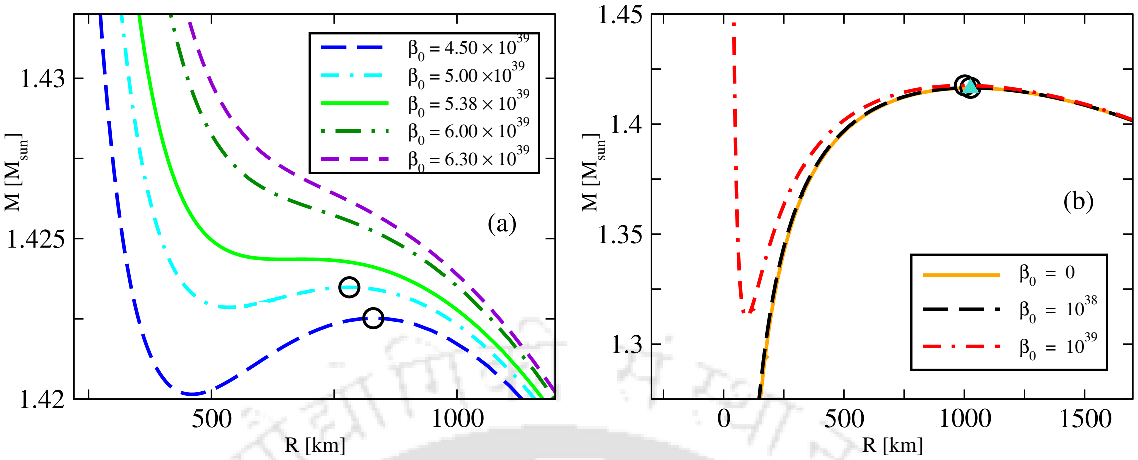

Figure 4.2: (a) Exact mass-radius relations for β_0 in the range $4.50 \times 10^{39} \leq \beta_0 \leq 6.30 \times 10^{39}$. The mass-radius relation for $\beta_0 = \bar{\beta}_0 = 5.38 \times 10^{39}$ demarcates these curves into two classes. For $\beta_0 > \bar{\beta}_0$, there occurs no maximal point whereas for $\beta_0 < \bar{\beta}_0$ maximal points $(R^*,\, M^*)$ exist (shown by open circles). (b) Exact mass-radius relations for $\beta_0 = 10^{39}$ and 10^{38} in comparison with that of the ideal case, $\beta_0 = 0$. Proximity of the maximal points $(R^*,\, M^*)$ are shown by open circles (for $\beta_0 = 10^{39}$ and 10^{38}) with that of the ideal case, shown as a solid triangle ($\beta_0 = 0$).

radius curves coincide with the Chandrasekhar's curve only for low values of the central Fermi momentum ξ_c, as shown in the right-hand part of the inset in Figure 4.1(b). This is evident from the fact that the TOV equation reduces to Newtonian equation in the low density regime. Moreover, we see from the right-hand part of Figure 4.1(a) that all curves nearly coincide irrespective of the strength of the GUP parameter β_0. This is due to the fact that β_0 disappears from the asymptotic equations in this regime as we have seen earlier in Section 4.2.1.1.

For higher ξ_c values, the exact mass-radius curve reaches a point where the radius is minimum $R_{\min}$. The $R_{\min}$ value is smaller for smaller β_0 values as seen in Figure 4.1(a). On further increasing ξ_c, both the mass and radius increase reaching terminal values as shown in Figure 4.1(b) denoted by a open circle. In this regime, we see that analytically obtained high momentum solution (Section 4.2.1.2) coincides with the exact mass-radius curve as shown in Figure 4.1(b). Moreover, the terminal values of radius $R_{\max}$ and mass $M_{\max}$ given by equation (4.35) are found to be nearly the same as given by the exact solutions. However these terminal values are excessively high, as evident from Figure 4.1(b).

Exact mass-radius curves for intermediate strengths of the GUP parameter β_0 (in the range $4.50 \times 10^{39} \leq \beta_0 \leq 6.30 \times 10^{39}$) are shown in Figure 4.2(a). We see a cross-over in the behavior of the curves around the value $\beta_0 = \bar{\beta}_0 = 5.38 \times 10^{39}$. For $\beta_0 > \bar{\beta}_0$, the mass-radius curves do not have a maximal point, whereas for $\beta_0 < \bar{\beta}_0$, there exist maximal points. Figure 4.2(b) compares the mass-radius relation for smaller values of β_0 ($= 10^{39}$ and 10^{38}) with the ideal case ($\beta_0 = 0$). We see that the maxima of the mass-radius curves for these values of β_0 nearly coincide with the maxima of the ideal case. It is also

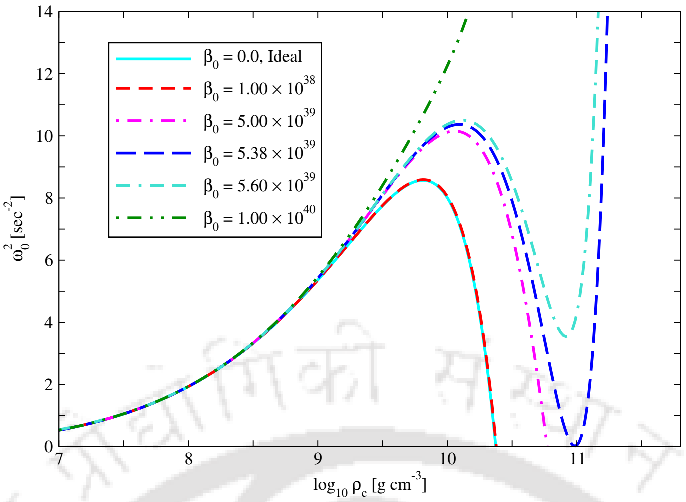

Figure 4.3: Eigenfrequency of the fundamental mode ω_0^2 against central density ρ_c for various values of the GUP parameter β_0.

important to note that the maxima shifts slightly towards the right [Figure 4.2(a)] as the value of β_0 is decreased until the maxima coincide with the ideal value [Figure 4.2(b)].

A more rigorous treatment is required to assert whether these maxima correspond to the onset of gravitational instability. Although Newtonian gravity gives the stellar structure of low-mass white dwarfs in the ideal case (with $\beta = 0$), the correct mass-radius curve and the dynamical instability for high-mass white dwarfs is determined by general relativity. Consequently, it is critical to analyze the role of GUP parameter in determining the dynamical instability of white dwarfs. In the following section we perform a rigorous stability analysis of the equilibrium configurations by investigation the dynamical instability in the framework of general relativity. It consists of studying dynamics of time dependent infinitesimal radial perturbation about the equilibrium configuration at every point inside the star in a homologous manner [50]. The time evolution of these perturbations determined by the central Fermi momentum ξ_c and the GUP parameter β_0 establish whether the system is stable or otherwise.

4.3 Eigenfrequency of the fundamental mode

Using equations in (1.90), the interior Schwarzschild metric potentials can be written in dimensionless variables as

$$e^{-\mu(\eta)} = 1 - 2q\frac{v}{\eta} \tag{4.36}$$

and

$$e^{\nu(\eta)} = \left(1 - 2q\frac{v_R}{\eta_R}\right)\left(\frac{1}{1 - q + q\sqrt{1+\xi^2}}\right)^2, \tag{4.37}$$

where the expression for e^{ν} is obtained from the equation of state given by equations (4.7) and (4.12).

The solution of the TOV equations (4.18) and (4.19), and equations (4.36) and (4.37) give all quantities necessary for the evaluation of the functions $U(r)$, $V(r)$ and $W(r)$ in (1.95). We may rewrite Eq. (1.100) in dimensionless form as

$$\omega_0^2 = \left(\frac{qc^2}{r_0^2}\right)\frac{\mathcal{I}+\mathcal{J}}{\mathcal{K}}, \tag{4.38}$$

where

$$\mathcal{I} = \int_0^{\eta_R} e^{(\mu+3\nu)/2}\frac{\gamma\tilde{P}}{\eta^2}\psi'^2 d\eta, \tag{4.39}$$

$$\mathcal{J} = \int_0^{\eta_R} \frac{e^{(\mu+3\nu)/2}}{\eta^2}\left[\frac{4}{\eta}\frac{d\tilde{P}}{d\eta} + 2qe^{\mu}\tilde{P}(\tilde{\varepsilon}+q\tilde{P}) - \frac{q}{\tilde{\varepsilon}+q\tilde{P}}\left(\frac{d\tilde{P}}{d\eta}\right)^2\right]\psi^2 d\eta, \tag{4.40}$$

and

$$\mathcal{K} = \int_0^{\eta_R} e^{(3\mu+\nu)/2}\frac{\tilde{\varepsilon}+q\tilde{P}}{\eta^2}\psi^2 d\eta. \tag{4.41}$$

We thus numerically evaluate the integrals in Eq. (4.39)—(4.41) with the trial function $\psi = c_0\eta^3$, where c_0 a disposable constant, for different choices of the GUP parameter β_0. Consequently we obtain the eigenfrequency of the fundamental mode ω_0^2 from equation (4.38). As stated earlier, stable configurations correspond to positive values of ω_0^2 whereas a zero frequency solution indicates the onset of a dynamical instability signifying the onset of a gravitational collapse.

We display the results of the numerical integrations in Figure 4.3, where the eigenfrequency ω_0^2 is plotted with respect to the central density ρ_c $(= \varepsilon_c/c^2)$ for different values of β_0. We observe that for low mass white dwarfs with central densities $\rho_c \lesssim 10^9$ g cm^{-3}, the pulsation frequencies overlap signifying the irrelevance of the effect of GUP in this range of central densities. The pulsation frequencies start to deviate from each other in the higher density regime depending on the value of β_0.

For $\beta_0 \leq \bar{\beta}_0 = 5.38 \times 10^{39}$, there exist zero eigenfrequency solutions at central densities ρ_c^*, suggesting the onset of gravitational collapse. The existence of imaginary eigenfrequency solution corresponding to unstable configuration is possible only for $\beta_0 < \bar{\beta}_0$. For $\beta_0 > \bar{\beta}_0$, zero eigenfrequency solutions are not possible even for arbitrarily high central densities ρ_c, signifying stability of excessively massive white dwarfs. We also see that the curve for $\beta_0 = 10^{38}$ nearly coincides with that for the ideal case ($\beta_0 = 0$). This means that all curves in the range $0 \leq \beta_0 \leq 10^{38}$ overlap (to a good approximation) giving rise to approximately the same onset density ρ_c^* for gravitational collapse. A legitimate upper bound is given by the electroweak limit $\beta_0 \sim 10^{34}$ [58] which is well within the range $0 \leq \beta_0 \leq 10^{38}$. Since this onset density is nearly 2.3588×10^{10} g cm^{-3}, Chandrasekhar's

Table 4.1: Critical values of the central density ρ_c^*, mass M^*, and radius R^* for different values of the GUP parameter β_0 (or alternative GUP parameter $\alpha = \sqrt{\beta_0}\frac{m_e}{M_P}$) at the onset of dynamical instability determined by the vanishing eigenfrequency of the fundamental mode.

β_0	α	ρ_c^* (g cm^{-3})	M^* (M$_\odot$)	R^* (km)
5.38×10^{39}	3.07×10^{-3}	1.0105×10^{11}	1.4244	655.5629
5.00×10^{39}	2.96×10^{-3}	5.8618×10^{10}	1.4235	776.3669
1.00×10^{38}	4.19×10^{-4}	2.3801×10^{10}	1.4165	1021.6162
1.00×10^{34}	4.19×10^{-6}	2.3588×10^{10}	1.4164	1024.3821

general relativistic mass ~ 1.42 M$_\odot$ is easily recovered in this range which extends four orders of magnitude beyond the electroweak bound.

The above discussions lead to parallel observations from Figure 4.2 (a) where $\beta_0 = \bar{\beta}_0$ demarcates a change in behavior of the mass-radius curves. The non-existence of a maximal point in the mass-radius curve for $\beta_0 > \bar{\beta}_0$ is evident from the fact that there exists no critical density ρ_c^* corresponding to a zero eigenfrequency solution. On the other hand, for $\beta_0 < \bar{\beta}_0$, the existence of maximal points (R^*, M^*) in the mass-radius curves are consequences of zero eigenfrequency solutions at ρ_c^*. The branches towards the right of the maximal point (R^*, M^*) correspond to lower central densities $\rho_c < \rho_c^*$ and thus the stability of this branch is confirmed by the fact that ω_0^2 is positive, as shown in Figure 4.3. On the other hand, the branches towards the left of the maximal point (R^*, M^*) correspond to instability as ω_0^2 becomes negative (not shown in Figure 4.3) and they correspond to $\rho_c > \rho_c^*$.

As β_0 is deceased towards 10^{38}, the maximal points (R^*, M^*) approach closer to each other and nearly coincide at $\beta_0 = 10^{38}$. The corresponding critical values are displayed in Table 4.1 where it is evident that the critical mass approaches the limit 1.416 M$_\odot$ and the radius 1024 km.

Thus in addition to asserting the existence of the Chandrasekhar limit, the stability analysis confirms the fact that the radius decreases as the mass increases for stable configurations of white dwarfs.

4.4 Discussion and Conclusion

There have been a few recent attempts to restore the Chandrasekhar limit when white dwarfs are described by GUP-enhanced equation of state. As we have discussed earlier, there are various scenarios [98, 190, 191] pointing to the possibility of β being negative. As shown in [156], a choice of a negative GUP parameter β gives rise to the mass-radius relation

$$R = \sqrt{|\beta|}\frac{M m_e^{1/3} c}{\sqrt{M_{\rm Ch}^{2/3} - M^{2/3}}}\ell_P, \tag{4.42}$$

in the relativistic limit, giving the Chandrasekhar mass M_{Ch} as an upper bound. However, this mass-radius relation has inconsistencies with observations, namely, (i) as the mass M increases, the radius R also increases, and (ii) the radius diverges as the mass approaches the Chandrasekhar limit, preventing the formation of more compact objects as the density would be infinitely diluted. In fact, observations indicate that the radius decreases with increase in mass of white dwarfs. Moreover we expect the formation of highly dense objects such as neutron stars or black holes when the mass exceeds the Chandrasekhar limit. These inconsistencies do not appear when we take β to a positive quantity.

In an alternative approach to circumvent the problem of non-existence of the Chandrasekhar mass, an extended GUP [157] was suggested by incorporating the effect of cosmological constant Λ, so that

$$\Delta x \Delta p \geq \frac{\hbar}{2}\left\{1+\beta(\Delta p)^2-\lambda\frac{(\Delta x)^2}{L_\Lambda^2}\right\}, \tag{4.43}$$

with $L_\Lambda^2 = \lambda/\Lambda$ which is positive for de-Sitter expansion of the Universe ($\lambda = +3$). Although the observed value of Λ is very small, namely $\Lambda \sim 10^{-52}\ \mathrm{m}^{-2}$, they showed that this reformulation of GUP leads to a mass-radius relation whose physically acceptable solution is strongly dominated by the cosmological terms and the contribution from β is insignificant, making the sign of β irrelevant. This mass-radius relation clearly shows that the Chandrasekhar mass is the upper bound. However, this mass-radius relation also suffers from the same inconsistencies as described above.

Because of this inconsistencies, it is essential to resolve the issue of non-existence of Chandrasekhar's limit in a cogent fashion so that all assumptions in the theory lead to results in agreement with observations. We therefore formulated the problem in a rigorous manner by adopting general relativity vis-à-vis GUP-enhanced equation of state with the assumption of positive a GUP parameter β. Importantly, we find that the Chandrasekhar mass is assured for β_0 values below $\bar{\beta}_0$, due to the onset of gravitational collapse. We also note that the electroweak upper bound for β_0 is much below $\bar{\beta}_0$ so that physical existence of Chandrasekhar's limit is guaranteed.

The above conclusion stems from a rigorous stability analysis of the equilibrium configurations as displayed in Figure 4.3, where the eigenfrequency of the fundamental mode ω_0^2 is plotted with respect to the central density ρ_c for different values of β_0. We see that a vanishing eigenfrequency exists when $\beta_0 \leq 5.38 \times 10^{39} = \bar{\beta}_0$, giving rise to a dynamical instability at critical central densities ρ_c^*. However, for $\beta_0 > \bar{\beta}_0$, no dynamical instability occurs because of the nonexistence of a zero eigenfrequency solution, implying that these configurations remain stable for arbitrarily high values of ρ_c leading to excessively massive white dwarfs. However, these solutions are physically unacceptable because the corresponding β_0 values are well above the electroweak bound.

An important point to observe from Figure 4.3 is that the eigenfrequencies for $\beta_0 = 10^{38}$

practically coincides with that of the ideal case, $\beta_0 = 0$. Thus in the range $0 < \beta_0 < 10^{38}$, the critical density ρ_c^* for the onset of gravitational collapse (determined by the vanishing eigenfrequency) remains practically unaltered. We find $\rho_c^* = 2.3801 \times 10^{10}$ g cm^{-3} for $\beta_0 = 10^{38}$, which is nearly the same as Chandrasekhar's critical value of 2.3×10^{10} g cm^{-3} (for $\beta_0 = 0$). It is thus evident that Chandrasekhar's general relativistic critical mass of 1.42 M$_\odot$ [52] remains practically unaffected. Moreover, since this critical density ρ_c^* is much below nuclear matter density, $\sim 10^{14}$ g cm^{-3}, our consideration of a free fermionic equation of state remains valid throughout the stable regime of white dwarfs.

In the context of the stability analysis, we can analyse the mass-radius curve obtained in Section 4.2. Since the Chandrasekhar limit exists only below $\bar{\beta}_0 = 5.38 \times 10^{39}$, all mass-radius plots in Figure 4.1 above this value would not correspond to reality. This is also evident from the fact that $\bar{\beta}_0$ is much higher than the electroweak bound $\beta_0 \sim 10^{34}$. For $\beta_0 < \bar{\beta}_0$, the mass-radius curves develop maximal points [see Figure 4.2 (a)] at which the eigenfrequencies ω_0^2 vanish as shown later in Section 4.3. These maximal points correspond to limiting Chandrasekhar mass lying below ~ 1.425 M$_\odot$. It is important to note that *the radius decreases as the mass increases* in the part of a mass-radius curve towards the right of the maximal point that corresponds to the *stable* branch. The mass-radius behavior in the stable branches is consistent with several astronomical observations of white dwarfs [101, 107, 129, 199–201, 219, 220]. Moreover, our stability analysis suggests that upon reaching beyond the Chandrasekhar mass the star would collapse to form highly dense compact objects such as neutron star or black hole.

The present scenario of describing white dwarfs in terms of general relativity and GUP-enhanced equation of state with a positive GUP parameter β rigorously leads to the existence of Chandrasekhar mass as well as the correct behavior of the mass-radius relation consistent with astronomical observations. Moreover, it suggests the onset of gravitational collapse beyond the Chandrasekhar mass. It is now well-known that the degenerate core of a Type II supernova progenitor undergoes a gravitational collapse with a mass of about 1.4 M$_\odot$, leading to the formation of a neutron star or a black hole.

It is important to note that the non-relativistic limit of equations (4.18) and (4.19) leads to Newtonian equations (2.47) and (2.48) of Chapter 2, that predicted the existence of "super-stable" white dwarfs of excessively high masses beyond the Chandrasekhar limit. The Chandrasekhar limit, 1.4518 M$_\odot$ and a radius of 601.8 km, could be recovered by imposing the restriction due to neutronization together with $\beta_0 = 10^{34}$, coming from the electro-weak bound. In contrast, general relativity alone (without having to impose neutronization) recovers the Chandrasekhar limit for β_0 values up to 10^{38} due to the dynamical instability inherent in general relativity. This dynamical instability property of general relativity will be lost by taking the non-relativistic limit.

Chapter 5

Existence of Chandrasekhar's limit with modified dispersion relation

As we have seen in Chapter 3, Newtonian gravity predicts the existence of white dwarfs with masses far exceeding the Chandrasekhar limit when the equation of state of the degenerate electron gas incorporates the effect of quantum spacetime fluctuations (via a modified dispersion relation) even when the strength of the fluctuations is taken to be very small. In this Chapter, we show that this Newtonian "super-stability" does not hold true when the gravitational pull is treated in the general relativistic framework. Employing dynamical instability analysis, we find that the Chandrasekhar limit can be reassured even for a range of high strengths of quantum spacetime fluctuations with the onset density for gravitational collapse practically remaining unaffected.

We have seen in Chapter 3 that a modified dispersion relation leads to a modified equation of state (EoS) so that the stellar structure of white dwarfs governed by its electron degenerate gas undergoes a measurable change. We found that white dwarfs with modified EoS can support masses much higher than the Chandrasekhar limit that become "super-stable" when the hydrostatic equilibrium is governed by Newtonian gravity.

However, the possibility of the existence of excessively massive white dwarfs is unlikely as it is inconsistent with an extensive amount of astronomical observations [107, 129, 199–201, 219, 220]. Although there have been speculations about super-Chandrasekhar white dwarfs, it has been argued [89, 203] that they are in fact double degenerate merges of two sub-Chandrasekhar white dwarfs. It is thus extremely important to investigate whether the above-mentioned "super-stability" prevails in general relativity (GR). It may be recalled that general relativity has a profound effect in determining the stability of massive stars

---

The content of this chapter is published: A. Mathew, M. K. Nandy, Gen. Relativ. Gravit. **52**, 38 (2020) against gravitational collapse although it may have an insignificant effect on their stellar structure.

We thus anticipate that a dynamical instability would set in at a critical value of the central density as generally predicted for relativistic stars [23, 50–52, 216, 229]. Following this standard method, we calculate the eigenfrequencies of the normal mode of radial oscillations with respect to various central densities of white dwarfs with the electron degenerate gas treated in the framework of modified dispersion relation. The existence of a vanishing eigenfrequency corresponds to the maximum central density in stable configuration. We identify the onset density of dynamical instability with respect to a parameter characterizing the strength of quantum spacetime fluctuations.

In this Chapter, we use the modified dispersion relation (3.5) and we analyze the stability of white dwarfs by calculating the eigenfrequencies of normal modes of small radial oscillations in the first order of perturbation. We find that general relativity is capable of causing a gravitational collapse even for high strengths of quantum spacetime fluctuations characterized by the parameter $\alpha = \lambda m_e c^2$. However, when this strength is very high ($\alpha > 3.7 \times 10^{-3}$), the quantum space-time fluctuations become strong enough to hold up against a gravitational collapse. A legitimate bound on such parameters occurring in equivalent formulations of quantum spacetime fluctuations indicate an upper bound for α much lower than 3.7×10^{-3} for which we find that the Chandrasekhar critical limit can be realized in the quantum gravitational regime.

The remainder of the Chapter is organized as follows. In Section 5.1, the dynamical instability is explored for white dwarfs with the equation of state governed by a modified dispersion relation to account for the effect of quantum spacetime fluctuations on the instability. Finally, we Conclude the chapter in Section 5.2.

5.1 Dynamical instability in white dwarfs with modified dispersion relation

As we have seen Chapter 3, in the Newtonian framework, white dwarfs can exist in excessively large masses beyond the Chandrasekhar limit, when quantum spacetime fluctuations are included in the equation of state of the electron gas. This "Newtonian super-stability" persists although the strength of quantum spacetime fluctuations is taken to be very small. However, it is well-known that, in the conventional problem of stability of white dwarfs, a dynamical instability sets in [51, 52] when the gravity is treated in the framework of general relativity. It is thus natural to speculate that a similar general relativistic instability may set in when the small effect of quantum spacetime fluctuations is included in the equation of state of the electron gas.

5.1.1 Modified equation of state

We shall take the modified dispersion relation (3.5) to model the effect of quantum space-time fluctuations. This imposes a momentum cutoff at $p_{\max} = (\lambda c)^{-1}$ above which the energy becomes unphysical. For small values of momentum it coincides with the ideal dispersion relation, but it deviates strongly for high values of momentum, becoming infinite at the cutoff $p_{\max}$.

Since the electron gas in white dwarfs is completely degenerate, we evaluate the pressure P, internal energy ε_{int}, and mass-density ρ_0 at absolute zero from the grand partition function as shown in Section 3.1.1. For convenience, we express we modified equation of state as

$$P = A\tilde{P}(\xi), \;\; \rho_0 c^2 = \frac{A}{q}\xi^3, \;\; \varepsilon = \rho_0 c^2 + \varepsilon_{\text{int}} = \frac{A}{q}\tilde{\varepsilon}(\xi) \tag{5.1}$$

where

$$\tilde{P}(\xi) = \xi^3 f(\xi) - 3g(\xi), \qquad \tilde{\varepsilon} = (1-q)\xi^3 + 3q\, g(\xi), \tag{5.2}$$

$$\xi = \frac{p_F}{m_e c}, \;\; A = \frac{8\pi m_e^4 c^5}{3h^3}, \;\; q = \frac{m_e}{\mu_e m_u} = 2.74297 \times 10^{-4}, \tag{5.3}$$

$$f(\xi) = \left[\alpha\xi^2 + \sqrt{(1-\alpha^2)\xi^2 + 1}\right]\left[1 - \alpha^2\xi^2\right]^{-1}, \tag{5.4}$$

and $g(\xi)$ given by equation (3.9) with $\alpha = \lambda m_e c^2$.

Employing the relativistic expression $\gamma = \frac{\tilde{\varepsilon}+q\tilde{P}}{\tilde{P}}\left(\frac{d\tilde{P}}{d\tilde{\varepsilon}}\right)_s$ for the adiabatic index γ, and using Eqs. (5.1–5.4 and 3.9), we obtain

$$\gamma = \frac{\tilde{\varepsilon}(\xi) + q\tilde{P}(\xi)}{\tilde{P}(\xi)}\left(\frac{\xi}{3}\right)\left(1 - q + q\frac{dg}{d\xi}\right)^{-1}\left(\frac{df}{d\xi}\right) \tag{5.5}$$

for the electron gas with the modified equation of state.

5.1.2 Stability Analysis

The Einstein field equation for the static interior Schwarzschild metric can be solved [159, 217] to obtain the metric components

$$e^{-\mu} = 1 - 2q\frac{\tilde{m}}{\eta} \tag{5.6}$$

and

$$e^{\nu} = \left(1 - 2q\frac{\tilde{M}}{\eta_R}\right) \times \exp\left\{-2q\int_0^{\eta} \frac{\tilde{P}'}{(\tilde{\varepsilon} + q\tilde{P})} d\eta\right\}, \tag{5.7}$$

where $\tilde{m} = m/m_0$ and $\eta = r/r_0$ are dimensionless variables with

$$r_0 = \frac{qc^2}{\sqrt{4\pi AG}} \quad \text{and} \quad m_0 = \frac{q^2c^4}{\sqrt{4\pi A}} \frac{1}{G^{3/2}}. \tag{5.8}$$

The dimensionless quantities $\tilde{M} = M/m_0$ and $\eta_R = R/r_0$ correspond to the mass M and radius R of the fluid sphere. Using Eqs. (5.1–5.4 and 3.9), Eq. (5.7) can be simplified to

$$e^{\nu} = \left(1 - 2q\frac{\tilde{M}}{\eta_R}\right)\left(\frac{1}{1 - q + qf(\xi)}\right)^2. \tag{5.9}$$

The dependence of the above field quantities on the radial coordinate η correspond to the Tolman-Oppenheimer-Volkoff equation [159, 217] of hydrostatic equilibrium expressed here as

$$\frac{d\tilde{P}}{d\eta} = \left(\frac{df}{d\xi}\right)\xi^3\frac{d\xi}{d\eta} = -\left(\frac{\tilde{\varepsilon} + q\tilde{P}}{\eta}\right)\left(\frac{\tilde{m} + q\tilde{P}\eta^3}{\eta - 2q\tilde{m}}\right) \tag{5.10}$$

with the mass equation

$$\frac{d\tilde{m}}{d\eta} = \tilde{\varepsilon}\eta^2. \tag{5.11}$$

The functions $U(\eta)$, $V(\eta)$ and $W(\eta)$ in the Sturm-Liouville equation (1.94) are readily obtained from Eqs. (1.95–1.97) employing Eqs. (5.6), (5.9) and (5.10). In consequence, Eq. (1.100) yields the eigenfrequency

$$\omega_0^2 = \left(\frac{qc^2}{r_0^2}\right)\frac{\mathcal{I} + \mathcal{J}}{\mathcal{K}}, \tag{5.12}$$

where

$$\mathcal{I} = \int_0^{\eta_R} e^{(\mu+3\nu)/2}\frac{\gamma\tilde{P}}{\eta^2}\psi_0'^2 d\eta, \tag{5.13}$$

$$\mathcal{J} = \int_0^{\eta_R} \frac{e^{(\mu+3\nu)/2}}{\eta^2}\left[\frac{4}{\eta}\frac{d\tilde{P}}{d\eta} + 2qe^{\mu}\tilde{P}(\tilde{\varepsilon} + q\tilde{P}) - \frac{q}{\tilde{\varepsilon} + q\tilde{P}}\left(\frac{d\tilde{P}}{d\eta}\right)^2\right]\psi_0^2 d\eta, \tag{5.14}$$

and

$$\mathcal{K} = \int_0^{\eta_R} e^{(3\mu+\nu)/2}\frac{\tilde{\varepsilon} + q\tilde{P}}{\eta^2}\psi_0^2 d\eta, \tag{5.15}$$

with ψ_0 the eigenfunction associated with the fundamental mode that minimizes the right-hand side of Eq. (1.99).

As stated earlier, we make the choice $\psi_0 = \eta^3$ as a trial function and evaluate the integrals $\mathcal{I}$, $\mathcal{J}$, and $\mathcal{K}$ given by Eqs. (5.13–5.15) for different values of the central Fermi momentum ξ_c. The corresponding eigenfrequencies are obtained from Eq. (5.12). Figure 5.1 displays the eigenfrequency against the central density ρ_c [related to ξ_c through $\rho = (A/qc^2)\{(1-q)\xi^3 + 3qg(\xi)\}$] for different strengths of quantum spacetime fluctuations parametrized by α, namely, $\alpha = 10^{-2}$, 10^{-3}, 10^{-4}, and 10^{-5}, including the ideal case ($\alpha = 0$).

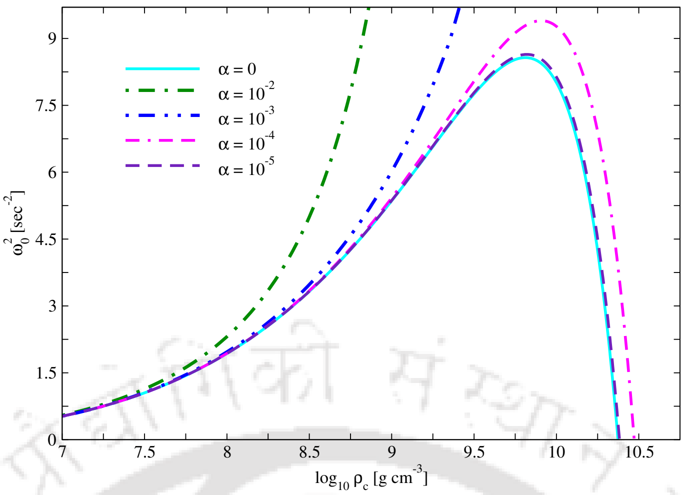

Figure 5.1: Eigenfrequency for normal modes against central density of relativistic white dwarfs for various values of the parameter α that characterizes the strength of quantum spacetime fluctuations. The scale of this plot cannot accommodate the cases $\alpha = 10^{-2}$ and 10^{-3}. It will be evident from Figure 5.2 that the case $\alpha = 10^{-3}$ gives a zero eigenfrequency solution whereas for the case $\alpha = 10^{-2}$, the curve reaches a terminal point without giving a zero eigenfrequency solution.

We observe from Figure 5.1 that for $\alpha = 10^{-5}$, the characteristic eigenfrequencies are close to the ideal values. As the strength is increased to $\alpha = 10^{-4}$, the eigenfrequencies depart from the ideal values but they follow a trend similar to the ideal case, and gravitational instability can set in dictated by general relativity by virtue of the existence of a vanishing eigenfrequency and a corresponding critical central density ρ_c^*. This signifies the dominance of gravitational pull determined by general relativity over the effect of quantum spacetime fluctuations on the equation of state.

However, for higher strengths of α, such as $\alpha = 10^{-3}$ and 10^{-2}, the scale of the ordinate in Figure 5.1 is not adequate to analyze their behaviors. For an adequate analysis of the situation, we show a log-log plot in Figure 5.2. It is clear from Figure 5.2 that, for $\alpha > 3.7 \times 10^{-3}$, the curves follow a trend completely different from the ideal case because they reach terminal points at non-zero eigenfrequencies and thus zero eigenfrequency solutions do not exist. This signifies the non-existence of any gravitational instability or collapse and the white dwarfs remain "super-stable". The central densities at which the curves terminate are higher than Chandrasekhar's value of 2.3×10^{10} g cm^{-3}. From this super-stability, we conclude that quantum spacetime fluctuations are sufficiently strong for $\alpha > 3.7 \times 10^{-3}$ so that the gravitational pull determined by general relativity is incapable of bringing about any instability.

On the other hand, for $\alpha \leq 3.7 \times 10^{-3}$, the trends of the eigenfrequencies are similar to that of the ideal case and general relativistic instabilities can set in due to the existence of vanishing eigenfrequencies of the normal mode. This obviously means that, for $\alpha \leq 3.7 \times 10^{-3}$, the gravitational pull determined by general relativity is strong enough to bring about an instability or collapse. Thus the value $\alpha = 3.7 \times 10^{-3}$ marks a transition

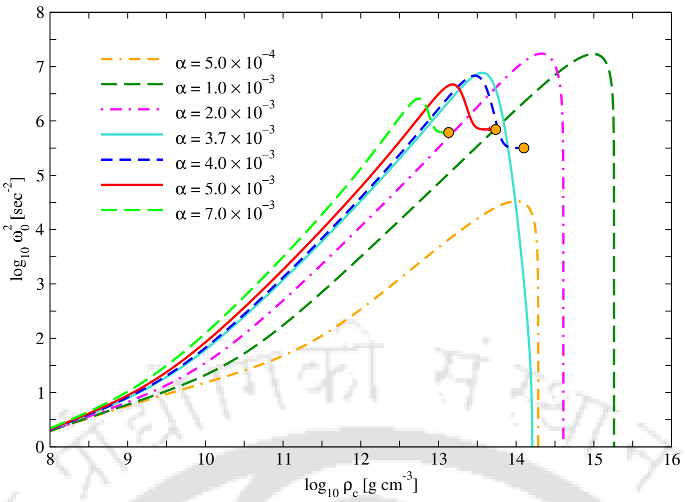

Figure 5.2: Eigenfrequency for normal modes versus central density of relativistic white dwarfs for various strengths of α higher than those in Figure 5.1. For $\alpha \leq 3.7 \times 10^{-3}$, the curves indicate the existence of zero eigenfrequency solutions leading to gravitational collapse. For $\alpha > 3.7 \times 10^{-3}$, the curves reach terminal points and zero eigenfrequency solutions do not exist excluding the possibility of gravitational collapse.

point for strength of quantum gravitational fluctuations competing against gravity pull that leads to the general relativistic instability.

Since the general relativistic instability (corresponding to the zero eigenfrequency) occurs at a critical central density ρ_c^* determined by the parameter α, it is worth studying the behavior of the corresponding critical values of the central Fermi momenta ξ_c^* with respect to the parameter α. We see from the right-hand part of Figure 5.3 that as the strength of α is increased from 10^{-5} to 10^{-4}, the critical value ξ_c^* (or equivalently ρ_c^*) remains approximately constant. In fact, our calculation shows that there is negligible variation in the value of ξ_c^* in the range $0 < \alpha < 10^{-5}$ (which is also evident from Figure 5.1 from the near-coincidence of the two ρ_c^* values). Thus in the range $0 < \alpha < 10^{-4}$, we expect that general relativistic instability would yield nearly the same critical masses. In this range, we find $\rho_c^* = 2.3 - 2.9 \times 10^{10}$ g cm^{-3} which is in the vicinity of Chandrasekhar's value of 2.3×10^{10} g cm^{-3} [52]. This indicates that Chandrasekhar general relativistic critical mass of 1.42 $M_\odot$ is negligibly affected in this range of the parameter α.

We thus see that the effect of general relativity is robust enough to cause an instability against the effect of quantum spacetime fluctuations even for strengths such as $\alpha = 10^{-4}$. Experimental bounds on such parameters occurring in equivalent formulations of quantum spacetime fluctuations is available in the literature. For example, Das and Vagenas [58] discussed various experimental bounds on the generalized uncertainty parameter β_0. Taking the bound $\beta_0 \sim 10^{34}$, which is a legitimate upper bound coming from the electroweak theory, it translates to $\alpha \sim 10^{-6}$ in our case. Thus $\alpha = 10^{-4}$ is in fact a large value for the strength of quantum spacetime fluctuations. If the strength of α is increased beyond 10^{-4}, we see from Figure 5.3 that the critical central Fermi momentum ξ_c^* also increases.

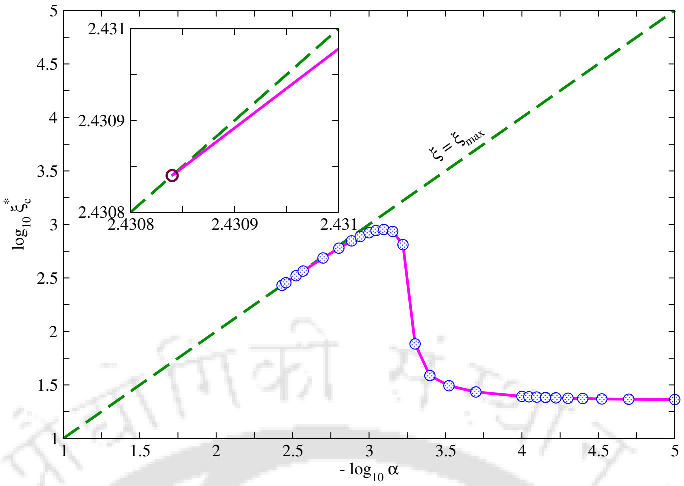

Figure 5.3: Critical value of the central Fermi momentum for the onset of gravitational instability versus the parameter α. The dashed straight line represents $\xi = \xi_{\max} = \alpha^{-1}$. The inset shows the intersection of the two curves at $\alpha = 3.7 \times 10^{-3}$.

However, after reaching a maximum it eventually falls off due to increased role of gravitating pressure in comparison to the gravitating mass. Finally, the curve approaches the line $\xi = \alpha^{-1} = \xi_{\max}$ until it makes an intersection at $\alpha = 3.7 \times 10^{-3}$, the maximum strength of α for the existence of a vanishing eigenfrequency and hence a gravitational collapse. This intersection is shown in the inset of Figure 5.3 by an open circle where $\xi_c^* = 2.7 \times 10^2$. It is obvious that the curve cannot cross the line $\xi = \alpha^{-1}$, having reached the maximum value $\xi_c^* = \alpha^{-1}$.

5.2 Conclusion

The modified dispersion relation is one of the scenarios in which the effect of quantum gravity is phenomenologically taken into account. We expect the effect of quantum gravity to have some signature when the density of the matter is very high. In this context it is worthwhile to recall that the standard Chandrasekhar limit of 1.44 $M_\odot$ is approached when the density of the electron degenerate gas in white dwarfs approaches infinity in the framework of Newtonian gravity. The problem thus calls for taking account of the effect of quantum gravity at very high densities of the electron degenerate gas. When this notion is followed and the electron gas is treated via a modified dispersion relation making the equation of state more stiff than the ideal one, it is found that white dwarfs become "super-stable" and higher masses beyond the Chandrasekhar limit are possible [133] when the gravity is treated in the Newtonian framework. However, as noted in the introduction and in more detail below, white dwarfs are most likely to exist below the Chandrasekhar limit. It is thus extremely important to resolve this paradoxical situation.

It is known from Chandrasekhar's study [50, 52] that a dynamical instability sets in when the gravity is treated general relativistically. Consequently it is natural to ask the question whether general relativity would be capable of resurrecting the Chandrasekhar limit when the effect of quantum space-time fluctuations is included in the equation of state. Motivated by this query, we analyzed the problem of stability of white dwarfs governed by general relativity and incorporating quantum space-time fluctuations in the electron degenerate gas via a modified equation of state.

To analyze the stability, we followed the standard methodology of perturbations generating radial pulsations in spherically symmetric white dwarfs and calculated the corresponding eigenfrequencies of the radial oscillations. The corresponding eigenvalue equation is in the Sturm-Liouville form whose eigenfrequencies can be related to a variational principle. With an appropriate trial function for the Lagrangian displacement, we calculated the eigenfrequencies for various strengths of the quantum space-time fluctuations parametrized by α.

We find that, for large values of α such that $\alpha > 3.7 \times 10^{-3}$, white dwarfs remain "super-stable" as they do not exhibit any zero eigenfrequency in the normal mode. Such white dwarfs can support maximum masses determined by the maximum values of the central density ρ_c where the curves terminate as shown in Figure 5.2. These values of ρ_c are higher than the critical density obtained by Chandrasekhar suggesting the possibility of white dwarfs of masses higher than Chandrasekhar's general relativistic value of 1.42 $M_\odot$. However, these cases are unlikely because we do not expect that the strength α of spacetime fluctuations to be as large as or higher than 0.0037, as discussed earlier on the basis of bounds on similar parameters. It may however be noted that there have been observations of some type Ia SNe events (SN 2003fg, SN 2006gz, SN 2007if, SN 2009dc) [89, 93, 188, 203, 230] which produced a high amount of $^{56}\mathbf{Ni}$ ranging from 1.2 $M_\odot$ to 1.7 $M_\odot$. This suggested that the progenitors of these SNe events had masses in the super-Chandrasekhar range from 2.2 $M_\odot$ to 2.8 $M_\odot$. However the unusually low and slowly declining Silicon velocity in SN 2006gz indicated that it is a double degenerate (DD) merger of two sub-Chandrasekhar white dwarfs as argued by Hicken et al. [89]. Moreover, Silverman et al. [203] argued, basis on simulations, that SN 2009dc was most likely due to the merger of two white dwarfs. Chen and Li [55] considered a single-degenerate white dwarf with differential rotation and accreting matter slowly from a normal companion. They predicted that white dwarf masses in excess of 1.7 $M_\odot$ are very much unlikely. On the other hand, in the presence of a strong magnetic field of the order of $\sim 10^{15}$ Gauss, Das and Mukhopadhyay [59] predicted that a white dwarf can support a mass of 2.3–2.6 $M_\odot$ due to the existence of Landau levels. However, pointing to various disagreements among the existing SNe Ia models, van Kerkwijk [218] argued that SNe Ia events generally take place due to the merger of two carbon-oxygen white dwarfs. Thus, for normal white dwarfs (without rotation or magnetic field), a super-Chandrasekhar mass seems to be unlikely.

For smaller strengths of quantum spacetime fluctuations, such that $\alpha \leq 3.7 \times 10^{-3}$, we find that general relativity is capable of bringing about an instability at finite central densities ρ_c^* because of the existence of a vanishing eigenfrequency in the normal mode as shown in Figure 5.2. This signifies that gravity governed by general relativity is strong enough to cause a gravitational collapse when the strength α of quantum spacetime fluctuations is $\alpha \leq 3.7 \times 10^{-3}$. Thus the special value $\alpha = 3.7 \times 10^{-3}$ marks a transition point between two regimes — gravity dominating over quantum spacetime fluctuations and vice-versa. It is important to note that, unlike Newtonian gravity, general relativity is robust enough to bring about a gravitational collapse for strengths of quantum spacetime fluctuations such as $\alpha \leq 10^{-3}$.

We have also seen from Figures 5.1 and 5.3 that in the range $0 < \alpha < 10^{-4}$, general relativistic instability yields comparable critical central densities, namely, $\rho_c^* = 2.3 - 2.9 \times 10^{10}$ g cm^{-3}. This range is in the vicinity of Chandrasekhar's value of 2.3×10^{10} g cm^{-3} [52]. This indicates that the stellar structure of relativistic white dwarfs is hardly affected in this range of the parameter α where the critical mass is about 1.42 $M_\odot$.

We may recall from Chapter 3 that when gravity was treated in the Newtonian framework, masses far exceeding the Chandrasekhar limit were found to be "super-stable" even for very low values of α such as 10^{-5}. However, by constraining the central Fermi momentum with the neutronization threshold, a mass nearly equal to the Chandrasekhar value (1.45 $M_\odot$) was obtained for $\alpha \leq 10^{-7}$. It is thus obvious that Newtonian gravity alone cannot dominate over the stiffness of the equation of state generated by quantum spacetime fluctuations. On the other hand, as we have seen in this Chapter, general relativity alone, by virtue of the inherent property of dynamical instability, without having to impose neutronization, does possess the capacity to overcome the stiffness of the equation of state that can lead to a gravitational collapse, so that Chandrasekhar's general relativistic limit of 1.42 $M_\odot$ is recovered.

Moreover, even for a high value of α, such as 10^{-4} or 10^{-5}, the onset density ρ_c^* for gravitational collapse is practically unaffected (with respect to the ideal case) when the gravity is treated general relativistically in spite of the effect of quantum spacetime fluctuations opposing gravitational collapse. This is of direct relevance to the core collapse supernovae where the degenerate core of the progenitors are found to have a mass of about 1.4 $M_\odot$. However it may be recalled that there may be no clear distinction between the gravitational core collapse and fast β-capture that may occur nearly simultaneously at the onset, effectively making no difference in the impending supernova explosion [229]. Thus our study suggests that when the inevitable effect of quantum spacetime fluctuations is included in the process, the situation practically remains indistinguishable from the ideal core collapse scenario.

Chapter 6

Stellar structure of quark stars in an extended gravity scenario

As we have seen in Section 1.6, there have been various proposal for extended gravity scenarios. In this Chapter, we propose a form of gravity-matter interaction given by ωRT *in the framework of* $f(R,T)$ *gravity and examine the effect of such an interaction in spherically symmetric compact stars. Treating the gravity-matter coupling as a perturbative term on the background of Starobinsky gravity, we develop a perturbation theory for equilibrium configurations. For illustration, we take the case of quark stars and explore their various stellar properties. We find that the gravity-matter coupling causes an increase in the stable maximal mass which is relevant for recent observations on binary pulsars.*

Modern day scenarios such as inflation [211, 221], late-time cosmic acceleration [61, 176, 181], flat rotation curves [22, 158, 205, 235] etc. are incompatible with the standard prescription of general relativity (GR). Although the predictions of GR in the weak-field regime are precise, it falls short in the higher curvature regime in the sense that it predicts singularities such as the big bang and the black hole singularities. It has been shown that quantum corrections generate higher order self-coupling curvature in addition to the original scalar curvature [38, 60]. This motivates one to consider non-linear curvature theories to see if they provide a better descriptions of gravitation phenomena.

A nonlinear curvature theory of gravity was proposed by Starobinsky [210] in order to address the issue of the big-bang singularity. He considered the Einstein field equations $G_{\mu\nu} = \kappa \langle T_{\mu\nu} \rangle$ where the right hand side gives quantum mechanical contributions due to coupling between quantum matter fields (having different spins) with classical gravitational

---

The content of this chapter is published: A. Mathew, M. Shafeeque & M. K. Nandy, Gen. Eur. Phys. J. C **80**, 615 (2020) field, with the assumption of isotropy and homogeneity and absence of radiation field. In one-loop approximation, and upon regularization, $\langle T_{\mu\nu} \rangle$ was found to be a function of the Riemann geometric quantities. Based on these findings, Starobinsky exhibited the existence of a one-parameter family of non-singular solutions of the de-Sitter type which could be analytically continued into the region $t < 0$. The de-Sitter phase naturally explains the inflation scenario without having to include any inflaton field.

However, another approach involves a generalization of the Einstein-Hilbert action where an arbitrary function $f(R)$ represents the Lagrangian density [37]. In the Starobinsky model, namely, $f(R) = R + \alpha R^2$, and its other generalizations, inflation has been explained to obtain increasingly better fits the observational data [19, 46]. Moreover, various forms of $f(R)$ gravity have been able to explain the late-time cosmic acceleration [19, 99]. In addition, a simple power-law form of $f(R)$ gravity is able to explain [43, 44] rotation curves in the spiral galaxies. The power-law form has been explored [24, 26, 141] to find a basis for the modified Newtonian dynamics (MOND) which is the most successful scenario in explaining rotation curves in many different types of galaxies [25, 138, 139, 145].

Inclusion of the effect of classical matter with $f(R)$ gravity came in two different forms, namely, $f(R, L_m)$ and $f(R, T)$, where L_m is the matter Lagrangian and T is the trace of energy-momentum tensor. While $f(R, L_m)$ gravity has been studied extensively in various contexts [81, 82], $f(R, T)$ gravity entered the literature somewhat recently [84]. It was noted that the T dependence may arise due to exotic imperfect fluid or quantum effects. Thus it is natural to expect that $f(R, T)$ gravity may be a suitable candidate for compact objects such as neutron stars and quark stars where quantum effects are expected to play a significant role.

Models of extended gravity have been employed to study the stellar structure of different compact objects. Starobinsky gravity with $f(R) = R + \alpha R^2$ has been applied to neutron stars treating αR^2 as perturbation with well-known models for the equation of state [18]. It was found for some cases that the maximal mass could approach $\sim 2\ \mathrm{M}_\odot$ only for negative values of α. Moreover the logarithmic model, $f(R) = R + \alpha R^2 + \alpha\gamma R^2 \ln(R/\mu^2)$ [3], was also studied perturbatively for neutron and quark stars that exhibited similar trends for different γ values. The Starobinsky model was further explored non-perturbatively for neutron stars [45]. They observed that, for positive values of α, GR yielded higher maximum mass values than the Starobinsky case. They also studied the model $f(R) = R + \alpha R^2(1 + \gamma R)$ which exhibited low sensitivity on the γ value. On the other hand, for their model $R^{1-\epsilon}$, GR gave the lowest maximum mass and the mass value increased to very high values approaching 2.5 to 3 $\mathrm{M}_\odot$.

Yazadjiev et al. [231] solved for the stable configurations of neutron stars in the Starobinsky model $f(R) = R + \alpha R^2$ for increasing values of the parameter α. By constructing an equivalent scalar-tensor theory, they obtained the stellar structure non-perturbatively and compared their results with perturbative estimates. While the perturbative result was unphysical because it gave a decreasing mass with respect to the radial distance in a region interior to the star [160], no such unphysical behaviour was observed in the non-perturbative framework. Staykov et al. [213] included a slow rotation in neutron and strange stars in a non-perturbative framework of Starobinsky gravity. While the slow rotation does not affect the mass and radius with respect to the static Starobinsky case, they found a measurable increase in the moment of inertia with respect to GR.

The Starobinsky model $R + \alpha R^2$ was further studied for neutron and quark stars non-perturbatively [21]. For positive and non-zero values of α, they observed that the scalar curvature does not decrease to zero at the surface (unlike the perturbative results) and it exponentially falls off outside the star. The stellar mass contribution until the surface plus the gravitational mass contribution outside the star constitute the total mass which is actually observed by a distant observer. The gravitational redshift for the distant observer will be determined by the total (stellar + gravitational) mass. The gravitational mass contribution from the outside of the star is remarkable in distinction with the perturbative approaches where the exterior solution is assumed to be Schwarzschild. For negative values of α, they [21] found that the Ricci scalar executes a damped oscillation beyond the surface of the star and the gravitational mass contribution increases indefinitely. In an earlier works, the same authors [20] compared the prediction of the Starobinsky model and the corresponding scalar-tensor theory. Their non-perturbative analysis indicated that the star is surrounded by a dilaton sphere whose contribution to the mass is negligible.

Models of $f(R,T)$ gravity and its generalisations were studied for equilibrium configurations of compact stars. Carvalho et al. [47] considered the model $f(R,T) = R - 2\lambda T$ to find the equilibrium configurations for white dwarfs. The maximum mass limit obtained was slightly above the Chandrasekhar limit. In comparison to GR and $f(R)$ predictions, the white dwarfs were found to have larger radii as the λ value was increased from zero. Deb et al. [63] considered the same model to obtain the equilibrium stellar structure of quark stars. They demonstrated that the $\mathcal{M}$-$\mathcal{R}$ curves are different for positive, negative and zero λ values.

It is important to note that, in the Starobinsky model $R + \alpha R^2$, a maximum value of 2 $M_\odot$ or beyond is reached only when the α value is chosen to be negative [21]. However, this leads to an issue, namely, the Ricci scalar executes a damped oscillation and the gravitational mass contribution increases indefinitely in the exterior region. On the other hand, the Ricci scalar smoothly decreases to zero at infinity for positive α values, for which the star can support a maximum mass lower than 2 $M_\odot$. Thus a physical theory based on Starobinsky model requires a positive α value whence the Ricci scalar behaves properly everywhere. However, in order to reach 2 $M_\odot$ or beyond, the Starobinsky model requires modification. We therefore consider the model $f(R,T) = R + \alpha R^2 + \omega RT$ with $\alpha > 0$. This modification implies inclusion of gravity-matter interaction in the description via the term ωRT. It would be sufficient to show that the maximum mass attainable is greater than the Starobinsky prediction even if we take a simple form $R(1+\alpha R+\omega T)$, and treat ωT perturbatively on the background of non-perturbative Starobinsky solution.

In this Chapter, we obtain the field equations for spherically symmetric distribution of matter for $f(R,T) = R + \alpha R^2 + \omega RT$ to $\mathcal{O}(\omega)$. With this, we solve for equilibrium configurations of quark stars with the equation of state given by the bag model, namely, $p = k(\varepsilon - 4B)$, where $B = 60$ MeV/fm^3 is the bag constant, and we take the physical value $k = 0.28$ which is valid for strange quark mass $m_s = 250$ MeV/c^2. For the pure Starobinsky case, a maximum mass of 1.832 $\mathrm{M}_\odot$ is obtained for $\alpha = 10r_g^2$, whereas GR gives a maximum mass of 1.764 $\mathrm{M}_\odot$ [20]. On the other hand, the present model yields a maximum mass $\sim$ 2 $\mathrm{M}_\odot$, which is consistent with different observations of binary millisecond pulsars, namely, J0348+0432, J1614-2230, and J0740+6620, with pulsar masses 2.01 ± 0.04 $\mathrm{M}_\odot$ [16], 1.93 ± 0.017 $\mathrm{M}_\odot$ [64, 71], and $2.14^{+0.20}_{-0.18}$ $\mathrm{M}_\odot$ [57], respectively.

The Chapter is organized as follows. In Section 6.1, we present the details of calculation for the proposed model with gravity-matter interaction. There, we also develop a perturbative treatment as the gravity-matter interaction is expected to be small. We thus obtain the stellar equation for equilibrium configurations in spherically symmetric stars. We apply these equations to quark stars in Section 6.2 and obtain the stellar properties. Section 6.3 contains a discussion on the obtained results and the main conclusions are given in Section 6.4.

6.1 Present model

In this section we define the present model of gravity-matter interaction in $f(R,T)$ gravity. We derive the corresponding field equations, the modified TOV equations and also discuss the far-field solution.

6.1.1 Gravity-matter interaction

We consider gravity-matter interaction in a modified gravity represented by

$$f(R,T) = R + \alpha R^2 + \omega RT, \tag{6.1}$$

where the last term represents the gravity-matter interaction. This form reduces the field equation (1.139) to

$$\begin{aligned}\phi G_{\mu\nu} + \frac{1}{2}\alpha R^2 g_{\mu\nu} + 2\alpha(g_{\mu\nu}\nabla^\alpha\nabla_\alpha - \nabla_\mu\nabla_\nu)R = \kappa T_{\mu\nu}\\ + \omega\Big[R(T_{\mu\nu} - p g_{\mu\nu}) - G_{\mu\nu}T - (g_{\mu\nu}\nabla^\alpha\nabla_\alpha - \nabla_\mu\nabla_\nu)T\Big]\end{aligned} \tag{6.2}$$

where $\phi = 1 + 2\alpha R$.

The corresponding trace equation is

$$6\alpha\nabla^\mu\nabla_\mu R + [2\alpha R - \phi]R = \kappa T + \omega\left[2(T - 2p)R - 3\nabla^\mu\nabla_\mu T\right] \tag{6.3}$$

Since the gravity-matter interaction is expected to be small, we shall take a perturbative approach about the exact solutions of $R + \alpha R^2$ by assuming $|\omega T| \ll 1$. To the first order in ω, we get

$$\begin{aligned} G_{\mu\nu} + \frac{\alpha R^2}{2\phi} g_{\mu\nu} + \frac{2\alpha}{\phi}(g_{\mu\nu}\nabla^\alpha\nabla_\alpha - \nabla_\mu\nabla_\nu)R = \kappa\frac{T_{\mu\nu}}{\phi} \\ + \frac{\omega}{\phi_0}\Big[R(T_{0\mu\nu} - p g_{0\mu\nu}) - G_{0\mu\nu}T - (g_{0\mu\nu}\nabla^\alpha\nabla_\alpha - \nabla_\mu\nabla_\nu)T_0\Big] \end{aligned} \tag{6.4}$$

where the subscript "0" indicates unperturbed quantities when $\omega = 0$, so that $\phi_0 = 1 + 2\alpha R_0$. The corresponding trace equation (6.3) is obtained as

$$6\alpha\nabla^\mu\nabla_\mu R + [2\alpha R - \phi]R = \kappa T + \omega\left[2(T_0 - 2p_0)R_0 - 3\nabla^\mu\nabla_\mu T_0\right] \tag{6.5}$$

up to $\mathcal{O}(\omega)$.

Since we are interested in the spherically symmetric and static case, we assume the metric

$$ds^2 = -e^{\nu(r)}c^2dt^2 + e^{\lambda(r)}dr^2 + r^2d\Omega^2 \tag{6.6}$$

along with $\phi = \phi(r)$ and $T = T(r)$, and $d\Omega^2 = d\theta^2 + \sin^2\theta\, d\varphi^2$. Thus the above trace equation reduces to

$$\begin{aligned} 6\alpha\left[\frac{d^2}{dr^2} + \left(\frac{\nu'}{2} - \frac{\lambda'}{2} + \frac{2}{r}\right)\frac{d}{dr}\right]R - Re^\lambda = \kappa T e^\lambda \\ + \omega\left[2(T_0 - 2p_0)R_0 e^{\lambda_0} - 3\left(\frac{\nu_0'}{2} - \frac{\lambda_0'}{2} + \frac{2}{r}\right)T_0' - 3T_0''\right] \end{aligned} \tag{6.7}$$

up to $\mathcal{O}(\omega)$.

The tt-component of the field equation (6.4) yields

$$\begin{aligned} \lambda' = \frac{1 - e^\lambda}{r} + \frac{1}{6}\frac{re^\lambda}{\phi}(2 + 3\alpha R)R - \gamma\nu' + \frac{\kappa}{3}\frac{re^\lambda}{\phi}(3\varepsilon + T) \\ + \omega\left[\frac{re^{\lambda_0}}{3\phi_0}(3\varepsilon_0 - p_0 + 2T_0)R_0 - \frac{1}{\phi_0}\left(rT_0'\frac{\nu_0'}{2} + T_0\lambda_0'\right) + \frac{1 - e^{\lambda_0}}{r\phi_0}T_0\right] \end{aligned} \tag{6.8}$$

up to $\mathcal{O}(\omega)$. The rr-component yields the following equation

$$\begin{aligned} \nu' = \frac{1}{1+\gamma}\left[\kappa\frac{re^\lambda}{\phi}p + \frac{e^\lambda - 1}{r} - \frac{\alpha}{2}\frac{re^\lambda}{\phi}R^2 - \frac{4}{r}\gamma\right] \\ - \frac{\omega}{1+\gamma_0}\left[\frac{1}{\phi}\left(T_0 + \frac{rT_0'}{2}\right)\nu_0' + \frac{1}{\phi}\left(\frac{1 - e^{\lambda_0}}{r}\right)T_0 + \frac{2}{\phi}T_0'\right] \end{aligned} \tag{6.9}$$

up to $\mathcal{O}(\omega)$, where $\gamma = \frac{r}{2}(\ln\phi)'$.

6.1.2 Extended TOV equation

Covariant divergence of the field equation (1.141) yields

$$(\kappa + f_T)\nabla^{\mu}T_{\mu\nu} = f_T\left[(pg_{\mu\nu} - T_{\mu\nu})\nabla^{\mu}\ln f_T + g_{\mu\nu}\nabla^{\mu}p\right] \tag{6.10}$$

Substituting $f_T = \omega R$, we obtain

$$\nabla_{\mu}T^{\mu\nu} = \frac{\omega R}{\kappa + \omega R}\left[(pg^{\mu\nu} - T^{\mu\nu})\nabla_{\mu}\ln R + g^{\mu\nu}\nabla_{\mu}p\right] \tag{6.11}$$

For the spherically symmetric static metric (6.6), we obtain from Eq. (1.138)

$$\nabla_{\mu}T^{\mu\nu} = e^{-\lambda}p' + (\varepsilon + p)\frac{\nu'}{2}e^{-\lambda}. \tag{6.12}$$

Since Ricci scalar R and pressure p are functions of r alone, the conservation equation (6.11) becomes

$$p' = -(\varepsilon + p)\left(\frac{\kappa + \omega R}{\kappa}\right)\frac{\nu'}{2} \tag{6.13}$$

To the first order in ω, we obtain

$$p' = -(\varepsilon + p)\frac{\nu'}{2} - \frac{\omega}{\kappa}(\varepsilon_0 + p_0)R_0\frac{\nu_0'}{2}. \tag{6.14}$$

For the case of vanishing ω, we recover the original TOV equation. For $\omega \neq 0$, we designate Eq.(6.14) as the extended TOV (ETOV) equation, where the pressure gradient depends on the value of ω as well as the Ricci scalar R. It is thus evident from Eq. (6.14) that the pressure gradient inside a spherically symmetric star will change as compared to the standard GR case. However, similarly to GR, the cumulative mass $m(r)$ is related to the metric potential $\lambda(r)$ as

$$m(r) = \frac{c^2 r}{2G}\left[1 - e^{-\lambda(r)}\right]. \tag{6.15}$$

6.1.3 Far field solution

In the region exterior to the star, the trace equation (6.5) takes the form

$$6\alpha\nabla^{\mu}\nabla_{\mu}R - R = 0. \tag{6.16}$$

which is identical to that obtained for $f(R) = R + \alpha R^2$ gravity in vacuum. This suggests that the exterior solution has an identical form in both Starobinsky gravity and for the given particular form of $f(R, T)$.

For spherically symmetric static metric (6.6), this equation takes the form

$$e^{-\lambda}\left\{R'' + \left(\frac{\nu'}{2} - \frac{\lambda'}{2} + \frac{2}{r}\right)R'\right\} - \frac{R}{6\alpha} = 0 \tag{6.17}$$

We note that the Starobinsky correction αR^2 is a very weak contribution as one approaches infinity. This is also immediately obvious from the above equation because the last term dominates in the limit $\alpha \to 0$ giving us back $R = 0$. Thus the choice of the Starobinsky form $R+\alpha R^2$ has to coincide with the solution of Einstein gravity at infinity. In order to see how the Einstein limit is approached at infinity, we must do an approximate analysis of Eq. (6.17). Since ν and λ and their first derivatives are expected to approach zero on approaching infinity (also confirmed by exact numerical calculations), we can approximate Eq. (6.17) to the form

$$R'' + \frac{2}{r}R' - \frac{R}{6\alpha} = 0 \tag{6.18}$$

Solution of this equation is given by

$$R(r) = c_1 \frac{e^{-r/\sqrt{6\alpha}}}{r} + c_2 \frac{\sqrt{6\alpha}}{2}\frac{e^{r/\sqrt{6\alpha}}}{r} \tag{6.19}$$

Since $R \to 0$ as $r \to \infty$, we have to set the integration constant $c_2 = 0$, giving

$$R(r) = c_1 \frac{e^{-\frac{r}{\sqrt{6\alpha}}}}{r}, \tag{6.20}$$

which approaches zero faster than r^{-1} as $r \to \infty$ for positive value of α. However, for negative values of α, the far field solution given by (6.19) is oscillatory in nature implying that negative α values are unphysical.

6.2 Quark stars with gravity-matter coupling

In this section, we examine in detail the stellar structure of quark stars in the modified gravity model $f(R,T) = R+\alpha R^2+\omega RT$ that incorporates gravity-matter interaction. In massive compact stars (such as quark stars and neutron stars), we expect the gravitational field to be strong enough so that the gravity-matter coupling has a appreciable contribution. With the above choice of $f(R,T)$ gravity, Sections 6.1.1 and 6.1.2 give a perturbative solution on the background of unperturbed Starobinsky gravity given by $f(R) = R+\alpha R^2$. The field equations (6.8), (6.9), (6.14), together with the trace equation (6.7), are reduced to a set of five first order differential equations, given by

$$R' = \Psi, \tag{6.21}$$

$$\begin{aligned}\Psi' = -\frac{2}{r}\Psi + \frac{\kappa}{6\alpha}Te^{\lambda} + \frac{e^{\lambda}}{6\alpha}R + \frac{\lambda' - \nu'}{2}\Psi \\ + \frac{\omega}{6\alpha}\left[2(T_0 - 2p_0)R_0 e^{\lambda_0} - 3\left(\frac{\nu_0'}{2} - \frac{\lambda_0'}{2} + \frac{2}{r}\right)T_0' - 3T_0''\right],\end{aligned} \tag{6.22}$$

$$\lambda' = \frac{1-e^{\lambda}}{r} + \frac{1}{6}\frac{re^{\lambda}}{\phi}\left(2+3\alpha R\right)R - \gamma\nu' + \frac{\kappa}{3}\frac{re^{\lambda}}{\phi}\left(3\varepsilon + T\right)$$
$$+ \ \omega\left[\frac{re^{\lambda_0}}{3\phi_0}(3\varepsilon_0 - p_0 + 2T_0)R_0 - \frac{1}{\phi_0}\left(rT_0'\frac{\nu_0'}{2} + T_0\lambda_0'\right) + \frac{1-e^{\lambda_0}}{r\phi_0}T_0\right], \quad (6.23)$$

$$\nu' = \frac{1}{1+\gamma}\left[\kappa\frac{re^{\lambda}}{\phi}p + \frac{e^{\lambda}-1}{r} - \frac{\alpha}{2}\frac{re^{\lambda}}{\phi}R^2 - \frac{4}{r}\gamma\right]$$
$$- \frac{\omega}{1+\gamma_0}\left[\frac{1}{\phi_0}\left(T_0 + \frac{rT_0'}{2}\right)\nu_0' + \frac{1}{\phi_0}\left(\frac{1-e^{\lambda_0}}{r}\right)T_0 + \frac{2}{\phi_0}T_0'\right], \quad (6.24)$$

$$p' = -(\varepsilon + p)\frac{\nu'}{2} - \frac{\omega}{\kappa}(\varepsilon_0 + p_0)R_0\frac{\nu_0'}{2}, \quad (6.25)$$

where we have defined a new field variable $\Psi = R'$.

To complete the solution of the above equations, we take the equation of state of the quark star as that of quark-gluon plasma given by the bag model [96, 204], namely, $p = k(\varepsilon - 4B)$, where $B = 60$ MeV fm^{-3} (or $B^{1/4} \approx 147$ MeV) is the bag constant and the value of the constant k is associated with the choice of the QCD coupling constant (α_c) and the mass (m_s) of strange quark; $k = 0.33$ if $m_s = 0$ and $k = 0.28$ for the realistic value $m_s = 250$ MeV/c^2. The values $B^{1/4} \approx 147$ MeV and $m_s = 250$ MeV correspond to the QCD coupling constant $\alpha_c = 0$, as seen from Figure 1 in Ref. [69].

Consistency of the perturbation theory requires $|\omega T| \ll 1$ at all densities. This condition is satisfied throughout the star if one requires that $|\omega T| \ll 1$ is true at the center. By defining

$$\omega = \frac{\beta}{4B}, \quad (6.26)$$

this condition becomes $(1-3k)\beta\frac{\varepsilon_c}{4B} + 3\beta k \ll 1$. For the choice of $\beta \sim 10^{-2}$ and $\frac{\varepsilon_c}{4B} \sim 10$, $|\omega T_c| \approx 4.48 \times 10^{-2}$, thus ensuring the validity of the perturbative approach.

We solve field equations (6.21)–(6.25) numerically upon making them dimensionless by defining $\eta = r/r_g$, $\chi = Rr_g^2$, $\chi_0 = R_0 r_g^2$, $\xi = \Psi r_g^3$, $\tilde{p} = p/4B$, $\tilde{p}_0 = p_0/4B$, $\tilde{\varepsilon} = \varepsilon/4B$, $\tilde{\varepsilon}_0 = \varepsilon_0/4B$, $\tilde{T} = T/4B$ and $\tilde{T}_0 = T_0/4B$, where $r_g = GM_\odot/c^2 = 1.4766 \times 10^5$ cm, is taken as the scaling parameter.

The numerical integrations of the above set of differential equations are carried out by requiring that the metric is asymptotically flat at infinity for the initial conditions $\lambda(0) = 0$ and $\nu(0) = \nu_c$. Since the metric potential $\nu(r)$ enters the field equations only through its derivatives, the central value ν_c remains arbitrary and fixed by specifying a value that satisfies $\nu \to 0$ for $r \to \infty$. The same initial conditions are imposed on the unperturbed metric, that is, $\lambda_0(0) = 0$ and $\nu_0(0) = \nu_{0c}$. The central value of pressure $p(0) = p_c$ is assigned by the equation of state for a given central density ρ_c. Correspondingly, the unperturbed pressure takes the value $p_0(0) = p_c$. The surface of the star is identified at a

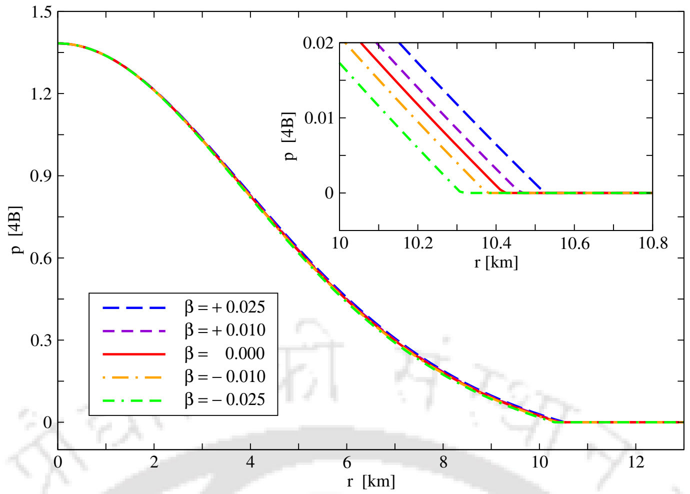

Figure 6.1: Radial profile of pressure $p(r)$ for different values of β ($\beta = 4B\omega$) with central density $\rho_c = 2.5414 \times 10^{15}$ g cm^{-3}. The inset shows the pressure profile near the stellar radius r_s for different values of β.

radial distance r_s (stellar radius) for which the pressure p vanishes. Moreover, since the value of the scalar curvature is maximum at the center, and it gradually decreases towards the surface, we have the boundary condition $\Psi(0) = 0$.

A unique choice for the central value of the scalar curvature in both the unperturbed scenario (Starobinsky gravity) and the actual case requires the knowledge of the exterior solution. This requires one to continue the integration outside the star with boundary conditions $\lambda(r_s) = \lambda_s$, $\nu(r_s) = \nu_s$, $R(r_s) = R_s$ and $\Psi(r_s) = \Psi_s$ at the surface, obtained from the interior solution for an initial guess for R_c. To set the above initial conditions, we first carry out a numerical integration for the unperturbed case, with similar boundary conditions $\lambda_0(r_s) = \lambda_{0s}$, $\nu_0(r_s) = \nu_{0s}$, $R_0(r_s) = R_{0s}$ and $\Psi_0(r_s) = \Psi_{0s}$, imposed for an initial guess R_{0c}.

For convenience, the initial guess in both the cases are taken to be the GR value ${}^{E}R_c = \kappa(\rho_c c^2 - 3p_c)$ since this value is not too far from the required values. The integration is carried out several times for different initial guesses until the required conditions $R \to 0$ and $|\Psi| \to 0$ as $r \to \infty$ and $R_0 \to 0$ and $|\Psi_0| \to 0$ as $r \to \infty$ are satisfied. This procedure gives the correct central values R_c and R_{0c}, which are found to be lower than the GR value. For the sake of accuracy, we fine-tune χ_c $(= R_c r_g^2)$ and χ_{0c} $(= R_{0c} r_g^2)$ up to twelve decimal figures by taking the exterior solution as far as $\eta_{\max}$ $(= r_{\max}/r_g)$, where $\eta_{\max}$ satisfies $\chi(\eta_{\max}) \sim 10^{-12}$ and $\chi_0(\eta_{\max}) \sim 10^{-12}$.

In the original framework of general relativity, the Ricci scalar vanishes immediately outside the surface, the trace equation being $R = -\kappa T$. In our present case, the vacuum solution is given by Eq. (6.16) and the Ricci scalar does not vanish but decays exponentially outside the star, as also implied by the far-field solution, Eq. (6.20). This gives rise to two distinct masses [20], namely, the stellar mass $M_s = m(r_s)$, the mass within the stellar

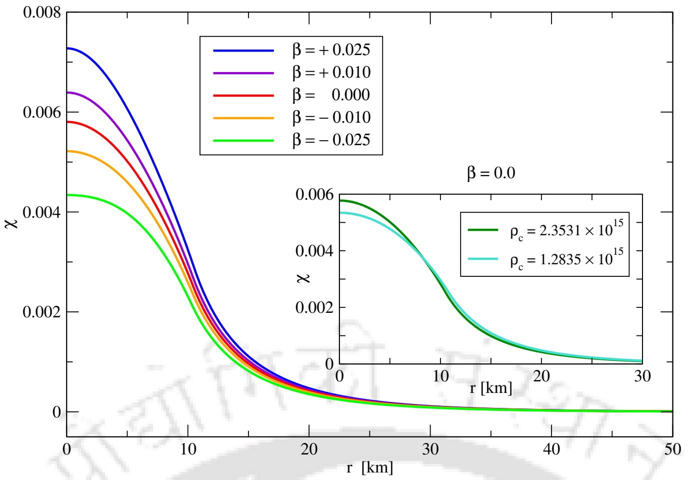

Figure 6.2: Radial profile of scalar curvature $R(r)$ for different values of β ($\beta = 4B\omega$) with central density $\rho_c = 2.5414 \times 10^{15}$ g cm^{-3}. The inset shows the scalar curvature profile for the Starobinsky model ($\beta = 0$) with two different central densities ρ_c (in g cm^{-3}).

radius r_s, and the mass M as seen by a sufficiently distant observer, estimated as

$$M = \frac{c^2}{2G} r_{\max} \left\{1 - e^{-\lambda(r_{\max})}\right\} \tag{6.27}$$

Since the numerical calculations are sufficiently accurate with a sufficiently large value of $r_{\max}$, this estimate for M is expected to be close to the one for $r \to \infty$.

In the following subsections, we analyze the exact numerical solutions of the field equations given by Eqs. (6.21)–(6.25) with the boundary conditions discussed above for quark stars with the equation of state given by the bag model. We also compare these results with the Starobinsky case, $\omega = 0$. We take $\alpha = 10r_g^2 = 2.1804 \times 10^{11}$ cm^2 (that is, $\sqrt{\alpha} = 3.16r_g = 4.6694 \times 10^5$ cm), which is smaller than the estimated upper bound $\sqrt{\alpha} < 7 \times 10^7$ cm as predicted by binary pulsar data [150].

6.2.1 Interior and exterior solutions

In this sub section we elaborate upon the interior and exterior solutions by looking at the radial profiles for pressure $p(r)$, mass $m(r)$ and Ricci scalar $R(r)$.

Figure 6.1 plots pressure p as a function of the radial coordinate r for the central density $\rho_c = 2.5414 \times 10^{15}$ g /cm^3 for $\beta = 0.025$, 0.01, -0.01 and -0.025. We see that the magnitude of pressure gradient increases (decreases) with respect to the pure Starobinsky case ($\beta = 0$) for positive (negative) value of β (or ω) due to the additional term in the extended TOV equation (6.25). This in fact pushes (pulls) the stellar boundary outward (inward) as compared with the pure Starobinsky case. The slight increase (decrease) in stellar radius r_s for positive (negative) values of β (or ω) can be seen in the inset of Figure 6.1.

Radial profiles of the scalar curvature $R(r)$ for different values of β with central density

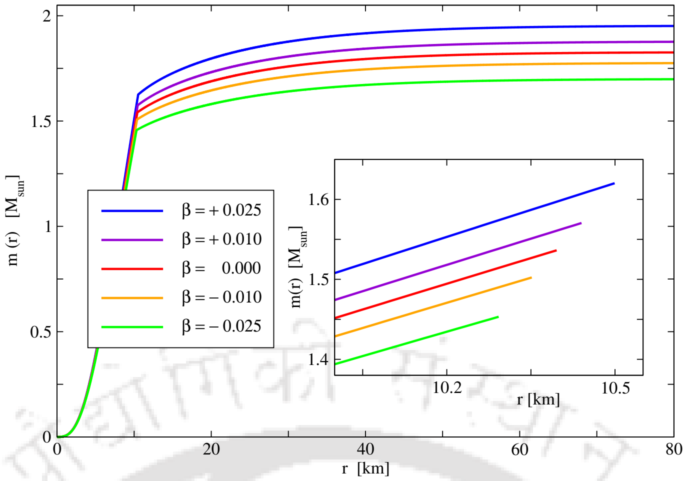

Figure 6.3: Radial profile of total mass $m(r)$ for different values of β ($\beta = 4B\omega$) with central density $\rho_c = 2.5414 \times 10^{15}$ g cm^{-3}. The inset shows the interior mass profile up to the stellar radius r_s.

$\rho_c = 2.5414 \times 10^{15}$ g /cm^3 are shown in Figure 6.2. It may be observed that the choice of the central scalar curvature R_c is strongly correlated with β (or equivalently ω) in that the value of R_c increases with increasing values of ω. On the other hand, when we fix $\beta = 0$ and vary ρ_c, the central value R_c is found to be higher for a higher value of ρ_c as shown in the inset of Figure 6.2. Although there is an increase in the value of R_c when ρ_c is increased, the scalar curvature R falls off rapidly for higher value of ρ_c than for the lower one. In the former case (with fixed ρ_c and varying β), the Ricci scalar maintains higher values throughout the star for higher value of β.This is consistent with the fact that the perturbative ω terms in Eq.(6.22) add with the term $\frac{\kappa}{6\alpha}Te^{\lambda}$, so that the effective value of T changes which is equivalent to a changed value of matter content with respect to the Starobinsky case. Since these perturbative terms disappear outside the star, they act as if they were an additional matter content in Starobinsky gravity.

Figure 6.3 shows the total mass profile $m(r)$ with $\rho_c = 2.5414 \times 10^{15}$ g /cm^3 for different values of β. The inset represents the mass profile up to the stellar surface $r = r_s$. In comparison with Starobinsky gravity ($\beta = 0$), we observe a slight increase (decrease) in the stellar mass M_s and stellar radius r_s when β is positive (negative). Further we observe that these changes in stellar mass M_s and radius r_s are larger for $\beta = \pm 0.025$ than $\beta = \pm 0.01$. On the other hand, we see that the mass M measured by a distant observer increases appreciably with increasing β.

As seen from Figure 6.2, the scalar curvature does not decrease to zero at the surface of the star and it falls off outside the star. This fall-off is similar to a Yukawa function (as shown in Section 6.1.3). There is a gravitational mass contribution due to the non-vanishing scalar curvature outside the star. The mass profiles shown in Figure 6.3 contains both contributions, stellar plus gravitational. The inset shows only the stellar mass contribution that does not extend beyond the stellar radius $r_s \sim 10$ km. The main graphs in

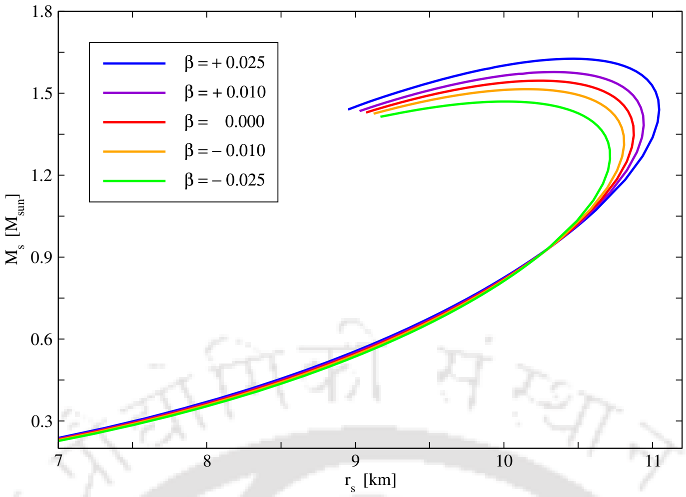

Figure 6.4: Mass-radius relation (between stellar mass M_s and stellar radius r_s) for different values of β.

Figure 6.3 show both contributions (stellar plus gravitational) extending beyond $r_s \sim 10$ km. We see that the combined mass profiles approach asymptotic values for large r (~ 60 km). A sufficiently distant body experiences the gravitational field of the combined mass.

6.2.2 Mass-radius relations

In this section we study the mass-radius ($\mathcal{M} - \mathcal{R}$) relations obtained from the field equations for a continuous range of central density ρ_c or equivalently the central Ricci scalar R_c. In addition, we verified that all energy conditions are satisfied.

Fig. 6.4 represents the relation between stellar mass M_s and stellar radius r_s for different values of β. We see that for a particular value of M_s, r_s increases with increase in β in the higher mass regime. In the same regime, if we fix r_s, M_s is found to increase with increasing β. This fact signify that the presence of the ω terms strengthens the effect of gravity to balance the increased pressure gradient as inferred from the pressure profiles studied in Section 6.2.1.

Figure 6.5 presents the mass M measured by a distant observer against the stellar radius r_s for different values of β. As noted earlier, the mass M consists of contributions from both the stellar mass and non-vanishing scalar curvature extending beyond the stellar radius r_s. This mass was calculated up to a sufficiently high radial distance ($r_{\max}$) until the scalar curvature approached very close to zero with the condition given by Eq. (6.27). The relationship between the curves in Figure 6.5 bear similarity with those in Figure 6.4 giving qualitatively similar conclusion. However we note the important fact that maximum observed mass M^* are appreciably higher than those in Fig. 6.4.

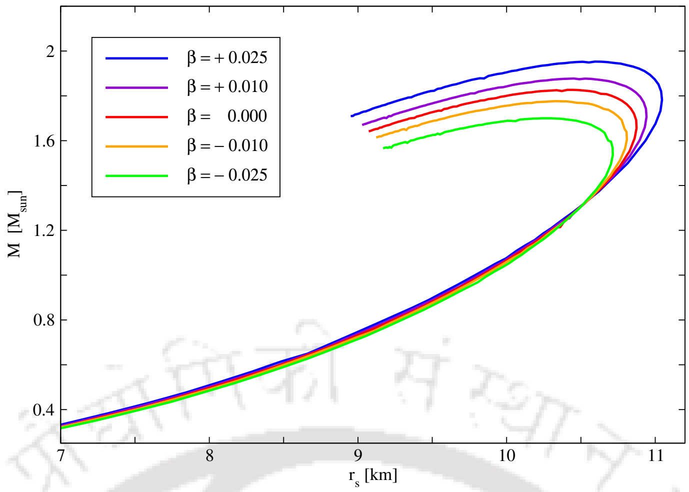

Figure 6.5: Total mass M measured by a distant observer versus stellar radius r_s for different values of β.

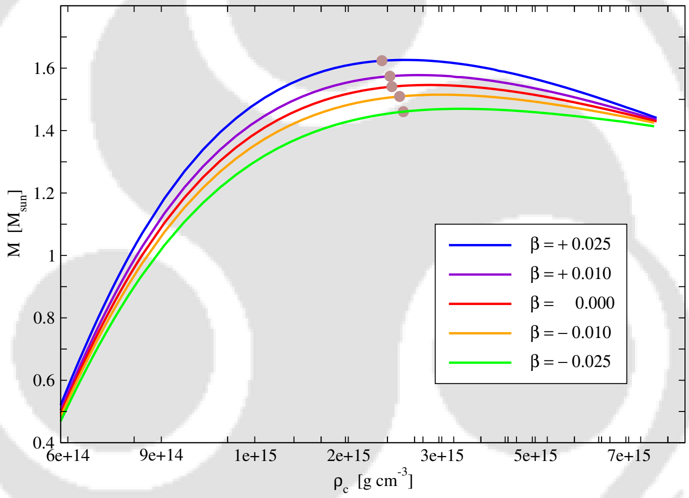

Figure 6.6: Stellar mass M_s versus central density ρ_c for different value of β, where the mass M_s^* is shown by open circle.

6.2.3 Stability and energy conditions

In this section, we study mass versus central density to find the maximal mass from the stability of equilibrium configurations. The stable configuration corresponds to the region in the mass-central density curve where $\frac{\partial M}{\partial \rho_c} > 0$, whereas the unstable region is given by $\frac{\partial M}{\partial \rho_c} < 0$ [197]. The onset of instability is identified as the point where $\partial M/\partial \rho_c = 0$, and the mass corresponding to this point is the maximal.

To study the stability, we first examine stellar mass M_s versus central density ρ_c in Fig. 6.6 for different values of β. We see that the maximal stable mass M_s^* (corresponding to the maximal total mass M^*) increases as β increases from $\beta = -0.025$ to $\beta = +0.025$.

A similar trend is observed in Fig. 6.7, where the mass M observed by a distant observer is plotted against the central density ρ_c. Here we see that the maximal mass M^*

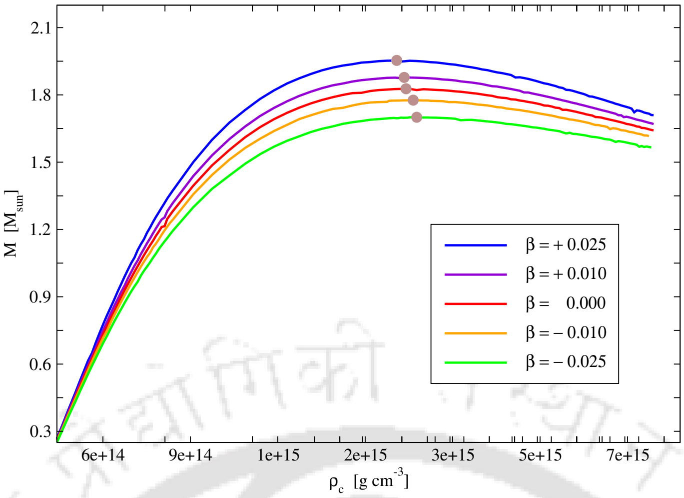

Figure 6.7: Total mass M versus central density ρ_c for different value of β, where the maximal mass M^* is shown by open circle.

(denoted by the open circle in the figure) shift to appreciably higher value with respect to the stellar values M_s^*.

Table 6.1 displays maximal mass values M^* observed by a distant observer for different values of β. The corresponding stellar mass values M_s^*, stellar radius r_s^*, central Einstein Ricci scalar ${}^E R_c^*$, central Starobinsky Ricci scalar R_{0c}^*, central Ricci scalar R_c^*, and central density ρ_c^* are also displayed. We see that the maximal mass value M^* increases and approaches $\sim$ 2 $\mathrm{M}_\odot$ as β is increased. We note that this increase is appreciable even for very small magnitudes of β, suggesting a measurable effect played by gravity-matter interaction.

We verify the validity of the perturbative results by estimating the maximal value of ωT corresponding to the maximal mass. For $\beta = 0.025$ (or $\omega = 0.025/4B$) and central density $\rho_c^* = 2.4173 \times 10^{15}$ g/cm^3, we get $|\omega T_c| = (1 - 3k)\beta\rho_c c^2/4B + 3\beta k = 4.36 \times 10^{-2}$. Thus the maximum value of ωT is of the order of 10^{-2}, giving assurance to the validity of the perturbative results.

Figure 8 displays the energy conditions [215], namely, null energy condition ($\varepsilon \geq 0$), weak energy condition ($\varepsilon + p \geq 0$), strong energy condition ($\varepsilon + 3p \geq 0$), and dominant energy condition ($\varepsilon - |p| \geq 0$). We see that all energy conditions are satisfied because they are positive in the entire region of the star. These energy conditions are valid to a good approximation since they are large throughout the star (lying between $\sim$ 1 and $\sim$ 10 in the units of $4B$) compared to the highest perturbation ($\sim 10^{-2}$ at the centre).

6.3 Discussion

In the original case of Einstein's gravity, the Ricci scalar is a linear function of the central density, expressed as $\chi = \kappa r_g^2\{(1 - 3k)\rho c^2 + 12kB\}$. One might expect such a linear

Table 6.1: Maximum stable mass M^* for different values of ω. The corresponding values of stellar mass M_s^*, stellar radius r_s^*, central Einstein Ricci scalar ${}^{E}R_c^*$, central Starobinsky Ricci scalar R_{0c}^*, central Ricci scalar R_c^* and central density ρ_c^* are also displayed.

β	ρ_c^* (g cm^{-3})	${}^{E}R_c^*$ ($10^{-2} r_g^{-2}$)	R_{0c}^* ($10^{-3} r_g^{-2}$)	R_c^* ($10^{-3} r_g^{-2}$)	r_s^* (km)	M_s^* (M$_\odot$)	M^* (M$_\odot$)
− 0.025	2.6526×10^{15}	3.189908	5.81876	4.286802	10.2686	1.46058	1.70031
− 0.01	2.6098×10^{15}	3.162040	5.81296	5.209743	10.3482	1.50937	1.77659
0.0	2.5242×10^{15}	3.106321	5.80072	5.800721	10.4265	1.54080	1.82725
0.01	2.5029×10^{15}	3.092391	5.79744	6.375852	10.4790	1.57427	1.87787
0.025	2.4173×10^{15}	3.036672	5.78384	7.180354	10.5851	1.62390	1.95371

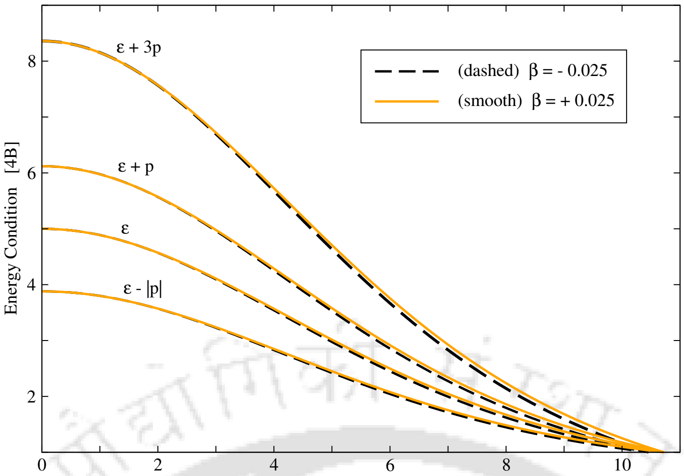

Figure 6.8: Radial profiles of energy conditions (ECs): null energy condition ($\varepsilon \geq 0$), weak energy condition ($\varepsilon + p \geq 0$), strong energy condition ($\varepsilon + 3p \geq 0$), and dominant energy condition ($\varepsilon - |p| \geq 0$).

relationship in the Starobinsky model in the low density regime where $\alpha R \ll 1$. Besides, the same behaviour is expected in the present model for low central densities where the term R dominates over αR^2 and ωRT. However, the situation is completely different in the high density regime in both Starobinsky and the present model. In the Starobinsky model, we found that at higher central densities, the central Ricci scalar R_{0c} varies slowly as a function of ρ_c, as shown in Figure 6.9. On the other hand, in the present model, depending on the sign of β (or ω), we find that the central Ricci scalar R_c would either increase or decrease with respect to the Starobinsky case. Figure 6.9 shows the variation of central Ricci scalar with respect to central density for different values of β. For positive β, we see that the R_c value increases compared to the Starobinsky model in the higher density regime. This was expected since the additional terms in the present model contribute at higher densities as previously noted in Section 6.2.1. The opposite is true for the case of negative β values where we found that the central Ricci scalar R_c values lie below the Starobinsky values for higher densities as shown in Figure 6.9. This happens because $\mathcal{O}(\omega)$ term gives a negative contribution in this case.

For any positive β, the curve in Figure 6.9 lies above the Starobinsky case, so that maximum mass values higher than the Starobinsky case would be obtained. On the other hand, the curve for any negative β lies below the Starobinsky case implying that the maximum mass values lower than the Starobinsky case would be obtained.

It may be recalled from the discussion in Introduction that, in the Starobinsky gravity ($\omega = 0$), the star is surrounded by a gravitational halo since the Ricci scalar is non-vanishing outside the star. In fact we see the same behaviour from Figure 6.2 in the present model ($\omega \neq 0$) as well. The far-field solution (given by equation 6.20) shows that the Ricci scalar (and the gravitational halo) falls off exponentially as $r \to \infty$.

Moreover, it is evident from Figure 6.2 that this fall-off is faster for higher values of the

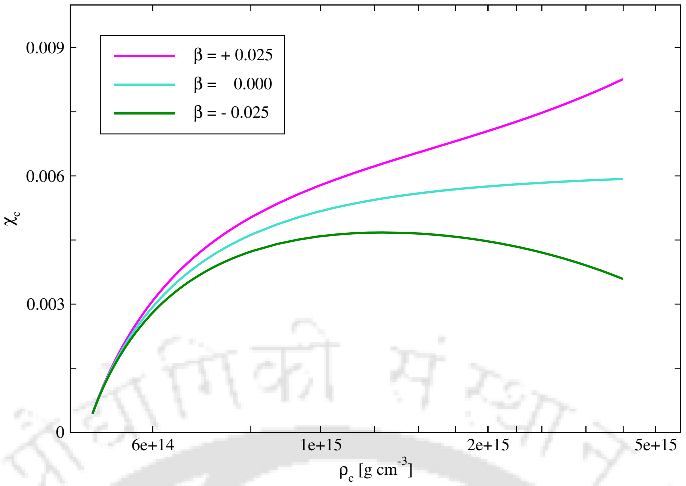

Figure 6.9: Central value of Ricci scalar χ_c $(= Rr_g^2)$ versus central density ρ_c for different values of β, namely, $\beta = \pm 0.025$ and $\beta = 0$.

central density ρ_c. Figure 6.10 plots an effective radius $r_{\rm H}$ of the gravitational halo (defined by $\chi(\eta_{\rm H}) = 10^{-7}$) with respect to the central density ρ_c until the onset of gravitational instability at ρ_c^*. (Densities beyond the threshold ρ_c^* are outside the scope of the present theory for equilibrium configurations.) It is seen from the right-hand part of the graphs in Figure 6.10 that the radius of the halo $r_{\rm H}$ decreases with increasing central density ρ_c. At the same time, the value of $r_{\rm Sch} = \frac{2GM}{c^2}$ increases with increasing central density ρ_c, as seen from Figure 6.7. These two opposite behaviours (shrinking and expansion) continue as ρ_c increases. Thus it is apparent that, when the star collapses to a black hole (with an infinite central density), the gravitational halo would shrink and will be well inside the horizon, leading to a vanishing Ricci scalar outside the horizon. This scenario is consistent with the fact that when the coefficient of R^2 term is positive, the only static spherically symmetric solution of a black hole with a regular horizon is the Schwarzschild solution, as shown in Ref. [143].

6.4 Conclusion

In this Chapter, we considered a form of $f(R, T)$ gravity that includes a coupling between gravity and matter on the background of the Starobinsky model. While the Starabinsky model takes account of quantum fluctuations [210] and $f(R, T)$ gravity may arise due to quantum effects [84], a coupling between matter and gravity is expected to bring about the features in quark stars where the gravitational field is extremely strong. In particular, the stellar structure of quark stars, with equation of state coming from the bag model, is expected to undergo an measurable change due to this coupling. Moreover, we speculate that the maximum mass limit would change appreciably so that astrophysical observations on binary pulsars could be given a theoretical basis.

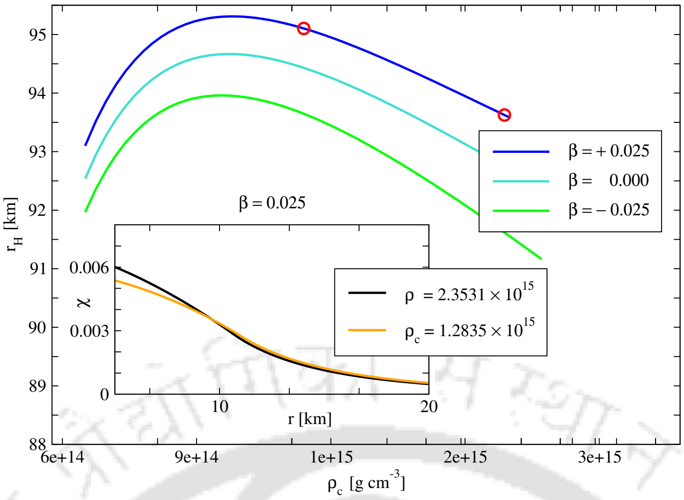

Figure 6.10: The radius of gravitational halo r_{H} versus the central density ρ_c until the onset of gravitational instability at ρ_c^*. The inset shows that the radial profiles for the scalar curvature χ (corresponding to the points denoted by the open circle in the main graph) falls off faster for a higher density, similar to the Starobinsky case ($\beta = 0$), as shown in the inset of Figure 6.2.

The Starobinsky model has been applied to quark stars by other authors [20, 21] to find their stellar structure. This produced a different stellar structure from the pure GR case and it was found that the maximum mass limit increased from the GR case due to an additional contribution from gravitational mass enveloping the stellar mass. In the present case, we find that this mass is further increased due to additional contribution from the coupling between gravity and matter (for positive values of ω).

To assert the above features, it was sufficient to treat the gravity-matter coupling as a perturbation keeping in mind that the coupling constant is sufficiently small for the validity of the perturbation treatment. We adopted this perturbation treatment in the background of unperturbed solutions of the Starobinsky case. Remarkably, such a treatment gives physically acceptable solutions for both signs of the coupling constant ω representing the strength of gravity-matter interaction.

The gravity-matter coupling term increases (decreases) the magnitude of the pressure gradient $p'(r)$ for positive (negative) values of ω pushing (pulling) the stellar boundary outward (inward) as compared to the pure Starobinsky case. Moreover the strength ω of the gravity-matter coupling determines the central value of the scalar curvature R_c for a given central density ρ_c. The scalar curvature maintains higher (lower) values throughout the star compared to the pure Starobinsky case for positive (negative) values of ω as the effective matter content increases (decreases) within the star. It is interesting to see that, although there is small increase (decease) in the stellar mass M_s for positive (negative) values of ω, the gravitational mass contribution enveloping the star increases (deceases) appreciably with respect to the Starobinsky case. This is because of the increased (decreased) scalar curvature exterior to the star contributing a greater (lesser) gravitational mass than the Starobinsky case. Consequently the quark star can support higher values of maximal total mass (M^*) than the Starobinsky case for positive values of ω.

Recent observations of binary millisecond pulsars, have yielded the pulsar masses to be ~ 2 M$_\odot$ [16, 57, 64, 71]. Such a high value of mass cannot be explained by models based on hyperon or boson condensate equations of state for neutron stars, leading to their possibility of being quark stars. We see that our present model with gravity-matter coupling, although treated as a perturbation, is capable of supporting high values of masses of quark stars.

In Chapters 4 and 5, we have seen that general relativity works very well at the scale of white dwarfs because of the fact that the observed Chandrasekhar's limit could be explained well within the framework of general relativity. On the other hand, we have seen in this Chapter that extended gravity works well at the scale of neutron stars or pulsars. This implies that the extended gravity scenario is a better formulation for higher energy scales. We may thus guess that the extended gravity scenario should give reliable estimates for physical processes with even higher energy scales such as in the inflationary and reheating phases of the Universe. We shall pursue this motivation in the next Chapter.

Chapter 7

Reheating after inflation in an extended gravity scenario

We have seen in the previous chapter that the extended gravity scenario is capable of explaining observations at the scale of compact stars such as neutron stars and pulsars. This implies that the extended gravity scenario works well at high energy scales.

It would therefore be interesting to study the consequences of the extended gravity scenario at very high energy scales such as in the inflationary and reheating phases of the Universe. With this motivation, in this chapter, we employ a viable $f(R)$ gravity model capable of giving an inflationary phase in order to study the subsequent reheating phase due to particle creation at the expense of energy in the scalaron field. Since quantum mechanics is expected to play a dominant role in particle creation, we formulate a plausible scenario of reheating obeying Heisenberg's uncertainty principle that imposes constraints on the particles that can be created in the configuration space. We show that, so long as the energy available in the scalaron field is sufficient to populate the entire configuration space, the energy density of the particles grows, attaining a maximum value giving an efficient reheating. Beyond this maximum, the available energy becomes insufficient to populate the entire configuration space leading to a declining energy density.

We further find that there is a negligible growth of energy density in the inflationary phase that lasts for $\sim 10^2\, t_{\rm P}$, although particles are constantly created in this phase. The subsequent reheating phase spans for $\sim 10^{11}\, t_{\rm P}$ and it begins with a well-defined preheating stage lasting for $\sim 10^5\, t_{\rm P}$, making a cross-over to a thermalization regime. The temperature at the cross-over is found to be $T_{\rm x} \sim 10^{12}$ GeV corresponding to a temperature of $T_r \sim 10^{13}$ GeV at the end of reheating.

The standard Friedmann model of cosmology [173, 227] has explained several observed features of our Universe such as primordial nucleosynthesis [70], abundances of

---

The content of this chapter will be available as arXiv preprint: A. Mathew & M. K. Nandy, Primordial reheating in $f(R)$ cosmology by spontaneous decay of scalarons, (preprint December 2020).

the light elements [194], the cosmic microwave background (CMB) radiation [130, 174], the Hubble expansion [214], apart from the fact that it has the well-known problem of the Big-Bang singularity. Moreover, after the observation of CMB radiation [175], the standard Friedmann model failed in several aspects giving rise to the monopole problem, the horizon problem, the flatness problem and the problem of large-scale structure formation [111, 227]. To solve these problems, it was suggested by Guth [79], Linde [116–118], Albrecht and Steinhardt [4] and others [209] that the universe underwent a fast exponential expansion, dubbed inflation, prior to the radiation dominated phase. A lot of efforts have been expended in understanding the inflationary era [120]. While Guth connected it to a first-order phase transition in a Grand Unified Theory, Linde and others [119–121] proposed slow-roll models with one or more inflaton fields driving the inflationary phase. Moreover, these theories can explain the subsequent radiation era via a reheating phase where the inflation field decays to generate Standard Model particles [102, 108, 109]. It is however not clear at the outset the intrinsic origin of the postulated inflaton field. Although initially the inflation field was understood to be the Higgs field of the Standard Model, it was later realized that observational data did not fit this assumption [29].

Interestingly, Satrobinsky [210] proposed a higher order theory of gravity that addressed the problem of Big-Bang singularity. He considered the Einstein field equation $G_{\mu\nu} = \kappa\langle T^{\rm QM}_{\mu\nu}\rangle$ with the right-hand side given by the vacuum expectation value due to quantum matter fields (having different spins) in the background of the classical gravitational field, with the assumption of isotropy and homogeneity in the absence of radiation field. The vacuum expectation value $\langle T^{\rm QM}_{\mu\nu}\rangle$ is determined by Riemann geometric quantities in the one-loop approximation [31, 38, 60]. The ensuing solution was found to be of non-singular de-Sitter type that analytically continues to the region $t < 0$. Thus an inflationary scenario, in the form of a de-Sitter phase, follows without the need for an inflaton field in the theory.

In addition, it is important to understand the origin of the radiation dominated era following the inflationary phase. In fact, there have been a few studies on particle creation due to varying gravitational field [36, 165–167, 232, 233]. Importantly, it was found that the particle production rate depends on the invariants of the Riemann curvature tensor for the creation of massless scalar particles in a weak Bianchi type-one metric [233]. For instance, the production rate of massless scalar particles in a weakly anisotropic metric goes like $C_{\alpha\beta\gamma\sigma}C^{\alpha\beta\gamma\sigma}$, where $C_{\alpha\beta\gamma\sigma}$ is the Weyl tensor. An analogous rate for the production of photons and neutrinos also holds true [233]. It was further shown that the graviton production rate in an isotropic metric is proportional to the square of the Ricci scalar [233]. Moreover, in the Starobinsky scenario, it is demonstrated that particles are created via decay of scalarons during the rapid oscillatory phase following the inflationary regime [212], giving rise to a thermalized radiation dominated era [221].

Ford [72] considered creation of particles due to a transition from a de-Sitter phase to another Robertson-Walker universe. He suggested that gravitational particle creation could be a dominant mechanism when the damping of the inflaton field is inefficient in the new inflation models that suffer from the difficulty of inefficient reheating in order to meet two conflicting criteria, namely, a sufficient inflation along with small density fluctuations, requiring a weak coupling between the inflaton and matter fields.

Mijic et. al. [144] considered a gravitational Lagrangian augmented by a quadratic term ϵR^2. This leads to a rapid oscillatory phase following the inflationary phase that may be viewed as coherent oscillations [221], collectively called scalarons, which are responsible for the creation of particles by exciting the matter fields. Considering a scalar matter field, it was found that the amplitude of the wave function follows a Schrödinger-like equation with the potential determined by the scale factor and the Ricci scalar [144]. An approximate solution for the particle production rate due to transition between initial and later stages turned out to be proportional to $R^2/\sqrt{\epsilon}$ having a $\pi/2$ phase shift in R. Identifying the reheating temperature with the energy density created in the early few oscillations led to bounds on the parameter ϵ by requiring that the reheating temperature must lie between two extremes determined by baryogengesis and GUT phase transition. This leads to a wide window for the value of ϵ which has the possibility of being narrowed down by considering perturbations in the inflationary phase.

Recently, Appleby et al. [17] considered dark energy $f(R)$ models that suffer from the weak singularity problem with the issue of the scalaron mass overshooting the Planck mass. They considered curing these pathological conditions by adding a term quadratic in the Ricci scalar so that a primordial inflationary phase could be invoked along with a late-time de-Sitter phase. However, such combined models were found to give insufficient reheating with a different primordial power spectrum index. Despite the additional R^2 term, the behaviour in the primordial period is entirely different from the original R^2 inflationary model. This suggests a profound influence of such modified dark energy models on the dynamics in the primordial phase. Their numerical solutions show abrupt jumps and very few oscillations following the de-Sitter phase which is a completely different behaviour from the standard oscillatory phase of the pure R^2 model. Moreover, this regime indicates inadequate reheating and the growth rate goes like $a \sim t^{1/2}$. This may signal that the universe goes into the present de-Sitter phase after an inflationary phase without a radiation or matter dominant era. However, upon considering the back-reaction, the behaviour was found to be significantly different from those without back-reaction, but the conclusions remained almost the same as before. Whereas their work was carried out in Jordan frame, Motohashi and Nishizawa [147] analyzed the same problem in the Einstein frame and gave constraints on the parameters involved.

In this Chapter, we consider the modified gravity model $f(R) = R+\alpha R^2+\beta R^2 \ln R/\mu^2$ in the Jordan frame. This functional form originates from considering one-loop vacuum fluctuations for a scalar field coupled to an electromagnetic field living in a de-Sitter spacetime [202]. This functional form nearly corresponds to a Robertson-Walker spacetime (with varying curvature) upto a good approximation for $\alpha \gg \beta$ [221]. Following Starobinsky [212], we implement particle creation via spontaneous decay of the scalaron field. Moreover, we employ the Heisenberg uncertainty principle to estimate the maximum number of particles that can be created in the configuration space of the Universe. We find that the energy available in the scalaron field is sufficient to completely populate the configuration space in the inflationary and reheating regimes, giving rise to an approximately constant rate of energy source in these phases. It turns out that the reheating phase ends when the Hubble rate approaches the decay rate of the scalaron field.

Our present formulation leads to a well-defined preheating stage where the created particles cannot attain thermal equilibrium as their collision rate, determined by their mean free path, lags behind the Hubble rate. When these two rates equalize, transition to a thermilization regime occurs. In subsequent times, the particles attain thermal equilibrium as their collision rate exceeds the Hubble rate.

The reheating temperature T_r is expected to lie between two bounds given by the energy scales of Grand Unified Theory (GUT) [75, 76, 168] and baryogengesis. Magnetic monopoles are expected to be created in the phase transition GUT → SU(3) × SU(2) × U(1) by spontaneous symmetry breaking around 10^{15} GeV [105]. Consequently, the reheating temperature should be well below 10^{15} GeV in order to avoid the creation of magnetic monopoles in the reheating phase. On the other hand, the reheating temperature should be above 10^{10}—10^{12} GeV in order that baryogengesis can happen [144]. Consequently, we take 10^{13} GeV as a typical value for the reheating temperature. With this choice for the end-of-reheating temperature, we find that the thermilization process starts with a temperature of $\sim 10^{12}$ GeV, following a preheating stage of time-span $\sim 10^5\, t_{\rm P}$. The entire reheating stage is found to span over a period of $\sim 10^{11}\, t_{\rm P}$, with an extremely short preheating stage.

The reminder of the chapter is organized as follows. In Section 7.1, we describe the field equations following from a relevant $f(R)$ gravity model that is capable of giving an inflationary phase. In Section 7.2, we formulate a model of particle creation based on Heisenberg's uncertainty principle. There, we also formulate the source term responsible for the growth of energy density following from the model of particle creation. We present in Section 7.3 an analysis of the inflationary phase. The main focus of the work is given in Section 7.4 where a detailed analysis of the reheating phase is given that follows from the present $f(R)$ gravity model coupled with the model of particle creation. There, we investigate the region of reheating in detail in three different stages, namely, the beginning, the intermediate, and the end stages of the reheating phase. Moreover, in Section 7.4, the preheating and thermilization stages are identified by estimating the growth in the collision rate between the particles created in the reheating process. Finally, Sections 7.5 and 7.6 give discussion and conclusion in relation to the findings in this Chapter.

7.1 A relevant $f(R)$ gravity model

In this Chapter, we shall consider an effective gravitational action in the form of $f(R)$ gravity, given by

$$S_{\text{grav}} = \frac{c^3}{16\pi G} \int d^4x \sqrt{-g}\, f(R), \tag{7.1}$$

where R is the Ricci scalar. Although the functional form of $f(R)$ can be arbitrary, we shall restrict its form suggested by quantum field theoretical calculations in curved spacetime [31, 38, 60, 202]. Since we are interested in the inflationary and reheating phases, it is important to choose a functional form of $f(R)$ which is relevant, albeit approximate, for these phases of the Universe.

For a de-Sitter spacetime with constant curvature, where a minimal conformal scalar field is coupled to an electromagnetic field, it was shown by Shore [202] that the one-loop vacuum fluctuations give rise to an effective potential that may be equivalently written as

$$f(R) = R + \alpha R^2 + \beta R^2 \ln \frac{R}{\mu^2}, \tag{7.2}$$

where μ is the scale of renormalization. Although this form is obtained for a strictly de-Sitter spacetime, it has approximate correspondence to the vacuum fluctuations calculated in a Robertson-Walker metric, namely, that giving rise to the vacuum expectation value of the energy-momentum tensor $\langle T^{\text{QM}}_{\mu\nu} \rangle$ due to quantum fluctuations of free, massless, conformally invariant scalar fields, as shown in the Refs. [31, 38, 60]. This gives rise to an effective Einstein field equation, $G_{\mu\nu} = \kappa \langle T^{\text{QM}}_{\mu\nu} \rangle$, with $\langle T^{\text{QM}}_{\mu\nu} \rangle = k_1\, H^{(1)}_{\mu\nu} + k_3\, H^{(3)}_{\mu\nu}$ where $\kappa = 8\pi G/c^4$, k_1 is an arbitrary constant and k_3 is determined by the number of quantum degrees of freedom. In fact, $H^{(1)}_{\mu\nu}$ can be directly obtained from the R^2 term in $f(R)$, whereas, $H^{(3)}_{\mu\nu}$ cannot be obtained by varying the action. Importantly, Vilenkin [221] showed that the functional form of $f(R)$ given by (7.2) is approximately correct for $\alpha \gg \beta$ for the case when the curvature of the background spacetime is not constant. Whereas the parameter α depends on the renormalization scale μ, the parameter β can be related to k_3 as $\beta = (8\pi k_3)\ell_P^2/6$, where $8\pi k_3 = 1.8$ [221].

The field equation for a general $f(R)$ gravity with a matter Lagrangian takes the form

$$f_R R_{\mu\nu} - \frac{1}{2} f g_{\mu\nu} + (g_{\mu\nu} \nabla^\alpha \nabla_\alpha - \nabla_\mu \nabla_\nu) f_R = \kappa T_{\mu\nu}, \tag{7.3}$$

where $f_R = \partial f / \partial R$ and $T_{\mu\nu}$ is the energy-momentum tensor of matter given by $T_{\mu\nu} = (\rho + p) u_\mu u_\nu - p g_{\mu\nu}$, with ρ and p being the proper energy density and proper pressure, respectively. Substituting the functional form of $f(R)$ from equation (7.2) in equation (7.3), we obtain the modified field equation as

$$G_{\mu\nu} + \beta R R_{\mu\nu} + \left\{ \alpha R + \beta R \ln \frac{R}{\mu^2} \right\} \left\{ 2R_{\mu\nu} - \frac{1}{2} R g_{\mu\nu} \right\} + (g_{\mu\nu} \Box - \nabla_\mu \nabla_\nu) \left\{ 2\alpha R + \beta R + 2\beta R \ln \frac{R}{\mu^2} \right\} = \kappa T_{\mu\nu}, \tag{7.4}$$

where $G_{\mu\nu} = R_{\mu\nu} - \frac{1}{2}g_{\mu\nu}R$ is the Einstein tensor.

It was shown by Vilenkin [221] that a long quasi-de-Sitter (or inflationary) phase can be obtained when the parameters are such that $\alpha \gg \beta$. Employing this approximation, the above field equation reduces to

$$G_{\mu\nu} + \beta R R_{\mu\nu} + \alpha R\left(2R_{\mu\nu} - \frac{1}{2}R g_{\mu\nu}\right) + 2\alpha(g_{\mu\nu}\Box - \nabla_\mu\nabla_\nu)R = \kappa T_{\mu\nu}, \tag{7.5}$$

with the corresponding trace equation as

$$6\alpha\Box R + \beta R^2 - R = \kappa T. \tag{7.6}$$

We shall assume a Friedmann-Lemaître-Robertson-Walker metric [113, 226] given by

$$ds^2 = -dt^2 + a^2(t)\left[\frac{dr^2}{1-kr^2} + r^2(d\theta^2 + \sin^2\theta\, d\varphi^2)\right], \tag{7.7}$$

where k is the curvature parameter.

The 00-component of the field equation (7.5) yields the dynamics of the Hubble rate $H = \frac{\dot{a}}{a}$ as

$$3\left\{H^2 + \frac{k}{a^2}\right\} - 18\beta\left\{\dot{H} + 2H^2 + \frac{k}{a^2}\right\}\left\{\dot{H} + H^2\right\} - 18\alpha\left\{\dot{H} + 2H^2 + \frac{k}{a^2}\right\}\left\{\dot{H} - \frac{k}{a^2}\right\} \\ + 36\alpha H\left\{\ddot{H} + 4H\dot{H} - 2H\frac{k}{a^2}\right\} = \kappa\rho. \tag{7.8}$$

Since we are interested in a long de-Sitter phase in the initial part of the evolution (which is also implied by the approximation $\alpha \gg \beta$), this signifies an exponential growth of the scale factor $a(t)$. This implies that the k-dependent terms in equation (7.8) are insignificant in determining the dynamics. Neglecting these terms, equation (7.8) further reduces to

$$3H^2 - 18\beta\left(2H^4 + 3\dot{H}H^2 + \dot{H}^2\right) + 18\alpha\left(2\ddot{H}H + 6\dot{H}H^2 - \dot{H}^2\right) = \kappa\rho, \tag{7.9}$$

which will be referred to as the field equation in the following.

The covariant derivative of the field equation (7.5) gives $\nabla_\nu T^{\mu\nu} = 0$, which in the metric (7.7), yields

$$\dot{\rho} + 3H(\rho + p) = 0. \tag{7.10}$$

Further, we shall assume that the matter is described by the equation of state $p = \omega\rho$, reducing the above equation to

$$\dot{\rho} + 3H(1+\omega)\rho = 0. \tag{7.11}$$

This equation expresses conservation of matter in the absence of any source. Since we start with an action without a non-trivial interaction between the curvature field and matter, the source term is not included in the dynamics.

We shall see that the scalar curvature falls off quickly in the inflationary phase and thereafter it performs a damped oscillation. This oscillation, dubbed scalaron, is coherent in nature [221], and it is a consequence of the αR^2 term in the Lagrangian. As shown by Birrell and Davies [31], the αR^2 term is an effective contribution from the quantum vacuum fluctuations of matter fields coupled to the Ricci scalar. Moreover, as shown by Starobinsky [212], the energy density of the scalarons acts like a source for spontaneous creation of particles.

In the next Section, we shall model this spontaneous decay of scalarons together with constraints due to the Heisenberg uncertainty principle.

7.2 A Model of Particle creation

Assuming the inflation to start near the GUT scale $\sim \ell_{\rm GUT}$, the Universe undergoes a quasi-de-Sitter expansion so that the size of universe grows as $\ell(t) = \ell_{\rm GUT}\, e^{N(t)}$, where $N(t)$ is the number of e-foldings. The corresponding volume of the universe $V(t) \sim \ell^3(t)$ also undergoes a similar expansion. Eventually, at time $t = t_e$, when $N(t_e) \approx 60$, the inflationary phase ends and an oscillatory phase begins, where the Hubble rate $H(t)$ and the scalar curvature $R(t)$ undergo damped oscillations. Starobinsky showed that particles are created by means of decay of scalarons in this oscillatory phase. The average energy density of the scalaron field $\langle \rho_R \rangle$ was found to be $\langle \rho_R \rangle = \alpha m_{\rm P}^2 \langle R^2 \rangle$ (see discussions following equation (38) in Ref. [212]).

It may be emphasized that the particle creation is essentially a quantum mechanical process. Although our present formulation is classical in nature, the quantum nature of particle production must be taken into account, albeit in an approximate fashion. To formulate the particle production, we employ the Heisenberg uncertainty principle, $\Delta x\ \Delta p_x \geq \frac{1}{2}\hbar$. If an ultra-relativistic particle of energy ε is created, the corresponding momentum uncertainty $\Delta p \sim \frac{\varepsilon}{c}$ gives a minimum position uncertainty $\Delta x \sim \frac{\hbar}{\Delta p} \sim \frac{\hbar c}{\varepsilon}$. Such particle production is expected to happen throughout the volume $V(t)$ of the Universe. For simplicity, we may assume that all such particles are created with the same energy ε so that we may partition the volume $V(t)$ into $\mathcal{N}(t) = V(t)/(\Delta x)^3$ cells. If sufficient energy is available in the scalaron field, $\mathcal{N}(t)$ particles can be created occupying all $\mathcal{N}(t)$ cells within a time-span of Γ^{-1}, where Γ is the decay rate of scalarons. It is important to note that no more than $\mathcal{N}(t)$ particles can be created within the time scale Γ^{-1} even if an excessive amount of energy resides in the scalaron field. This restriction is a direct consequence of quantum mechanics via the Heisenberg uncertainty principle. The number density of such created particles is given by $n(t) = \mathcal{N}(t)/V(t) \sim (\Delta x)^{-3} \sim \left(\frac{\varepsilon}{\hbar c}\right)^3$ with the corresponding energy density $\varepsilon\, n(t) \sim \frac{\varepsilon^4}{\hbar^3 c^3}$. Since particles are created from scalarons with the decay rate Γ, the production rate $\lambda(t)$ of the energy density, setting $\hbar = c = 1$, is given by

$$\lambda(t) = \Gamma\, \varepsilon\, n(t) = \Gamma\, \varepsilon^4, \tag{7.12}$$

so long as sufficient energy density ρ_R is available in the scalaron field. The corresponding *sufficiency condition* $\rho_R \geq \varepsilon^4$ translates to

$$\alpha m_{\mathrm{P}}^2 R^2 \geq \varepsilon^4. \tag{7.13}$$

The assumption of the created particles having the same energy ε is expected to give reasonable estimates for macroscopic quantities. Within every decay time Γ^{-1}, the volume $V(t)$ is populated with particles of different energies $\tilde{\varepsilon}$ with a probability determined by quantum mechanics. In the present formulation, we are interested in the time evolution of the macroscopic energy density $\rho(t)$, which is assumed to be uniform throughout the volume $V(t)$ by the postulate of homogeneity and isotropy of the Universe. Consequently, it is reasonable to take the average energy ε of all particles created within the time-span of inverse decay rate Γ^{-1}.

Since the scalar curvature $R(t)$ decreases in the course of evolution, the sufficiency condition (7.13) will not be satisfied at some point of time t_*. From that time onwards the available energy in the scalarons will be insufficient, and only a fraction $\zeta(t)$ of the $\mathcal{N}(t)$ cells could be occupied, given by

$$\zeta(t) = \frac{\alpha m_{\mathrm{P}}^2 R^2}{\varepsilon^4}, \tag{7.14}$$

so that the particle production rate becomes

$$\lambda(t > t_*) = \Gamma \varepsilon^4 \zeta(t) = \Gamma \alpha m_{\mathrm{P}}^2 R^2. \tag{7.15}$$

In order to account for the particle creation in the macroscopic dynamics, the energy density equation (7.11) has to be modified by including the particle production rate $\lambda(t)$ as a source, leading to

$$\dot{\rho} + 3H(1+\omega)\rho = \lambda(t). \tag{7.16}$$

The corresponding back-reaction is accounted for by modifying the trace equation (7.6) to

$$6\alpha(\ddot{R} + 3H\dot{R}) - \beta R^2 + R = \kappa \frac{\lambda(t)}{H} - \kappa T, \tag{7.17}$$

for the case of Friedmann-Lemaître-Robertson-Walker metric, where $T = (3\omega - 1)\rho$ is the trace of the energy-momentum tensor.

Due to the above modification in the dynamics, particles will be created both in the inflationary and reheating phases. However, the contribution due to particle production is expected to be insignificant in the inflationary phase due to the quasi-de-Sitter expansion.

7.3 Analysis of the inflationary phase

In this section, we investigate the region of inflation by imposing the slow-roll approximation in the field equation (7.9). In this region, the value of the Hubble parameter is expected to be large and is a slowly varying function given by the slow-roll condition $|\dot{H}| \ll H^2$. Defining a time-scale τ as $\rho/\tau \sim \lambda$, or $\tau \sim \rho/\lambda$, then $|\dot{H}| \sim H/\tau \sim H\lambda/\rho \ll H^2$ implies $H\rho \gg \lambda$. This implies $\dot{\rho} + 3H(1+\omega)\rho \approx 0$ in the slow roll regime so that there is no significant growth in the energy density and thus its back-reaction on the background spacetime is negligibly small. Under these considerations, the field equation (7.9) reduces to

$$\dot{H} - \frac{1}{3}\frac{\beta}{\alpha}H^2 + \frac{1}{36\alpha} \approx 0. \tag{7.18}$$

For a pure de-Sitter phase, the scalar curvature is a constant, say R_S, which in this case represents a constant Hubble rate H_S. From equation (7.18), we obtain $12H_S^2 = 1/\beta$. Thus, for a quasi-de-Sitter phase, the second and the third terms are of the same order. Consequently, the solution is given by

$$H(t) = \frac{1}{\sqrt{12\beta}} \tanh\left(\sqrt{12\beta}c_1 - \frac{\sqrt{12\beta}}{36\alpha}t\right), \tag{7.19}$$

where the constant c_1 is determined by the initial condition. Rewriting the above solution in terms of H_S, we obtain

$$H(t) = H_S \tanh\left(\frac{c_1}{H_S} - \frac{t}{36\alpha H_S}\right). \tag{7.20}$$

The validity of the above expression is well-founded so far as the slow-roll condition $|\dot{H}| \ll H^2$ is satisfied.

Using equation (7.20), the slow-roll condition gives $1/(6H_S\sqrt{\alpha}) \ll \sinh(c_1/H_S - t/36H_S\alpha)$. Since, the right-hand side is a decreasing function of time, we may guess that at some later time t_e, the inequality is no longer valid. This inequality is valid as long as the condition $c_1 \gg t/36\alpha$ is satisfied and one could identify $36\alpha c_1 = t_e$. Hence the condition $|\dot{H}| \ll H^2$ is satisfied for $t \ll t_e$. Consequently, the end of inflation, given by $|\dot{H}| \approx H^2$, is met when $t \approx t_e$. The expression for Hubble rate in the region of inflation [211] is thus obtained as

$$H(t) = H_S \tanh\left(\frac{t_e - t}{36\alpha H_S}\right). \tag{7.21}$$

From the above equation, one may immediately obtain t_e, if the initial value of the Hubble parameter H_0 at $t = t_0$ is known. For convenience, we shall set $t_0 = 0$ in the following. This yields

$$t_e = 18\alpha H_0 \ln\left(\frac{H_S + H_0}{H_S - H_0}\right). \tag{7.22}$$

The period of inflation t_e thus depends on the initial value of the Hubble rate H_0, and also on the values of the constant parameters α and $H_S = 1/\sqrt{12\beta}$.

Substituting equation (7.21) in $R = 6(\dot{H}+2H^2)$, we obtain the scalar curvature during inflation as

$$R = 12H^2 + \frac{1}{6\alpha}\left(\frac{H^2}{H_S^2} - 1\right). \tag{7.23}$$

The arbitrariness in the parameter α can be fixed by fixing the number of e-foldings during inflation. Number of e-foldings between time t_0 and t is given by

$$N(t) = \int_{t_0}^{t} H(t)\, dt. \tag{7.24}$$

Consequently, the number of e-foldings during the period of inflation N_e is obtained by substituting equation (7.21) in (7.24) so that

$$N_e = H_S \int_0^{t_e} \tanh\left(\frac{t_e - t}{36 H_S \alpha}\right) dt, \tag{7.25}$$

which gives

$$N_e = 36\alpha H_S^2 \ln\left\{\cosh\left(\frac{t_e}{36H_S\alpha}\right)\right\}. \tag{7.26}$$

Using equation (7.22), one may obtain a constraint relation connecting all parameters of the theory with the initial Hubble value H_0,

$$H_0 = H_S\sqrt{1 - e^{-\frac{2\beta}{3\alpha}N_e}}. \tag{7.27}$$

The corresponding value of the scalar curvature R_0 can be obtained by substituting this value in equation (7.23). We shall take $N_e = 60$ [179] and tune the initial value H_0 by tuning α and β. Since the quantity $\beta N_e/\alpha$ occurs in the exponent, it can make a significant contribution to H_0 only when $10^{-2} \lesssim \beta N_e/\alpha \lesssim 1$. This implies that $10^{-4} \lesssim \beta/\alpha \lesssim 10^{-2}$ can give an initial value of the Hubble parameter somewhat different from the pure de-Sitter value. This may also suggest an estimate for the value of α in terms of β as $10^2\beta \lesssim \alpha \lesssim 10^4\beta$, or

$$30\ \ell_{\rm P}^2 \lesssim \alpha \lesssim 3000\ \ell_{\rm P}^2, \tag{7.28}$$

in Planck units.

As stated earlier, the end of inflation is marked by the condition $|\dot{H}| \sim H^2$ so that

$$H_e \sim \frac{1}{6\sqrt{\alpha}}, \tag{7.29}$$

and the corresponding scalar curvature is obtained by substituting (7.29) in (7.23), giving

$$R_e \sim \frac{1}{6\alpha}. \tag{7.30}$$

Thus, during the inflationary phase, the scalar curvature decreases from R_0 to R_e and the Hubble rate decreases from H_0 to H_e.

The scalaron energy density $\alpha m_{\rm P}^2 R^2$ at the end of inflation, $\alpha m_{\rm P}^2 R_e^2 \sim 2.7\times 10^{-4}\, m_{\rm P}^4$, is much larger than the energy density $\varepsilon^4 \sim 10^{-24} m_{\rm P}^4$ required to create a particle of energy $\varepsilon \sim 10^{13}$ GeV. This indicates that, during the course of inflation, the decay rate λ would take the form $\lambda = \Gamma\varepsilon^4 = {\rm const}$, so long as the sufficiency condition (7.13) holds. Thus from (7.16), we can immediately write the solution as

$$\rho(t) = \Big\{\rho_0 + u(t)\Big\}\ \exp\Big\{-3(1+\omega)\int_0^t H(t')dt'\Big\}, \tag{7.31}$$

where ρ_0 is the initial seed density at $t = t_0 = 0$ and $u(t)$ is given by the integral

$$u(t) = \int_0^t \lambda(t')\ \exp\left\{3(1+\omega)\int_0^{t'} H(t'')\, dt''\right\} dt'. \tag{7.32}$$

The evolution of density during the inflationary phase can be obtained by substituting equation (7.21) in (7.31), so that the integral $u(t)$ can be expressed as

$$u(t) = \Gamma\varepsilon^4 \int_0^t dt' \exp\left\{3(1+\omega)H_S\int_0^{t'} \tanh\left(\frac{t_e - t''}{36\alpha H_S}\right) dt''\right\}, \tag{7.33}$$

giving

$$u(t) = \Gamma\varepsilon^4\left[\frac{H_S}{H_S - H}\right]^{\gamma}\int_0^t \left\{1 - \tanh\left(\frac{t_e - t'}{36\alpha H_S}\right)\right\}^{\gamma} dt', \tag{7.34}$$

where $\gamma = \frac{9\alpha}{\beta}$.

Substituting this expression in equation (7.31), we obtain

$$\rho(t) = \rho_0\left(\frac{H_S - H_0}{H_S - H(t)}\right)^{\gamma} + \left(\frac{H_S}{H_S - H(t)}\right)^{\gamma}\times\Gamma\varepsilon^4\int_0^t\left\{1 - \tanh\left(\frac{t_e - t'}{36\alpha H_S}\right)\right\}^{\gamma} dt'. \tag{7.35}$$

By the end of inflation, the Hubble rate $H_e \ll H_S$, since $\alpha/\beta \gg 1$. Consequently, the first term becomes insignificant by the end of inflation even when the initial seed density $\rho_0 \neq 0$. Thus any energy distribution (or seed) present initially is diluted infinitely in the inflationary era. On the other hand, the second term, coming from the source λ, contributes to the energy density during the inflationary phase. Thus the expression for energy density at the end of inflation $t = t_e$ can be approximated as

$$\rho(t_e) = \Gamma\varepsilon^4\left(\frac{2H_S}{H_S - H(t_e)}\right)^{\gamma}\int_0^{t_e}\left(\exp\left[\frac{t_e - t'}{18\alpha H_S}\right] + 1\right)^{-\gamma} dt', \tag{7.36}$$

so that

$$\rho_e = 3\beta H_S\Gamma\varepsilon^4\left(\frac{2H_S}{H_S - H_e}\right)^{\gamma} e^{-\frac{(t_e - t)}{3\beta H_S}} \times\ {}_2F_1\left(\gamma,\gamma;\gamma+1;-e^{-\frac{(t_e-t)}{18\alpha H_S}}\right)\Bigg|_0^{t_e}, \tag{7.37}$$

where ${}_2F_1$ is the hypergeometric function. Since $H_e \ll H_S$ and setting $N_e = 60$, we obtain an approximate value for ρ_e as

$$\rho_e \approx \frac{\sqrt{3\beta}}{2}\Gamma\varepsilon^4 = \frac{1}{4}\left(\frac{\Gamma}{H_S}\right)\varepsilon^4, \tag{7.38}$$

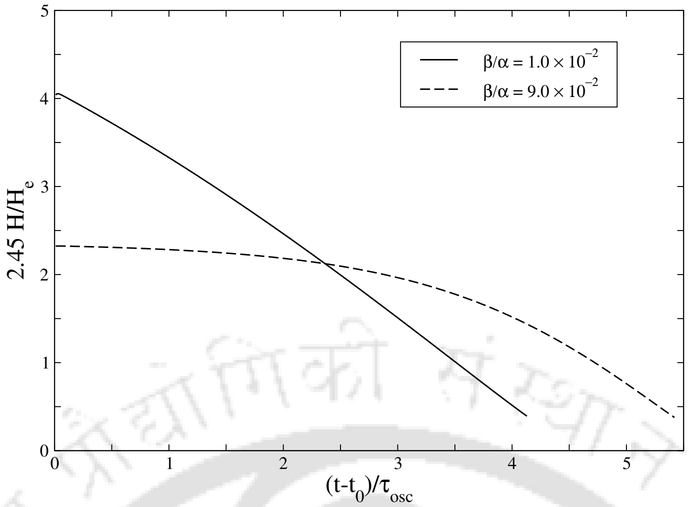

Figure 7.1: Hubble rate $H(t)$ in the inflationary phase for $\beta/\alpha = 9 \times 10^{-2}$ and 10^{-2}, with $N_e = 60$. The time axis $(t - t_0)$ is shown in the units of $\tau_{\rm osc} = 2\pi\sqrt{6\alpha}$ with t_0 indicating the time when inflation begins. We have set $t_0 = 0$ throughout the Chapter.

Since the particle production rate Γ is expected to be much smaller than the excessively large Hubble rate H_S in the de-Sitter phase, ρ_e is negligibly small. This will be clear from further discussion in the later sections.

To this end, we seek an exact solution in the inflationary phase $0 \leq t \leq t_e$ by numerically solving the field equation (7.9) coupled with the density growth equation (7.16) employing the source λ from equation (7.12). We apply the initial condition H_0 coming from equation (7.27) with $N_e = 60$ and for different choices of $\frac{\beta}{\alpha}$. In addition, we supply a second initial condition, $\dot{H}(0) = 0$, to begin the quasi-de-Sitter phase with an initial energy density $\rho(0) = 0$.

The inflationary phase with different values of the ratio β/α, namely, $\beta/\alpha = 9 \times 10^{-2}$ and 10^{-2}, are shown in Figure 7.1. For the ratio $\beta/\alpha = 9 \times 10^{-2}$, the initial value $H_0 = 0.99 H_S$, which is closer to the pure de-Sitter value H_S. Consequently, a plateau region prescribed by equation (7.21) is observed. This plateau is wider than that for $\beta/\alpha = 10^{-2}$ for which $H_0 = 0.57 H_S$. Numerically, the end of inflation is identified using the slow-roll condition $|\dot{H}|/H^2 = 1$. The value of the Hubble rate H satisfying $|\dot{H}|/H^2 = 1$ is found to be nearly the same as given by the analytical expression $H_e \sim 1/\sqrt{36\alpha}$. For instance, our numerical solution indicates that $H_e = 0.055 H_S$ for $\beta/\alpha = 10^{-2}$. This value compares well with analytical values $H_e = 0.058 H_S$.

Figure 7.2 displays the evolution of the scalar curvature $R(t)$ in this phase for $\beta/\alpha = 9 \times 10^{-2}$ and 10^{-2}. We see that the scalar curvature R falls off more rapidly than the Hubble rate in the inflationary phase. This is evident due to the fact that the scalar curvature is determined by the square of Hubble rate as given by analytical expression (7.23). Figure 7.3 plots the evolution of the density $\rho(t)$ in the inflationary phase for $\beta/\alpha = 9 \times 10^{-2}$ and 10^{-2}. We see that the growth in density is insignificant in this phase.

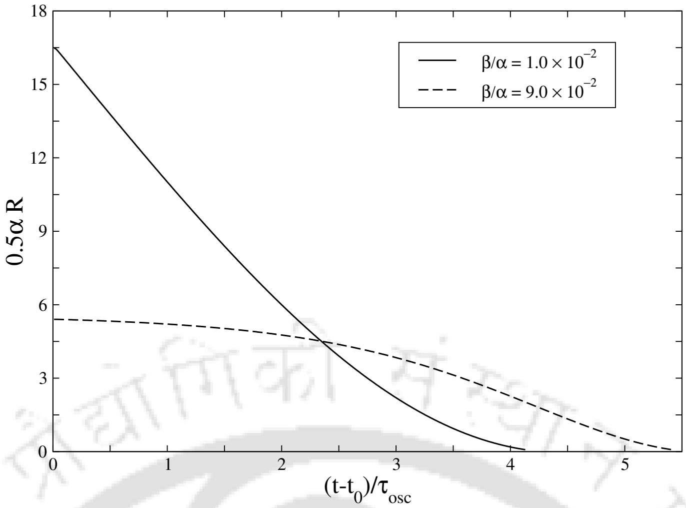

Figure 7.2: Scalar curvature $R(t)$ in the inflationary phase for $\beta/\alpha = 9 \times 10^{-2}$ and 10^{-2}, with $N_e = 60$. The time axis $(t - t_0)$ is shown in the units of $\tau_{\rm osc}$.

7.4 Analysis of the reheating phase

In the previous section, we saw that the inflationary phase given by equation (7.21) ends as t approaches t_e and the Hubble parameter falls to a very small value H_e. At this time, the growth in density given by equation (7.38) is insignificant. Comparing the expansion term $4H\rho$ and the source term λ in the density equation (7.16), we see that $4H_e\rho_e \ll \lambda$, as $H_e \ll H_S$. Since the expansion term is negligible compared to the source term, it gives the right condition for growth in density implying the beginning of reheating at a time $t_i \sim t_e$.

The Hubble parameter is small during the reheating phase, and initially $H \sim H_e$. Moreover, since $\beta \ll \alpha$, the field equation (7.9) reduces to

$$2H\ddot{H} + 6H^2\dot{H} - \dot{H}^2 + \frac{H^2}{6\alpha} = \frac{\kappa}{18\alpha}\rho, \tag{7.39}$$

for $t > t_i$, where t_i marks the initial time of the rehеating phase.

7.4.1 Beginning of Reheating

At the beginning of reheating, the initial density is negligible, $\rho_i \sim \rho_e \approx 0$. We can therefore write

$$2H\ddot{H} + 6H^2\dot{H} - \dot{H}^2 + \frac{H^2}{6\alpha} \approx 0, \tag{7.40}$$

in the beginning of reheating.

As the Hubble parameter is small, the term $6H^2\dot{H}$ is smaller compared to the other

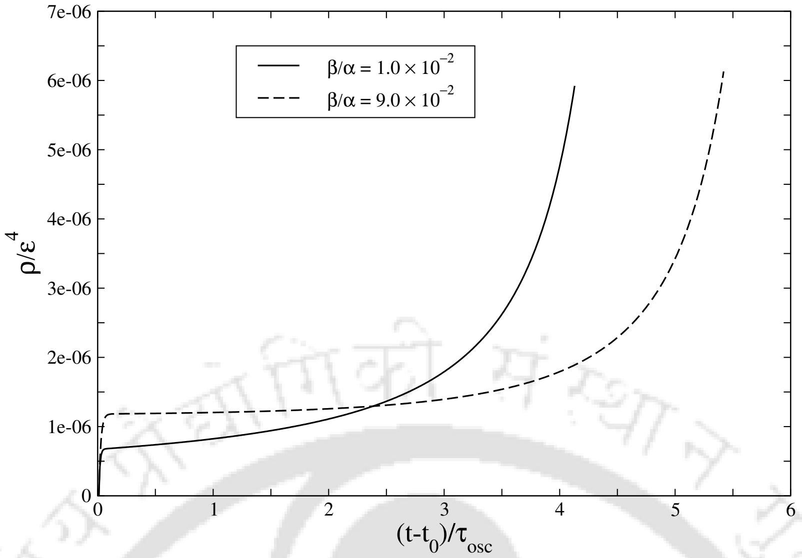

Figure 7.3: Density $\rho(t)$ in the inflationary phase for $\beta/\alpha = 9 \times 10^{-2}$ and 10^{-2}, with $N_e = 60$.

terms. Neglecting this term, we write

$$2H\ddot{H} - \dot{H}^2 + \frac{H^2}{6\alpha} = 0 \tag{7.41}$$

The solution of this equation can be immediately obtained as

$$H(t) = \psi \cos^2\left(\frac{t}{2\sqrt{6\alpha}} + \phi\right), \tag{7.42}$$

where ψ represents the amplitude and ϕ the initial phase. The phase of the above oscillation can be fixed by fixing the initial value of the Hubble parameter as $H(t_i) = H_i$ at the initial time $t = t_i$ of the reheating phase. Substituting this initial condition in equation (7.42), we have $H_i = \psi\cos^2(t_i/2\sqrt{6\alpha} + \phi)$. Now, if we set the initial phase $\phi = -t_i/2\sqrt{6\alpha}$, we obtain

$$H(t) = \psi \cos^2\left(\frac{t - t_i}{2\sqrt{6\alpha}}\right). \tag{7.43}$$

This expression obviously implies a Universe oscillating forever. This is an artefact of neglecting the term $6H^2\dot{H}$, whose contribution in determining the correct behaviour of the expansion rate is thus crucial. The effect of the neglected term can be obtained by promoting the amplitude ψ to a function of time, so that

$$H(t) = \psi(t) \cos^2\left(\frac{t - t_i}{2\sqrt{6\alpha}}\right) = \psi(t)\mu(t). \tag{7.44}$$

Since $6H^2\dot{H}$ is small, we expect the amplitude $\psi(t)$ to be a slowly varying function of time.

Substituting $\psi(t)\mu(t)$ for H in equation (7.40), we obtain

$$\mu\left(2\ddot{\psi}-\frac{\dot{\psi}^2}{\psi}\right)+2\dot{\mu}\dot{\psi}+6\mu\psi\left(\mu\dot{\psi}+\dot{\mu}\psi\right)=0. \tag{7.45}$$

Neglecting the small contribution from the terms $\dot{\psi}^2/\psi$, we obtain the solution

$$\psi(t)=4\left[3t-4c_2+3\sqrt{6\alpha}\sin\left(\frac{t-t_i}{\sqrt{6\alpha}}\right)\right]^{-1}. \tag{7.46}$$

This leads to the Hubble rate

$$H(t)=\frac{4}{3}\frac{\cos^2\left(\frac{t-t_i}{2\sqrt{6\alpha}}\right)}{t-\frac{4c_2}{3}+\sqrt{6\alpha}\sin\left(\frac{t-t_i}{\sqrt{6\alpha}}\right)}, \tag{7.47}$$

in the beginning of reheating phase.

The integration constant c_2 can be fixed from the initial value $H(t_i)=H_i$, giving $4c_2=3t_i-4/H_i$. Thus the Hubble parameter takes the form

$$H(t)=\frac{4}{3}\frac{\cos^2\left(\frac{t-t_i}{2\sqrt{6\alpha}}\right)}{(t-t_i)+\frac{4}{3H_r}+\sqrt{6\alpha}\sin\left(\frac{t-t_i}{\sqrt{6\alpha}}\right)} \tag{7.48}$$

in the beginning of reheating, $t\gtrsim t_i$. It is important to note that the amplitude of the Hubble rate varies approximately as $C+(t-t_i)^{-1}$, implying a damped oscillation in this region.

Using the above expression for the Hubble rate, the scalar curvature R is obtained as $R=-\sqrt{6/\alpha}H\tan[(t-t_i)/2\sqrt{6\alpha}]+3H^2$. Since the first term dominates, we can approximate this as

$$R(t)=\sqrt{\frac{8}{3\alpha}}\frac{\sin\left(\frac{t-t_i}{\sqrt{6\alpha}}+\pi\right)}{(t-t_i)+\frac{4}{3H_i}+\sqrt{6\alpha}\sin\left(\frac{t-t_i}{\sqrt{6\alpha}}\right)} \tag{7.49}$$

Note that the frequency of oscillation $1/\sqrt{6\alpha}$ is twice that of the Hubble rate.

Estimate for the end of reheating

An approximate estimate for the end of reheating occurring after a sufficiently long time $t\sim t_r$ can be obtained from the expression (7.49). From the sufficiency condition (7.13), a cross-over happens when the left-hand side is approximately equal to the right-hand side, that is

$$\alpha\langle R^2\rangle\approx\frac{\varepsilon^4}{m_{\rm P}^2}, \tag{7.50}$$

where we have taken average quantities, since the time period of oscillation $\tau_{\rm osc} = 2\pi\sqrt{6\alpha}$ is expected to be much smaller than the time span $t - t_i$.

During the phase $t_i \lesssim t \lesssim t_r$, the scalar curvature goes approximately as $R \sim \sqrt{\frac{8}{3\alpha}\frac{1}{t-t_i}}\sin\left(\frac{t-t_i}{\sqrt{6\alpha}}\right)$, and the above condition (7.50) is satisfied at a later time t_r, leading to

$$\frac{1}{t_r - t_i} \approx \sqrt{\frac{3}{4}}\frac{\varepsilon^2}{m_{\rm P}} \tag{7.51}$$

or

$$t_r - t_i \approx \sqrt{\frac{4}{3}}\left(\frac{m_{\rm P}}{\varepsilon}\right)^2 t_{\rm P}. \tag{7.52}$$

For a reheating temperature of $T_r \sim \varepsilon \sim 10^{13}$ GeV, we thus obtain

$$t_r - t_i \approx 6.85 \times 10^{10}\, t_{\rm P} \sim 10^{11}\, t_{\rm P}, \tag{7.53}$$

which is much larger than the time period $\tau_{\rm osc} \sim 10^3\, t_{\rm P}$.

Growth in density near the beginning of reheating

Since the sufficiency condition (7.13) is satisfied in the initial oscillations for $t > t_i$, the particle production occurs at a constant rate $\lambda = \Gamma\varepsilon^4$. Substituting the Hubble rate from equation (7.48), the integral $u(t)$, given by (7.32), is expressed as

$$u(t) = \Gamma\varepsilon^4 \int_{t_i}^{t} dt' \exp\left\{4(1+\omega)\int_{t_i}^{t'} dt'' \cos^2\left(\frac{t''-t_i}{2\sqrt{6\alpha}}\right)\left[(t''-t_i) + \frac{4}{3H_i} + \sqrt{6\alpha}\sin\left(\frac{t''-t_i}{\sqrt{6\alpha}}\right)\right]^{-1}\right\}. \tag{7.54}$$

Performing the inner integration, this reduces to

$$u(t) = \left(\frac{3H_i}{4}\right)^{2(1+\omega)} \Gamma\varepsilon^4 \int_{t_i}^{t} \left\{(t'-t_i) + \frac{4}{3H_i} + \sqrt{6\alpha}\sin\left(\frac{t'-t_i}{\sqrt{6\alpha}}\right)\right\}^{2(1+\omega)} dt'. \tag{7.55}$$

The first term in the above integrand is the only growing term compared to the other terms. Further, we see that the second and third terms are of the same order. Since the last term is oscillatory about zero, we shall drop its effect while taking the area under the curve. In this approximation, we obtain

$$u(t) \approx \left(\frac{3H_i}{4}\right)^{2\omega+2} \frac{\Gamma\varepsilon^4}{2\omega+3}\left\{t - t_i + \frac{4}{3H_i}\right\}^{2\omega+3} \tag{7.56}$$

Since the evolution of density in any region is given by the expression (7.31), we obtain

$$\rho(t) \approx \frac{3}{11}\Gamma\varepsilon^4\left\{t - t_i + \frac{4}{3H_i}\right\} \tag{7.57}$$

It is interesting to note that if we take the temperature as ~ 150 GeV corresponding to the electro-weak scale, the time-span turns out to be $t_{\rm EW} - t_i \sim 10^{32} t_{\rm P}$, which is approximately the correct time-span for the electro-weak transition to occur in the early Universe.

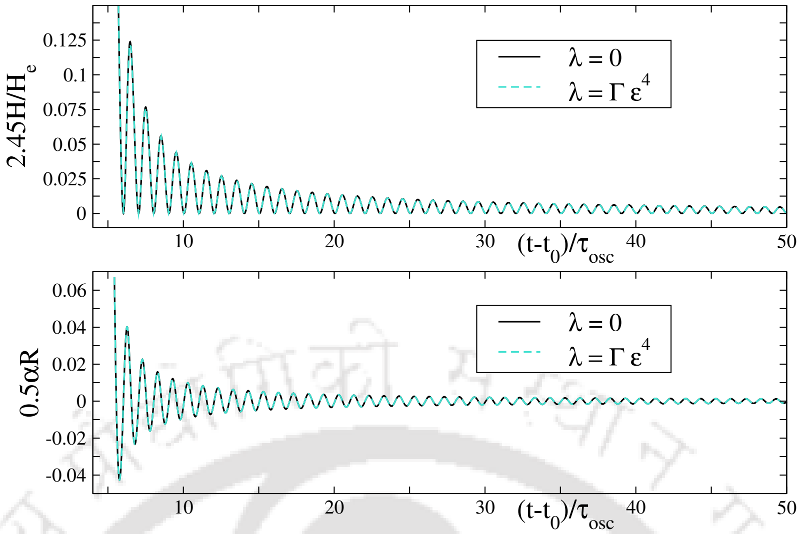

Figure 7.4: Hubble rate $H(t)$ (upper panel) and scalar curvature $R(t)$ (lower panel) in the reheating phase for $\beta/\alpha = 10^{-2}$ with $\lambda = 0$ and $\lambda = \Gamma\varepsilon^4$. In both panels, the curves for $\lambda = 0$ and $\lambda = \Gamma\varepsilon^4$ nearly coincide, signifying negligible back-reaction. The periods of oscillations are close to $2\pi\sqrt{6\alpha}$ (upper panel), $4\pi\sqrt{6\alpha}$ (lower panel).

In obtaining the above expression from (7.31), we dropped the effect of the initial density ρ_0, as the exponent $\exp\left\{-4\int H dt'\right\}$ makes this term insignificant as the Universe expands. On the other hand, there is a significant effective growth in density coming from $u(t)$ although the exponential factor attenuates with the expansion of the Universe. Thus to a good approximation, we find that the density grows linearly in this region.

In continuation with the previous numerical solution in the inflationary phase, we also obtain the exact solution in the beginning phase of reheating, $t \geq t_i$, from equations (7.9), (7.16) and (7.12) with the same initial conditions at $t = t_0 = 0$.

Figure 7.4 displays the evolution of the Hubble rate (upper panel) and the scalar curvature (lower panel) in the initial phase of reheating for $\lambda = 0$ and $\lambda = \Gamma\varepsilon^4$ with $\beta/\alpha = 10^{-2}$. In this region, we find that the Hubble rate (upper panel) performs a damped oscillation with the amplitude decaying like $\sim (t - t_i)^{-1}$, where t_i marks the beginning of the reheating phase. We have seen an identical behaviour in the analytical expression (7.48), when the back-reaction due to particle production is insignificant.

Using the expression $R = 6(\dot{H}+2H^2)$, we plot the time evolution of the scalar curvature R in Figure 7.4 (lower panel). We see that the Ricci scalar performs damped oscillation about a vanishing mean value. This can be easily seen from the trace equation (7.17), that represents a damped harmonic oscillator with frequency $1/\sqrt{6\alpha}$ and with a damping factor $3H(t)$ in the limit $R \ll \beta^{-1}$ and $\Gamma \ll H$ with $T = 0$ for $\omega = 1/3$. An approximate solution given by equation (7.49) indicates such oscillations about zero with the amplitude decaying like $(t - t_i)^{-1}$.

Figure 7.5 shows the time evolution of the density $\rho(t)$ in the inflationary and the beginning of the reheating phases. We see that the density grows negligibly in the infla-

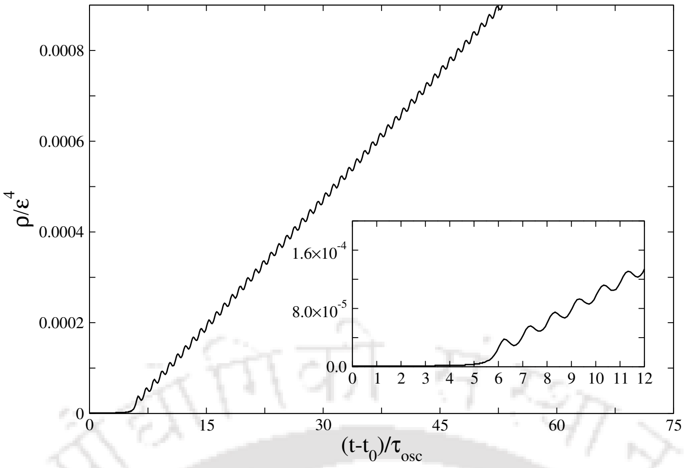

Figure 7.5: Evolution of density $\rho(t)$ for $\beta/\alpha = 10^{-2}$ in the inflationary and the subsequent initial phase of reheating with $\lambda = \Gamma\varepsilon^4$. The time $(t - t_0)$ is in the units of τ_{osc}. The inset shows the time evolution up to $t - t_0 = 12\tau_{\text{osc}}$.

tionary phase. On the other hand, the average density grows linearly with time in the beginning phase of reheating. The oscillatory growth of density is due to the oscillations in the Hubble rate and we shall discuss this behaviour in more detail later on.

7.4.2 Intermediate Region

The back-reaction of the particle creation on the background metric can be analyzed by considering the trace equation (7.17) with the production rate given by equation (7.12). Since the scalar curvature $R \ll \beta^{-1}$ during reheating, we shall drop the quadratic term giving

$$\ddot{R} + 3H\dot{R} + \frac{R}{6\alpha} = \frac{\kappa}{6\alpha}\frac{\Gamma\varepsilon^4}{H}. \tag{7.58}$$

The above equation represents a forced damped oscillator with a time dependent damping coefficient $3H(t)$ and a force inversely proportional to the Hubble rate. To solve this differential equation, the time average of the Hubble parameter obtained in the initial phase of reheating given by equation (7.48) can be employed. Since the amplitude of the Hubble rate is slowly varying compared to the rapidly oscillating term, its time average can be approximated as $\langle H\rangle \approx \frac{2}{3}(t-t_i)^{-1}$, leading to

$$\ddot{R} + \frac{2}{(t-t_i)}\dot{R} + \frac{R}{6\alpha} = \frac{\Gamma}{4\alpha}\frac{\varepsilon^4}{m_{\text{P}}^2}(t-t_i). \tag{7.59}$$

This gives the solution

$$R = \frac{3}{2}\frac{\Gamma\varepsilon^4}{m_{\text{P}}^2}\left\{(t-t_i) - \frac{12\alpha}{(t-t_i)}\right\} + M\frac{\sin\left(\frac{t-t_i}{\sqrt{6\alpha}} + \phi\right)}{t-t_i}. \tag{7.60}$$

The first term proportional to Γ represents the effect of back-reaction whereas the second term with the integration constant M represents the behaviour in the absence of back-reaction. Soon after one oscillation, the term $t - t_i$ becomes larger than $12\alpha(t-t_i)^{-1}$.

Moreover, in the absence of back-reaction, the oscillatory term should represent an approximation for the expression given by (7.49). Thus, to a good approximation, the integration constant M must coincide with $\sqrt{8/3\alpha}$, leading to

$$R \approx \frac{3}{2}\frac{\Gamma \varepsilon^4}{m_{\mathrm{P}}^2}(t-t_i) + \sqrt{\frac{8}{3\alpha}}\frac{\sin\left(\frac{t-t_i}{\sqrt{6\alpha}}+\phi\right)}{t-t_i}. \tag{7.61}$$

Thus, the back-reaction of particle production on the scalar curvature becomes important when

$$t-t_i \gtrsim \sqrt{\frac{16\pi}{3}}\left(\frac{\Gamma^{-1}}{\tau_{\mathrm{osc}}}\right)^{1/2} 10^{12}\, t_{\mathrm{P}} \tag{7.62}$$

An estimate for Γ can be obtained from the uncertainty relation $\Delta E\, \Delta t \sim \hbar$, giving $\varepsilon\, \Gamma^{-1} \sim \hbar$, so that $\Gamma \sim \varepsilon$. Thus $\Gamma^{-1} \sim \frac{m_{\mathrm{P}}}{\varepsilon}\, t_{\mathrm{P}} = 2.435 \times 10^5\, t_{\mathrm{P}}$, with the reduced Planck mass m_{P}, and $\varepsilon \sim 10^{13}$ GeV. Since $\Gamma^{-1}/\tau_{\mathrm{osc}} \sim 10^2$, the back-reaction becomes important long after the end of reheating, $t_r - t_i \sim 10^{11} t_{\mathrm{P}}$. Thus, the back-reaction on the curvature field is insignificant.

The Hubble rate in this region can be obtained by using equation (7.57) in (7.39), yielding

$$2H\ddot{H} + 6H^2\dot{H} - \dot{H}^2 + \frac{H^2}{6\alpha} = \frac{\Gamma}{66\alpha}\frac{\varepsilon^4}{m_{\mathrm{P}}^2}(t-t_i). \tag{7.63}$$

For vanishing right-hand side, the solution is given by equation (7.48) which has the form $H(t) = \mu(t)\psi(t)$. As a solution of equation (7.63), we shall assume an approximate form $H(t) = \psi(t)\mu(t) + \phi(t)$, with the same functional forms for $\psi(t)$ and $\mu(t)$ as before. Consequently, we seek a solution for the unknown function $\phi(t)$. Substituting in equation (7.63), we obtain a differential equation for $\phi(t)$, given by

$$\begin{aligned}
&2\mu^2\psi\ddot{\psi} + 2\mu\dot{\mu}\psi\dot{\psi} + \psi^2\left(2\mu\ddot{\mu} - \dot{\mu}^2 + \frac{\mu^2}{6\alpha}\right) + 2\mu\psi\ddot{\phi} + 6\mu^3\psi^2\dot{\psi} + 6\mu^2\dot{\mu}\psi^3 \\
&\qquad - \dot{\psi}^2\mu^2 + 2(\mu\ddot{\psi} + 2\dot{\psi}\dot{\mu} + \psi\ddot{\mu})\phi + 2\phi\ddot{\phi} + 6(2\psi\mu\phi + \phi^2)(\dot{\psi}\mu + \psi\dot{\mu}) \\
&+ 6(\psi^2\mu^2 + 2\psi\mu\phi + \phi^2)\dot{\phi} - (2\mu\dot{\psi}\dot{\phi} + 2\dot{\mu}\psi\dot{\phi} + \dot{\phi}^2) + \frac{1}{6\alpha}(2\mu\psi\phi + \phi^2) = \frac{\Gamma}{66\alpha}\frac{\varepsilon^4}{m_{\mathrm{P}}^2}(t-t_i)
\end{aligned} \tag{7.64}$$

Neglecting the term $\mu^2\dot{\psi}^2$, and using equation (7.44) and (7.46), a few terms in the above equation cancel out, reducing it to

$$\begin{aligned}
&2(\mu\ddot{\psi} + 2\dot{\psi}\dot{\mu} + \psi\ddot{\mu})\phi + 2\phi\ddot{\phi} + 6(2\psi\mu\phi + \phi^2)(\dot{\psi}\mu + \psi\dot{\mu}) + 6(\psi^2\mu^2 + 2\psi\mu\phi + \phi^2)\dot{\phi} \\
&\qquad - (2\mu\dot{\psi}\dot{\phi} + 2\dot{\mu}\psi\dot{\phi} + \dot{\phi}^2) + \frac{1}{6\alpha}(2\mu\psi\phi + \phi^2) = \frac{\Gamma}{66\alpha}\frac{\varepsilon^4}{m_{\mathrm{P}}^2}(t-t_i)
\end{aligned} \tag{7.65}$$

Since $\dot{\mu} = -\frac{1}{2\sqrt{6\alpha}}\sin\left(\frac{t-t_i}{\sqrt{6\alpha}}\right)$ and $\ddot{\mu} = \frac{1}{12\alpha}(1-2\mu)$, we have $\mu \propto (\tau_{\mathrm{osc}})^0$, $\dot{\mu} \propto (\tau_{\mathrm{osc}})^{-1}$, $\ddot{\mu} \propto (\tau_{\mathrm{osc}})^{-2}$. Since the right hand side involves a larger time scale, the average evolution of Hubble rate is affected only in such time scales. Therefore we shall neglect the terms that involve smaller time scales, namely $\tau_{\rm osc}$. Moreover, these terms average out to zero since they are rapidly oscillating. Thus equation (7.65) reduces to

$$2\mu\ddot{\psi}\phi+2\phi\ddot{\phi}+6(2\psi\mu\phi+\phi^2)\dot{\psi}\mu-2\mu\dot{\psi}\dot{\phi}-\dot{\phi}^2+6(\psi^2\mu^2+2\psi\mu\phi+\phi^2)\dot{\phi}=\frac{\Gamma}{66\alpha}\frac{\varepsilon^4}{m_{\rm P}^2}(t-t_i) \quad (7.66)$$

Substituting the time-averaged values of $\mu=\frac{1}{2}$ and $\psi=\frac{4}{3}\frac{1}{t-t_i}$, and assuming a power-like trial solution, $\phi=B(t-t_i)^{\nu}$, we obtain

$$\frac{4}{3}\Big\{2B-4B+2\nu B+\nu B\Big\}(t-t_i)^{\nu-3}+\Big\{2\nu(\nu-1)B^2-4B^2+8\nu B^2-\nu^2B^2\Big\}(t-t_i)^{2\nu-2}$$
$$+\,6\nu B^3(t-t_i)^{3\nu-1}=\frac{\Gamma}{66\alpha}\frac{\varepsilon^4}{m_{\rm P}^2}(t-t_i) \quad (7.67)$$

For $\nu\leq 0$, we observe that the powers on both sides of the above equation cannot be equated. On the other hand, for $\nu>0$, it is possible to equate the powers on both sides. For large times $t-t_i$, the last term on the left-hand side dominates. Thus, equating powers on both sides, we obtain

$$3\nu-1=1 \implies \nu=\frac{2}{3}, \quad (7.68)$$

and equating the coefficients, we have

$$B=\left(\frac{1}{264}\frac{\Gamma}{\alpha}\frac{\varepsilon^4}{m_{\rm P}^2}\right)^{1/3}. \quad (7.69)$$

Consequently, an approximate solution in the intermediate region has the form

$$H(t)=\psi(t)\,\mu(t)+\left(\frac{1}{264\alpha}\frac{\Gamma\varepsilon^4}{m_{\rm P}^2}\right)^{1/3}(t-t_i)^{2/3}. \quad (7.70)$$

The effect of back reaction thus gives rise to an increasing component (on an average) in the Hubble rate. We have previously seen a similar effect of back-reaction in the scalar curvature that goes like $t-t_i$.

The effect of back-reaction on the Hubble rate becomes important when

$$t-t_i\geq\left\{\frac{88}{27\pi^2}\left(\frac{\Gamma^{-1}\tau_{osc}^2}{t_{\rm P}^3}\right)\left(\frac{m_{\rm P}}{\varepsilon}\right)^4\right\}^{1/5}t_{\rm P} \quad (7.71)$$

or

$$t-t_i\geq 2.6\times 10^6\,t_{\rm P}. \quad (7.72)$$

Since $t_r-t_i\sim 10^{11}\,t_{\rm P}$, the Hubble rate encounters the effect of back-reaction within the reheating phase.

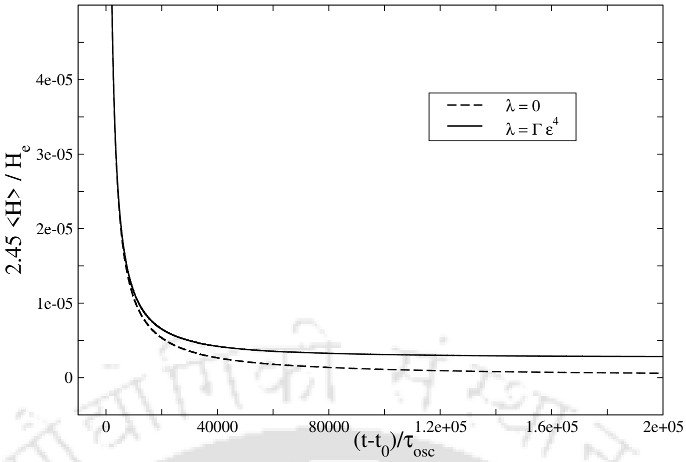

Figure 7.6: Averaged Hubble rate $\langle H \rangle$ in the reheating phase for $\beta/\alpha = 10^{-2}$. The averaging is each cycle of oscillation. The curves display the difference in behaviour between the cases $\lambda = 0$ (without particle creation) and $\lambda = \Gamma\varepsilon^4$ (with particle creation). The curves coincide so long as there is negligible back-reaction. The Hubble rate approaches a non-zero value due to back-reaction from particle creation.

In this region, the density equation can be written as

$$\dot{\rho} + 4\left\{\frac{2}{3}\frac{1}{t-t_i} + B(t-t_i)^{2/3}\right\}\rho = \Gamma\varepsilon^4 \tag{7.73}$$

giving the solution

$$\rho(t) = \Gamma\varepsilon^4 \frac{e^{-\frac{12}{5}B(t-t_i)^{5/3}}}{(t-t_i)^{8/3}} \int_{t_i}^{t} (t'-t_i)^{8/3} e^{\frac{12}{5}B(t'-t_i)^{5/3}} dt' \tag{7.74}$$

For $t \gtrsim t_i$, that is very close to the beginning of reheating, the above integration can be evaluated by substituting unity for the exponential so that $\rho(t) \approx \frac{3}{11}\Gamma\varepsilon^4(t-t_i)$ which corresponds well with equation (7.57) derived earlier in the beginning of reheating. The slight mismatch in the initial time is due to the approximations involved in deriving the above equation in the intermediate region.

For $t \gg t_i$, that is, in the intermediate region, we can evaluate the above integral by estimating the value of B obtained from equation (7.69), by writing it as $B = \left\{\frac{\pi^2}{11}\frac{t_{\mathrm{P}}^3}{\Gamma^{-1}\tau_{\mathrm{osc}}^2}\left(\frac{\varepsilon}{m_{\mathrm{P}}}\right)^4\right\}^{1/3} t_{\mathrm{P}}^{-5/3} \sim 1.4 \times 10^{-11}\, t_{\mathrm{P}}^{-5/3}$. Taking $t - t_i \sim 10^5\, t_{\mathrm{P}}$, we find that $\frac{12}{5}B(t-t_i)^{5/3} \sim 10^{-2}$, so that the exponent is a very small number. Consequently, for $t \gg t_i$, we can expand the exponential inside the integral, giving the approximate solution

$$\rho(t) \approx \frac{3}{11}\Gamma\varepsilon^4(t-t_i)e^{-\frac{12}{5}B(t-t_i)^{5/3}}\left\{1 + \frac{33}{20}B(t-t_i)^{5/3}\right\}. \tag{7.75}$$

This indicates that the density declines from the linear growth for $t \gg t_i$, that is in the intermediate region of the reheating phase. We see the same behaviour in the exact numerical solution displayed in Figure 7.7.

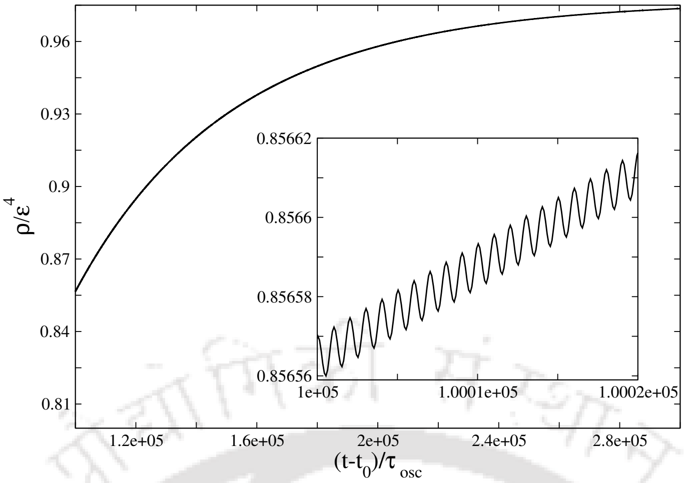

Figure 7.7: Evolution of energy density $\rho(t)$ for $\beta/\alpha = 10^{-2}$ with $\lambda = \Gamma\varepsilon^4$ in the intermediate region of reheating. The inset shows the oscillatory growth of the density for a time-span of $12\tau_{\rm osc}$.

7.4.3 End of Reheating

According to the present scenario, at t_r given by equation (7.52), the sufficiency condition (7.13) no longer holds so that t_r can be identified as the time when reheating ends. At subsequent times $t > t_r$, the available energy in the scalaron field becomes insufficient to populate all available cells in the configuration space and hence the energy density of the Universe will start declining. Thus $\rho(t)$ will have a maxima at time t_r where $\dot{\rho}(t_r) = 0$. Consequently, the density equation (7.16) gives the maxima as

$$\rho_r = \frac{\Gamma}{4H_r}\varepsilon^4, \tag{7.76}$$

where H_r is the average Hubble rate at the end of reheating. Since the reheating temperature can be identified as $T_r \sim \varepsilon$, this immediately implies $4H_r \sim \Gamma$ at the end of reheating.

To this end, we shall analyze the period $t \lesssim t_r$, that is, as the end of reheating is approached. Since the Hubble rate approaches a value $H \approx \frac{\Gamma}{4}$ at $t \approx t_r$, we suppose a solution of the form $H(t) = \frac{\Gamma}{4} + \chi(t)$ in the region $t \lesssim t_r$, where $\chi \ll \frac{\Gamma}{4}$. Using the change of variable $\xi = t_r - t$, equation (7.39) reduces to

$$\chi'' - \frac{3}{4}\Gamma\chi' + \frac{1}{6\alpha}\chi = \frac{1}{6\alpha}\frac{\Gamma}{8}\left(\frac{16}{3}\frac{\varepsilon^2}{m_{\rm P}^2} - 1\right), \tag{7.77}$$

up to linear order in χ. Here the primes denote differentiation with respect to ξ. Since $\varepsilon \ll m_{\rm P}$, this equation can be approximated as

$$\chi'' - \frac{3}{4}\Gamma\chi' + \frac{1}{6\alpha}\chi \approx -\frac{1}{6\alpha}\frac{\Gamma}{8}, \tag{7.78}$$

giving the solution

$$\chi(\xi) = -\frac{\Gamma}{8} + e^{\frac{3\Gamma\xi}{8}}\left\{C_1 e^{\Omega\xi} + C_2 e^{-\Omega\xi}\right\} \tag{7.79}$$

where $\Omega = \sqrt{\frac{9}{64\Gamma^{-2}} - \frac{1}{6\alpha}}$. Since $\tau_{\rm osc} = 2\pi\sqrt{6\alpha} \ll \Gamma^{-1}$, we can neglect the Γ term and Ω becomes imaginary, namely $\Omega = \frac{i}{\sqrt{6\alpha}}$. This leads to

$$\chi(\xi) = -\frac{\Gamma}{8} + Ce^{\frac{3\Gamma\xi}{8}}\sin\left(\frac{\xi}{\sqrt{6\alpha}} + \theta\right), \tag{7.80}$$

so that the Hubble rate becomes

$$H(t) = \frac{\Gamma}{8} + Ce^{\frac{3\Gamma}{8}(t_r - t)}\sin\left(\frac{t_r - t}{\sqrt{6\alpha}} + \theta\right). \tag{7.81}$$

Using the condition $H(t = t_r) = \frac{\Gamma}{4}$, the unknowns can be related as $C = \frac{\Gamma}{8\sin\theta}$, leading to

$$H(t) = \frac{\Gamma}{8}\left\{1 + e^{\frac{3\Gamma}{8}(t_r - t)}\frac{\sin\left(\frac{t_r - t}{\sqrt{6\alpha}} + \theta\right)}{\sin\theta}\right\}, \tag{7.82}$$

in the region $t \lesssim t_r$.

From the equation $R = 6(\dot{H} + 2H^2)$, we thus obtain

$$\begin{aligned} R(t) = -\frac{3}{4}\Gamma\left\{\frac{3\Gamma}{8}\sin\left(\frac{t_r - t}{\sqrt{6\alpha}} + \theta\right) + \frac{1}{\sqrt{6\alpha}}\cos\left(\frac{t_r - t}{\sqrt{6\alpha}} + \theta\right)\right\}\frac{1}{\sin\theta}e^{\frac{3\Gamma}{8}(t_r - t)} \\ + \frac{3}{16}\Gamma^2\left\{1 + e^{\frac{3\Gamma}{8}(t_r - t)}\frac{\sin\left(\frac{t_r - t}{\sqrt{6\alpha}} + \theta\right)}{\sin\theta}\right\}^2. \end{aligned} \tag{7.83}$$

Since $\Gamma \ll \frac{1}{\sqrt{6\alpha}}$, this can be approximated as

$$R(t) \approx -\frac{3}{4}\frac{\Gamma}{\sqrt{6\alpha}}e^{\frac{3\Gamma}{8}(t_r - t)}\frac{\cos\left(\frac{t_r - t}{\sqrt{6\alpha}} + \theta\right)}{\sin\theta} \tag{7.84}$$

As we have discussed earlier, the sufficiency condition (7.13) reaches the equality at $t = t_r$, that is, $\alpha m_{\rm P}^2 R^2 = \varepsilon^4$. Employing equation (7.84), this condition leads to

$$\cot\theta \approx \sqrt{\frac{32}{3}}\left(\frac{\varepsilon^2}{\Gamma m_{\rm P}}\right) \tag{7.85}$$

This implies $\cot\theta \ll 1$, since $\Gamma \sim \varepsilon \ll m_{\rm P}$. Thus the phase θ is approximately given by $\theta \approx \frac{\pi}{2} - \sqrt{\frac{32}{3}}\frac{\varepsilon}{m_{\rm P}}$, so that

$$R(t) \approx -\frac{3}{4}\frac{\Gamma}{\sqrt{6\alpha}}e^{\frac{3\Gamma}{8}(t_r - t)}\cos\left(\frac{t_r - t}{\sqrt{6\alpha}} + \frac{\pi}{2} - \sqrt{\frac{32}{3}}\frac{\varepsilon}{m_{\rm P}}\right), \tag{7.86}$$

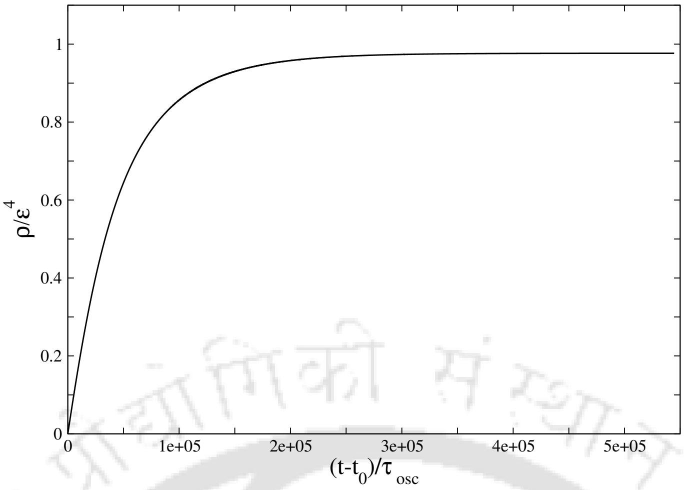

Figure 7.8: Long-time evolution of energy density $\rho(t)$ for $\beta/\alpha = 10^{-2}$ with $\lambda = \Gamma\varepsilon^4$.

in the region $t \lesssim t_r$.

In addition, the Hubble rate given by equation (7.82) is obtained as

$$H(t) \approx \frac{\Gamma}{8}\left\{1 + e^{\frac{3\Gamma}{8}(t_r - t)}\sin\left(\frac{t_r - t}{\sqrt{6\alpha}} + \frac{\pi}{2}\right)\right\} \tag{7.87}$$

in the region $t \lesssim t_r$.

Thus we see that the amplitude of oscillation decreases exponentially with a time scale of $\frac{8}{3\Gamma}$ as t_r is approached from below. It is obvious that this behaviour continues after the time t_r is crossed, that is for $t \gtrsim t_r$.

7.4.4 Preheating and Thermilization

In the previous subsections, we described the details of the dynamical evolution in different regions of the reheating phase. To this end, we identify and analyze the preheating stage with the physical process of thermilization in the reheating phase.

The mean free path $\ell_{\text{mean}}(t)$ of the particles is related to the energy density $\rho(t)$ as

$$\ell_{\text{mean}}(t) \approx \left\{\frac{3}{4\pi}\frac{\varepsilon}{\rho(t)}\right\}^{1/3}. \tag{7.88}$$

Since the particles are expected to be ultra-relativistic, an estimate for collision time-scale is given by

$$\tau_{\text{coll}}(t) \approx \ell_{\text{mean}}(t), \tag{7.89}$$

and the collision rate $\Gamma_{\text{coll}}(t)$ can be estimated as

$$\Gamma_{\text{coll}}(t) \approx \frac{1}{\tau_{\text{coll}}(t)}. \tag{7.90}$$

It is important to note that the collision rate $\Gamma_{\rm coll}(t)$ is a physically different quantity from the particle creation rate Γ.

In the beginning of the reheating phase, that is for $t \gtrsim t_i$, an approximate estimate for the energy density is $\rho(t) \approx \frac{3}{11}\Gamma\varepsilon^4(t-t_i)$, so that the collision rate is estimated as

$$\Gamma_{\rm coll}(t) \approx \left\{\frac{4\pi}{11}\frac{(t-t_i)}{\Gamma^{-1}}\right\}^{1/3}\varepsilon, \tag{7.91}$$

and the average Hubble rate has the behaviour $H(t) \approx \frac{2}{3}\frac{1}{t-t_i}$ in this region. These expressions indicate that $\Gamma_{\rm coll}(t) \ll H(t)$ for $t \gtrsim t_i$. Consequently, the collision rate cannot catch up with the Hubble expansion rate and the system of particles cannot reach thermal equilibrium. This stage is the preheating phase.

For longer times $t > t_i$, the collision rate $\Gamma_{\rm coll}(t)$ increases whereas the Hubble rate decreases. At a time $t_{\rm x}$ (say), the collision rate $\Gamma_{\rm coll}(t)$ catches up with the Hubble rate $H(t)$. Consequently, $\Gamma_{\rm coll}(t_{\rm x}) = H(t_{\rm x})$ gives an estimate for the beginning of thermilization at a time $t_{\rm x}$ as

$$t_{\rm x} - t_i = \left(\frac{22}{27}\frac{\Gamma^{-1}}{\pi\varepsilon^3}\right)^{1/4}, \tag{7.92}$$

from which we obtain an estimate $t_{\rm x} - t_i = 1.74 \times 10^5\, t_{\rm P}$.

This estimate for $t_{\rm x} - t_i$ is from the region when the back-reaction has a negligible effect on the dynamics. As we have seen earlier, the back-reaction becomes effective in the intermediate region of reheating. We can also obtain an estimate for $t_{\rm x} - t_i$ from the intermediate region, where $\rho(t) \approx \frac{3}{11}\Gamma\varepsilon^4(t-t_i)e^{-\frac{12}{5}B(t-t_i)^{5/3}}$, leading to the expression for the collision rate as

$$\Gamma_{\rm coll}(t) \approx \left\{\frac{4\pi}{11}\frac{(t-t_i)}{\Gamma^{-1}}\right\}^{1/3}\varepsilon e^{-\frac{4}{5}B(t-t_i)^{5/3}} \tag{7.93}$$

and the Hubble rate goes like $H \approx \frac{2}{3}\frac{1}{t-t_i} + B(t-t_i)^{2/3}$ in this region. Thus an estimate for $t_{\rm x} - t_i$ can be obtained from $\Gamma_{\rm coll}(t_{\rm x}) = H(t_{\rm x})$, leading to

$$\left\{\left(\frac{4\pi}{11}\frac{(t_{\rm x}-t_i)^4}{\Gamma^{-1}}\right)^{1/3}\varepsilon e^{-\frac{4}{5}B(t_{\rm x}-t_i)^{5/3}} - B(t_{\rm x}-t_i)^{5/3}\right\} = \frac{2}{3} \tag{7.94}$$

This leads to an estimate $t_{\rm x} - t_i = 1.76 \times 10^5\, t_{\rm P}$.

The closeness of the above two estimates for $t_{\rm x} - t_i$, obtained from the beginning and intermediate regions of the reheating phase, indicates that the thermilization process begins at around the same time when the back-reaction on the Hubble rate begins to be effective. At this cross-over, the estimate for the temperature is $T_{\rm x} \sim 6.3 \times 10^{12}$ GeV. For subsequent times $t > t_{\rm x}$, the condition $\Gamma_{\rm coll}(t) > H(t)$ holds and the process of thermilization continues.

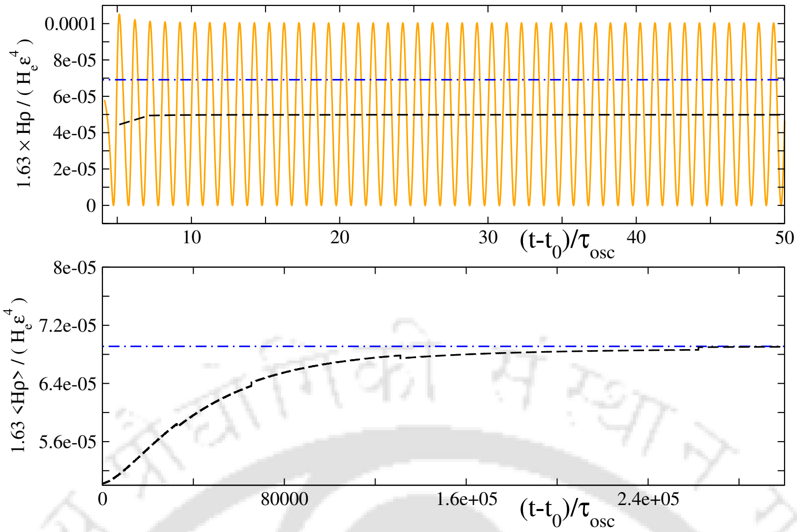

Figure 7.9: Evolution of $4H\rho$ for $\beta/\alpha = 10^{-2}$ and $\lambda = \Gamma\varepsilon^4$. The upper panel shows the initial 50 oscillations of $4H\rho$ in the reheating phase. For comparison with $\Gamma\varepsilon^4$ (horizontal dot-dashed lines), both panels show the time-evolution of $4\langle H\rho\rangle$ (dashed curves), averaged over each cycle. Initially, when $4\langle H\rho\rangle < \Gamma\varepsilon^4$, the average $4\langle H\rho\rangle$ grows with the growth of density. The asymptotic approach of $4\langle H\rho\rangle$ to $\Gamma\varepsilon^4$ corresponds to the density approaching a maxima ($\dot{\rho} = 0$), that follows from equation 7.16.

7.5 Discussion

In the previous sections, we analyzed the different phases by making approximate analytical estimates for average quantities. They represent good approximations because of the fact that the time scale of decay Γ^{-1} spans over many oscillations of the Hubble rate, that is, $\Gamma^{-1} \gg \tau_{\rm osc}$. In particular, since the source term in the density equation contains the time scale Γ^{-1}, the growth in density varies over the same time scale Γ^{-1}, so that the averaged Hubble rate yields a good approximation for the growth in energy density. However, it may be worthwhile to assess the growth in density more accurately by exact numerical solution of the field equation (7.9) coupled with the density equation (7.16) in the inflationary and reheating phases.

Figure 7.3 displays the time evolution of the density $\rho(t)$ for $\beta/\alpha = 10^{-2}$ and 9×10^{-2}. Despite the presence of a constant source $\lambda = \Gamma\varepsilon^4$ in equation (7.16), we see that the density undergoes negligible growth in the inflationary phase. This is due to the quasi-de-Sitter expansion of the Universe in this phase.

As we see from Figure 7.5, the density starts to grow once the inflationary phase is over and the reheating phase begins. Moreover, we see from Figure 7.4 that the Hubble rate starts a damped oscillation in this phase. Consequently, the density grows in periodic successions (as shown in Figure 7.5), happening in every cycle of oscillation of the Hubble rate. This periodic growth in density originates from the fact that the condition $4H\rho \ll \Gamma\varepsilon^4$ is satisfied in a periodic manner when $4H\rho$ passes through a minima (as seen in Figure 7.9) in every cycle of oscillation of the Hubble rate. Whenever this condition is met, the

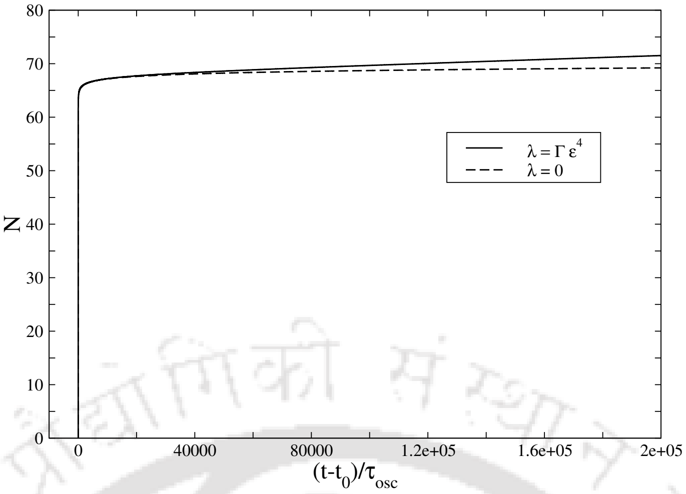

Figure 7.10: Evolution of the number of e-foldings $N(t) = \ln \frac{a(t)}{a_0}$ for $\beta/\alpha = 10^{-2}$ with $\lambda = \Gamma\varepsilon^4$ in the inflationary and reheating phases. $N(t)$ increases in the reheating phase due to the back-reaction of particle creation. The lower curve (for $\lambda = 0$) does not have such back-reaction.

expansion term becomes negligible and the density grows as $\dot{\rho} \approx \Gamma\varepsilon^4$ momentarily. In fact, the amplitude of the humps in the periodic growth of density becomes progressively smaller in size in successive periods of the density growth. This is because of the growing magnitude of ρ itself so that the minimum value of $4H\rho$ increases in succession in every cycle making its value slightly higher than that in the previous cycle.

We can analyze the growth in the density in an averaged fashion from Figure 7.9 that shows $4H\rho$ undergoes a fast oscillation which has a decaying envelop. Due to asymmetry of the oscillation, the time-averaged value $4\langle H\rho\rangle$ increases (7.9) so long as the density continues to grow as a result of meeting the sufficiency condition (7.13). Eventually, $4\langle H\rho\rangle$ approaches a constant value $\Gamma\varepsilon^4$ at long times (as shown in the lower panel of Figure 7.9). This asymptotic approach to a constant value corresponds to the density approaching a maxima ρ_r at a long time t_r, so that $\dot{\rho}$ approaches zero in equation (7.16), when the expansion term compensates for the source term, stopping further growth in density. We have seen in our analytical calculations that this condition is reached simultaneously with $4H_r \sim \Gamma$ that marks the end of the reheating phase. At this moment, the sufficiency condition (7.13) ends and a new phase begins with $\lambda(t)$ given by equation (7.15). However, we note that the maxima ρ_r cannot be accommodated within the time-span in Figure 7.8 because of the slow approach of the density towards ρ_r.

Figure 7.10 displays the number of e-foldings $N(t)$ in the inflationary and reheating phases. The quick growth of this number up to a value ~ 60 marks the inflationary phase. In the subsequent reheating phase, $N(t)$ grows very slowly. It is clear that there is an additional contribution to the growth in $N(t)$ due to back-reaction on the Hubble rate owing to particle creation in the reheating phase.

7.6 Conclusion

In this Chapter, we considered a physically plausible scenario of reheating following the inflationary phase of a modified gravity model $f(R) = R + \alpha R^2 + \beta R^2 \ln R/\mu^2$ in the Jordan frame. Since particle creation is essentially a quantum mechanical phenomenon, we formulated this scenario based on Heisenberg's uncertainty principle as described in detail in Section 7.2.

We find that although particle production happens in the inflationary phase, its contribution to the energy density ρ is negligibly small at the end of inflation because of the quasi-de-Sitter expansion. On the other hand, particle creation happening in the oscillatory regime following the inflationary phase gives rise to a significant growth in the energy density ρ. In the initial stage of this reheating regime, the average density grows linearly with time, whereas the growth in density deviates from linearity at longer times. Eventually, the reheating period ends when the density ρ grows to a maximum value where we find that the Hubble rate H attains a value of the order of the decay rate Γ. This is marked as the end of reheating which follows directly from the sufficiency condition determined by the availability of energy density in the scalaron field in comparison with the available states in the configuration space within a time-span of the inverse decay rate.

In the present scenario, we find that the particle production happens in periodic successions and lasts over several oscillations. This follows from an estimate for Γ obtained from the uncertainty relation $\Delta E\, \Delta t \sim \hbar$, giving $\Delta t \sim \varepsilon^{-1} \sim \Gamma^{-1}$. We find that the decay rate $\Gamma \sim \varepsilon \ll \tau_{\rm osc}^{-1}$, so that the time-scale of decay Γ^{-1} spans over many oscillations of the curvature field. This is consistent with our treatment of the time-evolutions of the Hubble rate and the curvature field in an averaged manner in our analytical calculations.

In the present scenario, the density continues to grow in periodic successions with the amplitude becoming smaller in the successive oscillations and the density approaches a maximum value after many oscillations of the Hubble rate. This behaviour in the growth of density has a negligible back-reaction on the dynamics of the Hubble rate in the initial period of reheating. However, the average Hubble rate decreases and approaching a constant value at long times. This behaviour of the averaged Hubble rate is more transparent in our analytical calculation signifying the effect of back-reaction at longer times. However the effect of back-reaction is negligible in the scalar curvature.

In this scenario of reheating, we find a well-defined period of preheating where the particles are unable to reach thermal equilibrium because their collision rate lags behind the Hubble expansion rate. The end of this preheating stage is marked by the time $t_{\rm x}$ determined by the time when the collision rate $\Gamma_{\rm coll}$ catches up with the Hubble expansion rate H. We find from our calculation that the preheating stage spans over a time of $t_{\rm x} - t_i \sim 1.7 \times 10^5\, t_{\rm P}$. Subsequently, themilization take place as the collision rate $\Gamma_{\rm coll}$ exceeds the Hubble expansion rate H for $t > t_{\rm x}$.

As the density keeps on growing beyond the time $t_{\rm x}$, thermilization keeps the system in thermal equilibrium. The reheating period continues so long as the inequality in the sufficiency condition (7.13) holds, that is, when sufficient energy is available in the scalaron field to completely populate the configuration space constrained by the Heisenberg uncertainty principle. At time t_r, the equality in the sufficiency condition (7.13) is reached when the available energy is just enough to populate the configuration space. We identify this time t_r as the end of reheating because, beyond t_r, sufficient energy is no longer available to populate the entire configuration space. Consequently, from this time t_r onwards, the energy density ρ starts declining. Thus density ρ_r is a maxima occurring at time t_r, implying $\dot{\rho}(t_r) = 0$. Consequently, we find from the density equation (7.16) that the condition $4H(t_r) \sim \Gamma$ is simultaneously reached at the end of reheating.

In the present scenario, the inflationary phase is determined by the parameter α whose value is set by the choice of 60 e-foldings in the inflationary phase. Although the reheating depends on the parameter Γ and ε, we find $\Gamma \sim \varepsilon$ upon employing the energy-time uncertainty relation. Our estimate indicates $\Gamma^{-1} \sim 10^5\, t_{\rm P}$ and $\tau_{\rm osc} \sim \sqrt{6\alpha} \sim 10^3\, t_{\rm P}$ implying Γ^{-1} is much larger that $\tau_{\rm osc}$. Consequently, the average behaviours of the macroscopic quantities pick up weak dependence on the parameter α that determines $\tau_{\rm osc}$.

Our present scenario, based on Heisenberg's uncertainty principle, facilitated a detailed analysis of all stages of the reheating phase. This includes an analysis of the preheating stage and the subsequent cross-over to the thermilization stage along with a proper identification of the end-of-reheating. It may be fair to say that the present scenario gives a fundamental understanding of the physical processes in the reheating phase although it rests on a few approximate but reasonable physical assumptions.

Chapter 8

Conclusion

The main motivation in this thesis started with the exploration of Chandrasekhar's limit in white dwarfs. Although Chandrasekhar obtained this limit a long time ago, its importance has prevailed many astronomical observations ever since. If we look at it in a simple way, it would appear that this limit is important only for compact objects such as white dwarfs. But, this limit has a far greater significance than the domain of compact objects like white dwarfs themselves.

It is now well-known that the type Ia supernovae (SN Ia) occur from the explosion of carbon-oxygen white dwarfs due to accretion from a companion star. Since the peak brightnesses of SN Ia are correlated well with the decay of their light curves, they serve the purpose of standard candles in observational astronomy. This remarkable property of SN Ia has been utilized to measure the accelerated expansion of the Universe. This conclusion could not have been reached without the existence of Chandrasekhar's limit.

It has been questioned whether Chandrasekhar's limit exists when quantum gravitational fluctuations are incorporated in some way or other. Since the theory of quantum gravity is still uncertain, it is usually more practical to account for quantum gravitational fluctuations via phenomenological means. A few phenomenological formulations already exist in the form of generalised uncertainty principle, non-commutative geometry, modified dispersion relation, as discussed in Chapter 1.

It has been shown that Chandrasekhar's limit ceases to exist giving rise to extraordinarily large masses of white dwarfs far exceeding Chandrasekhar's limit, even if the quantum gravity parameter is made arbitrarily small. Since quantum gravity corrections are inevitable, this leads to the conclusion that Chandrasekhar's limit cannot exist. This casts a big question mark on all astronomical observations relying on Chandrasekhar's limit made over several decades.

It thus becomes extremely important to find out whether Chandrasekhar's limit does not really exist. We therefore considered two different approaches, the generalized uncertainty principle in Chapter 2 and the modified dispersion relation in Chapter 3, and found their effects on the equation of state. We saw that this makes the equation of state more stiff than before. This leads to the formation of a hard core that becomes increasingly larger with mass, with no signature of collapse, when Newtonian gravity is employed. This very feature was the reason for the non-existence of Chandrasekhar's limit.

We resolved this paradoxical situation in two different ways. We first considered the effect of inverse β-decay (or neutronization) in Chapters 2 and 3 with Newtonian gravity. As the density becomes higher, it is natural to expect the protons and electrons would combine to give rise to neutrons and neutrinos. This sets a limit on the maximum stable mass that we found to be close to the Chandrasekhar limit. However, the process of neutronization should happen in a cascading manner to bring about the instability. In order to ascertain the instability, it therefore calls for a better formulation, such that the instability should be built into the equation of hydrostatic equilibrium. We thus formulated the problem of instability in the general relativistic framework and performed rigorous instability analyses in both scenarios, generalized uncertainty scenario in Chapter 4 and modified dispersion relation scenario in Chapter 5. Consequently, we saw that Chandrasekhar's limit is guaranteed even if we artificially enhance the energy scale four (two) orders higher than the elctro-weak bound in the generalized uncertainty (modified dispersion relation) scenarios. Thus we can rely on the astronomical observations including the accelerated expansion of the Universe in a satisfactory manner.

Other interesting astrophysical observations are those of pulsars which are usually thought to be neutron stars. However, some recent observations showed pulsars of rather high masses, $\sim 2\ \mathrm{M}_\odot$. Commonly utilized equations of state for neutron matter, when employed in general relativistic formulation, are unable to give rise to masses as high as $\sim 2\ \mathrm{M}_\odot$. It appears that both these assumptions need modification to resolve this issue. At such high densities, we would expect that most of the interior region is made of quark-gluon plasma. Moreover, at high densities, we expect that matter would be coupled to gravity due to quantum effects. This implies that we should work in an extended gravity framework such as $f(R,T)$ gravity in addition to employing the equation of state for quark-gluon matter. Upon doing so, we could see in Chapter 6 that such quark stars can approach masses as high as $\sim 2\ \mathrm{M}_\odot$. This explains that the observed pulsars of $\sim 2\ \mathrm{M}_\odot$ are basically quark stars.

The above finding indicates that the extended gravity scenario works satisfactorily at the scale of compact stars. A natural question then arises how efficient would be the extended gravity scenario at a higher energy scale such as in the inflationary cosmology. This motivated us to employ an extended gravity scenario in order to analyze its predictions in the reheating phase following the inflationary phase of the Universe. We have seen in Chapter 7 that this enables us to formulate a plausible scenario of reheating with constraints in particle creation due to Heisenberg's uncertainty principle. This leads to an efficient reheating in addition to a well-defined preheating stage. Thus an extended gravity scenario is capable of explaining the physics at such high energy scales as well.

As we waded through different problems in gravity at different energy scales, we showed that general relativity works well at the scale of white dwarfs whereas extended gravity works well at high energy scales such neutron stars or pulsars, or even at much higher energy scales such as the inflationary and reheating phases of the Universe.

The above observations give us the motivation to explore problems in the future by considering the energy scale of the system and by formulating the model accordingly. There exist various quantum gravity scenarios in the framework of generalized uncertainty and modified dispersion relation which could be employed to ascertain the validity of Chandrasekhar's limit in white dwarfs.

In this context, we note that Ali [6] proposed a different form of generalized uncertainty principle with the commutation relation $[x_i, p_j] = i\hbar[\delta_{ij} - \alpha(p\delta_{ij} + \frac{p_i p_j}{p})]$. This commutation relation will obviously lead to a different phase space structure than that employed in Chapters 2 and 4. Consequently, this will lead to a different equation of state for the electron degenerate gas. With this generalized uncertainty principle, it would be interesting to study the limiting mass behavior of white dwarfs in the Newtonian gravity as well as general relativity along the lines of Chapters 2 and 4, respectively.

Furthermore, there exist various phenomenologically motivated dispersion relations. A few of them, such as $E^2 - p^2c^2 4\lambda^2 E^2 (1 - e^{-2\lambda E})^{-2} = m^2c^4$ and $E^2 - p^2c^2(1+\lambda E)^{2\gamma} = m^2c^4$, were applied to solve the flatness and horizon problems of the Universe in Ref. [5]. These dispersion relations are therefore good candidates to study their effects on the stellar structure of white dwarfs. It would be worthwhile to study the instability behavior with these dispersion relations in parallel with Chapters 3 and 5 in Newtonian gravity and general relativity, respectively.

In addition, it would be interesting to explore inflationary and reheating phases and neutron stars in different extended gravity scenarios. Harko et al. [84] discussed various $f(R,T)$ models such as $R + \lambda T$ and $R + \lambda RT$. It would thus be interesting to see whether we can reach the observed $\sim 2\ \mathrm{M}_\odot$ for neutron stars and pulsars along the lines of Chapter 6 with these $f(R,T)$ models.

In a likewise manner, it would be worthwhile to study higher order corrections, such as $f(R) = R + \alpha R^2 + \beta R^3$, to study the inflationary and reheating phases of the Universe along the lines of Chapter 7. In addition, it would be interesting to explore the effects of generalized uncertainty principle and modified dispersion scenarios of quantum gravity in inflationary and reheating phases of the Universe described by various extended gravity scenarios.

Appendix A

Implication of extended gravity in the solar system

In this Appendix, we shall examine whether the $f(R,T)$ gravity model discussed in Chapter 6 and $f(R)$ gravity model discussed in Chapter 7 are consistent with the solar system observations.

A.1 Implication of the present $f(R,T)$ model

As discussed earlier in Section (1.6.2), an $f(R,T)$ model generates an extra contribution $\mathbf{a}_E$ to the gravitational acceleration due to gravity-matter coupling. The term ωRT may be relevant in the stellar structure of the star [84]. We shall quantify the magnitude of $\mathbf{a}_E$ by evaluating the potential Q.

The radiation pressure for a fully radiative star such as the Sun cannot be ignored due to its high temperature. Therefore, the solar equation of state is comprised of both gas pressure P_g and radiation pressure P_r,

$$P = P_g + P_r = \frac{k_B}{\mu m_H}\rho T + \frac{1}{3}aT^4, \tag{A.1}$$

where the mean molecular weight $\mu \approx 0.83$, and m_H is the atomic mass of hydrogen.

One can obtain the temperature as a function of density by defining the radiation pressure as $(1-\zeta)P = \frac{1}{3}aT^4$ and the gas pressure as $\zeta P = \frac{k_B}{\mu m_H}\rho T$, where $(1-\zeta) < 0.03$ for the Sun. Eliminating the pressure P, we obtain

$$T = \left\{\frac{k_B}{\mu m_H}\frac{3}{a}\frac{1-\zeta}{\zeta}\right\}^{1/3}\rho^{1/3}. \tag{A.2}$$

Substituting the above expression in $P = \frac{1}{\zeta}\frac{k_B}{\mu m_H}\rho T$, the total pressure P can be represented in the form [49]

$$P = \left\{ \left(\frac{k_B}{\mu m_H} \right)^4 \frac{3}{a} \frac{1-\zeta}{\zeta^4} \right\}^{1/3} \rho^{4/3}. \tag{A.3}$$

Thus the solar equation of state can be written in the polytropic form $P = K\rho^{\gamma} = K\rho^{1+\frac{1}{n}}$ with index $n = 3$.

Since the fluid pressure is high, the right hand side of the geodesic equation (1.144) gives a finite contribution. The fluid particles now experience a force given by

$$\nabla_r \ln \sqrt{Q} = \kappa \frac{\nabla_r P}{(\varepsilon + P)(\kappa + f_T)}. \tag{A.4}$$

Taking non-relativistic approximation and substituting $f_T = \omega R = \frac{\beta}{4B} R \approx \beta\kappa \frac{\rho c^2}{4B}$, the above equation reduces to

$$\frac{d}{dr} \ln \sqrt{Q} \approx \frac{1}{c^2} \left(1 - \beta \frac{\rho c^2}{4B} \right) \frac{1}{\rho} \frac{dP}{dr}. \tag{A.5}$$

Redefining the density as $\rho = \lambda\theta^n$, the polytropic equation of state transforms to $P = K\rho^{1+\frac{1}{n}} = K\lambda^{1+\frac{1}{n}}\theta^{n+1}$. Substituting this expression in equation (A.5), we obtain

$$\frac{d}{dr} \ln \sqrt{Q} = (n+1) \frac{K\lambda^{\frac{1}{n}}}{c^2} \frac{d\theta}{dr} - (n+1)\beta \frac{K\lambda^{\frac{1}{n}+1}}{4B} \theta^n \frac{d\theta}{dr}. \tag{A.6}$$

Integrating and setting $n = 3$, the potential Q is obtained in terms of density ρ as

$$\sqrt{Q}(\rho) = \exp\left(\frac{4K}{c^2} \rho^{\frac{1}{3}} - \beta \frac{K}{4B} \rho^{\frac{4}{3}} + C \right), \tag{A.7}$$

where the integration constant C can be set equal to zero.

The geodesic equation (1.144) can be obtained from the particle action [84]

$$S_p = \int \sqrt{Q\, g_{\mu\nu} u^{\mu} u^{\nu}}\, ds, \tag{A.8}$$

which can be expressed as

$$S_p \approx \int \left(1 + \frac{\phi}{c^2} - \frac{\mathbf{v}^2}{2c^2} + \frac{4K}{c^2} \rho^{\frac{1}{3}} - \beta \frac{K}{4B} \rho^{\frac{4}{3}} \right) dt \tag{A.9}$$

in the non-relativistic approximation. Consequently, Hamilton's principle of least action yields the equation of motion as

$$\frac{d^2 r}{dt^2} = -\frac{d\phi}{dr} - 4K \frac{d}{dr} \rho^{1/3} + \beta \frac{Kc^2}{4B} \frac{d}{dr} \rho^{\frac{4}{3}} = -\frac{d\phi}{dr} - \frac{1}{\rho} \frac{dP}{dr} + \beta \frac{c^2}{4B} \frac{dP}{dr}. \tag{A.10}$$

The extra acceleration generated by the gravity-matter interaction due to the term ωRT is thus obtained as

$$|\mathbf{a}_E| = \beta \frac{c^2}{4B}\left|\frac{dP}{dr}\right|. \tag{A.11}$$

A rough estimate for this acceleration can be obtained from $|\frac{dP}{dr}| = \bar{\rho}_\odot \frac{GM_\odot}{R_\odot^2}$, so that

$$|\mathbf{a}_E| \sim \beta\left(\frac{\bar{\rho}_\odot c^2}{4B}\right)\frac{GM_\odot}{R_\odot^2} \sim 10^{-13}\ \text{ cm/s}^2. \tag{A.12}$$

The constraint coming from the observed value of the precession of mercury requires that a_E must satisfy $a_E \leq 1.28 \times 10^{-9}$ cm/s^2, as discussed in Section 1.6.2. Thus it is clear from the estimate (A.12) that the gravity-matter coupling in the present $f(R,T)$ gravity model does not contribute measurably to the observed precession of the perihelion of mercury. The extreme smallness of the correction to the acceleration due to the term ωRT seems to suggest that it does not violate the observational predictions of the solar system tests.

This suggests that the term ωRT is irrelevant in weak gravity systems such as the solar system. Ignoring this term, we may write the trace equation (6.5) as

$$6\alpha\nabla^\mu\nabla_\mu R - R = \kappa T. \tag{A.13}$$

To analyze the validity of the solar system tests, it is only necessary to examine the vacuum solution of the field equation. An approximate solution for the scalar curvature R in the weak field case such as the Sun is given by equation (6.20) giving an estimate for the radius of the gravitational halo as $r_H \sim \sqrt{6\alpha}$. We thus have $r_H \sim 11.48$ km for $\alpha = 10\ r_g^2$. This estimate for r_H is extremely small compared to the solar radius $R_\odot = 6.96 \times 10^5$ km, so that the gravitational halo is well within the Sun. This also implies that the exponent in equation (6.20) takes a very high magnitude $\gtrsim 10^4$ outside the Sun, making the Ricci scalar practically zero. This implies that the standard solar system tests are practically unaffected due to the modified $f(R,T)$ gravity model of Chapter 6.

A.2 Implication of the present $f(R)$ model

We shall examine the implication of the $f(R)$ model discussed in Chapter 7 in the solar system following the analysis in Ref. [56]. In this analysis, a time independent spherically symmetric perturbation about an homogeneous isotropic (cosmological) background spacetime is considered. Consequently, the Ricci scalar can be written as $R(r,t) = R_0(t) + \chi(r)$. From (1.123), the trace equation for the background can be obtained as

$$f_R^{(0)}R_0 - 2f^{(0)} + 3\Box f_R^{(0)} = \kappa T_0, \tag{A.14}$$

with the background quantities labeled by “0”.

Since the time-scale of variation in the cosmological background (FLRW) spacetime is much longer than the time-scale involved in the solar system, all background quantities are henceforth taken to be time-independent.

Taylor expanding the trace equation upon substituting $T(r) = T_0 + \Theta(r)$, the linearized equation for the spherically symmetric perturbation $\chi(r)$ is obtained as

$$3f_{RR}^{(0)}\Box\chi - \left\{f_R^{(0)} - f_{RR}^{(0)}R_0\right\}\chi = \kappa\Theta, \tag{A.15}$$

where all derivatives of $f(R)$ are well-defined in the background spacetime.

To solve the trace equation (A.15) and the corresponding field equation, a spherically symmetric metric,

$$ds^2 = -\{1 + 2\Psi(r)\}\,dt^2 + \{1 + 2\Phi(r)\}\,dr^2 + r^2 d\Omega^2, \tag{A.16}$$

is assumed in the weak field approximation. In this approximation, the trace equation (A.15) reduces to the inhomogeneous Helmholtz equation, namely

$$(\nabla^2 - m^2)\chi(r) = -\frac{\kappa}{3f_{RR}^{(0)}}\rho(r), \tag{A.17}$$

where

$$m^2 = \frac{1}{3}\left(\frac{f_R^{(0)}}{f_{RR}^{(0)}} - R_0\right). \tag{A.18}$$

The Green function $G(r)$ for equation (A.17) is

$$G(r) = \begin{cases} -\dfrac{\cos mr}{4\pi r}, & m^2 < 0, \\[2ex] -\dfrac{e^{-mr}}{4\pi r}, & m^2 > 0, \end{cases} \tag{A.19}$$

For the case $mr \ll 1$, both Green functions reduce to the Green function of the Laplace equation, namely, $-\frac{1}{4\pi r}$. In this case, the exterior solution is given by

$$\chi(r) = \frac{\kappa}{12\pi f_{RR}^{(0)}}\frac{M}{r}, \tag{A.20}$$

where M is the total mass of the source.

Since $f(R)$ gravity contains an extra degree of freedom called the dilaton, m^{-1} can be interpreted as the range of the dilaton field. The condition $mr \ll 1$ can be written as

$$\left|\frac{1}{3}\left(\frac{f_R^{(0)}}{f_{RR}^{(0)}} - R_0\right)\right| r^2 \ll 1. \tag{A.21}$$

Provided this condition is true, equation (A.20) is the exterior solution to the trace equation. The case $mr \ll 1$, equivalently $m^{-1} \gg r$, thus implies that the range of the dilaton field spans over the entire exterior region of the system.

To determine the metric potentials appearing in (A.16), the field equations are expanded to the linear order. Upon employing the solution (A.20), the field equations can be expressed as

$$\Psi'(r) = \frac{\kappa}{6\pi f_R^{(0)}} \frac{M_r}{r^2} \quad \text{and} \quad \Phi'(r) = \frac{\kappa}{12\pi f_R^{(0)}} \frac{\mathrm{d}}{\mathrm{d}r}\left(\frac{M_r}{r}\right), \tag{A.22}$$

where M_r is the mass enclosed within a sphere of radius r. With vanishing metric potentials for $r \to \infty$, the exterior solutions are thus given by

$$\Psi(r) = -\frac{\kappa}{6\pi f_R^{(0)}} \frac{M}{r} \quad \text{and} \quad \Phi(r) = \frac{\kappa}{12\pi f_R^{(0)}} \left(\frac{M}{r}\right). \tag{A.23}$$

These solutions clearly indicate that $\Psi = -2\Phi = -\frac{GM}{r}$, provided the condition $mr \ll 1$ holds true. Thus, with this condition, the post-Newtonian parameter γ is obtained as $\gamma = \frac{1}{2}$. On the other hand, solar system tests require $\gamma = 1 \pm \mathcal{O}(10^{-5})$ [28, 198]. This indicates that $\gamma = \frac{1}{2}$, obtained for the case $mr \ll 1$, is in contradiction with solar system tests.

It is important to note that the arguments given above are centered around the validity of the condition $mr \ll 1$. This also implies that the $f(R)$ model will be in contradiction with solar system tests whenever the dilaton field spans over the entire system so that the range $m^{-1} \gg$ the size of the solar system.

In the following, we shall analyze whether the above condition ($mr \ll 1$) holds true for the present $f(R)$ model, when applied to the solar system. Consequently, we substitute $f(R) = R + \alpha R^2 + \beta R^2 \ln \frac{R}{\mu^2}$ in (A.18) and obtain

$$m^2 = \frac{1}{6\alpha} \left\{ \frac{1 - 2\beta R_0}{1 + \frac{3}{2}\frac{\beta}{\alpha} + \frac{\beta}{\alpha} \ln \frac{R_0}{\mu^2}} \right\} \tag{A.24}$$

Since $\frac{\beta}{\alpha} \sim 10^{-3}$, the second term in the denominator can be neglected. The background curvature R_0 is related to the present Hubble rate H_p as $R_0 = 12H_p^2$. Since $H_p \sim 10^{-42}$ GeV [183], therefore $R_0 \sim 12H_p^2 \sim 10^{-83}$ GeV^2. Taking the mass scale $\mu \sim 100$ GeV, we thus get $\frac{R_0}{\mu^2} \sim 10^{-87}$, so that $\frac{\beta}{\alpha} \ln \frac{R_0}{\mu^2} \sim 10^{-3} \ln(10^{-87}) \sim -0.2$. Thus the third term in the denominator is subdominant. Moreover, taking $\alpha = 10\ell_P^2$ implies $\beta \sim 10^{-2}\ell_P^2$ giving $\beta R_0 \sim 10^{-123}$, so that

$$m^2 \approx \frac{1}{6\alpha}. \tag{A.25}$$

In the solar system, we take three values of r, namely, the radius of the Sun, the semi-major axis of Mercury orbit, and the size of the solar system. The corresponding values of mr are shown in Table A.1. In all cases, we find that the above condition ($mr \ll 1$) is

Table A.1: Values of $mr = \frac{r}{\sqrt{6\alpha}}$, with $\alpha = 10^2\,\ell_P^2$, for different scales in the solar system.

Scales in the Solar System	r	mr
Radius of the Sun	6.963×10^{10} cm	5.618×10^{42}
Semi-major axis of Mercury orbit	5.791×10^{12} cm	4.672×10^{44}
Size of the solar system	2.875×10^{16} cm	2.320×10^{48}

grossly violated and the opposite condition $mr \gg 1$ is valid. This implies that the range of dilation field $m^{-1} = \sqrt{6\alpha} \sim 10^{-32}$ cm is extremely small compared to the system. Thus the extra degree of freedom coming from the modified gravity model cannot give rise to any observable effect in the solar system. We may therefore conclude that the modified $f(R)$ gravity model of Chapter 7 is consistent with the low-energy physics at various scales of the solar system.

Appendix B

Jeans instability in extended gravity

In this Appendix, we examine the modification in the Jeans instability due to the $f(R,T)$ gravity model employed in Chapter 6.

The $f(R,T)$ field equations (1.139) with the perfect fluid energy-momentum tensor reduces to

$$f_R R_{\mu\nu} - \frac{1}{2} f g_{\mu\nu} + (g_{\mu\nu}\nabla^\alpha\nabla_\alpha - \nabla_\mu\nabla_\nu) f_R = (\kappa + f_T) T_{\mu\nu} - f_T P g_{\mu\nu}. \tag{B.1}$$

The Newtonian approximation to the above field equation is obtained by assuming a static metric perturbation about the Minkowski spacetime, given by

$$g_{00} = -1 - 2\Phi \quad \text{and} \quad g_{ij} = \delta_{ij} - \frac{2}{3}\delta_{ij}\Psi. \tag{B.2}$$

In this approximation, the only significant component of the energy-momentum tensor is $T_{00} = \rho c^2$. Moreover, we may expand $f(R,T)$ about the empty Minkowski spacetime. Thus any deviation from $R = 0$ and $T = 0$ is assumed to be perturbation coming from the metric perturbations. We shall thus Taylor expand $f(R,T)$ and its derivatives about $R = 0$ and $T = 0$ to the linear order, giving

$$f(R,T) = \bar{f} + \bar{f}_R R + \bar{f}_T T, \qquad f_R(R,T) = \bar{f}_R + \bar{f}_{RR} R + \bar{f}_{RT} T \tag{B.3}$$

and

$$f_T(R,T) = \bar{f}_T + \bar{f}_{TR} R + \bar{f}_{TT} T, \tag{B.4}$$

where an overbar indicates that the quantity is evaluated at $R = 0$ and $T = 0$.

Thus the 00-component of the field equation becomes

$$\begin{aligned}\left[\bar{f}_R + \bar{f}_{RR}R + \bar{f}_{RT}T\right]R_{00} - \frac{1}{2}\left[\bar{f} + \bar{f}_R R + \bar{f}_T T\right]g_{00} \\ + (g_{00}\nabla^{\alpha}\nabla_{\alpha} - \nabla_0\nabla_0)\left[\bar{f}_R + \bar{f}_{RR}R + \bar{f}_{RT}T\right] = \left[\kappa + \bar{f}_T + \bar{f}_{TR}R + \bar{f}_{TT}T\right]T_{00} \\ - g_{00}\left[\bar{f}_T + \bar{f}_{TR}R + \bar{f}_{TT}T\right]P\end{aligned} \tag{B.5}$$

Using the metric (B.2), the component of Ricci tensor in the linear order becomes $R_{00} = -\frac{1}{2}\nabla^2 g_{00} = \nabla^2\Phi$ and $R_{ij} = -\frac{1}{2}\nabla^2 g_{ij} = \frac{1}{3}\delta_{ij}\nabla^2\Psi$. Further, the scalar curvature becomes $R = -\nabla^2\Phi + \nabla^2\Psi$. For the current model, $f(R,T) = R + \alpha R^2 + \omega RT$, the values of $f(R,T)$ and its derivatives about $R = 0$ and $T = 0$ yield

$$\bar{f} = 0, \quad \bar{f}_R = 1, \quad \bar{f}_T = 0, \quad \bar{f}_{RR} = 2\alpha, \tag{B.6}$$

$$\bar{f}_{RT} = \bar{f}_{TR} = \omega, \quad \bar{f}_{TT} = 0. \tag{B.7}$$

Hence, the 00-component of the field equation (B.5) reduces to

$$\{1 + 2\alpha R + \omega T\}\, R_{00} - \frac{1}{2}Rg_{00} + (g_{00}\nabla^{\alpha}\nabla_{\alpha} - \nabla_0\nabla_0)\{2\alpha R + \omega T\} = (\kappa + \omega R)T_{00} - \omega RPg_{00}. \tag{B.8}$$

Using the approximate expression for R_{00} and R obtained above, and employing $T \approx -\rho c^2$, the above field equation becomes

$$\nabla^2(\Phi + \Psi) + 4\alpha\nabla^4(\Phi - \Psi) + 2\omega c^2\nabla^2\rho = 2\kappa\rho c^2 \tag{B.9}$$

up to linear order.

We expect that the correction due to gravity-matter coupling to be small, so that the metric potentials Φ and Ψ are connected via the post-Newtonian parameter Γ as $\Psi = \Gamma\Phi$ in the first approximation. This may be justified from the analogy of a similar connection between the metric potentials in general relativity and $f(R)$ gravity. This further reduces field equation (B.9) to

$$(1 + \Gamma)\nabla^2\Phi + 4\alpha(1 - \Gamma)\nabla^4\Phi + 2\omega c^2\nabla^2\rho = 2\kappa\rho c^2, \tag{B.10}$$

which is the modified Poisson equation.

The dynamics of a self gravitating fluid in the non-relativistic approximation is governed by the Euler equation

$$\frac{\partial \mathbf{v}}{\partial t} + \mathbf{v}\cdot\nabla\mathbf{v} = -\frac{\nabla P}{\rho} - \nabla\Phi, \tag{B.11}$$

and the equation of continuity

$$\frac{\partial \rho}{\partial t} + \nabla \cdot (\rho \mathbf{v}) = 0, \tag{B.12}$$

where $\mathbf{v}$ is the velocity of the fluid and Φ the gravitational potential.

To obtain the Jeans instability condition, we consider the behavior of small perturbations about a uniform fluid. The background unperturbed fluid is assumed to be static with uniform density ρ_0 and pressure P_0, and velocity $\mathbf{v}_0 = 0$. To account for perturbations, we write the field quantities as

$$\rho(r,t) = \rho_0 + \tilde{\rho}(r,t), \qquad P(r,t) = P_0 + \tilde{P}(r,t), \qquad \mathbf{v}(r,t) = \mathbf{v}_0 + \tilde{\mathbf{v}}(r,t), \qquad \Phi(r) = \Phi_0 + \tilde{\Phi}(r). \tag{B.13}$$

The gravitational potential is assumed to be static. Moreover, the zero order Euler equation implies $\nabla\Phi_0 = 0$, so that $\Phi_0 =$ constant. However, Poisson's equation requires $\nabla^2\Phi_0 > 0$. This contradiction is sometimes called the Jeans swindle.

To the first order, the modified Poisson equation (B.10) becomes

$$\left\{(1+\Gamma)\nabla^2 + 4\alpha(1-\Gamma)\nabla^4\right\}\tilde{\Phi} = 2c^2(\kappa - \omega\nabla^2)\tilde{\rho}. \tag{B.14}$$

with the gravitational potential generated by the density perturbation $\tilde{\rho}$. The fluid equations (B.11) and (B.12) yield

$$\rho_0 \frac{\partial \tilde{\mathbf{v}}}{\partial t} = -\nabla\tilde{P} - \rho_0\nabla\tilde{\Phi}, \tag{B.15}$$

and

$$\frac{\partial \tilde{\rho}}{\partial t} + \rho_0 \nabla \cdot \tilde{\mathbf{v}} = 0, \tag{B.16}$$

up to the first order.

Combining equations (B.15) and (B.16), we obtain

$$\left\{\frac{\partial^2}{\partial t^2} - c_s^2\nabla^2\right\}\tilde{\rho} = \rho_0\nabla^2\tilde{\Phi} \tag{B.17}$$

To analyze how each mode of the perturbation behaves, we shall use the plane wave solution for $\tilde{\rho}$ and $\tilde{\Phi}$, namely

$$\tilde{\rho} = \tilde{\rho}_k e^{i(\mathbf{k}\cdot\mathbf{x} - \Omega t)} \quad \text{and} \quad \tilde{\Phi} = \tilde{\Phi}_k e^{i(\mathbf{k}\cdot\mathbf{x} - \Omega t)}, \tag{B.18}$$

in equations (B.14) and (B.17). This yields

$$\left\{(1+\Gamma)k^2 - 4\alpha(1-\Gamma)k^4\right\}\tilde{\Phi}_k = -2c^2(\kappa + \omega k^2)\tilde{\rho}_k. \tag{B.19}$$

and

$$\left(\Omega^2 - c_s^2 k^2\right)\tilde{\rho}_k = k^2\rho_0\tilde{\Phi}_k. \tag{B.20}$$

From the above equations, we thus immediately obtain $\tilde{\Phi}_k$ as

$$\tilde{\Phi}_k = -2c^2 \frac{\kappa + \omega k^2}{(1+\Gamma)k^2 - 4\alpha(1-\Gamma)k^4} \tilde{\rho}_k. \tag{B.21}$$

and the dispersion relation

$$\Omega^2 = c_s^2\, k^2 - \frac{2c^4}{1+\Gamma} \frac{\kappa + \omega k^2}{\left\{1 - 4\alpha\left(\frac{1-\Gamma}{1+\Gamma}\right)k^2\right\}} \rho_0. \tag{B.22}$$

For the case $f(R) = R$, we recover the original Jeans dispersion relation,

$$\Omega^2 = c_s^2\, k^2 - \frac{2c^4}{(1+\Gamma)} \kappa \rho_0. \tag{B.23}$$

For the present case $f(R,T) = R + \alpha R^2 + \omega R T$, we obtain the modified Jeans wavenumber k_J as

$$k_J = \left(\frac{c^2}{c_s}\right) \sqrt{\frac{2}{1+\Gamma} \frac{\kappa + \omega k^2}{\left\{1 - 4\alpha\left(\frac{1-\Gamma}{1+\Gamma}\right)k^2\right\}} \rho_0} \tag{B.24}$$

The corresponding free-fall time scale is thus obtained as

$$\tau_{\text{free}} = \frac{2\pi}{c_s} \frac{1}{k_J} = \left(\frac{2\pi}{c^2}\right) \sqrt{\frac{1+\Gamma}{2} \frac{\left[1 - 4\alpha\left(\frac{1-\Gamma}{1+\Gamma}\right)k^2\right]}{\kappa + \omega k^2} \frac{1}{\rho_0}} \tag{B.25}$$

For estimating the free-fall time scale, we shall choose the observed value of post-Newtonian parameter $\Gamma = 3 \pm \mathcal{O}(10^{-5})$. Thus for $\Gamma \approx 3$, the free-fall time becomes

$$\tau_{\text{free}} = \frac{2\sqrt{2}\pi}{c^2} \sqrt{\frac{1 + 2\alpha k^2}{\kappa + \omega k^2} \frac{1}{\rho_0}}. \tag{B.26}$$

Both corrections, due to αR^2 and gravity-matter coupling $\omega R T$, in the free-fall time depend on the wavelength $\lambda = \frac{2\pi}{k}$ of the perturbation. For long wavelengths, such as in the interstellar gas cloud of size ~ 10 pc [80],

$$2\alpha k^2 \sim 10^{-26} \quad \text{and} \quad \frac{\omega}{\kappa} k^2 \sim 10^{-27}, \tag{B.27}$$

for the representative values of parameters $\alpha = 10\, r_g^2$ and $\omega = \frac{\beta}{4B}$ with $\beta = 10^{-2}$ (in Chapter 6). Consequently, there is insignificant contributions from the terms αR^2 and $\omega R T$ on the free-fall time scale of typical gas clouds that form stars of mass $\sim 10\ \mathrm{M}_\odot$. Thus, for the typical density $\rho_0 \sim 10^{-24}$ g cm^{-3}, the free-fall time scale,

$$\tau_{\text{free}} = \frac{2\sqrt{2}\pi}{c^2} \sqrt{\frac{1}{\kappa \rho_0}} = \sqrt{\frac{\pi}{G \rho_0}} \sim 10^8 \text{ yr}, \tag{B.28}$$

remains practically unaffected due to the modified gravity model considered in Chapter 6.

Bibliography

[1] R. J. Adler and D. I. Santiago. On gravity and the uncertainty principle. *Mod. Phys. Lett. A*, 14(20):1371–1381, 1999.

[2] F. Aharonian and et al. The temporal characteristics of the TeV γ-emission from Mkn 501 in 1997 II: Results from HEGRA CT1 and CT2. *Astron. Astrophys.*, 349:29, 1999.

[3] H. Alavirad and J. M. Weller. Modified gravity with logarithmic curvature corrections and the structure of relativistic stars. *Phys. Rev. D*, 88:124034, Dec 2013.

[4] A. Albrecht and P. J. Steinhardt. Cosmology for Grand Unified Theories with radiatively induced symmetry breaking. *Phys. Rev. Lett.*, 48:1220–1223, Apr 1982.

[5] S. Alexander and J. Magueijo. Non-commutative geometry as a realization of varying speed of light cosmology. *arXiv:hep-th/0104093v2*, 2004.

[6] A. F. Ali. Minimal length in quantum gravity, equivalence principle and holographic entropy bound. *Class. Quantum Grav.*, 28(6):065013, 2011.

[7] A. F. Ali and A. N. Tawfik. Effect of the generalized uncertainty principle on compact stars. *Int. J. Mod. Phys. D*, 22(05):1350020, 2013.

[8] D. Amati, M. Ciafaloni, and G. Veneziano. Can spacetime be probed below the string size? *Phys. Lett. B*, 216(1):41 – 47, 1989.

[9] G. Amelino-Camelia. Limits on the measurability of space-time distances in (the semiclassical approximation of) quantum gravity. *Mod. Phys. Lett. A*, 09(37):3415–3422, 1994.

[10] G. Amelino-Camelia. On local observations in quantum gravity. *Mod. Phys. Lett. A*, 11(17):1411–1416, 1996.

[11] G. Amelino-Camelia. Enlarged bound on the measurability of distances and quantum κ-Poincaré group. *Phys. Lett. B*, 392(3):283 – 286, 1997.

[12] G. Amelino-Camelia. Relativity in spacetimes with short-distance structure governed by an observer-independent (Planckian) length scale. *Int. J. Mod. Phys. D*, 11(01):35–59, 2002.

[13] G. Amelino-Camelia, J. Ellis, N. E. Mavromatos, D. V. Nanopoulos, and S. Sarkar. Tests of quantum gravity from observations of γ-ray bursts. *Nature*, 393:763–765, Jun 1988.

[14] G. Amelino-Camelia, N. Loret, G. Mandanici, and F. Mercati. UV and IR quantum-spacetime effects for the Chandrasekhar model. *Int. J. Mod. Phys. D*, 21(06):1250052, 2012.

[15] G. Amelino-Camelia and S. Majid. Waves on non-commutative spacetime and γ-ray bursts. *Int. J. Mod. Phys. A*, 15(27):4301–4323, 2000.

[16] J. Antoniadis, P. C. C. Freire, N. Wex, T. M. Tauris, R. S. Lynch, M. H. van Kerkwijk, M. Kramer, C. Bassa, V. S. Dhillon, T. Driebe, J. W. T. Hessels, V. M. Kaspi, V. I. Kondratiev, N. Langer, T. R. Marsh, M. A. McLaughlin, T. T. Pennucci, S. M. Ransom, I. H. Stairs, J. van Leeuwen, J. P. W. Verbiest, and D. G. Whelan. A massive pulsar in a compact relativistic binary. *Science*, 340(6131), 2013.

[17] S. A. Appleby, R. A. Battye, and A. A. Starobinsky. Curing singularities in cosmological evolution of $f(R)$ gravity. *J. Cosmol. Astropart. Phys.*, 2010(06):005–005, Jun 2010.

[18] S. Arapoğlu, C. Deliduman, and K. Y. Ekşi. Constraints on perturbative $f(R)$ gravity via neutron stars. *J. Cosmol. Astropart. Phys.*, 2011(07):020–020, Jul 2011.

[19] M. Artymowski and Z. Lalak. Inflation and dark energy from $f(R)$ gravity. *J. Cosmol. Astropart. Phys.*, 2014(09):036–036, Sep 2014.

[20] A. V. Astashenok, S. Capozziello, and S. D. Odintsov. Nonperturbative models of quark stars in $f(R)$ gravity. *Phys. Lett. B*, 742:160 – 166, 2015.

[21] A. V. Astashenok, S. D. Odintsov, and Á. de la Cruz-Dombriz. The realistic models of relativistic stars in $f(R) = R + \alpha R^2$ gravity. *Class. Quantum Gravity*, 34(20):205008, Sep 2017.

[22] H. W. Babcock. The rotation of the Andromeda Nebula. *Lick Obs. Bull.*, 19:41, 1939.

[23] J. M. Bardeen, K. S. Thorne, and D. W. Meltzer. A catalogue of methods for studying the normal modes of radial pulsation of general-relativistic stellar models. *Astrophys. J.*, 145:505, 1966.

[24] E. Barrientos and S. Mendoza. MOND as the weak field limit of an extended metric theory of gravity with a matter-curvature coupling. *Phys. Rev. D*, 98(5):084033, Oct 2018.

[25] J. D. Bekenstein. The modified Newtonian dynamics—MOND and its implications for new physics. *Contemp. Phys.*, 47(6):387–403, 2006.

[26] T. Bernal, S. Capozziello, J. C. Hidalgo, and S. Mendoza. Recovering MOND from extended metric theories of gravity. *Eur. Phys. J. C*, 71(11):1794, Nov 2011.

[27] O. Bertolami and C. A. D. Zarro. Towards a noncommutative Astrophysics. *Phys. Rev. D*, 81:025005, Jan 2010.

[28] B. Bertotti, L. Iess, and P. Tortora. A test of general relativity using radio links with the Cassini spacecraft. *Nature*, 425(6956):374–376, Sept. 2003.

[29] F. Bezrukov and M. Shaposhnikov. The standard model higgs boson as the inflaton. *Phys. Lett. B*, 659(3):703 – 706, 2008.

[30] S. D. Biller, A. C. Breslin, J. Buckley, M. Catanese, M. Carson, D. A. Carter-Lewis, M. F. Cawley, D. J. Fegan, J. P. Finley, J. A. Gaidos, A. M. Hillas, F. Krennrich, R. C. Lamb, R. Lessard, C. Masterson, J. E. McEnery, B. McKernan, P. Moriarty, J. Quinn, H. J. Rose, F. Samuelson, G. Sembroski, P. Skelton, and T. C. Weekes. Limits to quantum gravity effects on energy dependence of the speed of light from observations of TeV flares in Active Galaxies. *Phys. Rev. Lett.*, 83:2108–2111, Sep 1999.

[31] N. D. Birrell and P. C. W. Davies. *Quantum Fields in Curved Space*. Cambridge Monographs on Mathematical Physics. Cambridge University Press, 1982.

[32] H. E. Bond, P. Bergeron, and A. Bédard. Astrophysical implications of a new dynamical mass for the nearby white dwarf 40 Eridani B. *Astrophys. J.*, 848(1):16, 2017.

[33] F. Brau. Minimal length uncertainty relation and the Hydrogen atom. *J. Phys. A*, 32(44):7691, 1999.

[34] F. Brau and F. Buisseret. Minimal length uncertainty relation and gravitational quantum well. *Phys. Rev. D*, 74:036002, Aug 2006.

[35] P. Brax, C. van de Bruck, and A. C. Davis. Swampland and screened modified gravity. *Phys. Rev. D*, 101:083514, Apr 2020.

[36] R. Brout, F. Englert, J.-M. Frère, E. Gunzig, P. Nardone, C. Truffin, and P. Spindel. Cosmogenesis and the origin of the fundamental length scale. *Nucl. Phys. B*, 170(2):228 – 264, 1980.

[37] H. A. Buchdahl. Non-Linear Lagrangians and Cosmological Theory. *Mon. Not. R. Astron. Soc.*, 150(1):1–8, 1970.

[38] T. S. Bunch and P. C. W. Davies. Stress tensor and conformal anomalies for massless fields

in a Robertson-Walker Universe. *Proc. R. Soc. A*, 356(1687):569–574, 1977.

[39] L. Buoninfante, G. G. Luciano, and L. Petruzziello. Generalized Uncertainty Principle and Corpuscular gravity. *Eur. Phys. J. C*, 79:663, Sep 2019.

[40] M. J. Burke, S. Raychaudhury, R. P. Kraft, N. J. Brassington, M. J. Hardcastle, J. L. Goodger, G. R. Sivakoff, W. R. Forman, C. Jones, K. A. Woodley, S. S. Murray, J. Kainulainen, M. Birkinshaw, J. H. Croston, D. A. Evans, M. Gilfanov, A. Jordán, C. L. Sarazin, R. Voss, D. M. Worrall, and Z. Zhang. A transient Sub-Eddington black hole X-ray binary candidate in the dust lanes of Centaurus A. *Astrophys. J.*, 749(2):112, Mar 2012.

[41] A. Camacho. White dwarfs as test objects of Lorentz violations. *Class. Quantum Grav*, 23(24):7355, 2006.

[42] R. Canal, J. Isern, and J. Labay. The collapse of Carbon-Oxygen white dwarfs. *Astrophys. J. Lett.*, 241(1):L33, 1980.

[43] S. Capozziello, V. Cardone, S. Carloni, and A. Troisi. Can higher order curvature theories explain rotation curves of galaxies? *Phys. Lett. A*, 326(5):292 – 296, 2004.

[44] S. Capozziello, V. F. Cardone, and A. Troisi. Low surface brightness galaxy rotation curves in the low energy limit of R^n gravity: No need for dark matter? *Mon. Not. R. Astron. Soc.*, 375(4):1423–1440, 02 2007.

[45] S. Capozziello, M. De Laurentis, R. Farinelli, and S. D. Odintsov. Mass-radius relation for neutron stars in $f(R)$ gravity. *Phys. Rev. D*, 93:023501, Jan 2016.

[46] S. M. Carroll, V. Duvvuri, M. Trodden, and M. S. Turner. Is cosmic speed-up due to new gravitational physics? *Phys. Rev. D*, 70:043528, Aug 2004.

[47] G. A. Carvalho, R. V. Lobato, P. H. R. S. Moraes, J. D. V. Arbañil, E. Otoniel, R. M. Marinho, and M. Malheiro. Stellar equilibrium configurations of white dwarfs in the $f(R, T)$ gravity. *Eur. Phys. J. C*, 77(12):871, Dec 2017.

[48] R. Casadio, A. Giugno, and A. Giusti. Global and local horizon quantum mechanics. *Gen. Relativ. Gravit.*, 49:32, sep 2017.

[49] S. Chandrasekhar. *An Introduction to the Study of Stellar Structure.* Dover Publications, 1939.

[50] S. Chandrasekhar. Dynamical instability of gaseous masses approaching the Schwarzchild limit in general relativity. *Phys. Rev. Lett.*, 12, 1964.

[51] S. Chandrasekhar. The dynamical instability of gaseous masses approaching the Schwarzschild limit in general relativity. *Astrophys. J.*, 190:417, 1964.

[52] S. Chandrasekhar and F. R. Tooper. The dynamical instability of the white dwarf configurations approaching the limiting mass. *Astrophys. J.*, 139:1396, 1964.

[53] L. N. Chang, D. Minic, N. Okamura, and T. Takeuchi. Effect of the minimal length uncertainty relation on the density of states and the cosmological constant problem. *Phys. Rev. D*, 65:125028, Jun 2002.

[54] P. Chen, T. Suyama, and J. Yokoyama. Spontaneous-scalarization-induced dark matter and variation of the gravitational constant. *Phys. Rev. D*, 92:124016, Dec 2015.

[55] W.-C. Chen and X.-D. Li. On the progenitors of Super-Chandrasekhar mass Type Ia Supernovae. *Astrophys. J.*, 702(1):686, 2009.

[56] T. Chiba, T. L. Smith, and A. L. Erickcek. Solar system constraints to general $f(r)$ gravity. *Phys. Rev. D*, 75:124014, Jun 2007.

[57] H. T. Cromartie, E. Fonseca, S. M. Ransom, P. B. Demorest, Z. Arzoumanian, H. Blumer, P. R. Brook, M. E. DeCesar, T. Dolch, J. A. Ellis, R. D. R. D. Ferdman, E. C. Ferrara, N. Garver-Daniels, P. A. Gentile, M. L. Jones, M. T. Lam, D. R. Lorimer, R. S. Lynch, M. A. McLaughlin, C. Ng, D. J. Nice, T. T. Pennucci, R. Spiewak, I. H. Stairs, K. Stovall,

J. K. Swiggum, and W. W. Zhu. Relativistic Shapiro delay measurements of an extremely massive millisecond pulsar. *Nat Astron*, 4:72–76, 2020.

[58] S. Das and E. C. Vagenas. Universality of quantum gravity corrections. *Phys. Rev. Lett.*, 101:221301, Nov 2008.

[59] U. Das and B. Mukhopadhyay. Strongly magnetized cold degenerate electron gas: Mass-Radius relation of the magnetized white dwarf. *Phys. Rev. D*, 86:042001, Aug 2012.

[60] P. C. W. Davies, S. A. Fulling, S. M. Christensen, and T. S. Bunch. Energy-momentum tensor of a massless scalar quantum field in a Robertson-Walker Universe. *Ann. Phys. (N. Y.)*, 109(1):108 – 142, 1977.

[61] P. de Bernardis et al. A flat Universe from high-resolution maps of the cosmic microwave background radiation. *Nature*, 404:955–959, Apr 2000.

[62] A. De Felice and S. Tsujikawa. $f(R)$ theories. *Living Rev. Relativ.*, 13(1):3, 2010.

[63] D. Deb, F. Rahaman, S. Ray, and B. K. Guha. Strange stars in $f(R,T)$ gravity. *J. Cosmol. Astropart. Phys.*, 2018(03):044–044, Mar 2018.

[64] P. B. Demorest, T. Pennucci, S. M. Ransom, M. S. E. Roberts, and J. W. T. Hessels. A two-solar-mass neutron star measured using Shapiro delay. *Nature*, 467(11):1081–1083, 2010.

[65] S. Doplicher, K. Fredenhagen, and J. E. Roberts. Spacetime quantization induced by classical gravity. *Phys. Lett. B*, 331(1):39 – 44, 1994.

[66] S. Doplicher, K. Fredenhagen, and J. E. Roberts. The quantum structure of spacetime at the Planck scale and quantum fields. *Commun. Math. Phys.*, 172(1):187–220, Aug 1995.

[67] J. Ellis, N. E. Mavromatos, and D. V. Nanopoulos. Quantum-gravitational diffusion and stochastic fluctuations in the velocity of light. *Gen. Rel. and Gravit.*, 32(1):127–144, Jan 2000.

[68] J. Ellis, N. E. Mavromatos, and D. V. Nanopoulos. Probing a possible vacuum refractive index with γ-ray telescopes. *Phys. Lett. B*, 674(2):83 – 86, 2009.

[69] E. Farhi and R. L. Jaffe. Strange matter. *Phys. Rev. D*, 30:2379–2390, Dec 1984.

[70] B. D. Fields and K. A. Olive. Model-independent predictions of big bang nucleosynthesis. *Phys. Lett. B*, 368(1):103 – 111, 1996.

[71] E. Fonseca, T. T. Pennucci, J. A. Ellis, I. H. Stairs, D. J. Nice, S. M. Ransom, P. B. Demorest, Z. Arzoumanian, K. Crowter, T. Dolch, R. D. Ferdman, M. E. Gonzalez, G. Jones, M. L. Jones, M. T. Lam, L. Levin, M. A. McLaughlin, K. Stovall, J. K. Swiggum, and W. Zhu. The nanograv nine-year data set: Mass and geometric measurements of binary milisecond pulsars. *Astrophys. J.*, 832(2):167, Dec 2016.

[72] L. H. Ford. Gravitational particle creation and inflation. *Phys. Rev. D*, 35:2955–2960, May 1987.

[73] A. Friedmann. On the curvature of space. *Z. Phys.*, 10:377, 1922.

[74] L. J. Garay. Quantum gravity and minimum length. *Int. J. Mod. Phys. A*, 10(02):145–165, 1995.

[75] H. Georgi and S. L. Glashow. Unity of all elementary-particle forces. *Phys. Rev. Lett.*, 32:438–441, Feb 1974.

[76] H. Georgi, H. R. Quinn, and S. Weinberg. Hierarchy of interactions in Unified Gauge Theories. *Phys. Rev. Lett.*, 33:451–454, Aug 1974.

[77] J. Greensite. Is there a minimum length in $D = 4$ Lattice Quantum Gravity? *Phys. Lett. B*, 255(3):375 – 380, 1991.

[78] M. Gregg and S. A. Major. On modified dispersion relations and the Chandrasekhar mass limit. *Int. J. Mod. Phys. D*, 18(06):971–982, 2009.

[79] A. H. Guth. Inflationary Universe: A possible solution to the horizon and flatness problems. *Phys. Rev. D*, 23:347–356, Jan 1981.

[80] D. T. Haar. The size of Interstellar Clouds. *Zeitschrift fur Astrophysik*, 32:251–256, 1953.

[81] T. Harko and F. S. N. Lobo. $f(R, L_m)$ gravity. *Eur. Phys. J. C*, 70(1):373–379, Nov 2010.

[82] T. Harko and F. S. N. Lobo. Generalized dark gravity. *Int. J. Mod. Phys. D*, 21(11):1242019, 2012.

[83] T. Harko and F. S. N. Lobo. *Extensions of $f(R)$ gravity curvature-matter couplings and hybrid metric-Palatini gravity*. Cambridge monographs on mathematical physics. Cambridge University Press, 2018.

[84] T. Harko, F. S. N. Lobo, S. Nojiri, and S. D. Odintsov. $f(R,T)$ Gravity. *Phys. Rev. D*, 84:024020, Jul 2011.

[85] S. W. Hawking. Spacetime Foam. *Nucl. Phys. B*, 144(2):349 – 362, 1978.

[86] W. K. Heisenberg. The development of quantum mechanics. *Nobel Lecture*, Dec 1933.

[87] W. K. Heisenberg, C. Eckart, and F. C. Hoyt. *The physical principles of quantum theory*. Dover Publications, 1930.

[88] A. Hewish, S. J. Bell, J. D. H. Pilkington, P. F. Scott, and R. A. Collins. Observation of a rapidly pulsating radio source. *Nature*, 217:709–713, 1968.

[89] M. Hicken, P. M. Garnavich, J. L. Prieto, S. Blondin, D. L. DePoy, R. P. Kirshner, and J. Parrent. The luminous and Carbon-rich Supernova 2006gz: A double degenerate merger? *Astrophys. J. Lett.*, 669(1):L17, 2007.

[90] K. Hinterbichler and J. Khoury. Screening long-range forces through local symmetry restoration. *Phys. Rev. Lett.*, 104:231301, Jun 2010.

[91] P.-M. Ho and H.-C. Kao. Noncommutative quantum mechanics from noncommutative quantum field theory. *Phys. Rev. Lett.*, 88:151602, Mar 2002.

[92] S. Hossenfelder. A note on theories with a minimal length. *Class. Quantum Grav.*, 23(5):1815, 2006.

[93] A. Howell, M. Sullivan, P. E. Nugent, R. S. Ellis, A. J. Conley, D. Le Borgne, R. G. Carlberg, J. Guy, D. Balam, S. Basa, D. Fouchez, I. M. Hook, E. Y. Hsiao, J. D. Neill, R. Pain, K. M. Perrett, and C. J. Pritchet. The Type Ia supernova SNLS-03D3bb from a Super-Chandrasekhar-mass white dwarf star. *Nature*, 443(7109):308–311, 09 2006.

[94] K. Huang. *Statistical Mechanics*. Wiley, 1987.

[95] L. Husdal. On effective degrees of freedom in the early Universe. *Galaxies*, 4:78, Feb 2016.

[96] R. L. Jaffe and F. E. Low. Connection between quark-model eigenstates and low-energy scattering. *Phys. Rev. D*, 19:2105–2118, Apr 1979.

[97] P. Jizba, H. Kleinert, and F. Scardigli. Uncertainty relation on a world crystal and its applications to micro black holes. *Phys. Rev. D*, 81:084030, Apr 2010.

[98] T. Kanazawa, G. Lambiase, G. Vilasi, and et al. Noncommutative Schwarzschild geometry and generalized uncertainty principle. *Eur. Phys. J. C*, 79:95, Sep 2019.

[99] A. Kehagias, M. A. Dizgah, and A. Riotto. Remarks on the Starobinsky model of inflation and its descendants. *Phys. Rev. D*, 89:043527, Feb 2014.

[100] A. Kempf, G. Mangano, and R. B. Mann. Hilbert space representation of the minimal length uncertainty relation. *Phys. Rev. D*, 52:1108–1118, Jul 1995.

[101] S. O. Kepler, S. J. Kleinman, A. Nitta, D. Koester, B. G. Castanheira, O. Giovannini, A. F. M. Costa, and L. Althaus. White dwarf mass distribution in the SDSS. *Mon. Not. Roy. Astron. Soc.*, 375(4):1315–1324, 2007.

[102] S. Y. Khlebnikov and I. I. Tkachev. Classical decay of the inflaton. *Phys. Rev. Lett.*, 77:219–222, Jul 1996.

[103] J. Khoury and A. Weltman. Chameleon Cosmology. *Phys. Rev. D*, 69:044026, Feb 2004.

[104] J. Khoury and A. Weltman. Chameleon Fields: Awaiting surprises for tests of gravity in space. *Phys. Rev. Lett.*, 93:171104, Oct 2004.

[105] T. W. B. Kibble. Some implications of a cosmological phase transition. *Phys. Rep.*, 67(1):183 – 199, 1980.

[106] T. Kifune. Invariance violation extends the cosmic-ray horizon? *Astrophys. J. Lett.*, 518(1):L21, 1999.

[107] M. Kilic, C. A. Prieto, W. R. Brown, and D. Koester. The lowest mass white dwarf. *Astrophys. J.*, 660(2):1451, 2007.

[108] L. Kofman, A. Linde, and A. A. Starobinsky. Reheating after Inflation. *Phys. Rev. Lett.*, 73:3195–3198, Dec 1994.

[109] L. Kofman, A. Linde, and A. A. Starobinsky. Towards the theory of reheating after inflation. *Phys. Rev. D*, 56:3258–3295, Sep 1997.

[110] T. Koivisto. A note on covariant conservation of energy–momentum in modified gravities. *Class. Quantum Gravity*, 23(12):4289–4296, Jun 2006.

[111] E. W. Kolb and M. S. Turner. *The Early Universe.* Westview Press, New York, 1990.

[112] K. Konishi, G. Paffuti, and P. Provero. Minimum physical length and the generalized uncertainty principle in string theory. *Phys. Lett. B*, 234(3):276 – 284, 1990.

[113] L. D. Landau and E. M. Lifschits. *The Classical Theory of Fields, (Course of Theoretical Physics) Volume 2.* Pergamon Press, Oxford, 1975.

[114] L. D. Landau and E. M. Lifshitz. *Statistical Physics,* Part 1. Pergamon, 1969.

[115] L. D. Landau and E. M. Lifshitz. *Mechanics, (Course of Theoretical Physics) Volume 1 Third Edition.* Butterworth-Heinemann, 1976.

[116] A. Linde. Coleman-Weinberg theory and the new Inflationary Universe scenario. *Phys. Lett. B*, 114(6):431 – 435, 1982.

[117] A. D. Linde. A new inflationary Universe scenario: A possible solution of the horizon, flatness, homogeneity, isotropy and primordial monopole problems. *Phys. Lett. B*, 108(6):389 – 393, 1982.

[118] A. D. Linde. Scalar field fluctuations in the expanding Universe and the new Inflationary Universe scenario. *Phys. Lett. B*, 116(5):335 – 339, 1982.

[119] A. D. Linde. Chaotic Inflation. *Phys. Lett. B*, 129(3):177 – 181, 1983.

[120] A. D. Linde. The Inflationary Universe. *Rep. Prog. Phys.*, 47(8):925–986, Aug 1984.

[121] A. D. Linde. Initial conditions for inflation. *Phys. Lett. B*, 162(4):281 – 286, 1985.

[122] J. Liu, H. Zhang, A. W. Howard, Z. Bai, Y. Lu, R. Soria, S. Justham, X. Li, Z. Zheng, T. Wang, K. Belczynski, J. Casares, W. Zhang, H. Yuan, Y. Dong, Y. Lei, H. Isaacson, S. Wang, Y. Bai, Y. Shao, Q. Gao, Y. Wang, Z. Niu, K. Cui, C. Zheng, X. Mu, L. Zhang, W. Wang, A. Heger, Z. Qi, S. Liao, M. Lattanzi, W.-M. Gu, J. Wang, J. Wu, L. Shao, R. Shen, X. Wang, J. Bregman, R. Di Stefano, Q. Liu, Z. Han, T. Zhang, H. Wang, J. Ren, J. Zhang, J. Zhang, X. Wang, A. Cabrera-Lavers, R. Corradi, R. Rebolo, Y. Zhao, G. Zhao, Y. Chu, and X. Cui. A wide star-black-hole binary system from radial-velocity measurements. *Nature*, 575(7784):618–621, 2019.

[123] M. Maggiore. A generalized uncertainty principle in quantum gravity. *Phys. Lett. B*, 304(1):65 – 69, 1993.

[124] M. Maggiore. Quantum groups, gravity, and the generalized uncertainty principle. *Phys. Rev. D*, 49:5182–5187, May 1994.

[125] J. a. Magueijo and L. Smolin. Lorentz invariance with an invariant energy scale. *Phys. Rev. Lett.*, 88:190403, Apr 2002.

[126] S. Majid. *Foundations of Quantum Group Theory.* Cambridge University Press, 1995.

[127] S. Majid and R. Oeckl. Twisting of quantum differentials and the Planck scale Hopf algebra. *Commun. Math. Phys.*, 205(3):617–655, 1999.

[128] S. Majid and H. Ruegg. Bicrossproduct structure of κ-Poincare group and non-commutative

geometry. *Phys. Lett. B*, 334(3):348–354, 1994.

[129] M. C. Marsh, M. A. Barstow, D. A. Buckley, M. R. Burleigh, J. B. Holberg, D. Koester, D. O'Donoghue, A. J. Penny, and A. E. Sansom. An EUV-selected sample of DA white dwarfs from the ROSAT All-Sky Survey–I. Optically derived stellar parameters. *Mon. Not. Roy. Astron. Soc.*, 286(2):369–383, 1997.

[130] J. C. Mather, E. S. Cheng, D. A. Cottingham, J. Eplee, R. E., D. J. Fixsen, T. Hewagama, R. B. Isaacman, K. A. Jensen, S. S. Meyer, P. D. Noerdlinger, S. M. Read, L. P. Rosen, R. A. Shafer, E. L. Wright, C. L. Bennett, N. W. Boggess, M. G. Hauser, T. Kelsall, J. Moseley, S. H., R. F. Silverberg, G. F. Smoot, R. Weiss, and D. T. Wilkinson. Measurement of the cosmic microwave background spectrum by the COBE FIRAS instrument. *Astrophys. J*, 420:439, Jan. 1994.

[131] J. C. Mather, D. J. Fixsen, R. A. Shafer, C. Mosier, and D. T. Wilkinson. Calibrator design for the COBE far-infrared absolute spectrophotometer (FIRAS). *Astrophys. J.*, 512(2):511–520, feb 1999.

[132] A. Mathew and M. K. Nandy. Effect of minimal length uncertainty on the mass-radius relation of white dwarfs. *Ann. Phys. (N. Y.)*, 393:184 – 205, 2018.

[133] A. Mathew and M. K. Nandy. Noncommutative dispersion relation and mass-radius relation of white dwarfs. *Res. Astron. Astrophys.*, 18(12):151, Dec 2018.

[134] A. Mathew and M. K. Nandy. Primordial reheating in $f(R)$ cosmology by spontaneous decay of scalarons. *preprint*, 2020.

[135] A. Mathew and M. K. Nandy. Prospect of Chandrasekhar's limit against modified dispersion relation. *Gen. Relativ. Gravit.*, 52:38, 2020.

[136] A. Mathew and M. K. Nandy. Existence of Chandrasekhar's limit in generalized uncertainty white dwarfs. *R. Soc. open sci.*, 8:210301, 2021.

[137] A. Mathew, M. Shafeeque, and M. K. Nandy. Stellar structure of quark stars in a modified Starobinsky gravity. *Eur. Phys. J. C*, 80:615, 2020.

[138] S. S. McGaugh. Novel test of modified Newtonian dynamics with gas rich galaxies. *Phys. Rev. Lett.*, 106:121303, Mar 2011.

[139] S. S. McGaugh and W. J. G. de Blok. Testing the hypothesis of modified dynamics with low surface brightness galaxies and other evidence. *Astrophys. J.*, 499(1):66–81, May 1998.

[140] C. A. Mead. Possible connection between gravitation and fundamental length. *Phys. Rev.*, 135:B849–B862, Aug 1964.

[141] S. Mendoza. MOND as the basis for an extended theory of gravity. *Can. J. Phys.*, 93(2):217–231, 2015.

[142] Mignani, R. P., Zharikov, S., and Caraveo, P. A. The optical spectrum of the Vela pulsar. *A&A*, 473(3):891–896, 2007.

[143] S. Mignemi and D. L. Wiltshire. Black holes in higher-derivative gravity theories. *Phys. Rev. D*, 46:1475–1506, Aug 1992.

[144] M. B. Mijić, M. S. Morris, and W.-M. Suen. The R^2 cosmology: Inflation without a phase transition. *Phys. Rev. D*, 34:2934–2946, Nov 1986.

[145] M. Milgrom. A modification of the Newtonian dynamics as a possible alternative to the hidden mass hypothesis. *Astrophys. J.*, 270:365–370, Jul 1983.

[146] S. Morisaki and T. Suyama. Spontaneous scalarization with an extremely massive field and heavy neutron stars. *Phys. Rev. D*, 96:084026, Oct 2017.

[147] H. Motohashi and A. Nishizawa. Reheating after $f(R)$ inflation. *Phys. Rev. D*, 86:083514, Oct 2012.

[148] M. Moussa. Quantum gases and white dwarfs with quantum gravity. *J. Stat. Mech: Theory*

Exp., 2014(11):P11034, nov 2014.

[149] M. Moussa. Effect of generalized uncertainty principle on main-sequence stars and white dwarfs. *Adv. in High Energy Phys.*, 2015(343284):9, 2015.

[150] J. Näf and P. Jetzer. On the $\frac{1}{c}$ expansion of $f(R)$ gravity. *Phys. Rev. D*, 81(8):104003, May 2010.

[151] J. Narlikar and T. Padmanabhan. The problems of singularity particle horizon and flatness in quantum cosmology. *Ann. Phys. (N. Y.)*, 150(2):289 – 306, 1983.

[152] J. V. Narlikar. *An introduction to cosmology.* Cambridge University Press, 2002.

[153] V. V. Nesvizhevsky, A. K. Petukhov, H. G. Börner, T. A. Baranova, A. M. Gagarski, G. A. Petrov, K. V. Protasov, A. Y. Voronin, S. Baeßler, H. Abele, A. Westphal, and L. Lucovac. Study of the neutron quantum states in the gravity field. *Eur. Phys. J. C*, 40(4):479–491, Apr 2005.

[154] K. Nozari and B. Fazlpour. Generalized uncertainty principle, modified dispersion relations and the early Universe thermodynamics. *Gen. Rel. Grav.*, 38(11):1661–1679, Nov 2006.

[155] R. Oeckl. Classification of differential calculi on Uq(b+), classical limits, and duality. *J. Math. Phys.*, 40(7):3588–3603, 1999.

[156] Y. C. Ong. Generalized uncertainty principle, black holes, and white dwarfs: A tale of two infinities. *J. Cosmol. Astropart. Phys*, 2018(09):015, 2018.

[157] Y. C. Ong and Y. Yao. Generalized uncertainty principle and white dwarfs redux: How the cosmological constant protects the Chandrasekhar limit. *Phys. Rev. D*, 98:126018, Dec 2018.

[158] J. H. Oort. The force exerted by the stellar system in the direction perpendicular to the galactic plane and some related problems. *Bull. Astron. Inst. Netherlands*, 6:249, 1932.

[159] J. R. Oppenheimer and G. M. Volkoff. On massive neutron cores. *Phys. Rev.*, 55:374–381, Feb 1939.

[160] M. Orellana, F. García, F. A. Teppa Pannia, and G. E. Romero. Structure of neutron stars in R-squared gravity. *Gen. Relativ. Gravit.*, 45(4):771–783, Apr 2013.

[161] T. Padmanabhan. Physical significance of Planck length. *Ann. Phys. (N. Y.)*, 165(1):38 – 58, 1985.

[162] T. Padmanabhan. Planck length as the lower bound to all physical length scales. *Gen. Rel. Gravit.*, 17(3):215–221, Mar 1985.

[163] T. Padmanabhan. The role of general relativity in the uncertainty principle. *Class. Quantum Grav.*, 3(5):911, 1986.

[164] T. Padmanabhan. Limitations on the operational definition of spacetime events and quantum gravity. *Class. Quantum Grav.*, 4(4):L107, 1987.

[165] L. Parker. Particle creation in expanding universes. *Phys. Rev. Lett.*, 21:562–564, Aug 1968.

[166] L. Parker. Quantized fields and particle creation in expanding Universes: I. *Phys. Rev.*, 183:1057–1068, Jul 1969.

[167] L. Parker. Quantized fields and particle creation in expanding Universes: II. *Phys. Rev. D*, 3:346–356, Jan 1971.

[168] J. C. Pati and A. Salam. Unified Lepton-Hadron symmetry and a Gauge Theory of the basic interactions. *Phys. Rev. D*, 8:1240–1251, Aug 1973.

[169] T. G. Pavlopoulos. Breakdown of Lorentz invariance. *Phys. Rev.*, 159:1106–1110, Jul 1967.

[170] E. Pechlaner and R. Sexl. On quadratic Lagrangians in General Relativity. *Comm. Math. Phys.*, 2:165–175, 1965.

[171] P. Pedram. A higher order GUP with minimal length uncertainty and maximal momentum. *Phys. Lett. B*, 714(2):317 – 323, 2012.

[172] P. Pedram. A higher order GUP with minimal length uncertainty and maximal momentum II: Applications. *Phys. Lett. B*, 718(2):638 – 645, 2012.

[173] P. J. E. Peebles. *Principles of physical cosmology*. Princeton University Press, 1993.

[174] P. J. E. Peebles, D. N. Schramm, E. L. Turner, and R. G. Kron. The case for the relativistic hot big bang cosmology. *Nature*, 352(6338):769–776, 1991.

[175] A. A. Penzias and R. W. Wilson. A Measurement of Excess Antenna Temperature at 4080 Mc/s. *Astrophys. J.*, 142:419–421, July 1965.

[176] S. Perlmutter et al. Measurements of ω and λ from 42 high-redshift supernovae. *Astrophys. J.*, 517(2):565, 1999.

[177] J. L. Powell and B. Crasemann. *Quantum Mechanics*. Addison-Wesley, 1961.

[178] R. J. Protheroe and H. Meyer. An infrared background-Tev γ-ray crisis? *Phys. Lett. B*, 493(1):1 – 6, 2000.

[179] S. Rahvar. Cosmic initial conditions for a habitable Universe. *Mon. Not. R. Astron. Soc.*, 470(3):3095–3102, 2017.

[180] R. Rashidi. Generalized uncertainty principle and the maximum mass of ideal white dwarfs. *Ann. Phys. (N. Y.)*, 374:434–443, 2016.

[181] A. G. Riess et al. Observational evidence from supernovae for an accelerating Universe and a cosmological constant. *Astron. J.*, 116(3):1009, 1998.

[182] H. P. Robertson. Kinematics and World-Structure. *Astrophys. J*, 82:284, nov 1935.

[183] H.-S. Roh. Fundamental constants and conservation laws. *hep-ph/0102057*, 2 2001.

[184] M. Rotondo, J. A. Rueda, R. Ruffini, and S.-S. Xue. Relativistic Feynman-Metropolis-Teller theory for white dwarfs in general relativity. *Phys. Rev. D*, 84:084007, Oct 2011.

[185] C. Rovelli. Quantum reference systems. *Class. Quantum Grav.*, 8(2):317, 1991.

[186] C. Rovelli. What is observable in classical and quantum gravity? *Class. Quantum Grav.*, 8(2):297, 1991.

[187] E. E. Salpeter. Energy and pressure of a zero-temperature plasma. *Astrophys. J.*, 134:669, 1961.

[188] R. A. Scalzo, G. Aldering, P. Antilogus, C. Aragon, S. Bailey, C. Baltay, S. Bongard, C. Buton, M. Childress, N. Chotard, Y. Copin, H. K. Fakhouri, A. Gal-Yam, E. Gangler, S. Hoyer, M. Kasliwal, S. Loken, P. Nugent, R. Pain, E. Pécontal, R. Pereira, S. Perlmutter, D. Rabinowitz, A. Rau, G. Rigaudier, K. Runge, G. Smadja, C. Tao, R. C. Thomas, B. Weaver, and C. Wu. Nearby supernova factory observations of SN 2007if: First total mass measurement of a Super-Chandrasekhar-mass progenitor. *Astrophys. J.*, 713(2):1073, 2010.

[189] F. Scardigli. Generalized uncertainty principle in quantum gravity from micro-black hole gedanken experiment. *Phys. Lett. B*, 452(1):39 – 44, 1999.

[190] F. Scardigli. The deformation parameter of the generalized uncertainty principle. *J. Phys. Conf. Ser*, 1275:012004, Sep 2019.

[191] F. Scardigli and R. Casadio. Gravitational tests of the generalized uncertainty principle. *Eur. Phys. J. C*, 75:425, Sep 2015.

[192] F. Scardigli, G. Lambiase, and E. C. Vagenas. GUP parameter from quantum corrections to the Newtonian potential. *Phys. Lett. B*, 767:242 – 246, 2017.

[193] B. E. Schaefer. Severe limits on variations of the speed of light with frequency. *Phys. Rev. Lett.*, 82:4964–4966, Jun 1999.

[194] D. N. Schramm. Cosmological implications of light element abundances: Theory. *Proc. Natl. Acad. Sci. U.S.A.*, 90(11):4782–4788, 1993.

[195] I. I. Shapiro, C. C. Counselman, and R. W. King. Verification of the principle of equivalence for massive bodies. *Phys. Rev. Lett.*, 36:555–558, Mar 1976.

[196] S. L. Shapiro and S. A. Teukolsky. *Black holes, white dwarfs, and neutron stars: the physics of compact objects*. Wiley, 1983.

[197] S. L. Shapiro and S. A. Teukolsky. *Black holes, white dwarfs, and neutron stars: The physics*

of compact objects. Wiley, 1983.

[198] S. S. Shapiro, J. L. Davis, D. E. Lebach, and J. S. Gregory. Measurement of the solar gravitational deflection of radio waves using Geodetic Very-Long-Baseline Interferometry Data, 1979–1999. *Phys. Rev. Lett.*, 92:121101, Mar 2004.

[199] H. L. Shipman. Masses and Radii of white dwarfs. *Astrophys. J.*, 177:723, 1972.

[200] H. L. Shipman. Masses, radii, and model atmospheres for cool white-dwarf stars. *Astrophys. J.*, 213:138, 1977.

[201] H. L. Shipman. Masses and Radii of white-dwarf stars. III - results for 110 Hydrogen-rich and 28 Helium-rich stars. *Astrophys. J.*, 228:240, 1979.

[202] G. M. Shore. Radiatively induced spontaneous symmetry breaking and phase transitions in curved spacetime. *Ann. Phys. (N. Y.)*, 128(2):376 – 424, 1980.

[203] J. M. Silverman, M. Ganeshalingam, W. Li, A. V. Filippenko, A. A. Miller, and D. Poznanski. Fourteen months of observations of the possible Super-Chandrasekhar mass Type Ia Supernova 2009dc. *Mon. Not. R. Astron. Soc.*, 410(1):585–611, 2011.

[204] Y. A. Simonov. The quark compound bag model and the Jaffe-low P-matrix. *Phys. Lett. B*, 107(1):1 – 4, 1981.

[205] S. Smith. The mass of the Virgo cluster. *Astrophys. J.*, 86:23, 1936.

[206] H. S. Snyder. The electromagnetic field in quantized spacetime. *Phys. Rev.*, 72:68–71, Jul 1947.

[207] H. S. Snyder. Quantized Spacetime. *Phys. Rev.*, 71:38–41, Jan 1947.

[208] T. Stanev and A. Franceschini. Constraints on the extragalactic infrared background from γ-ray observations of Markarian 501. *Astrophys. J. Lett.*, 494(2):L159, 1998.

[209] A. A. Starobinsky. Spectrum of relict gravitational radiation and the early state of the Universe. *JETP Lett.*, 30:682, 1979.

[210] A. A. Starobinsky. A new type of isotropic cosmological models without singularity. *Phys. Lett. B*, 91(1):99 – 102, 1980.

[211] A. A. Starobinsky. The perturbation spectrum evolving from a nonsingular initially de-sitter cosmology and the microwave background anisotropy. *Sov. Astron. Lett.*, 9:302–304, June 1983.

[212] A. A. Starobinsky. Nonsingular model of the Universe with the quantum-gravitational de-Sitter stage and its observational consequences. In M. A. Markov and P. C. West, editors, *Quantum Gravity*, pages 103–128. Springer US, Boston, MA, 1984.

[213] K. V. Staykov, D. D. Doneva, S. S. Yazadjiev, and K. D. Kokkotas. Slowly rotating neutron and strange stars in R^2 gravity. *J. Cosmol. Astropart. Phys.*, 2014(10):006–006, Oct 2014.

[214] G. A. Tammann. Cosmic expansion and deviations from it. *Physica Scripta*, T43:31–44, Jan 1992.

[215] Tello-Ortiz, Francisco, Maurya, S. K., Errehymy, Abdelghani, Singh, Ksh. Newton, and Daoud, Mohammed. Anisotropic relativistic fluid spheres: an embedding class i approach. *Eur. Phys. J. C*, 79(11):885, 2019.

[216] K. S. Thorne. Relativistic gravitational effects in pulsars. *Comments on Astrophysics and Space Physics*, 1:12, 1969.

[217] R. C. Tolman. Static solutions of einstein's field equations for spheres of fluid. *Phys. Rev.*, 55:364–373, Feb 1939.

[218] M. H. van Kerkwijk. Merging white dwarfs and thermonuclear supernovae. *Philos. Trans. Roy. Soc. A*, 371(1):20120236, 2013.

[219] S. Vennes. Properties of hot white dwarfs in extreme-ultraviolet/soft X-ray surveys. *Astrophys. J.*, 525(2):995, 1999.

[220] S. Vennes, P. A. Thejll, R. G. Galvan, and J. Dupuis. Hot white dwarfs in the extreme ul-

traviolet explorer survey–II Mass distribution, space density, and population age. *Astrophys. J.*, 480(2):714, 1997.

[221] A. Vilenkin. Classical and quantum cosmology of the starobinsky inflationary model. *Phys. Rev. D*, 32:2511–2521, Nov 1985.

[222] A. G. Walker. On Milne's theory of World-Structure*. *Proc. Lond. Math. Soc.*, s2-42(1):90–127, 1937.

[223] J. L. Walsh, A. J. Barth, L. C. Ho, and M. Sarzi. The M87 black hole mass from gas-dynamical models of space telescope imaging spectrograph observations. *Astrophys. J.*, 770(2):86, May 2013.

[224] P. Wang, H. Yang, and X. Zhang. Quantum gravity effects on statistics and compact star configurations. *J. High Energy Phys.*, 8:43, Aug 2010.

[225] A. H. Wapstra and K. Bos. The 1977 atomic mass evaluation. *At. Data Nucl. Data Tables*, 19(3):177 – 214, 1977.

[226] S. Weinberg. *Gravitation and Cosmology: Principles and Applications of the General Theory of Relativity*. John Wiley and Sons, New York, 1972.

[227] S. Weinberg. *Cosmology*. Oxford University Press, USA, 2008.

[228] J. A. Wheeler. *Gravitational Collapse and the Creation and Annihilation of Matter.* in "Relativity Groups and Topology", ed. B. S. DeWitte and C. M. DeWitte (Gordan and Breach), 1964.

[229] J. C. Wheeler, C. J. Hansen, and J. P. Cox. General relativistic instability in white dwarfs. *Astrophys. J. Lett.*, 2:253, 1968.

[230] M. Yamanaka, K. S. Kawabata, K. Kinugasa, M. Tanaka, A. Imada, K. Maeda, K. Nomoto, A. Arai, S. Chiyonobu, Y. Fukazawa, O. Hashimoto, S. Honda, Y. Ikejiri, R. Itoh, Y. Kamata, N. Kawai, T. Komatsu, K. Konishi, D. Kuroda, H. Miyamoto, S. Miyazaki, O. Nagae, H. Nakaya, T. Ohsugi, T. Omodaka, N. Sakai, M. Sasada, M. Suzuki, H. Taguchi, H. Takahashi, H. Tanaka, M. Uemura, T. Yamashita, K. Yanagisawa, and M. Yoshida. Early phase observations of extremely luminous Type Ia Supernova 2009dc. *Astrophys. J. Lett.*, 707(2):L118, 2009.

[231] S. S. Yazadjiev, D. D. Doneva, K. D. Kokkotas, and K. V. Staykov. Non-perturbative and self-consistent models of neutron stars in R-squared gravity. *J. Cosmol. Astropart. Phys.*, 2014(06):003–003, Jun 2014.

[232] Y. B. Zeldovich and A. A. Starobinsky. Particle production and vacuum polarization in an anisotropic gravitational field. *Sov. Phys. JETP*, 34:1159–1166, 1972.

[233] Y. B. Zel'dovich and A. A. Starobinsky. Rate of particle production in gravitational fields. *JETP Lett.*, 26, 1977.

[234] X.-M. Zhang, J.-X. Sun, and L. Yang. Effect of the minimal length on the thermodynamics of ultra-relativistic ideal fermi gas. *Chin. Phys. Lett.*, 31(4):047301, Apr 2014.

[235] F. Zwicky. Die rotverschiebung von extragalaktischen nebeln. *Helvetica Physica Acta.*, 6:110–127, 1933.

[236] B. Zwiebach. *A First Course in String Theory*. Cambridge University Press, 2nd edition, 2009.